"In order for the light to shine so brightly,
the darkness must be present."
~Francis Bacon~

Members of the jury

Chairman

Prof. dr. S. Hendrix, Hasselt University, Diepenbeek, Belgium.

Promoters

Prof. dr. M. Ameloot, Hasselt University, Diepenbeek, Belgium.

Prof. dr. M. Roeffaers, Catholic University of Leuven, Leuven, Belgium.

Co-promoters

Prof. dr. I. Lambrichts, Hasselt University, Diepenbeek, Belgium.

Prof. dr. H. Van Oosterwyck, Catholic University of Leuven, Leuven, Belgium.

Other members

Prof. dr. L. Michiels, Hasselt University, Diepenbeek, Belgium.

Prof. dr. T. Nawrot, Hasselt University, Diepenbeek, Belgium.

Prof. dr. J. Hofkens, Catholic University of Leuven, Leuven, Belgium.

Prof. dr. K. Braeckmans, Ghent University, Ghent, Belgium.

Prof. dr. R. Samson, University of Antwerp, Antwerp, Belgium.

Preface

Starting the engine of your car, lighting the fireplace or BBQ, standing next to the copy machine, … These all seem harmless activities, but in fact during each of them soot particles are produced and emitted. Research has already proven that inhaling these very small, pitch-black carbon-based particles can cause tremendous adverse health effects to the human body. As a result, each year, a staggering amount of people die prematurely due to these carbonaceous particles and the associated cost to the global economy amounts over 225 billion dollars.

It is an urgent matter to come up with a solution for this global burden and to safeguard everyone's health. Unfortunately, up to now, researchers have been *groping in the dark* about the exact toxicological mechanisms of carbonaceous particles, since there is no available detection technique to adequately monitor these materials in biological settings. Hence, the first part of this dissertation focuses on the development of novel optical-based analytical tools, which allow readily qualitative and quantitative determination of carbon-based particles. In the second part, these novel tools are evaluated in different biological settings and the toxicological mechanism of the particulates is elucidated.

This dissertation is a composition of five manuscripts, preceded by an introduction and followed by a general discussion. The introduction reviews currently available techniques for the detection of carbon-based particles and already known toxicological effects of the particles. In the general discussion and outlook, all findings are put in perspective to address the different research aims, and sections are devoted to the future perspectives with regard to carbonaceous particle detection in both toxicological and epidemiological research.

Table of contents

Preface I
Table of contents III
List of figures IX
List of tables XIII
List of abbreviations XV

Chapter 1 Introduction and aims 1

1.1 Air pollution 2
1.1.1 Composition and associated mortality 2
1.1.2 Particulate matter as main culprit? 2
1.1.3 Carbonaceous subcomponent of PM drives adverse health effects 4
1.2 Combustion-derived carbonaceous particles 6
1.2.1 Carbon black 6
1.2.2 Black carbon 9
1.3 Available techniques for determination of CDPs 11
1.3.1 Determination of CDPs in polluted air 11
1.3.2 Determination of CDPs in exposed biological systems 13
1.4 Toxicological effects of CDPs 23
1.4.1 General pathobiological processes 23
1.4.2 General molecular toxicology mechanism 25
1.4.3 General genotoxic and cell death mechanisms 27
1.5 Research aims and outline 29
1.5.1 Aims of the study 29
1.5.2 Dissertation structure 30

Chapter 2 Carbon black detection by femtosecond pulsed laser microscopy 33

2.1 Abstract 34
2.2 Introduction 35

2.3 Materials and methods 37
2.3.1 Materials and products 37
2.3.2 Characterization of carbon black particles 37
2.3.3 CB imaging in various solutions, air and polydimethylsiloxane 37
2.3.4 Absorption spectra CBs 38
2.3.5 Emission spectra CBs 38
2.3.6 Time correlated single photon counting 39
2.3.7 Raman spectra CBs 39
2.3.8 Femtosecond fluorescence up-conversion 40
2.3.9 Cell culture conditions 41
2.3.10 Immunohistochemistry 41
2.3.11 Laser scanning microscopy imaging of CB engulfed by cells 42
2.4 Results and discussion 43
2.5 Supplementary information 53

Chapter 3 Carbon black detection by pump-probe microscopy 67

3.1 Abstract 68
3.2 Introduction 69
3.3 Materials and methods 72
3.3.1 Materials and products 72
3.3.2 Carbon black particles 72
3.3.3 Carbon black solution preparation 72
3.3.4 Cell culture 73
3.3.5 Immunohistochemistry 73
3.3.6 Pump-probe setup 73
3.3.7 Urine samples 74
3.3.8 Microfluidic setup 75
3.4 Results and discussion 77
3.5 Supplementary information 84

Chapter 4 Fibril-based quantification of large cell-induced deformations 89

4.1 Abstract 90
4.2 Introduction 91
4.3 Materials and methods 94
4.3.1 Materials and products 94
4.3.2 Cell culture 94
4.3.3 Synthesis of Collagen Type I Gels with high density of attached beads 94
4.3.4 Image acquisition 95
4.3.5 Sham experiments 96
4.3.6 Assay for cell-induced deformations 98
4.3.7 Pre-processing of acquired images 98
4.3.8 Image registration for displacement field calculation 98
4.3.9 Removal of errors caused by engulfed beads in bead-based displacement fields 99
4.3.10 Comparison of cell-induced displacement fields 100
4.3.11 Implementation 100
4.4 Results 101
4.4.1 Sham experiments show spurious displacement patterns 101
4.4.2 Spurious displacement patterns can be corrected 103
4.4.3 Multiscale FFD allows the recovery of large deformations induced by MRC-5 fibroblasts 104
4.4.4 Both fibrils and beads provide comparable displacement fields 108
4.5 Discussion 112
4.6 Supplementary information 115

Chapter 5 Application of WL detection technique in real biological samples 133

5.1 Abstract 134
5.2 Introduction 135
5.3 Materials and methods 137

5.3.1 Calibration experiments for black carbon detection in urine 137
5.3.2 Optimized experimental protocol for black carbon detection in urine. 138
5.3.3 Validation experiments of optimized urinary carbon load technique 139
5.3.4 Study population and sample collection 140
5.3.5 Residential exposure estimates 140
5.3.6 Statistical analyses 141
5.4 Results 143
5.4.1 Calibration, optimization and validation of the label-free optical detection of carbon particles in urine 143
5.4.2 Urinary carbon load and residential black carbon exposure 145
5.5 Discussion 151
5.6 Supplementary information 155

Chapter 6 Multiparametric analysis of the detrimental effects of carbon black particles on human lung fibroblasts 163

6.1 Abstract 164
6.2 Introduction 165
6.3 Materials and methods 168
6.3.1 Materials and products 168
6.3.2 Carbon black particles 168
6.3.3 Characterization of carbon black particles 168
6.3.4 Cell culture and CB treatment 169
6.3.5 Detection of abiotic ROS generation 169
6.3.6 Detection of biotic ROS generation 169
6.3.7 Mitochondrial morphology imaging 170
6.3.8 Mitochondrial function assay 170
6.3.9 Metabolic activity assay 170
6.3.10 Actin cytoskeleton imaging 171
6.3.11 Quantification of cell-induced displacements 171
6.3.12 Collagen type I matrix remodeling imaging 172
6.3.13 Statistical analysis 173

6.4 Results and discussion 174
6.4.1 Characterization of CBs 174
6.4.2 Various CBs have similar inherent oxidative capacity 175
6.4.3 CBs enhance oxidative stress in human lung fibroblasts 176
6.4.4 Interconnections of ROS production, mitochondrial damage and ATP depletion 178
6.4.5 CBs inhibit cell-mediated matrix remodeling 183
6.4.6 ATP depletion as plausible inhibitory mechanism of cell-mediated matrix remodeling? 187
6.5 Supplementary information 189

Chapter 7 General discussion and outlook 191

7.1 Need smoke to be black to constitute an offence? 192
7.2 Novel optical-based analytical techniques for the detection of CDPs 192
7.3 Application of the novel detection techniques in real biological samples 193
7.4 Air quality regulations 195

Summary 197
Nederlandse samenvatting 201
References 205
Curriculum vitae 231
Dankwoord 237

List of figures

Main text

Chapter 1
Figure 1–1: Deposition of PM in the lungs. 3
Figure 1–2: Structure of carbon black. 8
Figure 1–3: Light microscopy observation of carbonaceous particles in biological systems..... 14
Figure 1–4: Deconvoluted Raman spectra of carbon black and diesel soot..... 17
Figure 1–5: Overview of the various pathobiological processes that result in the adverse health effect endpoint associated with CDPs. 23
Figure 1–6: Common molecular toxicology pathway of CDPs. 26
Chapter 2
Figure 2–1: White-light detection of CB. 44
Figure 2–2: Extinction and 2D excitation-emission of CB..... 45
Figure 2–3: White-light emission and temporal response of aqueous CB suspensions. 46
Figure 2–4: Signal of CB particles combined with various conventional contrast-enhancing fluorophores. 49
Figure 2–5: Co-localization study of the tubulin cytoskeleton of MRC-5 lung fibroblasts and engulfed carbon particles. 51
Chapter 3
Figure 3–1: Pump-probe imaging of CB particles. 78
Figure 3–2: Signal of CB particles by pump-probe imaging combined with the detection of conventional contrast-enhancing fluorophores visualizing the cytoskeleton. 80
Figure 3–3: Detection of BC in urine samples by pump-probe imaging..... 82
Chapter 4
Figure 4–1: Schematic overview of the performed analyses and validations. . 101
Figure 4–2: Spurious displacements present in cell-free sham experiments... 103
Figure 4–3: 3D displacements in cell-populated hydrogels. 104
Figure 4–4: Cell-induced alignment of collagen fibrils. 105
Figure 4–5: FFD-based image registration of the cell-induced stressed vs. unstressed hydrogel. 106

Figure 4–6: Symmetric Green-Lagrange strain tensor for a sample cell in 2.4 mg/mL collagen depicted in Figure S10A. 107
Figure 4–7: Representative 3D displacements induced by two different MRC-5 fibroblasts embedded collagen hydrogels. 109
Figure 4–8: Quantitative comparison between the displacements computed from fibril- and bead-based images for cells in 2.4 mg/mL collagen hydrogels. 110
Figure 4–9: Quantitative comparison between the displacements computed from fibril- and bead-based images for cells in 4.0 mg/mL collagen gels. 111

Chapter 5

Figure 5–1: Flowchart of the optimized experimental protocol for black carbon detection in urine..... 143
Figure 5–2: Black carbon particles in urine..... 144
Figure 5–3: Correlation between urinary black carbon load and residential exposure to recent up to chronic black carbon or proximity to major roads. .. 149
Figure 5–4: Receiver operating characteristics (ROC) curve for urinary carbon load distinguishing between high and low residential black carbon exposure. 150

Chapter 6

Figure 6–1: ROS production of CBs under abiotic conditions. 176
Figure 6–2: ROS production of CBs under biotic conditions. 177
Figure 6–3: Mitochondrial damage by CBs in human lung fibroblasts. 180
Figure 6–4: Intracellular ATP content depletion by CBs in human lung fibroblasts..... 182
Figure 6–5: Impaired human lung fibroblast displacements in 3D collagen type I hydrogels induced by CBs. 185
Figure 6–6: Inhibited collagen type I matrix remodeling by human lung fibroblasts exposed to CBs. 186

Supplementary information

Chapter 2

Figure S2–1: TEM images of the four different types of carbon black particles. 54
Figure S2–2: CCB imaging in glycerol and immersion oil. 55
Figure S2–3: Studying optical trapping in PDMS. 56
Figure S2–4: Two-dimensional excitation-emission plot of fCB particles. 57
Figure S2–5: Raman data of ufPL..... 58

Figure S2–6: Normalized white light spectra of CBs. 60
Figure S2–7: Raw data WL emission spectra of aqueous ufP90 suspensions. ... 61
Figure S2–8: Temporal response of CCB particles. 62
Figure S2–9: White-light generation under femtosecond and picosecond illumination. 63
Figure S2–10: Emission power dependence of CB. 64
Figure S2–11: Co-localization study of the tubulin cytoskeleton of MRC-5 lung fibroblasts and engulfed ufP90. 65

Chapter 3

Figure S3–1: TEM images of the different carbon black particles. 84
Figure S3–2: Schematic representation of the pump-probe microscopy approach for CB particles. 85
Figure S3–3: Pump-probe imaging of dry ufPL particles. 86
Figure S3–4: Sketch of the microfluidics setup which was used for particle counting. 87
Figure S3–5: Pump probe delay scan of CCB particles. 88

Chapter 4

Figure S4–1: Schematic representation of the PIV algorithm in TFM. 117
Figure S4–2: Schematic representation of the FFD algorithm in TFM. 118
Figure S4–3: Neighbor bead-bead distance distribution histograms of fiducial markers in collagen hydrogels. 121
Figure S4–4: Evaluation of the attachment of fiducial markers to collagen fibrils. 123
Figure S4–5: Spurious displacements obtained from bead-based images in cell-free sham experiments. 124
Figure S4–6: Evaluation of detection limit of the FFD-based displacement calculation method with synthetic data. 125
Figure S4–7: Detection limit of the FFD-based displacement calculation method from sham experiments. 126
Figure S4–8: FFD-based image registration of the cell-induced stressed vs. unstressed 4.0 mg/mL hydrogel. 127
Figure S4–9: Symmetric Green-Lagrange strain tensor. 128
Figure S4–10: Representative 3D displacements induced by 4 different MRC-5 fibroblasts embedded in 2.4 mg/mL hydrogels. 129

Figure S4–11: Representative 3D displacements induced by 4 different MRC-5 fibroblasts embedded in 4.0 mg/mL hydrogels. 130
Figure S4–12: Quantitative comparison between the displacements computed from fibril- and bead-based images for cells in 2.4 mg/mL collagen hydrogels. 131
Figure S4–13: Quantitative comparison between the displacements computed from fibril- and bead-based images for cells in 4.0 mg/mL collagen hydrogels. 132

Chapter 5

Figure S5–1: Evidence of carbon aggregates in dried urine samples. 157
Figure S5–2: Relation between the added concentration CB in artificial urine and the amount of particles detected per mL urine. 158
Figure S5–3: Unadjusted and adjusted Pearson correlation coefficient. 159

Chapter 6

Figure S6–1: Co-localization study of the actin cytoskeleton of MRC-5 lung fibroblasts and engulfed carbon particles. 189
Figure S6–2: Extent and mode of cell death of human lung fibroblasts after CB exposure. 190

List of tables

Main text

Chapter 1

Table 1–1: Key characteristics of carbon black and black carbon. 7

Table 1–2: Summary of the applicability of a range of detection methods to provide information on carbon black and black carbon. 22

Chapter 5

Table 5–1: Characteristics of the participants. 146

Table 5–2: Residential exposure characteristics. 147

Chapter 6

Table 6–1: Physico-chemical characteristics of the three different types of carbon black particles. 174

Supplementary information

Chapter 2

Table S2–1: Physico-chemical characteristics of the four considered types of carbon black particles. 53

Table S2–2: Raman bands Lorentzian fits. 59

Chapter 5

Table S5–1: Recent, medium-term and chronic NO_2 and $PM_{2.5}$ exposure characteristics. 160

Table S5–2: Sensitivity analysis on the association between urinary carbon load and annual residential black carbon exposure. 161

List of abbreviations

^{111}In	Indium-111 radionuclide
2D	Two-dimensional
3D	Three-dimensional
^{99m}-Tc	Technetium-99m radionuclide
ANOVA	Analysis of variance
a.u.	Arbitrary units
AUC	Area under the curve
ATP	Adenosine triphosphate
BC	Black carbon
BMI	Body mass index
BP	Band-pass
BSA	Bovine serum albumin
CB	Carbon black
CCB	Conductive carbon black particles
CCD	Charge-coupled device
TFM	Traction force microscopy
CDM	Cell-induced displacement microscopy
CDPs	Combustion-derived particles
CI	Confidence interval
CNT	Carbon nanotube
COGNAC	COGition and Air pollution in Children study
COPD	Chronic obstructive pulmonary disease
D-mode	Disordered-mode
DCF-DA	2’,7’-dichlorodihydrofluorescein diacetate
DEP	Diesel exhaust particles
DRS	Diffuse reflectance spectroscopy
DTT	Dithiothreitol
ECM	Extracellular matrix
EDX	Energy-dispersive X-ray
EELS	Electron energy loss spectroscopy
EM	Electron microscopy

EU	Endotoxin units
FBS	Fetal bovine serum
fCB	Fine carbon black particles from Sigma-Aldrich
FFD	Free form deformation
fs	Femtosecond
G-mode	Graphitic-mode
IARC	International Agency for Research on Cancer
ID	Individual
IMDM	Iscove's modified Dulbecco's medium
IQR	Interquartile range
IRF	Instrument response function
LAL	Limulus amebocyte lysate
LII	Laser induced incandescence
LSCM	Laser scanning confocal microscopy
MAPK	Mitogen-activated protein kinases
MEM	Minimum essential medium
MMP	Mitochondrial membrane potential
MRC-5	Human lung fibroblast cell line
NA	Numerical aperture
NC	Negative control
NF-κB	Nuclear factor- κB
NO_2	Nitrogen dioxide
OPO	Optical parametric oscillator
PBS	Phosphate buffered saline
PDMS	Polydimethylsiloxane
PIV	Particle image velocimetry
PL	Photoluminescence
PM	Particulate matter
$PM_{0.1}$	Ultrafine particulates; Ø < 0.1 μm
$PM_{2.5}$	Fine particulates; Ø < 2.5 μm
PM_{10}	Coarse particulates; Ø < 10 μm
PMT	Photomultiplier tube
PTV	Particle tracking velocimetry

ROC	Receiver-operating characteristic
ROS	Reactive oxygen species
RS	Raman spectroscopy
SD	Standard deviation
SEM	Scanning electron microscopy
SHG	Second harmonic generation
SI	Supplementary information
SIRM	Saturation isothermal remanent magnetization
STICS	Spatio-temporal image correlation spectroscopy
TEM	Transmission electron microscopy
TFM	Traction force microscopy
ufP90	Ultrafine carbon black (Printex 90) particles from Orion Engineered Carbons
ufPL	Ultrafine carbon black particles from PlasmaChem
US EPA	United States Environmental Protection Agency
UV	Ultraviolet
WHO	World Health Organization
WL	White-light

Chapter 1
Introduction and aims

1.1 Air pollution

One of the most familiar and obvious types of air pollution is the thick greyish-brown blanket of smog covering cities. Nonetheless, there are various kinds of contaminating compounds – some visible, others invisible – attributing to the pollution of the Earth's atmosphere. Generally, any type of substances naturally occurring or introduced by people into the atmosphere that have injurious effects on living organisms, ecosystems, the climate, and subsequently the society and economy are considered air pollution.

1.1.1 Composition and associated mortality

Air pollution can consist of solid particles, liquid droplets as well as gases. These polluting substances may be classified as either primary (*i.e.* directly emitted in the atmosphere) or secondary (*i.e.* formed in the atmosphere from so-called precursors), and as natural or anthropogenic depending on their origin of emission or precursor [1].

The exact composition of polluted air depends on the emission source. In Western countries, where vehicle traffic is a major contributor to ambient air pollution, the most abundant and important air pollutants include nitrogen oxides, ozone, toxic metals, black carbon, inorganic carbon compounds (*i.e.,* carbon monoxide), and organic compounds like polycyclic aromatic hydrocarbons and benzene [1].

According to recent research, worldwide more than 6.5 million people die prematurely every year due to air pollution [2]. As a result, ambient air pollution exposure is the 4th highest-ranked health risk factor for death in the world [3].

1.1.2 Particulate matter as main culprit?

Particulate matter (PM), alternatively referred to as particulates or atmospheric particles, is a complex, heterogeneous mixture of fine solid or liquid particles suspended in air that varies continuously in size and chemical composition in space and time [4]. Anthropogenic sources of PM include solid-fuel combustion (*e.g.,* coal, heavy oil and biomass), industrial emission, and abrasion of road surfaces, tires and brakes [5]. Generally, PM is classified by its aerodynamic equivalent diameter, which is the main criterion to describe its transport ability

in the atmosphere and/or inhaling ability through a respiratory organism (Figure 1-1) [6]. Particles with a diameter smaller than 10 μm (PM_{10}) are of particular interest as they can deposit in the respiratory system. These coarse particles have an aerodynamic diameter between 2.5 and 10 μm, and are deposited in the nasal cavities and upper airways. They are predominantly constituted of salt, nitrate, and road dust elements [7, 8]. Fine particles, smaller than 2.5 μm in diameter ($PM_{2.5}$), are deposited into the trachea-bronchial or even the alveolar region depending on their actual size. This category of particles mainly embodies sulfates, nitrates, organic compounds, black carbon (*vide infra*, section 1.2.2), and metals such as iron and lead [7-9]. Ultrafine particles have an aerodynamic diameter of less than 0.1 μm ($PM_{0.1}$) and are mainly deposited in the alveoli from which they can even translocate to the systemic circulation (Figure 1-1) [10].

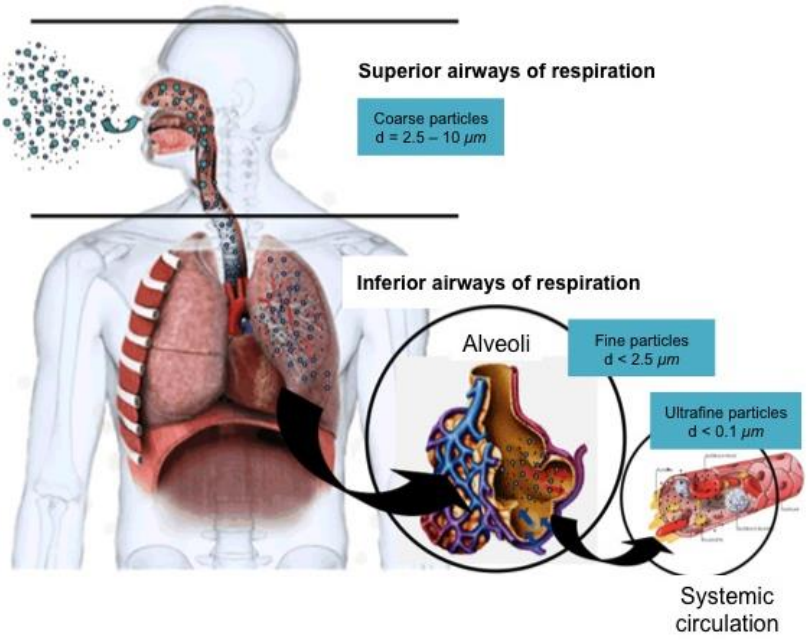

Figure 1–1: Deposition of PM in the lungs.

The deposition of PM is dependent on the aerodynamic diameter of the particles. Adapted from (open access) Guarieiro et al. [11]; originally published under CC-BY 3.0 license, copyright © 2013. Available from: DOI 10.5772/52513.

Among the premature deaths due to air pollution, PM is responsible for the mortality of approximately 4.2 million people, or more than 50%, per year [2]. The presence of PM poses more danger to the human health than other common air pollutants, such as carbon monoxide or ozone [12, 13]. Hence, PM is often designated as the main culprit of air pollution-related health problems.

As a consequence of its complex composition, PM causes a broad range of adverse health effects to the human body. Exposure to PM is associated with respiratory diseases, such as chronic obstructive pulmonary disease [14], asthma [15], and underdevelopment of the lungs in children [16]. Besides pulmonary diseases, PM is associated with cardiovascular morbidity and mortality including stroke, myocardial infarction, cardiac arrhythmia, and heart failure [17-19]. PM is even considered carcinogenic by the International Agency for Research on Cancer (IARC) [20, 21]. Additionally, in a recent study it was shown that $PM_{2.5}$ can be related to dementia [22]. This is in agreement with other studies, which report PM as being neurotoxic resulting in decreased cognitive functioning in children [23, 24] and impaired cognitive aging [25].

1.1.3 Carbonaceous subcomponent of PM drives adverse health effects

PM is a heterogeneous mixture of various particle types, but it is unlikely that all are equally important in causing the wide array of adverse health problems reported in PM-related studies [26]. Hence, the hypothesis has arisen that a specific constituent of PM drives the most detrimental effects [26-28]. Already some research has been, and is being, undertaken to verify different hypotheses about which of the subcomponents of PM are in fact responsible [26, 28-30]. In the light of these studies, combustion-derived carbonaceous particles (CDPs) are thought to be more harmful to human health than those generated by other means [26, 29, 31, 32]. For example, Grahame and Schlesinger concluded that black carbon particles, an exemplar CDPs, are a major environmental cause of cardiovascular mortality and morbidity [33]. They even suggested that it may be desirable to promulgate a black carbon $PM_{2.5}$ standard under the National Ambient Air Quality Standards.

So far however, no detection methods have been reported that enable adequate probing of carbonaceous particles in relevant samples such as exposed cells and body fluids. Hence, despite the increased comprehension and awareness of the

health consequences related to CDPs and the need for other/additional metrics of PM, a critical barrier to progress in the field is the limited ability to adequately monitor these types of particles (*vide infra*, section 1.3). Consequently, it is highly desirable that novel detection methods are developed for the qualitative and quantitative analysis of CDPs in order to fully elucidate their detrimental effects. This will readily allow associations with adverse health effects and will result in an improved understanding of their specific toxicological effects. Eventually, CDPs may become an additional indicator for more precise air quality strategies and management plans.

1.2 Combustion-derived carbonaceous particles

Scientists and regulators often group CDPs together. CDPs present a diverse group of materials originating from incomplete combustion processes and include among others coal fly ash, diesel soot and carbon black. These primary particles arise directly from combustion processes, even though their chemistry may alter with aging as they undergo interactions with various components like other air pollutants. Both combustion material and mode of combustion determine the characteristics of the primary particles. Therefore, CDPs varieties not only show distinguishable heterogeneity in origin but also in diverse physical and chemical characteristics (*e.g.,* particle solubility and size) and related health effects [27, 34]. The exemplar CDPs discussed here are carbon black (CB) and black carbon (BC). As discussed previously by others [34, 35], these two terms have often been, and are still, used interchangeably while CB being a manufactured product having well-controlled properties and BC being an undesired byproduct with divers characteristics. A summary and comparison of the main characteristics of both particle types can be found in Table 1-1.

1.2.1 Carbon black

According to the Scientific Committee on Consumer Safety of the European Commission, CB can be defined as follows: "*A material comprising of elemental carbon in the form of near spherical colloidal particles and coalesced particle aggregates/agglomerates, obtained by partial combustion or thermal decomposition of gaseous or liquid hydrocarbons*" [36]. Like the definition already indicates, CB particles are produced via several well-established manufacturing processes (oil furnace, thermal black, acetylene black, lamp black, channel black, and gas black processes; for an overview of these processes see [37, 38]). The most predominantly used process in the worldwide carbon black production is the oil furnace method [37-39].

Table 1–1: Key characteristics of carbon black and black carbon.

Characteristics	Carbon Black (CB)	Black Carbon (BC)
Origin/Generation	Upscaled commercially manufactured product from thermal decomposition or controlled combustion	Unwanted byproduct from pyrolysis or incomplete combustion
Production Scale	Approx. 9.8 million tons/year	Approx. 8.5 million tons/year
Starting Material	Petroleum oils, natural gas, acetylene, coal-tar residues	Any carbon-containing material (*e.g.,* waste oil, diesel/gasoline fuel, coal, wood, rubber, plastics, household refuse, etc.)
Elemental Carbon Content	Almost pure elemental carbon; > 97%	Extremely variable, source dependent; Often < 50%
General Morphology (shape, form)	Aciniform aggregates and agglomerates	Diesel exhaust: aciniform Other types: predominately non-aciniform
Primary Particle Size (diameter)	Typically ~ 15 – 300 nm Ranging between < 10 – 500 nm	Smaller than many primary CB particles *E.g.,* 15 – 40 nm for diesel exhaust particles
Aggregation/ Agglomeration State and Sizes	Aggregates: typical diameters between ~ 85 – 500 nm Agglomerates: typical diameters between 1 – 100+ *μ*m	Extremely variable, source dependent; Ranging from several tens of nm to microns *E.g.,* mean number of 60 – 100 nm for diesel exhaust aggregates
Exposure Sources	Predominantly occupational: CB manufacturing plants and user industries (*e.g.,* rubber manufacturers) Exposure from ambient air Exposure from consumer products under debate Exposure from anthropogenic sources (*e.g.,* erosion of pavement, abrasion of brakes and tires)	Environmental: omnipresent in environment due to numerous anthropogenic and natural biomass burning sources
References	[34, 35, 37-40]	[34, 35, 41-43]

CB is known to comprise predominantly particle aggregates and agglomerates, and is therefore classified as an industrial aciniform (grape-like) aggregate (Figure 1-2). Primary CB particles, also known as nodules, with typical diameters ranging between 15 – 300 nm are the elementary units [44, 45]. Their molecular structure consists of a condensed aromatic ring system of carbon atoms organized in sheets of various sizes and alignments (*i.e.*, graphite platelets). These sheets are arbitrary arranged around an axis, packed by van der Waals forces, and superimposed to form structures called nodules [37, 46]. Generally, CB primary particles rapidly and irreversibly form fused aggregates within which these particles no longer have discrete physical boundaries [38, 40, 45]. As shown in Figure 1-2, typical CB aggregates have approximately diameters ranging between 85 – 500 nm and consist of a few up to hundreds of particles [44, 45]. Furthermore, larger clusters known as agglomerates may be formed promoted by electrical forces (*e.g.,* van der Waals forces) ranging in diameters between 1 – 100+ μm and consisting of tens to thousands of adhering aggregates (Figure 1-2) [38, 45, 47]. As a result, CB generally exists as complex particle aggregates and agglomerates rather than free individual particles.

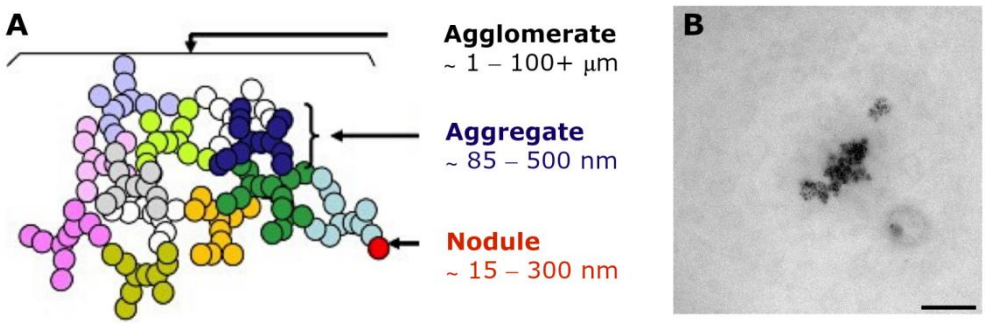

Figure 1–2: Structure of carbon black.

(A) Typical CB structural entities and related size ranges (not drawn to scale), as reported by the International Carbon Black Association [45]. Adapted by permission from Elsevier Ltd.: Environmental Pollution, Long *et al.* [34], copyright © 2013. (B) Transmission electron microscopy image of furnace black agglomerates (Printex 90, provided by Orion Engineered Carbons). Scale bar: 500 nm.

Approximately 90% of CB consumed in the US, Western Europe, and Japan is used in rubber applications like tire-related automotive uses, rubber automotive products, and non-automotive industrial rubber [38, 39]. The remaining 10% is divided among special CB applications including usage as pigment, and UV-absorbing and/or conducting agent in inks, plastics, and coatings [37-39, 45].
The highest risk for CB exposure is during CB manufacturing, collection and handling [38, 39]. Occupational CB exposures can also occur to employees in downstream user industries, like rubber, paint, battery and ink manufacturing [38, 48]. Additionally, CB is emitted in the ambient air during various stages of its manufacturing [39]. CB exposure from consumer products is still under debate. Studies from the United States Environmental Protection Agency (US EPA) and IARC concluded: "*Exposure to carbon black does not occur during the use of products in which carbon black is bound to other materials, such as rubber, printing ink or paint*" [39, 49]. However, authors of the EPA report called their own study "very limited" due to a small number of samples investigated. Nevertheless, there is a growing concern about the safety of CB-containing products, such as tire-derived flooring [50] and black toner powder released from printer ink [51]. Undisputable is the ambient exposure resulting from abrasion of tires and brake blocks [52, 53].

1.2.2 Black carbon

In contrast to CB, there is no universally accepted definition that accurately describes BC. BC is a collective term that comprises a range of carbonaceous substances from partially carbonized plant residues to highly graphitized soot [54]. It is the unwanted byproduct generated by pyrolysis or incomplete combustion of biomass and fossil fuels [34]. The BC particle size depends strongly on the source; ranging from a few nanometers for atmospheric/soot particulates to centimeters for coal fragments of combusted plant materials [54].

According to Bond *et al*. [55] and Petzold *et al*. [56], BC particles are characterized by four fundamental properties discriminating them from other aerosol particles:

1. Insolubility in water and common organic solvents;
2. Aggregated morphology of graphitic sp^2-bonded carbon;
3. Strong visible wavelength-independent light absorption with a mass-specific absorption coefficient of at least 5 $m^2\ g^{-1}$ at 550 nm;
4. Refractory with vaporization temperature near 4000 K.

Condensed aromatic rings and few functional groups dominate the bulk composition of BC [57]. At their onset, BC particles arrange as hydrophobic primary spherule aggregates with irregular shape providing active sites for chemical species deposition [58, 59]. Due to large variability in combustion precursor and conditions (*e.g.,* duration and temperature of combustion, extent of post-combustion aging or weathering), BC particles can be found in a huge variety of different morphology, macromolecular structure, and surface functional group composition [34, 60]. Note that the BC composition not only exhibits large variability between different BC source types, but also within the same type. For an overview of the physical and chemical variations between the different BC particulates, the following reference is recommended [34].

BC particles are ubiquitous in ambient air resulting in routinely exposure of humans to BC from a variety of sources. The global BC emission is estimated to be approximately 7.6 million ton each year [41]. Diverse anthropogenic and natural sources are responsible for the emission of BC particulates. Anthropogenic sources include mobile and stationary diesel and gasoline engines, power generation sources, industrial/commercial boilers, residential combustion sources like woodstoves and fireplaces, and open biomass burning such as agricultural burning [32, 41]. On the other hand, wildfires are the dominant natural BC source [41]. In urban areas, motorized road traffic is a major source of BC particles. The ambient BC concentrations to which humans are actually exposed are depending on their daily activity pattern.

1.3 Available techniques for determination of CDPs

Various studies have provided the irrefutable proof that CDPs are more harmful to human health than those generated by other means like mineral dust (*vide supra*, section 1.1.3). Hence, exposure, risk, and safety issues of CDPs to humans have raised and attracted serious attention from society, academia, and government [13, 36, 61-63].

In order to understand the severity of exposure and to assess the biosafety of CDPs, it is crucial to adequately determine CDPs in a qualitative and quantitative manner in different systems under various conditions. Yet, this is a fairly difficult task due to several reasons: (i) CB and BC are inherently complex materials that show considerable variability [34, 64]; (ii) the background signals in biosystems, especially in body fluids, cells and tissues, are omnipresent and quite intense compared to the CDPs content [65-67]; (iii) due to the variety in biological settings (*e.g.,* air vs. aqueous environments) it is difficult to develop generally applicable techniques [64, 65, 68]; (iv) a characteristic, quantifiable signal of CDPs in aqueous systems is lacking [65], and (v) the technique(s) should be preferably non-destructive and biocompatible in biological settings limiting the determination possibilities. Up to now, the determination of CDPs is limited to techniques, like absorption photometry in air, and light and electron microscopy in aqueous environments or after drying on a substrate. Each technique has its own advantages and disadvantages, as well as application purposes. Still, more reliable and sensitive determination techniques, for sure those probing aqueous environments, are in high demand.

In this subchapter, currently available techniques that are most generally used for the investigation of CDPs are summarized, including their advantages, limitations, and application fields (for a summary see Table 1-2). The techniques can be divided into two categories based on the sample environment, namely air and aqueous (*i.e.,* biological) systems. Note, this review is limited to techniques used for CDPs (CB and BC).

1.3.1 Determination of CDPs in polluted air

Currently, there are no analytical methods that generate a consistent and accurate determination of the carbonaceous content in atmospheric particles.

Usually, they do not readily allow specific detection of PM subcomponents [27, 29, 69]. To date, measurements of polluted air are mainly performed using light-absorption photometry and laser-induced incandescence [55, 56, 70-74]. As the detection of CDPs in air is beyond the scope of this dissertation, only a brief, general description of both techniques will be provided. Interested readers should consult the following review papers for a detailed overview of all available techniques, and detailed information and discussion about these methods: [55, 56, 70]. Nonetheless, a critical analysis of their information input in epidemiological studies is provided here.

One of the most common approaches to determine CB/BC qualitatively and quantitatively in air is the light-absorption method. This method exploits CB/BC's light absorbing properties (*i.e.,* third fundamental property, section 1.2) by correlating the light attenuated or absorbed by a sample to the mass of the absorbing material via a mass-specific absorption coefficient. Here, the assumption is made that the light absorbance or attenuation is equivalent to the mass of CB/BC [55, 56, 70]. However, several limitations are associated with this technique including among others scattering from the filter fibers, shadowing and false response from non-BC particles as a result of internal and external mixing [56, 75]. In the second approach, named laser-induced incandescence, carbon-containing particles are detected by their absorption of intense radiative energy that is transformed into heat resulting in the emission of thermal radiation. Despite the primary signal being generated by radiation absorption, the method response is derived from the thermal emission from the heated matter. Hence, incandescence-based methods are also mass-based [56, 70]. A major obstacle currently limiting these instruments is the absence of established standards or reference materials for calibration [76].

In most epidemiological studies, exposure to PM air pollution, including carbonaceous particles, is estimated using spatial-temporal interpolation models. In these models, data from air pollution stations employing the aforementioned techniques are combined with land use data based on multiple primary sources (*e.g.,* road networks, population and/or building density, etc.) [77, 78]. Beside the shortcomings related to each individual detection technique in air [55, 56, 70], a more general and extremely challenging problem has been raised, namely exposure misclassification [79, 80]. Although air pollution associations are

established as causal [19], risks might be considerably underestimated as the measurements are not performed at the individual or time-activity pattern level resulting in incomplete information about residential mobility. Hence, the critical barrier to progress in the field is imposed by the lack of measurements to monitor adequately personalized exposure over the life course. This suggests that it is extremely important that researchers develop novel detection methods to close this tremendous knowledge gap. It would be most appropriate to develop a technique that allows detection of CDPs in aqueous environments, *i.e.* biological samples, so up-to-date knowledge can be gained on both real exposure values of humans to this type of particles as well as personal values allowing more accurately linkage to detrimental health effects.

1.3.2 Determination of CDPs in exposed biological systems

Toxicology readily studies the effect of carbonaceous particles using one of the following techniques that are available to detect these particles in biological settings: optical and electronic microscopic investigation, Raman spectroscopy, radiolabeling detection, and magnetic-based determination. However, these techniques often lack in sensitivity and specificity.

Optical microscopy

Optical microscopic observation is widely used for the detection of CB and BC in biological systems, like particle suspensions in fluids or particle adsorption and uptake by cells, tissues and organs. This observation is based on the brownish-black color of CB/BC that is directly observable under the optical microscope [65].

For example, optical microscopy is used to investigate CB particle suspensions in biological fluids, such as culture media or bronchoalveolar lavage fluid, to determine their aggregation and agglomeration states (Figure 1-3A). Additionally, the considerable adsorption, uptake and aggregation of both CB and BC by cells after exposure make the direct observation of these particles possible (Figure 1-3B). In epidemiological studies, optical microscopic observation is even the preferred method to assess chronic carbon loading in alveolar macrophages [81]. The high accumulation and aggregation after inhalation also allow direct observation of CB/BC in for example lung tissue

under microscopic visualization (Figure 1-3C) [82]. Even the color change of whole organs can be easily observed even with naked eyes (Figure 1-3D) [82].

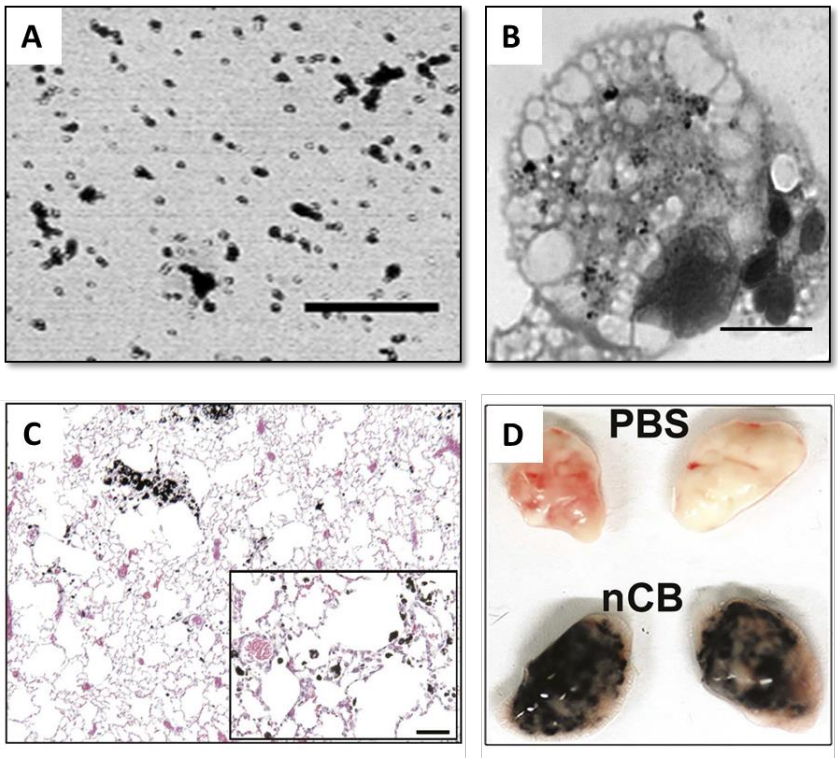

Figure 1–3: Light microscopy observation of carbonaceous particles in biological systems.

(A) Aggregation/agglomeration state of settled CB particles (2 mg/mL, mesoporous fine carbon nanopowder, provided by Sigma-Aldrich) in ultrapure water at room temperature. Scale bar: 30 μm. (B) Carbon loading in macrophages from human induced sputum. Scale bar: 10 μm. (C) Hematoxylin and eosin staining of formalin-fixed lung sections containing nanoparticulate carbon black (nCB) [82]. Scale bar: 100 μm. (D) Image of fresh lungs harvested from mice exposed to vehicle (phosphate buffered saline, PBS) or nCB [82]. C and D reprinted from (open access) You *et al*. [82]; originally published under CC-BY license, copyright © 2015. Available from: DOI 10.7554/elife.09623.

Optical observation of CB/BC is a straightforward method to determine their adsorption, uptake, and aggregation/accumulation in biological systems. It is a label-free and direct method, without the need of additional sample treatment or preparation. Optical microscopy of carbonaceous particles is solely based on

their dark color and thus absorptive character, which should be distinguished from the background by the operator. Consequently, it is a non-specific method since other absorbing and/or light-scattering species may also appear black to the human eye. Additionally, the resolution limit of a light microscope using visible light is about 200 nm, which is insufficient since carbonaceous particles may be as small as 10 nm diameter or less, depending on their origin [56]. Hence, only larger aggregates are detectable making the technique inapplicable to visualize low concentrations and/or single dose administrations. In summary, the sensitivity and specificity of the technique is inadequate to detect CDPs in aqueous environments and it should only be used for illustrative purposes [65].

Electron microscopy

Electron microscopic (EM) observation is the technique of reference for studying CDPs in biological settings [65, 83, 84]. When using EM, carbonaceous particles can be identified as typically black aggregates within tissues, cells and cellular organelles [84, 85]. EM uses a focused, high-energy electron beam that is transmitted through (TEM) or used to scan (SEM) a sample. The electrons interact with atoms in the sample generating various signals, which contain information about the sample such as the size distribution or agglomeration state of carbonaceous materials.

In the first place, EM is used for physicochemical characterization of nanomaterials like CB and BC (Figure 1-2B) [85]. Different parameters can be derived from TEM analysis including size distribution, shape, and agglomeration state of the particulates [85]. However, it is important to realize that the agglomeration state might be affected by the extensive sample preparation procedure. SEM can provide additional information like the surface topography [85].

Moreover, EM is used to study CB/BC internalization in biological samples, like cells and tissues. If CB/BC aggregates or agglomerates are found in the investigated samples, plenty of information is derived about their location, such as the specific cell type incorporating these particles and their distribution pattern at the (sub-)cellular level [65]. For example, by observing ultrathin lung sections of mice exposed to CB, Zhang *et al.* found that these particles were mainly trapped inside alveolar macrophages [86]. Additionally, information can

be derived at the organelle level. In the same study by Zhang *et al.* it was shown that the number of primary and secondary lysosomes of the macrophages was increased and the mitochondrial cristae were broken [86]. While EM is quantitative, it has rarely been used to quantify particles internalization due to the cumbersome sample preparation and small field of view [84].

While EM is regarded as the most conventional visual method to study CDPs internalization in biological samples [65] it only relies, like optical microscopy, on the discrimination of contrasting – in this case electron dense – aggregates from their background. However, often more electron dense structures are present in biological samples or are introduced during sample staining that is generally based on heavy metals. In this regard, conventional EM is not a specific method for visualizing CDPs in biological environments. Hence, EM is often combined with other methods such as energy-dispersive X-ray (EDX), electron energy loss spectroscopy (EELS) or Raman spectroscopy (RS) to obtain more accurate and complementary information, like for example the elemental composition of the particles (*vide infra*, metal-based detection). Additionally, high resolution EM can provide specific information about CDPs based on their characteristic, turbostratic particle morphology, *i.e.* stacking of few carbonaceous layers with a random rotation angle between them and concentrically oriented in space to form an onion-like structure [87-89]. On the other hand, EM is more sensitive than optical microscopy, owing to the smaller wavelength of electrons. Therefore, detailed information about particle aggregates and agglomerates inside cells and tissues can be acquired. But still, due to the lack of contrast between the particles and their background in biological samples, it is not possible to detect low/realistic particle concentration or accumulation levels in cells or tissues [65, 84]. Also, EM does not allow imaging of living cells, and samples require complex and time-consuming preparation protocols. As a result, EM cannot be used for routinely screening purposes. The sample preparation is of great importance and requires careful selection and execution, as it will determine the quality and trustworthiness of the obtained results. Moreover, EM is a time-consuming and expensive method [65].

Raman spectroscopy

Raman imaging, using the spectroscopic properties of carbon-based particles, can overcome the issues of labeling (*vide infra*, radiolabeling detection) and the difficulty to track carbon-based materials in biological systems. CB and BC can be identified and distinguished from other materials by their Raman fingerprints (Figure 1-4) [90]. RS measures the inelastic light scattering; yielding direct information on the vibrational mode of chemical bonds. RS provides sensitive information about systems showing crystalline (ordered) or amorphous (disordered) properties and is extremely selective towards sp^2-hydridized carbon because of its polarizability [91]. If the hexagonal lattices exhibit a long-range order, the material is referred to as graphite. In contrast, carbon produced during combustion of fuels results in short range (disordered) hexagonal lattices [70, 91]. Within an intact lattice, carbon-carbon (C-C) bonds produce characteristic RS-modes at 1575 cm^{-1}, referred to as graphitic or 'G'-mode (D_2). C-C bonds at incomplete hexagonal lattices generate RS-modes at 1500 (D_3) and 1345 (D_1) cm^{-1}, also called the disordered or 'D'-mode. For CB a fourth peak can be observed (D_4), which takes into account the disordered graphitic lattice due to polyenes and/or ionic impurities [90].

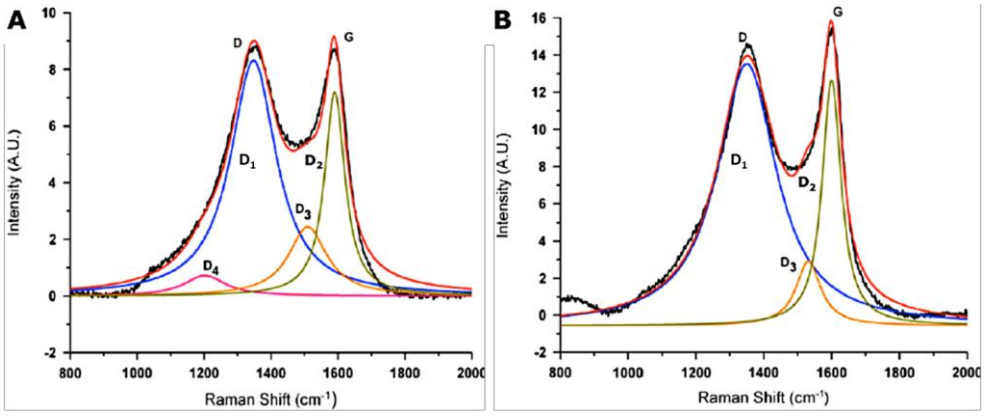

Figure 1–4: Deconvoluted Raman spectra of carbon black and diesel soot.

Deconvoluted Raman spectra of (A) carbon black and (B) diesel soot using Lorentzian curve fit for the D_1, D_2, D_3 and D_4, and D_1, D_2 and D_3, respectively. Detailed information about the various peaks can be found in the accompanying text. Reprinted by permission from Elsevier Ltd.: Tribiology International, Patel *et al.* [90], copyright © 2012.

RS is already widely used for the detection of carbon-based materials such as nanodiamond, graphene, fullerenes and carbon nanotubes in biological systems [65]. However, when screening the literature, it becomes clear that the applicability of the technique for the detection of CB/BC in aqueous environments is rather small. Few studies report RS to detect carbon black in cells, like You *et al.* who identify CB deposition in lung cells isolated from mice exposed to cigarette smoke for four months [82]. In most cases, RS is used as supporting evidence by determining the physicochemical characteristics of carbon black or black carbon (*e.g.,* [92]).

The intrinsic RS-modes are sensitive and stable and do not disappear, quench, or will not diminish under prolonged excitation. It is an intrinsically label-free method. However, RS is a rather slow method and background luminescence overwhelms in biological environments. Usually, bio-samples need to be homogenized, solubilized in suitable buffer solutions, and pre-separated to achieve better results [65]. RS can be considered as semi-quantitative, since a lower signal can be attributed to lower levels of the carbonaceous material or to increased damage of the carbon hexagonal lattices [65]. RS is often combined with other methods to gain complementary information.

Metal-based detection

Particulate matter, including BC, contains trace metals of anthropogenic origin introduced through the emission from the abrasion of tires and brake pads, corrosion of automotive parts, lubricating oils or fuel additives [93]. Additionally, resuspension of soil material formerly enriched with trace metals can act as a possible source. Trace metals often include Fe, Cu, Zn and Pb but their presence and the proportion depends on the local sources [94]. Taking advantage of their non-degradability in the environment [95], metal impurities can be used to indirectly identify airborne particulates in biosystems using various techniques like (high-resolution) EM in combination with EELS- or EDX-analysis, and saturation isothermal remanent magnetization (SIRM) [9, 88].

Metal-based detection using EDX- or EELS-analysis is generally used to indirectly identify combustion-derived particles in biological samples. First of all, the particles are spotted based on their black/absorptive character and/or morphology using EM (*vide supra*, electron microscopy). Next, to obtain

complementary information, elemental analysis is performed to check for trace metals. For example, Maher *et al*. recently detected the abundant presence of magnetite nanoparticles in the human brain, which match perfectly the high-temperature magnetite nanospheres produced during combustion and/or friction-derived heating that are present in large numbers in airborne particulate matter [88]. Here, they also use high-resolution EM and EELS as complementary techniques to gain complementary information on the particles due to lack in specificity of both individual techniques. For example, also endogenous magnetite is present in the brain but could be distinguished by the morphology of the particles (euhedral vs. spherical and turbostratic).

In the last decades, magnetic measurements using SIRM have been increasingly employed to investigate soils, sediments, street and roof dust, or vegetation samples (*e.g.,* plant leaves) as bio-indicator of air pollution ([9], and references therein). It is a simple, robust and cost-effective method to determine the ferromagnetic fraction of atmospheric particulates. The technique has proven its utility, for example as rapid discriminatory tool for ferromagnetic-based pollution facilitating PM source attribution [9]. However, the magnetic signal can vary depending on various parameters such as the fuel type, temperature of combustion or abrasion material. In this regard, it has been found that SIRM values are not necessarily comparable to the estimated content derived by EDX-analysis using SEM [9]. An increasing iron content does not necessarily corresponds to an increasing magnetic signal or vice-versa, since it may contain strongly (magnetite) and/or weakly magnetic (hematite) particles in various proportions.

Magnetic-based detection is an indirect technique for the tracing of metal impurities introduced in airborne particles during their synthesis. The detection sensitivity and specificity is dependent on the employed technique. A major advantage of magnetic-based detection is the high stability of metal impurities. Yet, it is a non-specific technique since these impurities are present at most PM-related particles [96] and, for example, the presence of magnetite can also be attributed to a biological rather than an external pollution-derived source [97]. Moreover, not all CDPs contain trace metals as these are introduced by anthropogenic sources.

Radiolabeling detection

Isotope tracing is an effective and indispensable technique in tracking carbon-based nanomaterials in biological systems [65]. Radiolabeled carbonaceous particles have been used for some time and are mainly employed to study both *in vitro* and *in vivo* uptake and translocation of carbonaceous particles in cells, laboratory animals and even humans (*e.g.,* references [98-100]). For these studies, carbon particle-containing aerosols are labeled or tagged with gamma-radiation emitting radioisotopes. The gamma emission serves as a marker of particle location and amount in the cells, tissues or organs. By tracing the emission over time, data about particle clearance/translocation can be derived [101].

Predominantly, Technetium-99m radionuclide labeled particles (^{99m}Tc-Technegas) are used to study the controversial issue of particle translocation in humans. ^{99m}Tc-Technegas is a suspension of ^{99m}Tc-labeled, ultrafine carbon particles produced in an atmosphere of high-purity argon [101]. Yet, the results obtained from these studies are contradictory. Some human studies show slow clearance rates with most particles retained in the lungs after two days [100, 102], while others report rapid passage of the particles into the systemic circulation [10]. These discrepancies among published data can be explained by the disadvantages of the employed isotope: (i) short physical half-life (6h), (ii) high chemical instability of the labeled particles, (iii) 2.6% activity leaching 48 h after generation, and (iv) presence of free pertechnetate in the generated aerosol [100, 103]. Therefore, a new method for labeling carbon particles with indium-111 (^{111}In) has been recently suggested, offering the advantages of longer physical half-life (2.8 days) and improved chemical stability (97% at 7 days after generation) [103, 104]. Still, various limitations are present: (i) labeling techniques are employed, which implies the insurmountable need of introducing exotic carbon particles (*i.e.,* administration of labeled carbon black instead of the detection real exposure levels) and it may possibly change the properties of the particles [65], (ii) short-term exposure conditions, (iii) limited post-administration follow-up (up to four weeks) due to decay of the radionuclides [103], and (iv) exposure of the subject to radiation. On the positive side, the labeling methods are often simple, reliable and effective [65], and the detection is relatively sensitive and specific.

Conclusion

In summary, all current available methods including light and electron microscopy, Raman spectroscopy, metal-based detection and radiolabeling detection, lack specificity and/or sensitivity. By specificity it is meant that the signal provided by the technique is not characteristic and cannot be attributed solely to the presence of carbonaceous particles. The lack of sensitivity is due to various reasons including limited resolution, overwhelming background signal, and limited half-life in the case of radionuclide labeled particles. To date, the different techniques often are combined to identify CDPs in biological samples. However, this is neither practical nor providing reliable results. Hence, it is highly desirable that novel techniques are developed which allow readily detection of CDPs in biological samples.

Table 1–2: Summary of the applicability of a range of detection methods to provide information on carbon black and black carbon.

	Available detection method						
	Light-absorption photometry	Laser-induced incandescence	Optical microscopy	Electron microscopy	Raman spectroscopy	Radiolabeling detection	Metal-based detection
Main application in air	⊙	⊙					
Main application in biological settings			⊙	⊙	⊙	O	•
Label-free	✓	✓	✓	✓	✓	×	✓
No additional sample preparation	✓	✓	✓	×	~	✓	✓
Straightforward	✓	✓	✓	~	~	×	~
Non-destructive/ biocompatible	NA	NA	✓	×	✓	✓	×
Sensitive	✓	✓	×	✓	~	~	✓
			Optical resolution		Omnipresent background	Half-life probe	
Specific	~	~	~	~	✓	~	~
	e.g. external mixing	e.g. pyrolysis OC	Non-CDPs absorbers	Non-CDPs absorbers		Pertechnetate and leaching	e.g. strong vs. weak magnetization
References	[56, 70, 71, 73, 74, 79, 112]	[56, 70-73]	[65, 81, 111]	[65, 83-85, 110]	[65, 70, 90, 109]	[65, 98, 100, 103, 104, 108]	[9, 88, 95-97, 105-107]

⊙ CB + BC, O CB, • BC, ✓ yes, ~ in some cases, × no, NA not applicable.

1.4 Toxicological effects of CDPs

Epidemiological studies have already associated several health risks with the exposure to combustion-derived particles (*vide supra*, section 1.1.3). In this section, the evidence for detrimental health effects of CDPs is placed in the context of a unifying hypothesis that CDPs have the generic ability to cause inflammation *via* oxidative stress and activation of redox-sensitive transcription factors [27, 113].

As mentioned earlier, the exemplar CDPs discussed here are carbon black and black carbon. These different particles should not be confused with each other, since they have quite different characteristics. However, they also have some similarities like their insoluble carbon core and large surface area. Hence, carbon black particles are often used in toxicology research as simplified model for black carbon [114, 115].

1.4.1 General pathobiological processes

Exposure to CDPs is associated with a range of detrimental health effects including cardiovascular and pulmonary diseases, cancer, dementia, and impaired cognitive functioning (*vide supra*, section 1.1.3). These endpoints are found across several pathobiological routes as schematized in Figure 1-5.

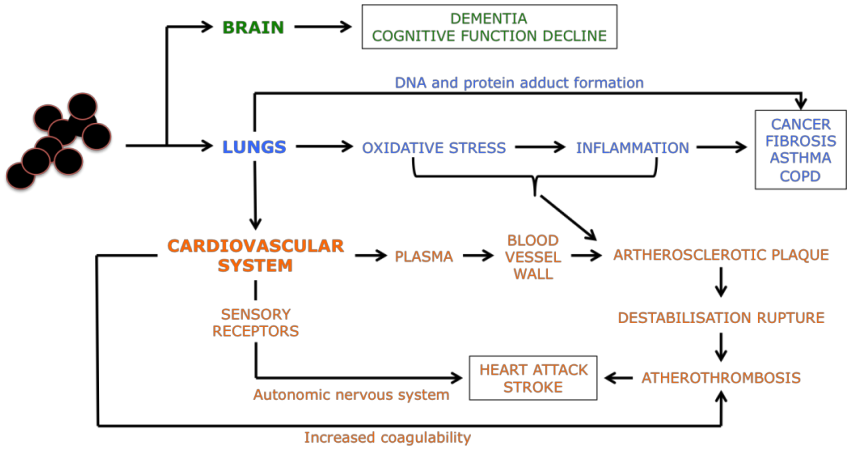

Figure 1–5: Overview of the various pathobiological processes that result in the adverse health effect endpoint associated with CDPs.

COPD, chronic obstructive pulmonary disease.

CDPs and the lungs

CDPs deposition after inhalation depends largely on the aerodynamic diameter of the aggregates/agglomerates (*vide supra*, section 1.1.2) rather than on their chemical nature [116]. In contrast, the toxicity is influenced by the composition of the particles. As mentioned previously (*vide supra*, section 1.2), BC particles consist of a carbon core with adsorbed organics and transition metals while CB particles are generally almost free of metals and organic compounds. Still, their overall toxicological mechanism can be generalized as described in detail in section 1.4.2. In general, CB and BC can induce oxidative stress resulting in inflammation in the lung environment [27, 113].

Additionally, the direct interaction of organic components or their related ROS can cause DNA or protein adduct formation, which can be involved in the listed pathogenesis (Figure 1-5, blue) [27]. This process of adduct formation is well understood for cancer, where guanine adduction is a common feature after exposure to metabolites of polycyclic aromatic hydrocarbons [117]. Also, protein adduction and oxidation are profoundly involved in altering the cellular redox balance and the initiation of gene expression for components of the inflammatory pathways [113].

The resulting enhanced inflammation will aggravate pulmonary diseases in susceptible individuals [113]. Chronic inflammation can lead to airway remodeling and fibrosis, and can have a role in the induction of lung cancer [113, 118-120].

CDPs and the cardiovascular system

In general, three hypothetical pathways are differentiated whereby CDPs deposited in the lungs might induce impaired cardiovascular functioning. These pathways include, detrimental effects *via*: (i) inflammation, (ii) translocation into the cardiovascular system, and (iii) the autonomic nervous system [113].

Oxidative stress and inflammation in the lung can exacerbate effects *via* host-derived mediators. These components can translocate into the circulation as well as the organic compounds, metals, and particles, which can pass directly into the bloodstream in varying degrees. In the circulation, atherosclerotic plaques might be present that can be directly affected by the translocated compounds resulting in their destabilization or/and rupture [113]. Additionally, changes in

the plasma may occur due to increased coagulability. Consequently, this might result in a propagated thrombus that is also larger in size [121]. Further, carbonaceous particles are hypothesized to stimulate sensory receptors within the lungs. This signal may pass *via* the central nervous system leading to changes in cardiac function, such as changes in heart rate variability [122].
Eventually, all these effects may lead to atherothrombotic events cumulating in a heart attack or stroke (Figure 1-5, orange).

CDPs and the brain

Oberdörster *et al.* have demonstrated the transfer of radiolabeled particulates from the nose of rats directly into the brain [123]. It has been postulated that this transfer occurs *via* the olfactory nerves running to the olfactory lobes of the brain. This part of the brain is well vascularized providing a potential portal of deposition [27]. A search of relevant terms showed only a few published studies about CDPs particulates related to deleterious effects on the brain. Most of these publications only focus on associations between air pollution concentrations and impaired cognitive functioning and aging (*e.g.,* [22, 24]). However, recent research by Maher *et al.* showed the abundant presence of magnetite-containing particles in the brain that are consistent with high-temperature formation, suggesting that these are airborne combustion-derived particulates [88]. Still, further work is required to improve our understanding about the transfer of CDPs to the brain, but for this appropriate detection methods will be required (*vide supra*, section 1.3).

1.4.2 General molecular toxicology mechanism

Given the fact that both animal and human epidemiological studies show inflammation as a common response to inhalation of CDPs, a unifying hypothesis for their molecular toxicity has been formulated [27, 113]. Both CB and BC have the generic ability to cause their adverse effects through common pathways that produce inflammation *via* oxidative stress. Figure 1-6 shows that different components of CDPs can result in oxidative stress, which acts through redox-sensitive pathways, like mitogen-activated protein kinases (MAPK) and nuclear factor-κB (NF-κB), to cause inflammation. Although the mediating components

differ greatly between both particle types, commonality is found in their ability to cause oxidative stress resulting in inflammation [27].

The role of oxidative stress-sensitive signaling pathways in the transcription of pro-inflammatory gene is generally well-documented and understood as shown diagrammatically in Figure 1-6 for CB and BC [27, 113]. These pathways are mainly stimulated in macrophages and epithelial cells, which encounter and engulf most particles, leading to the expression of pro-inflammatory genes.

Despite the fact both CB and BC share a common molecular toxicological pathway, they are discussed separately in the next paragraphs.

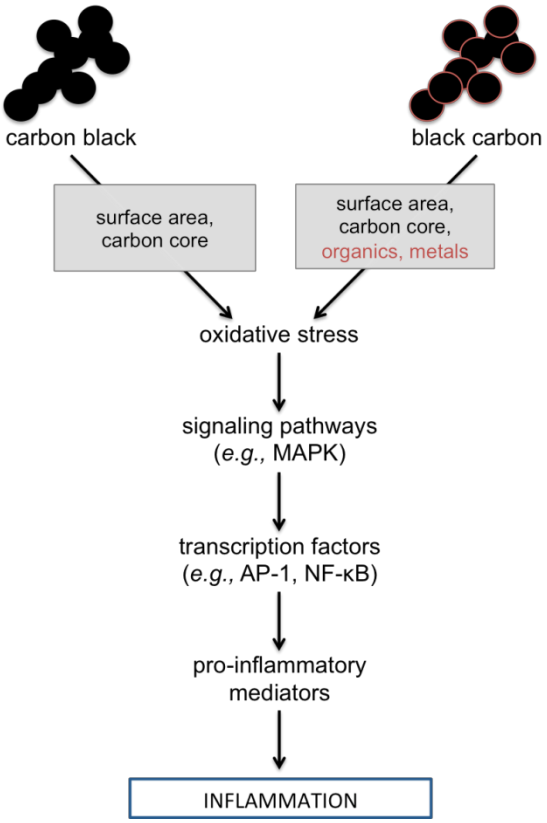

Figure 1–6: Common molecular toxicology pathway of CDPs.

Signaling pathway involved in oxidative stress-responsive pro-inflammatory gene expression by CDPs. MAPK, mitogen-activated protein kinase; AP-1, activator protein-1; NF-κB, nuclear factor-κB. Content of figure based on [27].

Carbon black

ROS production by CB has been demonstrated in both *in vitro* cell-free systems [124, 125] and exposed cells [125, 126]. Unlike black carbon, the ROS production of CB is not related to metal or any other soluble component [127]. As ROS production is also observed in abiotic circumstances, it has been postulated that surface reactivity might play an important role [125, 128].
Already various *in vitro* studies have shown pro-inflammatory responses after incubation with CB involving MAPK, NF-κB, and/or receptor activation for cytokine production (for a review see references [27, 129]). In line, inflammation after *in vivo* subchronic inhalation of CB particles has been illustrated [127, 130].

Black carbon

Particulate matter is capable of producing substantial quantities of radicals [131] that can result in oxidative stress in various environments such as exposed lungs [132, 133]. The components that provoke the oxidative stress and subsequent pro-inflammatory signaling are predominately the organic fraction [134, 135] and transition metals [136, 137]. The organic fraction contains or can be metabolized to compounds like quinones [138]. These species and transition metals are available for redox cycling in cells [136] that can generate ROS such as superoxide and hydroxyl radicals [137]. Various studies have shown the activation of signaling pathways for pro-inflammatory gene expression using for example diesel-exhaust particles (DEP) (for a review see reference [27]). Accordingly, inflammatory responses are found in lungs of mice after short-term exposure to particulates [132, 139, 140].

1.4.3 General genotoxic and cell death mechanisms

CB particles have been shown to produce lung tumors in rats following chronic inhalation and instillation studies; while generally they are almost free of adsorbed organic compounds [141, 142]. Their genotoxicity pathway involves the phenomenon of lung particle overload resulting in chronic inflammation. The excessive ROS production related to this chronic inflammation will lead to DNA damage [27]. As mentioned earlier, genotoxicity by BC is caused directly by the interactions of PAHs that are known to cause DNA and protein adduct formation

[143] or alternatively via DNA stand breakage by ROS associated with transition metals [139].

Already various *in vitro* and *in vivo* studies have demonstrated the ability of CDPs to induce toxicity, although most of them did not properly address the molecular pathways of cell death induction. However, a detailed study of CB induced toxicity in human bronchial epithelial cells was performed [125]. The researchers show that CB exposure results in mitochondrial membrane potential loss, pro-apoptotic protein BAX activation and release of cytochrome c from damaged mitochondria leading to apoptosis of the cells. In general, it can be stated that both CB and BC exposure result in the induction of various cell death modalities, namely apoptosis and pyroptosis [113, 144, 145].

Generally, it can be concluded that both CB and BC are carcinogenic in humans and laboratory animals [20, 21, 120, 141, 146].

1.5 Research aims and outline

1.5.1 Aims of the study

Although efforts have been made in understanding the interaction of CDPs, *i.e.* carbon black and black carbon, with biological systems, enhanced analytical methods to detect these particles in biological systems and to acquire detailed knowledge about their corresponding adverse impact, are still lacking. In this regard, the **first aim** of this dissertation is to develop novel detection techniques for the qualitative and quantitative determination of CB/BC in biological environments by employing their intrinsic characteristics.

Generally, the detrimental effects of carbonaceous particles on cells are evaluated by traditional two-dimensional (2D) assays checking for cell death or damage. These assays have limited complexity, less physiological relevance and – most importantly – they do not examine whether normal cell behavior and functioning like extracellular matrix (ECM) contraction or (re)modeling is preserved. Hence, to enhance our toxicological understanding, three-dimensional (3D) traction force microscopy (TFM) is employed to study the contractile behaviour of cells imbedded in 3D collagen type I hydrogels. Usually, TFM is used to study cellular mechanics in physiological or pathological processes in which cell-induced deformations are derived from the displacement of embedded fiducial markers. However, to our knowledge, TFM has never been used in particle toxicology research. The **second aim** of this research is to expand the existing TFM method to make large cell-induced deformations quantification possible and to study these displacements in a label-free fashion by second harmonic generation (SHG) from collagen fibrils. So, this advanced method can be employed to investigate the effect of CB on the ECM displacements exerted by human lung fibroblasts.

The novel developed probing techniques for the detection of carbonaceous particles – as a result of the first research aim – were evaluated using carbon black as a model compound. However, humans are mainly exposed to black carbon particulates in realistic concentrations. Hence, the **third aim** is to examine the general applicability of the novel probing methods for the detection of black carbon particulates in real biological samples.

During the evaluation of the detection methods, co-localization studies between carbonaceous particles and cellular cytoskeleton revealed heavily disturbed cytoskeletal fibrils after particle incubation periods exceeding four hours. Therefore, the **fourth aim** is to perform a multiparametric analysis including TFM of the detrimental effects of the diverse employed carbon black particles on human lung fibroblasts and to elucidate the interconnecting pathway.

1.5.2 Dissertation structure

(i) Development of novel techniques for qualitative and quantitative detection of CDPs

In **chapter 2** and **chapter 3** two novel tools are described for the biocompatible and label-free imaging of carbonaceous particles. The first technique (chapter 2) is based on white-light generation by these carbon materials under illumination with femtosecond pulsed near-infrared light. The white light emission is characterized using various spectroscopic methods, and is applied to detect the uptake of carbonaceous particles by cells and to check their toxicological effects. In the second technique (chapter 3), particulate detection is performed using pump-probe microscopy, which directly probes the strong light absorption by the particles. The method is evaluated on the detection of carbonaceous particles in cells and human urine, and the versatility is shown by microfluidic analysis of CB-spiked urine samples.

(ii) Advancing TFM: fibril-based quantification of large cell-induced deformations

In **chapter 4**, it is tested whether the traditional TFM procedure can be expanded: (i) to retrieve a similar amount of information from the SHG-signal from the fibrils of 3D collagen hydrogel in which the cells are residing as from embedded fiducial markers, and (ii) to quantify large cell-induced deformations as the studied human lung fibroblasts (MRC-5 cell line) are extremely contractile by nature. Later, in chapter 7, the advanced TFM method is applied to investigate the effect of carbonaceous particles on the matrix displacements induced by human lung fibroblasts.

(iii) Evaluation of novel detection techniques in real biological samples

In **chapter 5**, it is investigated whether the white-light generation method (chapter 2) can be extrapolated to the detection of black carbon particles. For this, a dose-response curve is generated using CB-spiked urine samples and real urine samples are investigated by Raman spectroscopy. Furthermore, it is studied if urinary black carbon in children can be related to ambient air pollution exposure.

(iv) Investigation of CB toxicology in human lung fibroblasts

In **chapter 6**, the specific toxicity of three different types of carbon black particles is investigated in the MRC-5 human lung fibroblast cell line. First, the endotoxin level of the particles is explored. Next, several specific but traditional tests are conducted to check both the abiotic and biotic oxidative potential of CB particulates. Next, their effect on the metabolic activity and the mitochondrial integrity of the cells is tested. Additionally, the effect of the CB particles on the displacements of lung fibroblasts is checked by the advanced TFM technique, described in chapter 4.

Chapter 2
Carbon black detection by femtosecond pulsed laser microscopy

This chapter is based on:

Biocompatible label-free detection of carbon black particles by femtosecond pulsed laser microscopy.

Bové H.*, Steuwe C.*, Fron E., Slenders E., D'Haen J., Fujita Y., Uji-I H., vandeVen M., Roeffaers M., Ameloot M.

Nano Letters. 2016 Apr;16(5):3173-78. IF(2015)=13.779.

* Authors contributed equally.

Declaration of own contribution: Hannelore Bové jointly designed the experiments. She performed characterization of the carbonaceous materials, CB white-light imaging of CB in various solutions, and absorption and time correlated single photon measurements of CB. Additionally, she did the cell preparations, cell exposure, and immunohistochemistry. She also contributed in writing the manuscript.

2.1 Abstract

While adverse health effects of carbon black (CB) exposure are generally accepted, a direct, label-free approach for detecting CB particles in fluids and at the cellular level is still lacking. Here, we report non-incandescence related white-light (WL) generation by dry and suspended carbon black particles under illumination with femtosecond (fs) pulsed near-infrared light as a powerful tool for the detection of these carbonaceous materials. This observation is done for four different CB species with diameters ranging from 13 to 500 nm, suggesting this WL emission under fs near-infrared illumination is a general property of CB particles. As the emitted radiation spreads over the whole visible spectrum, detection is straightforward and flexible. The unique property of the described WL emission allows optical detection and unequivocal localization of CB particles in fluids and in cellular environments while simultaneously co-localizing different cellular components using various specific fluorophores as shown here using human lung fibroblasts. The experiments are performed on a typical multiphoton laser-scanning microscopy platform, widely available in research laboratories.

2.2 Introduction

Carbon black (CB) consists of aciniform aggregates of primary particles with an elemental carbon content greater than 97 % [35, 147]. It is produced through well-controlled incomplete combustion of organics like heavy petroleum or vegetable oil. This distinguishes CB from soot or black carbon, the unwanted by-product released during incomplete combustion processes such as in the exhausts of diesel engines and one of the main contributing factors to atmospheric particulate pollution [35, 148]. Nonetheless, due to the (physico)chemical similarity CB is widely used as a model compound for soot [114, 149]. The total global black carbon emission was estimated to be approximately 8.5 million tons after having constantly increased throughout the preceding decade [150-152]. As a consequence of the increasing environmental and occupational exposure to these carbonaceous particles, deeper insight into the (eco-) toxicological impact of these materials is of critical importance.

So far however, no experimental methods have been reported that enable direct detection of carbon black/black carbon in relevant samples such as polluted water and consumer products as well as exposed cells and body fluids. To date, only measurements [72, 153, 154] in polluted air (see references [56, 112, 153] for an overview) such as absorption photometry and laser induced incandescence (LII) have been used to determine particle concentrations or alternatively labeling methods [10, 98, 155] have been explored such as the technetium-99-m radionuclide labeling in epidemiological studies and toxicology research.

In LII, the emission from carbonaceous materials has been linked to black-body radiation from the severely heated CB particles [156], *i.e.* incandescence. Already various models have been proposed to explain the origin of incandescence and its dependence on illumination power and pulse duration [157-159]. Recently, substantial scientific efforts have focused on white light (WL) emission from carbonaceous materials including graphene [160], fullerenes [161] and carbon nanotubes [162]. Also for these materials the emitted radiation has been linked to incandescence. However, visible emission from CB particles in solution and biological matter has so far not been sufficiently explored, despite reports of CB suspensions serving as optical limiters and

nonlinear scatterers due to their broadband and flat absorption [157, 158]. The interpretation of these effects is not straightforward as they strongly depend on the experimental conditions [163]. Recently, luminescence of carbon particles has been described but this phenomenon seems to be limited to carbon nano-dots, *i.e.* carbon nanoparticles with sizes below 10 nm [164, 165].

To the best of our knowledge, we report here for the first time non-incandescence related WL emission of CB particles in aqueous environments under femtosecond pulsed illumination using a multiphoton laser-scanning microscope and demonstrate its potential in a biological context. This label-free approach to directly visualize CB offers additional advantages (schematic representation in Figure 2-1A) such as inherent 3D sectioning and high imaging depths owing to the multiphoton approach. We anticipate that this method will play an important role in health related studies where the impact and role of CB particles is to be assessed at the organism, tissue, cellular and subcellular level.

2.3 Materials and methods

2.3.1 Materials and products

All chemicals were purchased from Sigma-Aldrich (Belgium) unless stated otherwise.

2.3.2 Characterization of carbon black particles

Four types of carbon black particles (CBs) were used in this study: ultrafine carbon black nanopowder (ufPL; PlasmaChem GmbH, Germany), ultrafine Printex 90 (ufP90; Orion Engineered Carbons, Germany), conductive carbon black nanopowder (CCB; US Research Nanomaterials, USA) and mesoporous fine carbon nanopowder (fCB; Sigma-Aldrich, Belgium). The mean aerodynamic diameters as determined by the manufactures are 13, 14, 150 and 300 nm for ufPL, ufP90, CCB and fCB, respectively (Supplementary information (SI), Table S2-1). The average primary particle sizes and aggregation levels of the CBs were confirmed by transmission electron microscopy (TEM; Tecnai G² spirit twin, FEI, the Netherlands), Figure S2-1. Aqueous stock suspensions (2 mg/mL) were prepared, ultrasonicated for 30 min and stored at 4 °C in the dark until further use. Immediately before use, stock suspensions were ultrasonicated for 20 min prior to dilution in either water, phosphate buffered saline (PBS) or Iscove's Modified Dulbecco's Medium (IMDM; Life Technologies, Belgium) supplemented with 10 % fetal bovine serum (FBS; Biochrom AG, Germany), 100 U/mL penicillin, and 100 μg/mL streptomycin. Hydrodynamic diameters of the particles suspended in ultrapure water and supplemented cell culture medium were measured by dynamic light scattering with a ZetaPALS particle analyzer (Brookhaven Instruments Corp., USA), Table S1. This instrument was also used for Zeta potential determination of the CBs in potassium chloride solution (KCl; 1 mM, pH 7.4) and supplemented cell culture medium.

2.3.3 CB imaging in various solutions, air and polydimethylsiloxane

CCB particles were dispersed at a concentration of 600 μg/mL in ultrapure water, ethanol (Ethanol absolute, VWR Chemicals, Belgium), glycerol (Glycerol BioXtra ≥ 99 %, Sigma-Aldrich, Belgium), microscope oil (Immersol^{TM} 518 F, Carl Zeiss, Germany), and a 10:1 weight-ratio mixture of polydimethylsiloxane

(PDMS) base polymer and curing agent (Dow Corning, Germany) degassed at 0.55 Bar and cured for 30 minutes at 70 °C. The solutions were prepared using the same ultrasonication steps as described before and the dried sample was made by air drying a droplet of CCB in suspension onto a glass cover slide. The images were collected using a Zeiss LSM510 META NLO (Carl Zeiss, Germany) mounted on an Axiovert 200 M equipped with a femtosecond pulsed laser (810 nm, 150 fs, 80 MHz, MaiTai, Spectra Physics, USA) tuned to a central wavelength of 810 nm with a 5 or 10 mW radiant power at the sample position and using a 40x/1.1 water immersion objective (LD C-Apochromat 40x/1.1 W Korr UV-Vis-IR, Carl Zeiss). The resulting 1024x1024 images with a pixel size of 0.22 μm were recorded with a 1.6 μs pixel dwell time at room temperature.

2.3.4 Absorption spectra CBs

The absorption spectra of the CB suspensions were measured with a Lambda 950 UV/Vis/NIR spectrometer (Perkin Elmer, USA) double beam, double mono-chromator, ratio recording UV/Vis/NIR spectrophotometer. The suspensions were prepared as described above and measured in a quartz cuvette (1 cm optical path length) immediately after preparation to minimize sedimentation. Single scans were recorded in the visible spectral range between 400 and 800 nm with a scanning speed of 0.25 nm/s and a slit width of 5 nm.

2.3.5 Emission spectra CBs

CB suspensions were contained in optical chambers fabricated by two glass cover slides held together by double sided adhesive tape (8153LE, 3M, Belgium) with a central punched hole of 5 mm. These CB suspensions or CB particles dried on a cover glass (SI, Figure S2-2) were excited with a conventional femtosecond titanium-sapphire laser (810 nm, 150 fs, 80 MHz, MaiTai, Spectra Physics, USA). The illumination power was set to 8 mW after a 60x/0.95 air objective (CFI Plan Apo Lambda 60x/0.95, Nikon, Japan). A 750 nm short pass dichroic filter was separating the visible emission from the near infrared illumination. The emitted light was focused onto a pinhole and then imaged onto a spectrograph with an attached electron-multiplying charge-coupled device (EM-CCD camera; ImagEM Enhanced C9100-13, Hamamatsu, Japan). An additional short pass filter blocked any fundamental laser light. Integration times

of 45 s were sufficient to generate spectra with high signal-to-noise ratio (> 100).

2.3.6 Time correlated single photon counting

Following femtosecond illumination (810 nm, 80 MHz, 5 mW) of CBs suspended in ultrapure water or dried on a cover glass, the temporal response of the emitted signal was detected using a GaAsP photomultiplier tube (PMT; 7422, Hamamatsu, Germany) after spectral filtering using a dichroic mirror KP 650, a KP 685 short-pass filter and a 450 – 650 nm band-pass (BP) filter. The PMT was connected to an SPC830 card (Becker and Hickl, Germany) which was synchronized to the pulse train of the laser. Recordings of the 256x256 pixel images with a pixel size of 0.11 μm were performed using a pixel dwell time of 6.4 μs.

2.3.7 Raman spectra CBs

Raman spectra were collected with a CCD camera (Newton, Andor, UK) equipped with a blazed grating monochromator (IHR320, Horiba, Japan) with a grating of 1200 l/mm. A 633 nm Helium Neon Laser with an average power at the sample of 15 mW was used (Research and Electro-Optics INC, USA). The Raman signal passed a 645 nm long pass filter after a 100 μm pinhole for confocal detection and the grating monochromator. The slit width was set to 2000 μm. Suspended CB samples were contained in optical chambers described above. The integration time was set to 10 s and averages of 6 scans are shown. Data were collected on a dry powder sample in air at room temperature.

Raman spectra for all samples collected with 633 nm laser illumination displayed very broad D- and G-peaks typical of amorphous carbon [166-171]. Raman spectra were analyzed with the peak fit package as described most recently by O'Haver *et al*. [172]. Background correction was carried out as described by Cadusch *et al.* [173] and references therein.

The Raman spectral feature centering around 1650 cm^{-1} and extending to 1700 cm^{-1} is well-known. It can be assigned to bending-caused broken cylindrical symmetry [174]. These modes are characteristic for strongly deformed bent or dented single walled carbon nanotubes (SWCNT) [175]. Meteorite impact shocked carbon materials show similar internal structures

expected to be in disarray as presented by Ferroir *et al* for shocked graphite [176]. Almost identical triple spectral bands were observed by Yoo *et al* for the transition of shocked C-60 to graphite amorphous carbon mixtures [177]. All Raman spectra were superposed on a reasonable background that fitted well to a Gaussian profile.

2.3.8 Femtosecond fluorescence up-conversion

An amplified femtosecond double optical parametric amplifier laser system was used as illumination source. The power of the laser was set to 150 μW (150 nJ/pulse) at the sample position and the emitted light from the sample was efficiently collected using an off-axis parabolic mirror. The emission was filtered using long pass filters for suppressing the scattered light, directed and overlapped with a gate pulse (810 nm, ca. 10 μJ) derived from the regenerative amplifier onto a lithium triborate crystal. By tuning the incident angle of these two beams relative to the crystal plane the sum frequency of the fluorescence light and the gate pulse was generated. The time resolved traces were then recorded by detecting this sum frequency light while changing the relative delay of the gate pulse versus the sample illumination time. Fluorescence gating was done under magic angle conditions in time windows of 6, 50 and 250 ps.
Monochromatic detection in heterodyne mode was performed using a photomultiplier tube (R928, Hamamatsu, Japan) placed at the second exit of the spectrograph mounted behind a slit. Optical heterodyne detection is a highly sensitive technique to measure very weak changes in absorption induced by a frequency modulated pump beam. The electrical signal from the photomultiplier tube was gated by a boxcar averager (SR250, Stanford Research Systems, USA) and detected by a lock-in amplifier (SR830, Stanford Research Systems, USA).
An additional BP filter 260 – 380 nm was placed in front of the monochromator to reject light from the illumination and the gate pulse. The instrument response function (IRF) of this setup (including laser sources) was determined by detection of scattered light of the laser pulse under identical conditions and found to be approximately 120 fs (full width half maximum). This value was used in the analysis of all measurements for curve fitting using iterative reconvolution of the data sets while assuming a Gaussian shape for the IRF. The sample was prepared in a concentration that yielded an absorbance of ca. 0.4

per mm at the illumination wavelength and was contained in a quartz cuvette with an optical path length of 1 mm. To improve the signal to noise ratio, every measurement was averaged 15 times at 256 delay positions where a delay position is referred to as the time interval between the arrival of the pump and the gate pulses at the sample position. After each experiment the integrity of the samples was checked by recording the steady state absorption and emission spectra and comparing them with those obtained before the experiments. No differences were observed.

2.3.9 Cell culture conditions

Human fetal lung fibroblast (MRC-5 cell line, ATCC CCL-171, LGC Standards, France) cells were maintained (37 °C, 5 % CO_2) in Minimum Essential Medium (MEM) supplemented with 10 % FBS, 100 U/mL penicillin, and 100 μg/mL streptomycin. When 80-90 % confluency was reached, cells were routinely subcultured. Cells for imaging were seeded on 96-well culture plates at a density of 10,000 cells/well and incubated overnight to allow for cell adherence. After washing three times with PBS, cells were treated with 200 μL cell medium containing 5 μg/cm² CB particles. After the exposure for various time periods (4, 8 and 24 h), the cells were washed three times with IMDM before performing immunohistochemistry. Cells that did not undergo CB treatment were used as controls at the various time points.

2.3.10 Immunohistochemistry

Cells were fixed using 4% paraformaldehyde in PBS for 20 min. Permeabilization and blocking was performed for 2 h using 0.3% Triton X-100, 1% bovine serum albumin, and 10% goat serum (Merck Millipore, Belgium) in PBS containing 0.3 M glycine (VWR Chemicals, Belgium) and 5% sucrose. Antibodies were diluted in a blocking buffer consisting of 1% BSA and 0.1% Triton X-100 in PBS. The primary antibodies were monoclonal mouse anti-α-tubulin (1:1,000 for 1 h at room temperature, Sigma-Aldrich, Belgium), monoclonal rat anti-human vimentin (10 μg/mL for 3 h at room temperature, Bio-Techne, UK), and monoclonal rabbit anti-paxillin (1:100 overnight at 4°C, Abcam, UK). The secondary antibodies were donkey anti-mouse Alexa Fluor 488, goat anti-rat Alexa Fluor 555, and goat anti-rabbit Alexa Fluor 647 (1:250, 1 h, Life

Technologies, Belgium). All washes were done three times with PBS for at least 5 min. Before confocal imaging, all wells were aspired and 200 μL Immu-Mount (Thermo Scientific ShandonTM Immu-MountTM, Thermo Fisher Scientific, Germany) was added.

2.3.11 Laser scanning microscopy imaging of CB engulfed by cells

All images were collected at room temperature using a Zeiss LSM510 META NLO scan head mounted on an inverted laser scanning microscope (Zeiss Axiovert 200 M, Germany) and a 40x/1.1 water immersion objective. CB particles were illuminated with a femtosecond laser pulse and 4 mW average laser power at the sample (810 nm, 150 fs, 80 MHz, MaiTai, Spectra Physics, USA). Emission of the particles in the non-descanned mode was observed after spectral separation and filtering of the signal and a 400 – 410 nm BP filter was used to additionally filter the emission light. In the descanned mode, the emitted signal was detected with a BP 650 – 710. The pinhole was opened completely. To avoid cross-talk with the CB white light emission when imaging fluorophore-labelled cellular structures sequential imaging was used.

For imaging the tubulin cytoskeleton of the cells, the microscope was coupled to a 30 mW air-cooled Argon ion laser (LASOS Lasertechnik GmbH, Germany) emitting at 488 nm (~ 3 μW maximum radiant power at the sample). The band-pass filter 500 – 530 was used for filtering the emission signal. For imaging both the actin cytoskeleton and the whole cell, excitation at 543 nm was performed using a 5 mW Helium Neon laser (LASOS Lasertechnik GmbH, Germany, ~ 3 μW maximum radiant power at the sample). The band-pass filter 565 – 615 was used for filtering the emission signal. The resulting 1024x1024 images with a pixel size of 0.06 μm were recorded using a pixel dwell time of 14.2 μs. A fixed pinhole size of 100 μm was used.

Images were captured using the AIM 4.2 software (Carl Zeiss, Germany) and processed with the image processing package Fiji (ImageJ v1.47, Open source software, http://fiji.sc/Fiji).

2.4 Results and discussion

In this study a variety of carbonaceous particles, representative for those to which humans are typically exposed, is used ranging from powders used in copy machines to materials that are typically employed as model for soot. Information on the physico-chemical characteristics of these different commercial CB materials (ufPL, ufP90, CCB and fCB) can be found in Table S2-1 in SI. According to manufacturer's data, the aerodynamic diameter of the particles varies between 13 and 500 nm. Transmission electron microscopy (TEM) images (Figure 2-1B and S2-1) show the typical appearance of CB consisting of aciniform aggregates of primary carbon particles with arbitrary shape. These TEM images and the results from dynamic light scattering summarized in Table S2-1 show that CB particles aggregate when suspended in aqueous solutions, and absorb corona proteins from the complete medium onto their surface resulting in an increased hydrodynamic diameter and a zeta-potential corresponding to approximately -20 mV regardless of their native potential. In conclusion, the physico-chemical characteristics of the different CB particles in suspension are similar although when selecting the particles we aimed for as much difference as possible.

Figure 2-1C displays CB suspended in ultrapure water, ethanol and glycerol illuminated with a femtosecond laser at 810 nm (150 fs, 80 MHz) and recorded using a commercial multiphoton laser-scanning microscope (detailed information on sample preparation and microscopy modalities can be found in SI). Intense signals were detected with an emission band pass filter of 450 to 650 nm in front of the detector. Depending on the suspension medium, the laser power needs to be adjusted to generate similar emission intensity: in glycerol and immersion oil the illumination power was about twice that of the experiment in ethanol or water (SI, Figure S2-2). Note the horizontal smearing of the CB particles in Figure 2-1C (pixel dwell time of 1.60 μs, pixel size of 220 nm). This phenomenon is observed at all combinations of scan speeds and zooms (data not shown), suggesting susceptibility of the particles to optical trapping under these conditions. This hypothesis is further supported by the absence of this smearing when CB particles are embedded in polydimethylsiloxane (Figure S2-

3). Trapping by femtosecond laser pulses has already been shown for other types of nanoparticles [178, 179].

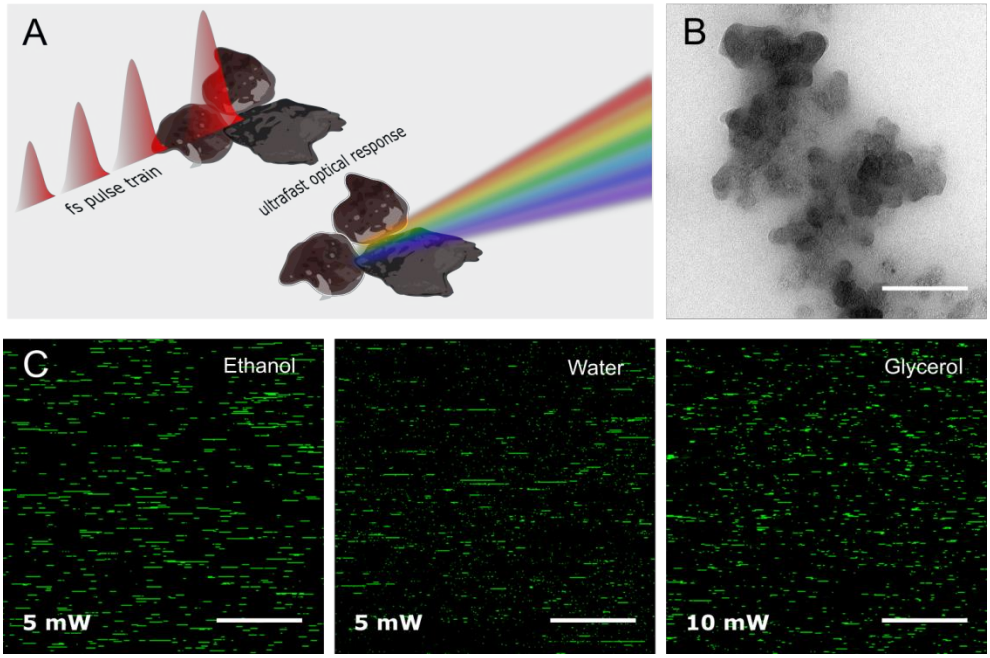

Figure 2–1: White-light detection of CB.

(A) Schematic representation of the illumination and emission process of CB particles for the presented detection method. (B) TEM image of an ufPL aggregate. Scale bar: 300 nm. (C) CCB (600 μg/mL) imaging in ultrapure water, ethanol and glycerol at room temperature upon illumination with 5 or 10 mW average laser power at the sample (excitation 810 nm, 80 MHz). Scale bars: 15 μm. Emission band: 450 – 650 nm.

Additional spectroscopic measurements were performed to investigate the observed visible light emission under femtosecond near-infrared illumination.

Firstly, we rule out photoluminescence (PL) reported for very small carbonaceous particles (below 10 nanometer) [164, 165, 180] as a cause of the observed emission. Carbonaceous particles, in particular soot, consist of aggregated particles that are heterogeneous in nature [112] and therefore contain multiple absorbing species possibly responsible for radiative transitions. The extinction spectra of aqueous suspensions of the CB particles considered here cover the whole visible range (Figure 2-2A), presumably due to a continuum of electronic states in the amorphous carbon. The slight increase of

the extinction towards lower wavelengths for the two smaller particles (ufPL and ufP90) is likely due to increased light scattering.

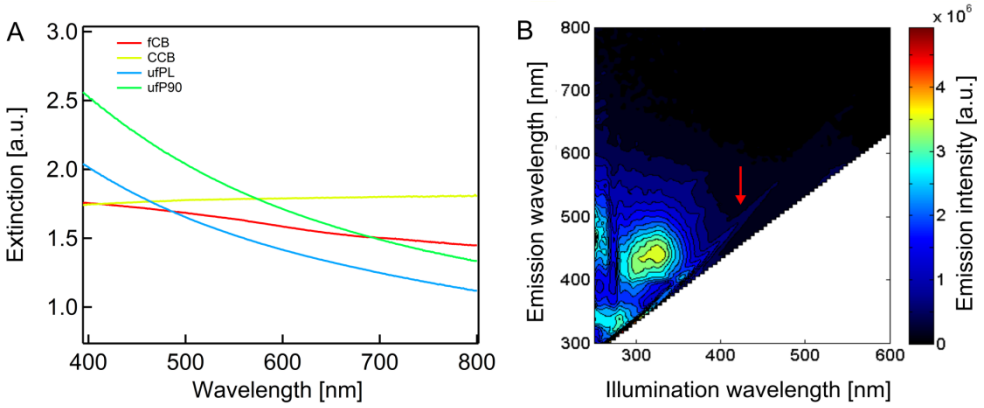

Figure 2–2: Extinction and 2D excitation-emission of CB.

(A) Extinction spectra of aqueous CB suspensions in arbitrary units (a.u.). (B) Two-dimensional excitation-emission plot of ufPL particles in water under single photon excitation with a false color map based on the emission intensity in arbitrary units. The red arrow points towards the Raman line of water.

Two-dimensional single photon excitation-emission plots (Figure 2-2B) of ufPL (similar plot for fCB: SI, Figure S2-4) however, show only weak emission; note in comparison the weak Raman line (red arrow) of water, the suspension medium. The luminescence under excitation in the ultraviolet (UV) region (280 – 380 nm) looks similar to the observations described by Kwon *et al.* for carbon nano-dots [181, 182] and hints towards micro-crystalline graphite exhibiting only a low number of tetrahedral sp^3-sites [182-184] which is also confirmed by Raman spectra (SI, Figure S2-5 and Table S2-2).

In contrast to single photon excitation, illumination with femtosecond pulsed near-infrared light (810 nm, 150 fs, 80 MHz) generates a strong, feature-less white light emission stretching the whole visible spectrum (Figure 2-3A and B). This observation was made for all four types of aqueous CB suspensions used in this study and even for dry particles (SI, Figure S2-6). This WL emission is independent of the illumination wavelength within the range of 780 to 900 nm for a constant average power of 8 mW at the sample (Figure 2-3B, see also SI, Figure S2-7).

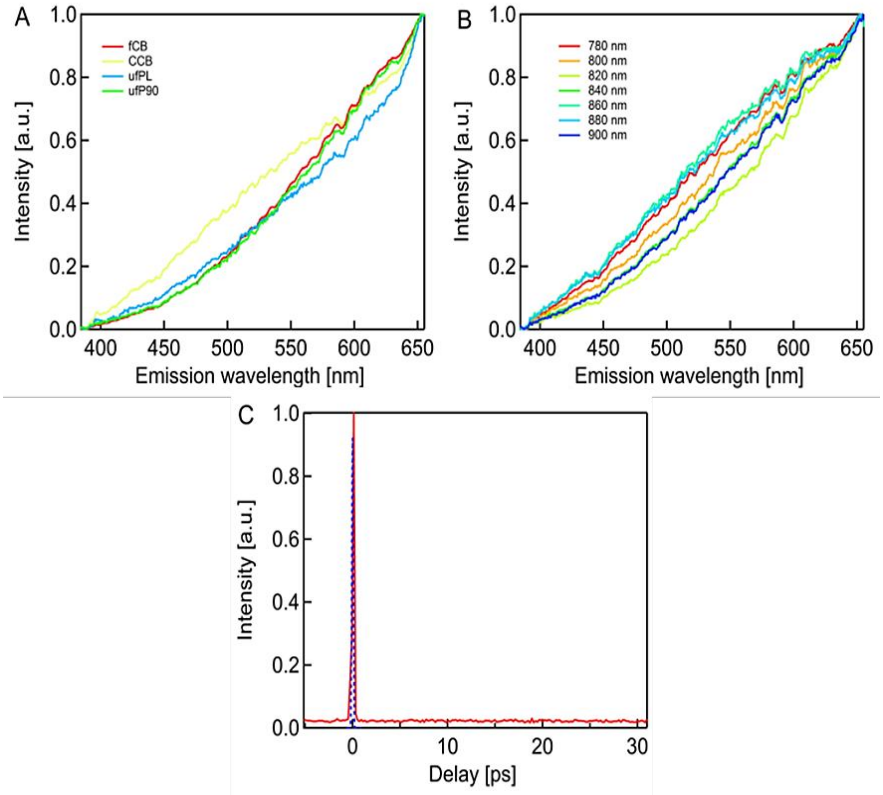

Figure 2–3: White-light emission and temporal response of aqueous CB suspensions.

(A) Normalized WL emission spectra of aqueous CB particle suspensions using femtosecond 810 nm laser illumination (8 mW, 150 fs, 80 MHz). (B) Normalized WL emission spectra of aqueous ufP90 suspensions recorded at different femtosecond illumination wavelengths. (C) Temporal response of aqueous carbon suspension measured by femtosecond photoluminescence up-conversion experiments. Also shown is the instrument response function (dashed line).

While PL as visible in Figure 2-2B cannot explain the strong WL emission observed under femtosecond illumination (Figure 2-1C, 2-3A and B), time-resolved investigations are indicative. Using time correlated single photon equipment, an instantaneous nature of the WL radiation is noticed when looking at the picosecond timescale (SI, Figure S2-8). Also in femtosecond up-conversion experiments with a higher temporal resolution the emitted signal of the CB particles is witnessed to be instantaneous (Figure 2-3C). On further note,

illumination with 7 ps pulses results in a strongly reduced luminescence intensity (SI, Figure S2-9). The WL emission from the suspended CB particles is therefore only efficiently triggered by femtosecond illumination with high peak electromagnetic fields and once the femtosecond illumination pulse ceases, the WL emission terminates immediately.

The instantaneous nature of the observed signal confirms that we are not dealing with incandescence despite using laser illumination with fluences of about 0.05 J/cm² at 0.1 nJ pulse energy, similar to previous experiments. In those reports, the observed incandescence showed clear decay times in the microsecond time scale regime [183] due to the cooling down of the lattice at these time scales. In fact, heating of the particle lattice, which is required for incandescence, only occurs on a picosecond time scale when remaining non-emitted energy will be converted into lattice vibrations [184-186]. The femtosecond illumination employed here is too fast.

The observed instantaneous WL emission is also not related to local refractive index changes in the CB nanoparticle environment upon pulse arrival. Gold nanoparticles are for example known to form nanometer-sized bubbles when illuminated with pulsed lasers at laser fluencies similar to those applied here [183, 187] and those have been observed leading to scattering [187-189]. If a related principle would be underlying the observed WL emission in CB suspension, the emission spectra would be strongly influenced by the surrounding refractive index. However, even dry particles show the same spectral profile as those suspended in water (SI, Figure S2-6).

We believe that the observed visible light emission under femtosecond near-infrared illumination is related to the broad anti-Stokes emission with non-linear power dependence that was previously observed by other groups for noble metal nanoparticles. In those experiments, the emission arose from femtosecond illumination of gold and silver particles or nanostructures [190-193]. We can confirm that also the WL emission of CB displays a nonlinear, second order response with respect to the incident power (SI, Figure S2-10). The WL emission of gold was recently succinctly investigated by Haug *et al*. [194]. Here, plasmonic confinement of electric fields in metal along with the small dimensions of the emitting particle can presumably relax symmetry selection and momentum conservation rules to allow for (continuous) intraband dipole

transitions, which would otherwise be impossible. The observed emission is independent of the type of metal and the preparation conditions. Even though carbon particles are not metallic in nature and do not show plasmonic modes in the visible or near UV spectral range (see Figure 2-2A), an electron gas could emerge on arrival of a femtosecond pulse. At very high energies, even plasmons or plasmon-like effects have been discovered with electron energy loss spectroscopy in carbon nanotubes and its parent material graphene [195-197] or in graphitic spheres [198]. Buckminsterfullerene [199] and other carbonaceous materials [200] show strong multiphoton ionization. The intense and spectrally broad absorption of the particles could give rise to this phenomenon, promoting resonant multiphoton transitions leading to ionizations [201]. Therefore, consecutive intraband transitions similar to those noticed in plasmonically active metals could be a valid explanation for the observed results.

As a result of visible WL generation by carbon black particles under femtosecond pulsed near-infrared illumination, the signal of the particles can easily be combined with various conventional contrast-enhancing fluorophores used to visualize biological features. As shown in Figure 2-4, the emitted WL can be probed at different wavelengths at laser powers compatible with life cell imaging. Hence, CB detection can be combined with the imaging of cellular compartments stained by different color-label fluorophores (labeling strategy can be found in SI). This simultaneous detection enables unequivocally localization of the particles inside the cells and puts the CB location directly into its biological context.

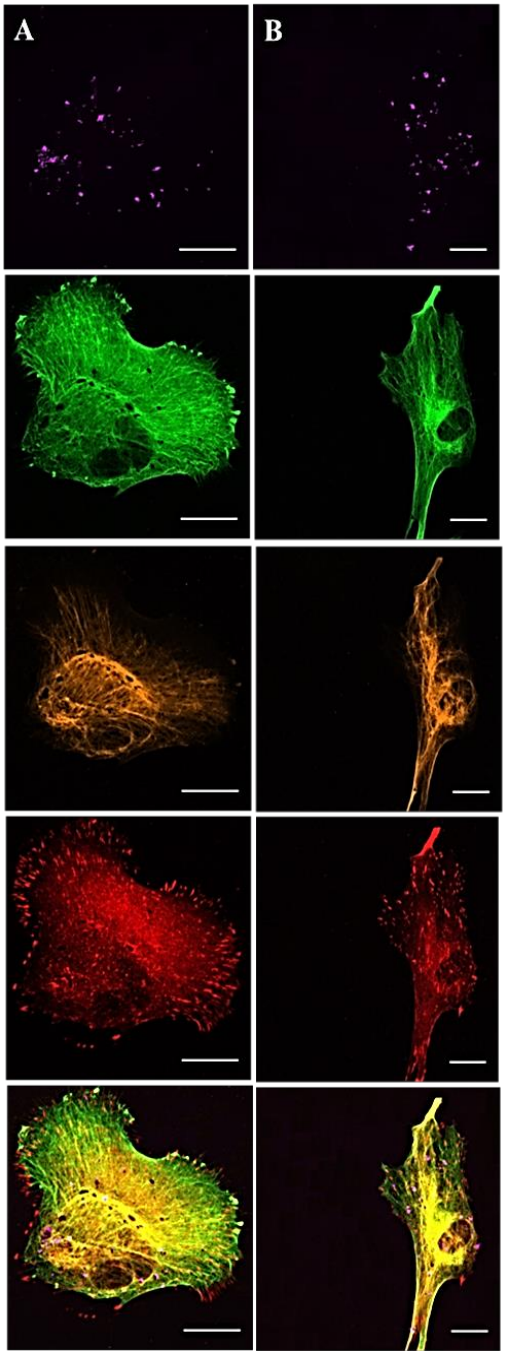

Figure 2–4: Signal of CB particles combined with various conventional contrast-enhancing fluorophores.

Caption on next page.

Imaging of cellular compartments of fixed MRC-5 cells stained with commonly utilized fluorophores and in combination with the detection of CCB particles (4 h incubation of 5 μg/cm2 CCB at 37°C prior to imaging). Emission of the carbonaceous particles can be probed at different wavelengths, here shown at (A) 400 – 410 nm in the non-descanned mode and (B) 650 – 710 nm in descanned mode (4 mW average laser power at the stage). From top to bottom: CCB particles, tubulin cytoskeleton (Ex/Em 495/519 nm, ~ 3 μW radiant power at the sample), vimentin which is an intermediate filament protein of the cytoskeleton (Ex/Em 555/565 nm, ~ 3 μW radiant power at the sample), paxillin expressed at focal adhesions (Ex/Em 650/665 nm, ~ 3 μW radiant power at the sample), and overlay image. Scale bars: 25 μm.

To further illustrate the versatility of the technique in a biological setting, a co-localization study of the tubulin cytoskeleton of MRC-5 lung fibroblasts and engulfed carbon particles was performed (Figure 2-5). The images show a clear impact of CCB on the architecture of the tubulin cytoskeleton of the cells for an incubation that exceeds four hours at 37°C. More specifically, the supporting cytoskeleton network evolves from the commonly observed fiber-like structure to a partial diffuse and holey configuration. The cytoskeletal alteration is also reflected in the overall morphology of the cells. Their appearance changed from the normal bipolar and stretched morphology to a smaller and more irregular shaped one, which is an indication of apoptosis (these biological findings are also true for the other smaller CB particles, for an additional example with ufP90, see SI, Figure S2-11) [126, 202, 203]. These images do not only pinpoint the versatility in biological settings but also immediately indicate the social relevance and significance of this detection technique. Potential advantageous information arising from this simultaneous detection comprises the correlations that can be made between the location of the particles and the altered cellular structure (*e.g.,* cytoskeleton and focal adhesions). This makes the observed WL emission an extremely interesting label-free detection mechanism for biomedical research including toxicology and epidemiology.

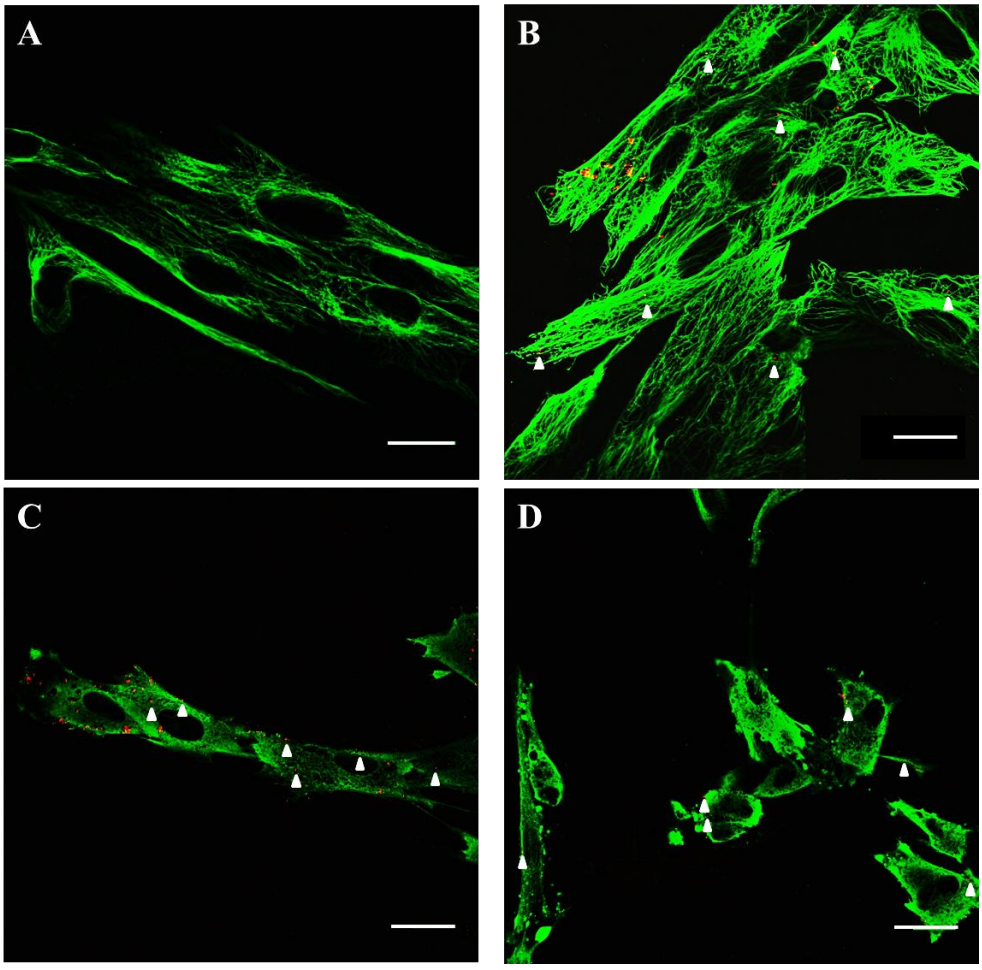

Figure 2–5: Co-localization study of the tubulin cytoskeleton of MRC-5 lung fibroblasts and engulfed carbon particles.

Tubulin cytoskeleton (green, Ex/Em 495/519 nm, ~ 3 μW radiant power at the sample) of normal human lung fibroblasts incubated with 5 μg/cm^2 CCB particles (red, 4 mW average laser power at the sample, emission detection: 400 – 410 nm in non-descanned mode) at 37 °C. (A) Control cells. (B) 4 h incubation. (C) 8 h incubation. (D) 24 h incubation. Scale bars: 30 μm. Arrow heads: some locations of very small, engulfed CCB particles.

To conclude, femtosecond pulsed illumination of CB followed by detection of emitted WL is a straightforward approach without the need of particular sample pretreatment and which can easily be implemented in multiphoton imaging experiments. The nature of the signal makes it very versatile in terms of choice of additional fluorophores. The ease of the reported approach broadens the potential applicability in the fast growing field of nanotechnology. Additionally, it will advance epidemiological and toxicological studies since this is the first time a technique is described to directly detect carbon black in a biological setting without any additional treatment or labeling required. We anticipate that this technology will make it possible to screen human tissues and body fluids for the presence of CB owing to the multiphoton approach which results in inherent 3D sectioning and high imaging depths. This may eventually lead to valuable information about, for example, the actual uptake and clearance of CB particles by the human body.

2.5 Supplementary information

Table S2–1: Physico-chemical characteristics of the four considered types of carbon black particles.

	Aerodynamic diameter (nm) [a]	Hydrodynamic diameter (nm)		Zeta potential (mV) (Mean ± SD)	
		Ultrapure water	Complete medium	KCl solution	Complete medium
ufPL	13	112	171	-12 ± 1	-17 ± 2
ufP90	14	156	218	+29 ± 6	-22.45 ± 0.01
CCB	150	165	226	-48 ± 2	-24 ± 3
fCB	< 500	387	585	-26 ± 3	-21 ± 6

[a] Manufacturer's data

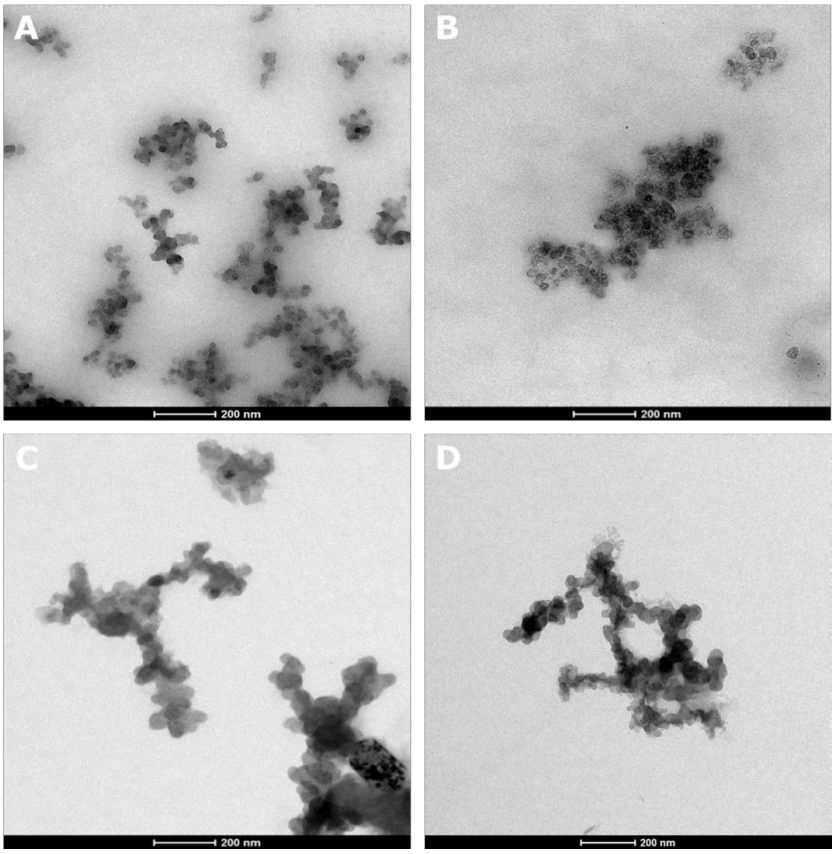

Figure S2–1: TEM images of the four different types of carbon black particles.
(A) ufPL, (B) ufP90, (C) CCB, and (D) fCB. Scale bar: 200 nm.

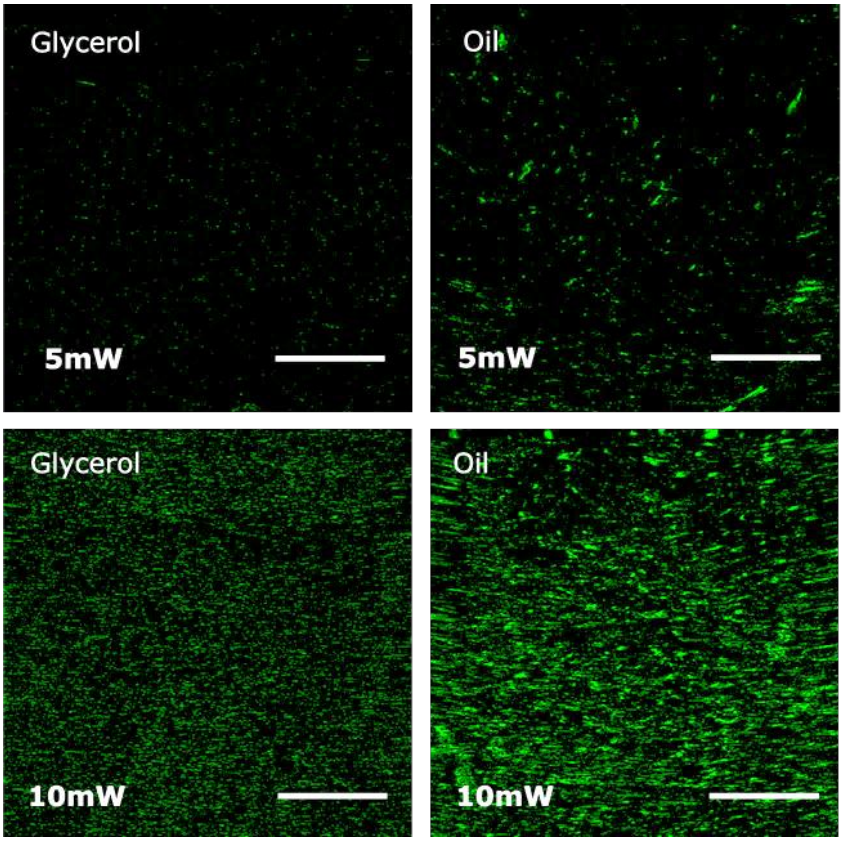

Figure S2–2: CCB imaging in glycerol and immersion oil.

CCB imaging in glycerol and immersion oil using two different illumination powers of 5 and 10 mW at the sample (810 nm, 150 fs, 80 MHz, MaiTai laser, Spectra Physics, USA). Scale bars: 50 μm. Emission band: 450 – 650 nm.

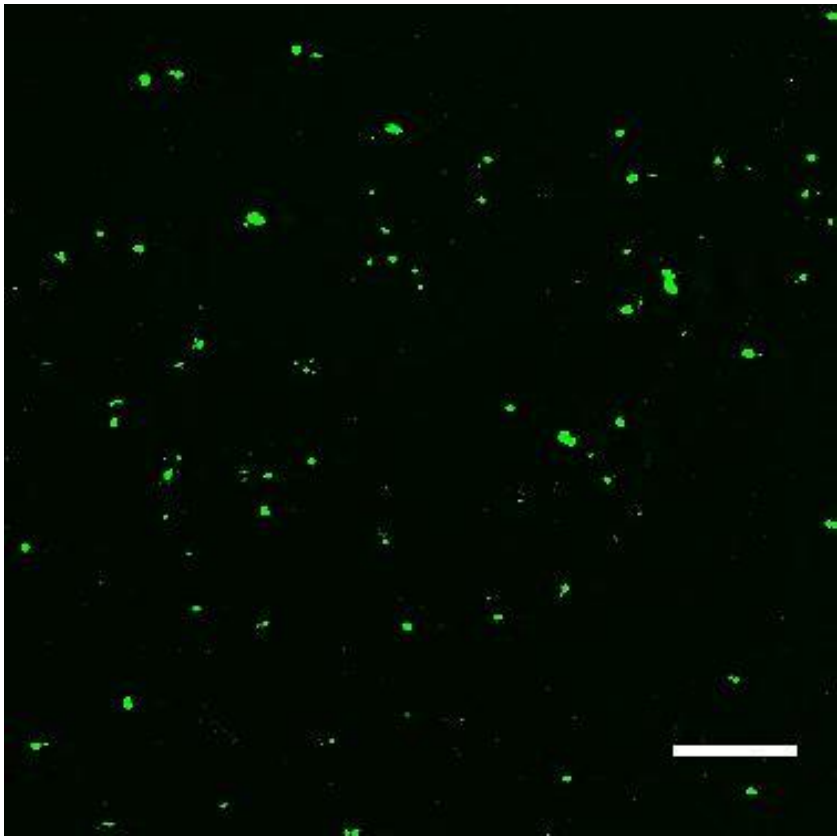

Figure S2–3: Studying optical trapping in PDMS.

CCB imaging in PDMS at room temperature upon illumination with 5 mW average laser power at the sample (excitation 810 nm, 80 MHz). Scale bar: 50 μm. Emission band: 450 – 650 nm.

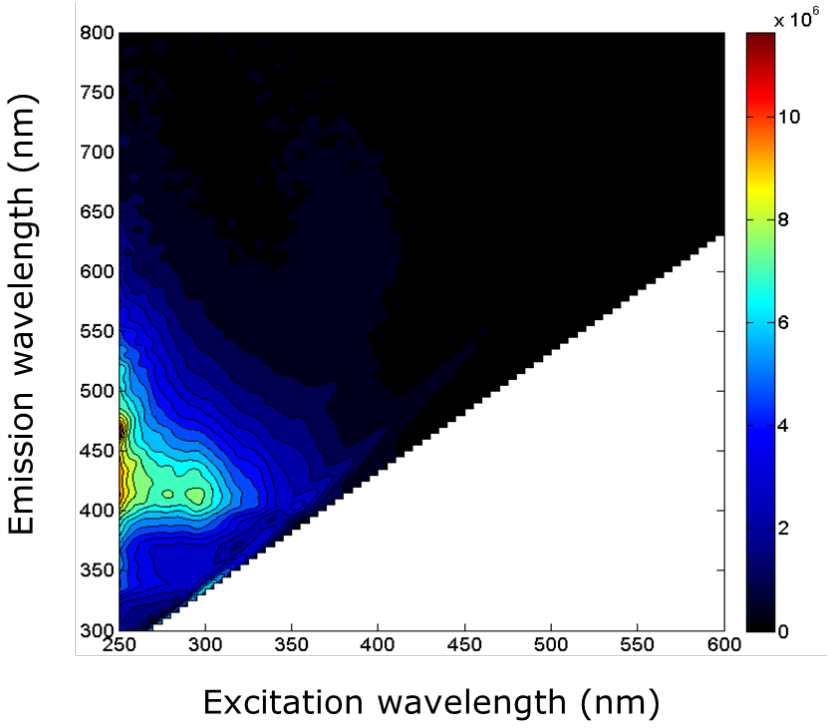

Figure S2–4: Two-dimensional excitation-emission plot of fCB particles.

Two-dimensional excitation-emission plot (similar to figure 2B of the main manuscript) of fCB particles in water under single photon excitation. Each vertical slice corresponds to an emission spectrum at the excitation wavelength.

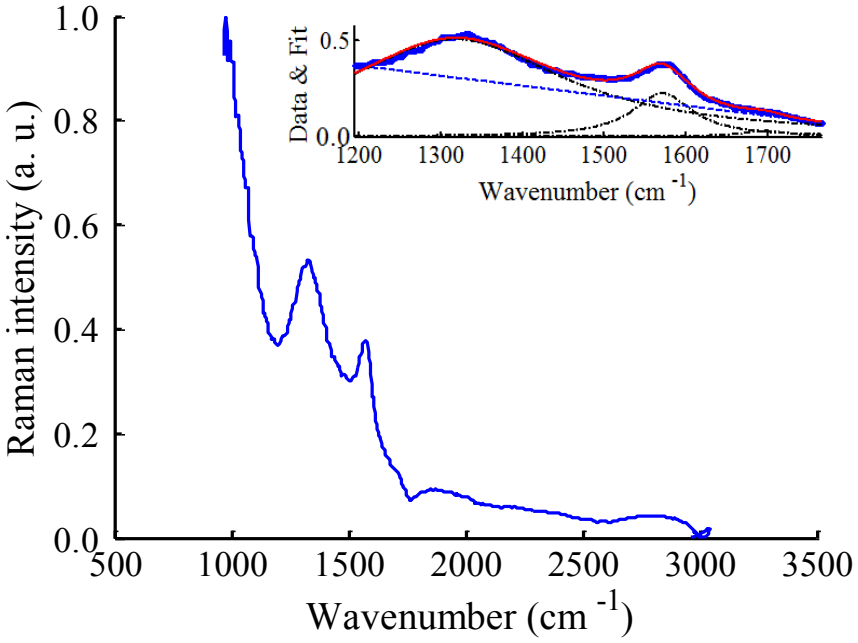

Figure S2–5: Raman data of ufPL.

Raman data of ufPL superposed on a reasonable luminescence background. Insert shows data typical for amorphous carbon (blue), triple Lorentzian line fit (red), baseline correction (blue, dashed line), spectral components (black, dash dot) fit results for D- and G-bands. For clarity two components are displayed shifted vertically. Summary of fit results can be found in Table S2-2.

Table S2–2: Raman bands Lorentzian fits.

Brackets indicate standard deviation around the mean, N = 3.

	ufPL (13 nm)			fCB (500 nm)		
	Position (cm^{-1})	**Width (cm^{-1})**	**Area**	**Position (cm^{-1})**	**Width (cm^{-1})**	**Area**
D-band	1326 (10)	288 (59)	54 (16)	1325 (19)	484 (131)	74 (55)
G-band	1569 (3)	95 (11)	23 (8)	1571 (6)	148 (30)	48 (12)
Bent SWCNT	1695	65	3	1695	90	13

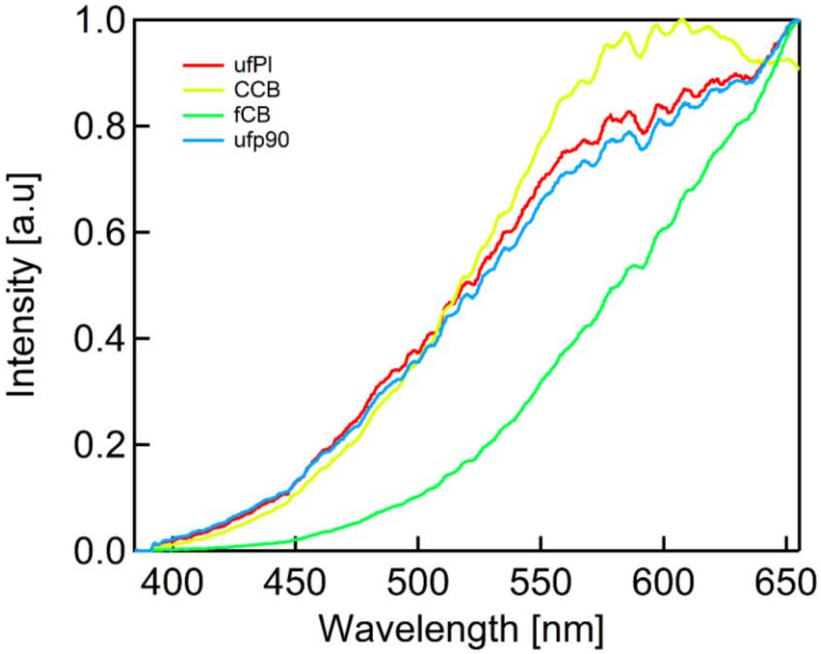

Figure S2–6: Normalized white light spectra of CBs.

Droplets of CB suspensions were dried on cover glasses and illuminated using a femtosecond laser (810 nm, 150 fs, 80 MHz repetition rate, MaiTai, Spectra Physics, USA).

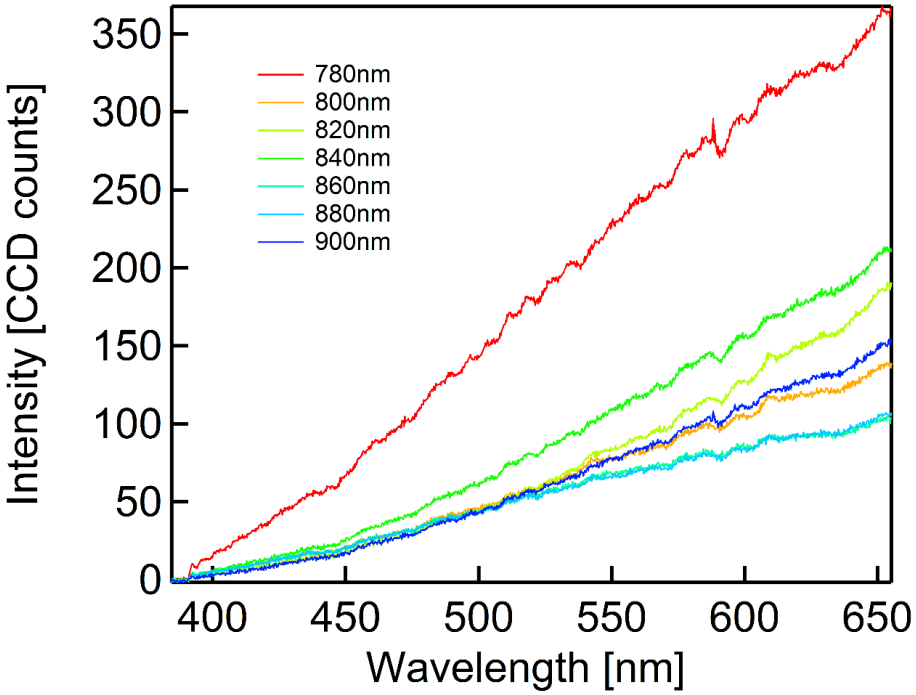

Figure S2–7: Raw data WL emission spectra of aqueous ufP90 suspensions.
Raw data of Figure 2-3B, main article. WL emission spectra of aqueous ufP90 suspensions recorded at different femtosecond illumination wavelengths.

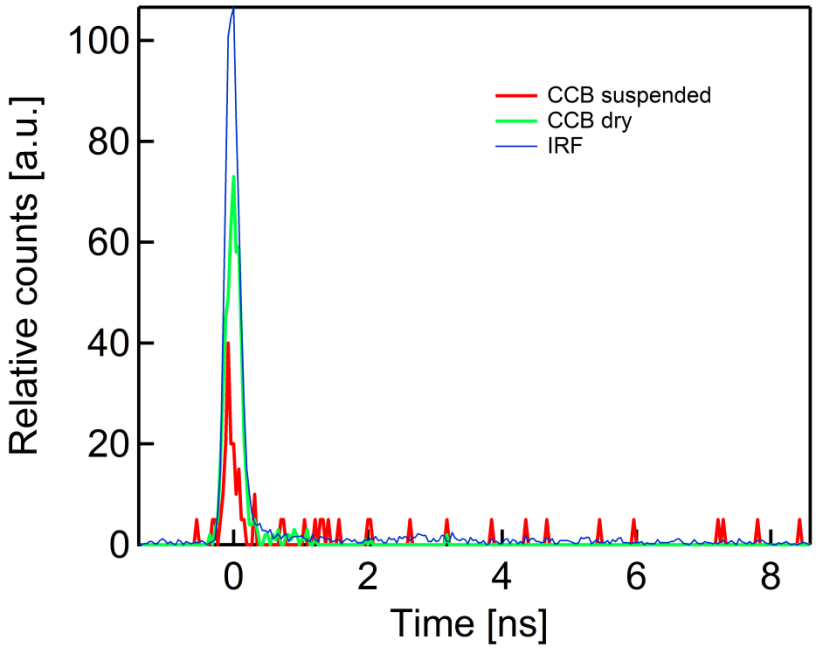

Figure S2–8: Temporal response of CCB particles.

Temporal response of CCB particles dried on glass and in aqueous suspension measured by time correlated single photon counting timing. The instrument response function (IRF) is overlaid in blue. The relative strength of the signal cannot be deduced from the relative peak values of the curves as different particle concentrations were used when performing the experiment in dry and aqueous state.

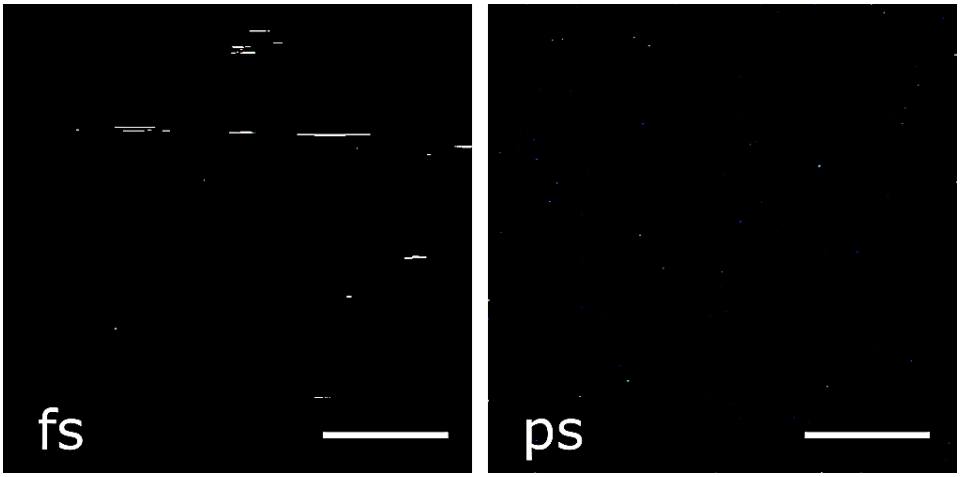

Figure S2–9: White-light generation under femtosecond and picosecond illumination.

Comparison of femtosecond and picosecond illumination of CB particles at 810 nm. 10 mW average laser power at the sample was applied to fCB similar to the experimental conditions above. The same area was consecutively imaged with a seven picosecond laser system (Levante OPO, APE, Berlin pumped by a 532 nm pulse train from a Picotrain laser, HighQ, Austria) and a femtosecond laser (810 nm, 150 fs, 80 MHz, MaiTai, Spectra Physics, USA). The lasers were switched between individual frames. Scale bars: 5 μm.

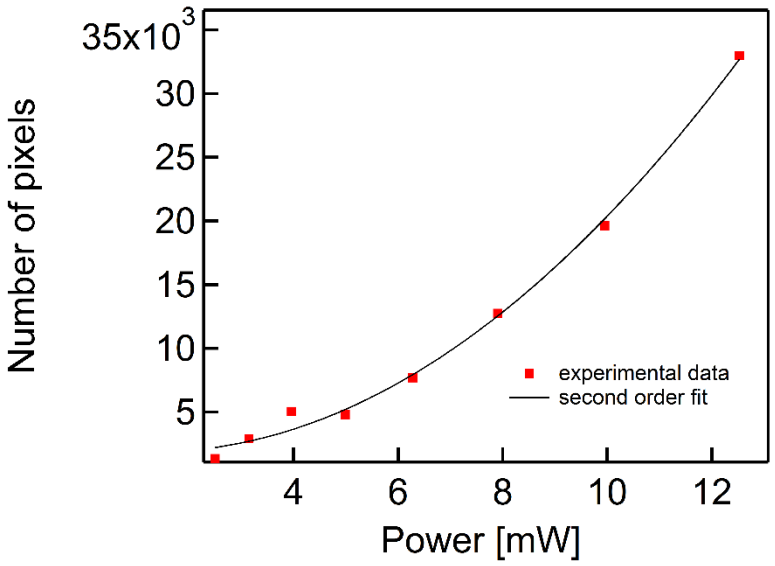

Figure S2–10: Emission power dependence of CB.

Emission power dependence of a sample of immersed ufPL particles. Power spectra were recorded by using a multiphoton microscope with 800 nm excitation by a femtosecond laser (150 fs, 80 MHz repetition rate, MaiTai, Spectra Physics, USA) and a 1.05 NA Objective (Olympus, Japan). As the photomultiplier tubes were quickly saturated on CB emission, the effective number of pixels visible in a scan was measured. Therefore a constant threshold was set and the number of pixels calculated by means of a MATLAB routine.

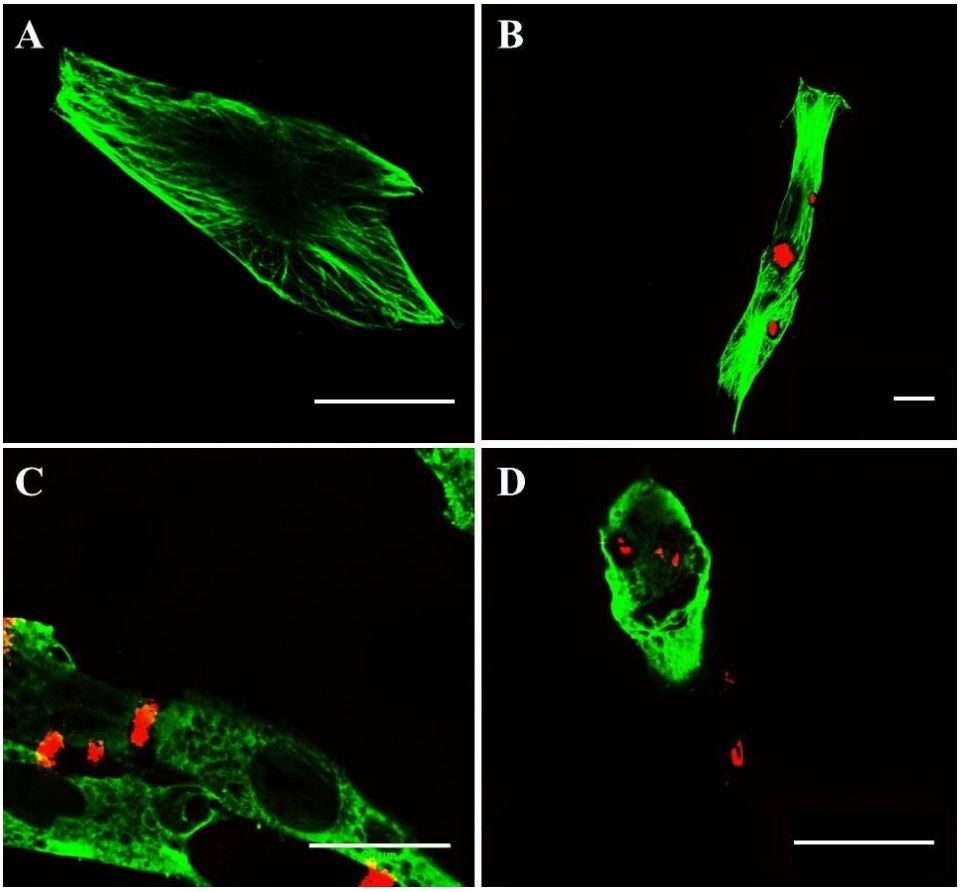

Figure S2–11: Co-localization study of the tubulin cytoskeleton of MRC-5 lung fibroblasts and engulfed ufP90.

Tubulin cytoskeleton (green, ex/em 495/519 nm) of fixed normal human lung fibroblasts (MRC-5 cell line) incubated at 37 °C with 5 μg/cm² ufP90 particles (red, 4 mW average illumination power at the samples at 810 nm, emission band detection: 400 – 410 nm in non-descanned mode). (A) Control cells. (B) 4 h incubation. (C) 8 h incubation. (D) 24 h incubation. Scale bar: 20 μm.

Chapter 3
Carbon black detection by pump-probe microscopy

This chapter is based on:
Rapid and label-free optical detection of individual carbon air pollutant nanoparticulates in biomedical samples.
Steuwe C.*, **Bové H.***, Clerinx J., vandeVen M., Fron E., Nawrot T., Ameloot M., Roeffaers M.
Manuscript under review.

* Authors contributed equally.

Declaration of own contribution: Hannelore Bové jointly designed the experiments. She performed the cell preparations, cell exposure, and immunohistochemistry. She also participated in writing the manuscript.

3.1 Abstract

Carbonaceous particle exposure and air pollution in general lead to a multitude of adverse human health effects and pose multiple challenges in terms of exposure, risk and safety assessment. Highly desirable for fast screening are label-free approaches for detecting these particle types in biological or medical context. We report a powerful approach for detecting carbonaceous particles using pump-probe microscopy, which directly probes their strong light absorption. The principle and reliability of the new approach is demonstrated by examining four different carbon black (CB) species modelling soot with diameters ranging from 13 to 500 nm. Our results suggest that this proposed approach is applicable to a large number of CB types as well as particulates. As the particles show a much-elevated absorption as compared to other absorbing species we can image CB particles virtually background free. Our pump-probe approach allows label-free optical detection and unambiguous localization of CB particles in (bio)fluids and 3D cellular environments. In combination with fluorescence microscopy, this method allows for simultaneous co-localization of CB with different cellular components using fluorophores as shown here for human lung fibroblasts. We further demonstrate the versatility of pump-probe detection in a microfluidic setup.

3.2 Introduction

Despite continuous improvements during recent decades, air pollution and in particular particulate matter remain the single largest environmental health risk today [204]. This chronic pollution not only shortens people's lifespan but also provokes and puts an additional burden to heart diseases, respiratory problems and cancer [22, 205]. According to the European Environment Agency report 'Air quality in Europe – 2015 report', air pollution causes more than 430,000 premature deaths in Europe [204]. Often, atmospheric pollutant particulates in densely populated areas are carbonaceous particles produced during incomplete combustion of organic carbon as emitted from traffic, fossil fuels and biomass burning, and industry [204]. In order to understand the severity of exposure and to take measures to effectively reduce the impact of air pollution, enhanced probing methods are required to gain detailed knowledge about the impact and long term effect on human health, ecosystems, environment and climate.

Carbon detection and exposure measurements in polluted air already delivered important information to fuel scientific and socio-political discussions. For example, absorption photometry and LII have been used to determine particle concentrations [72, 153, 154]. Non-invasive direct carbon particulate detection in aqueous media is far from straightforward. For cellular imaging and tracing particles inside the human body, labeling methods were developed such as the technetium-99-m radionuclide labeling [10, 98, 155]. However, direct label-free, economically feasible and sensitive detection of carbonaceous particles in medically or biologically relevant samples such as polluted water and consumer products as well as exposed cells and body tissues or fluids, is not well explored and remains in high demand. Recently, we demonstrated white light generation of suspended and dry CB particles as a contrast mechanism for biomedical imaging purposes [206]. This white light emission triggered by femtosecond (fs) pulses in the infrared region is instantaneous and not related to fluorescence or incandescence.

Here, we present a different approach for carbon particulate visualization and counting. It is advantageous as it is based on directly probing their absorption characteristics by pump-probe microscopy and not on a secondary emission effect. Our approach to directly visualize CB comprises all advantages of

multiphoton microscopy such as inherent 3D sectioning and increased imaging depths when near infrared wavelengths are being used [207, 208]. Additionally, it allows almost background free imaging as it is not based on emission and the absorption of the particles is overwhelmingly stronger than that of fluorophores. Therefore, the pump-probe approach can easily be combined with visualizing all conventional fluorophores.

Pump-probe spectroscopy has been introduced as a tool in physical chemistry related experiments [209-214]. Acquiring spatial information via image generation based on the same process, however, is gaining popularity. In 2009, Wei Min *et al.* imaged non-fluorescent, absorbing proteins by probing their stimulated emission [215]. In this case, the (fast) non-radiative pathway after irradiation of a femtosecond excitation pulse was probed by a depleting probe pulse with several 100 fs delay. Consequently, the intensity of the probe beam increases as molecules radiatively relax through the stimulated emission pathway [215]. In contrast, in transient absorption microscopy, the pump beam induces the absorption of probe photons which consequently leads to short term changes in the intensity of the probe beam [216, 217]. In transient absorption bleaching or ground state depletion microscopy (Figure 3-1A), the population of the ground state of a molecule or complex particle is changed which results in a reduced absorption of the probe field for a delay time period after the initial excitation pump pulse respectively [218]. In material science, pump-probe microscopy has been applied to follow the electron–hole recombination dynamics in individual zinc oxide nanorods [219] and in a similar manner to visualize propagating surface plasmon polariton modes of gold nanowires [220]. By applying near-infrared excitation wavelengths, semiconducting and metallic nanotubes could be distinguished by strong transient absorption signals [216]. In optoelectronics, the transient absorption response of a composite organometallic lead halide perovskite film and its charge carrier distributions has been explored [221].

Biophotonics related applications of pump-probe microscopy are not very common. It has been used to interrogate transient changes of absorption to study the dynamic behavior of nano-diamonds, and metallic and semiconducting carbon nanotubes inside cells, cellular structures and bio-fluids [216, 222, 223]. The principle can be applied to naturally occurring dyes to distinguish, for

example, melanin and eumelanin [224] or for biological imaging of mouse T-cells labelled with quantum dots and the yellow fluorescent protein expressing axons of neurons in the cerebral cortex [225]. We demonstrate in this paper that pump-probe microscopy is perfectly suited to generate contrast from highly absorbing and non-fluorescent particulate matter and to resolve nanoparticles with diffraction-limited localization.

3.3 Materials and methods

3.3.1 Materials and products

All chemicals were purchased from Sigma-Aldrich (Belgium) unless stated otherwise.

3.3.2 Carbon black particles

As a model component for soot we employed commercially available CB particles, which are known to have similar (physico)chemical properties [114, 115]. In contrast to black carbon or soot, CB is produced commercially through well-controlled incomplete (industrial) combustion of organics and commonly found as color pigment in paints, plastic materials and also rubber [35]. CB comprises aggregated primary aciniform particles with an elemental carbon content exceeding 97 % [35, 147]. Details of the physicochemical parameters of these different commercial CB materials ufPL (PlasmaChem GmbH, Germany), ufP90 (Orion Engineered Carbons, Germany), CCB (US Research Nanomaterials, USA) and fCB (Sigma-Aldrich, Belgium), can be found in SI of chapter 2 (Table S2-1). Although the aerodynamic diameters of the particles – according to the manufacturer's data – were ranging between 13 and 500 nm, it is clear from Figure S3-1 in SI that the CB particles tend to aggregate when suspended in aqueous solutions resulting in fairly comparable specifications. The degree of aggregation is visualized in Figures S3-1A - D, which show transmission electron microscopy (TEM; Tecnai G² spirit twin, FEI, the Netherlands) images of CB aggregates.

3.3.3 Carbon black solution preparation

Aqueous stock suspensions of CBs (2 mg/mL) were prepared in either ultrapure water or Iscove's Modified Dulbecco's Medium (IMDM; Life Technologies, Belgium) supplemented with 10 % fetal bovine serum (FBS; Biochrom AG, Germany), 100 U/mL penicillin, and 100 μg/mL streptomycin. These solutions were ultrasonicated for 30 min and stored in the dark at 4 °C until further use. Prior to use, stock suspensions were 20 min ultrasonicated before further dilution in ultrapure water or cell culture medium.

3.3.4 Cell culture

Human fetal lung fibroblasts (MRC-5 cell line, ATCC CCL-171, LGC Standards, France) were maintained in Minimum Essential Medium (MEM; Life Technologies, Belgium) supplemented with 10 % FBS, 100 U/mL penicillin, and 100 μg/mL streptomycin at 37 °C and 5 % CO_2. At 80-90% confluency, cells were routinely subcultured using trypsin-EDTA to detach cells. Cells for imaging were seeded on Ø 12 mm cover slips at a density of 10,000 cells/cover slip and incubated overnight to allow cell adherence. Cells were washed three times with phosphate buffered saline (PBS) and treated with 200 μL IMDM medium with 5 μg/cm² CB particles. After an incubation period of 4 hours, cells were washed 3 times with IMDM to remove the CBs that were not taken up by the cells before conducting immunohistochemistry.

3.3.5 Immunohistochemistry

For visualization of the tubulin cytoskeleton, cells exposed to CB particles were fixed with 4 % paraformaldehyde in PBS for 20 min. Cells were permeabilized and blocked for 2 h using 0.3 % Triton X-100 and 2 % bovine serum albumin (BSA) in PBS containing 5 % sucrose. Subsequently, cells were incubated for 1 h with mouse anti-α-tubulin antibodies diluted 1:1000 in blocking buffer consisting of PBS containing 1 % BSA and 0.1 % Triton X-100. After washing the unbound fraction, donkey anti-mouse antibodies conjugated with Alexa Fluor 488 (Life Technologies, Belgium) were applied for 1 h diluted 1:250 in blocking buffer. After washing extensively, the cover slips were aspired and mounted using Immu-Mount (Thermo Fisher Scientific, Germany).

3.3.6 Pump-probe setup

Pump-probe imaging was performed on an upright microscope (BX61WI/FV1000, Olympus, Japan) with a 25x/1.05 water immersion objective (XLPLAN, Olympus). The 'pump' beam was provided by a 7 ps pulsed, frequency-doubled Nd:YVO4 laser (picoTRAIN, High-Q, Austria) lasing at a fundamental centre wavelength of 1064 nm with a repetition rate of 80 MHz. A portion of the 1064 nm fundamental beam was frequency doubled for consecutively pumping an optical parametric oscillator (OPO; Levante Emerald,

APE-Berlin, Germany) providing the 'probe' beam 7 ps pulse train. Continuous tuning (700 to 980 nm) of the OPO signal output was achieved by a temperature-tuned noncritically phase-matched LBO crystal and an intracavity Lyot filter. The pulses were overlaid in three dimensions and in time by a mirror/ dichroic mirror combination and motorized, automated delay stage. To measure modulation transfer upon pump-probe interaction, the pump beam was amplitude-modulated at 9.7 MHz with a Pockels cell (model 360-80, ConOptics, USA) triggered by a function generator (model 29, Wavetek, USA). Typically, the average power of each beam at focus was adjusted to 100 μW to 10 mW. After passing objective and sample, the transmitted beams were collected with an oil immersion condenser (U-UCD8, Olympus) and were reflected off the microscope with a dichroic mirror (FF750, Semrock, USA). A broad band-pass filter (CARS 890/220 m, Chroma Technology, USA) was used to block the pump beam, and the modulated probe beam was detected by a large-area silicon PIN photodiode (S8650, Hamamatsu, Japan) with reversed bias of 60 V and flange-mounted low noise RF amplifier. Afterwards, the output photocurrent was band-pass-filtered (Mini-Circuits, USA) and analysed by a lock-in amplifier (HF2LI, Zurich Instrument, Switzerland, see also Figure S3-3 (iii)). For image acquisition, the output of the lock-in amplifier is fed into the analog-to-digital converter (FV-10-ANALOG, Olympus, Japan) synchronized with the scanning unit (Olympus FV1000MP, Japan). In these experiments, the scanning speed was about 2 ms/line. Optical transmission images of the samples were recorded with a digital camera (XC50, Olympus). Green (auto-)fluorescence was read out using a 520-570 nm green filter in front of a photomultiplier.

3.3.7 Urine samples

The urine samples used in this manuscript were collected in the framework of the COGNAC (COGNition and Air pollution in Children) study, which enrolled children (9 – 12 years old) from three different primary schools in Flanders, Belgium. Written informed consent was obtained from the parents and oral consent from the children. The study protocol was approved by the Ethical Committee of Hasselt University (Diepenbeek, Belgium) and East-Limburg Hospital (Genk, Belgium). The samples were collected using designated metal-

free sample jars (Yvsolab, Belgium) and placed at 4°C until long-term storage at -80°C. The specific samples used in this study were randomly selected without taking into account their ambient exposure level.

3.3.8 Microfluidic setup

The proof of principle microfluidic setup was manufactured by gluing a square glass capillary (Vitrotubes, Vitrocom, New Jersey, USA) with 1 mm inner diameter and 200 μm wall thickness onto a cover slip (# 1, Menzel Glaeser, Germany). A syringe pump was attached to one side of the capillary by PTFE tubing to generate suction. The other capillary side was extended by PTFE tubing which eventually ended in a containment for suspended CB particles. The generated flow through the capillary was constant with a speed of 0.1 mL / min and we measured 5 minutes for each sample. In terms of optics and laser sources, the same setup was used as described earlier for imaging. Here, however, we read the signal trace from the lock-in amplifier by using a data acquisition card. The signal was initially sampled with a rate of 500 kHz with the lock-in time constant set to 10 μs. Due to technical issues, the starting 25% of each acquired signal trace where not processed.

Flow rate considerations:

The suspension flows through a square capillary with a wall length of $l = 1mm$ at a rate of $v = \frac{0.1mL}{min} = \frac{0.1mL}{60s}$. This implies that particles travel with a speed of $\varrho = 0.1\frac{mL}{60\,s} \times 10^{-6}\frac{m^3}{mL} \times \frac{1}{l} = 1.7\frac{mm}{s}$.

We estimate the lateral focus diameter to be about $d = 650\,nm$ for $\lambda = 1064\,nm$ according to the Rayleigh criterion. A particle can therefore cross the focus in $t = 400\,\mu s$ with a frequency of events of 2.5 kHz respectively. The effective acquisition frequency is set to the double of this frequency observing the Nyquist theorem: $t_{acq} = 5\,kHz$. As the signal was initially sampled at 500 kHz, we therefore downsample the acquired data by a factor of 100. All events above a noise threshold (given by the NI card) of -8 V are being counted.

Considerations regarding the expected number of particles in focus during sampling.

The cross section of a diffraction limited spot, calculated based on the Rayleigh limit *d* at $\lambda = 1064\,nm$ and with a numerical aperture of 1.5, is about 1 x 10^6 times smaller than the lateral cross section of the capillary ($A_{capillary} = 1\,mm^2$, flow in axial direction).

We further approximate a carbon particle to be a round sphere with in this case $r = 75\,nm$ (according to the manufacturer's information). A particle therefore has a volume of $V_p = 1.8 \times 10^{-21} m^3$ and a mass of $4 \times 10^{-15} g$ with a carbon density of $= 2.27 \times 10^{-6} \frac{g}{m^3}$ [226].

In 0.375 mL (75% of 0.5mL) suspension of $2mg$ CCB per *mL* we therefore expect 1.9×10^{11} particles and 2.4×10^5 particles flowing through the focus. The other solutions then have less particles according to the dilution.

Matlab routines for all calculations are available.

3.4 Results and discussion

To probe the absorption of the particles, we performed diffuse reflectance spectroscopy (Figure 3-1B). As already visible by eye (the powders appear black), the absorption is about similar for all four scrutinized particle types and is broad and uniform over the whole visible and near-infrared spectrum. This broad absorption can result from a continuum of electronic states present in amorphous carbon [227-229]. Consequently, there is hardly any fluorescence to be expected as emission is effectively quenched by a multitude of non-radiative pathways (see also chapter 2 or Bové *et al*.[206]). This continuum of electronic states constitutes the basis for the contrast mechanism in pump-probe microscopy which we apply during the following imaging experiments.

In Figure 3-1C and D, we demonstrate pump-probe imaging of single CB particles or aggregates at different wavelengths of the indicated probe beam (the pump beam is fixed at 1064 nm). All particles were dispersed in ultrapure water and a droplet was squeezed between two coverslips for imaging. Average powers in both beams can be as low as several 100 μW but this comes at the expense of a weaker signal/lower sensitivity. We also prove the applicability of this technique for dry particles (SI, Figure S3-3). Note that the diameter of the point spread functions of individual particles or small aggregates is at the diffraction limit which proves that this technique is perfectly applicable for bio-imaging in wet environments. The probe beam can be tuned over a wide range of wavelengths (Figure 3-1C), which is the result of the broad absorption indicated in Figure 3-1B. Visible pulsed laser beams can therefore be used as well. While we are restricted to pulses with seven picosecond duration due to the available laser system, we have evidence that this detection mechanism should be fairly flexible with respect to available pulse durations. The temporal delay between pump and probe pulses was set to zero picoseconds, a position where we noticed the highest signals. This proved to be very uncritical (see Figure S3-5) in comparison with instantaneous phenomena such as stimulated Raman scattering [207]. By changing the temporal delay between the pulses, we can demonstrate that the changes in absorption are lasting for at least several tens of picoseconds (SI, Figure S3-5). This means that also cheaper light sources with longer pulses (up to 100 ps) should work for detecting particulates by

pump-probe spectroscopy. For very short fs pulse durations however, hot carrier dynamics on a picosecond time scale is expected and might cause unwanted side effects [182].

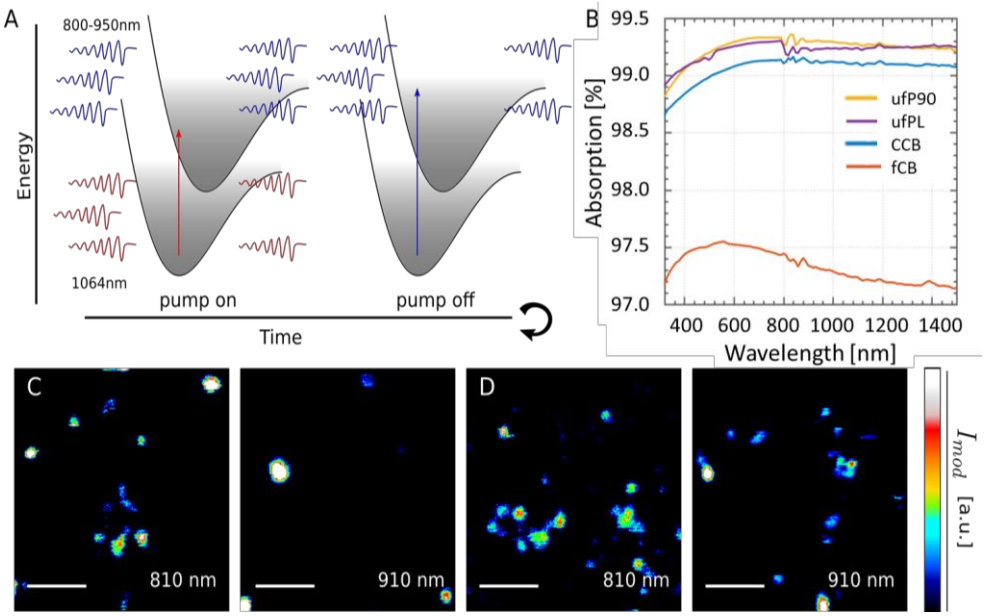

Figure 3–1: Pump-probe imaging of CB particles.

(A) Principle of pump-probe interrogations based on transient absorption bleaching or ground state depletion. When the pump beam is on, the pump photons interact with the continuum of electronic states inside a carbon particle and temporarily deplete the ground state. As a result, the probe photons will no longer be absorbed by the particle. In absence of the pump beam, some probe photons will be absorbed. Rapid modulation of the pump laser hence leads to a modulated probe beam transmission which is detected and translated into a signal. (B) Absorption spectra of CB particles (indicated in the legend) taken from 300 nm to 1500 nm. See the supplementary information for measurement details. (C) fCB (2 mg/mL) pump-probe imaging at zero ps delay of CB in ultrapure water at room temperature upon illumination with 3 mW average laser power at the sample in each beam at 1064 nm (pump) and the indicated probe wavelength. Different sample positions were scanned in each image. The numerical aperture of the employed water immersion objective is 1.05. (D) Analogous to (C) but with ufPL particles. The typical dwell time is 6 μs per pixel at a resolution of 512x512 pixels, 20 nm/pixel. Scale bars: 3 μm.

In pump-probe microscopy, a large experimental parameter space is available where one can vary the wavelength of both pump and probe excitation pulses, the detection wavelengths, the timing between the excitation pulses, and the detection gating window after excitation [230]. The rich parameter space offers great advantages in specificity. For example, when strong absorbers are present, as might be the case in biological cells, fluids and tissues, one can tune away from the interfering absorption band by selecting other excitation wavelengths while still probing the broad absorption of carbonaceous particles. Moreover, the absorption of carbonaceous particles is substantially stronger than that of fluorophores. The absorption cross section of organic dyes are typically on the order of $\sim 10^{-16}$ – 10^{-15} cm² [231-233], which is significantly larger than cross sections of endogenous ones leading to autofluorescence having values around 10^{-17} cm² [234]. In comparison, the absorption cross sections of carbonaceous particles are generally 4 – 5 orders of magnitude higher ($\sim 10^{-11}$ cm²) compared to the former [112, 235]. Therefore, the signal of the carbonaceous particles acquired by pump-probe microscopy can conveniently be combined with all conventional contrast-enhancing fluorophores typically used in biological characterizations like immunohistochemistry. One of the major advances of this simultaneous detection is that it enables unambiguous dynamic localization of the particles inside cells. As shown in Figure 3-2, the majority of the engulfed carbonaceous particles are located laterally inside the cell when imaged after four hours of exposure. At this early time point, the particles are invaginated by the plasmic membrane of the cell and are therefore mainly located as clustered particles near the membrane [236]. This observation is in agreement with the results published by Belade *et al.* showing *via* TEM images that carbon black particles taken up by fibroblasts are aggregating near the cell surface and cannot be found in mitochondria, nuclei, or other organelles when incubated for 6 h [84].

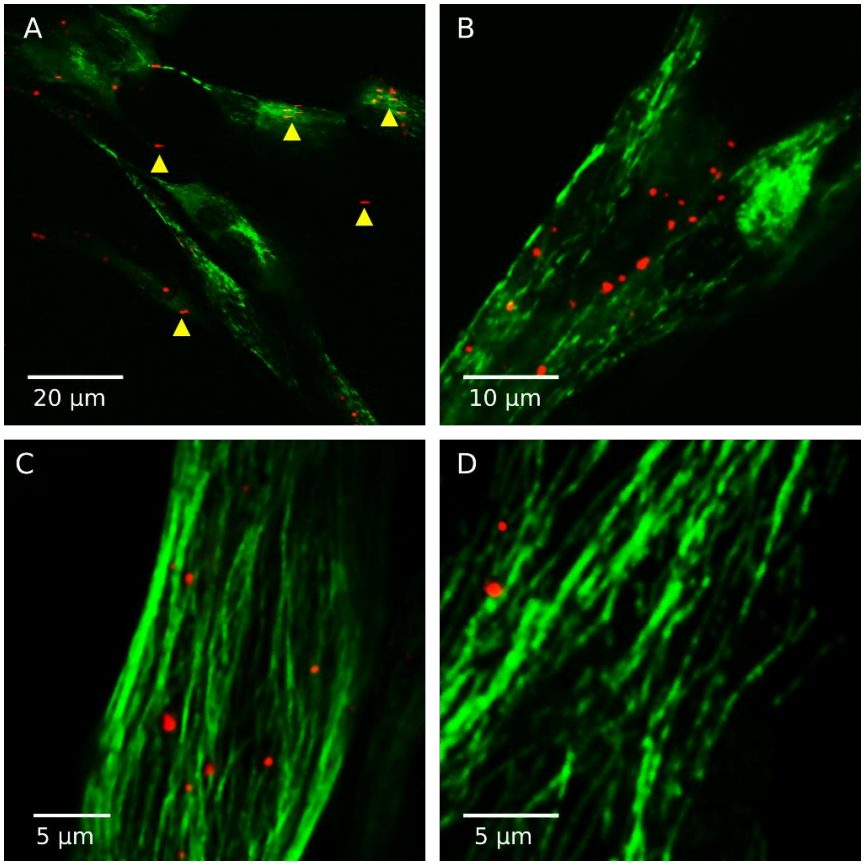

Figure 3–2: Signal of CB particles by pump-probe imaging combined with the detection of conventional contrast-enhancing fluorophores visualizing the cytoskeleton.

Two-photon excited fluorescence imaging of the tubulin cytoskeleton of fixed MRC-5 cells labelled with Alexa Fluor 488 (Ex/Em 495/519 nm, labelling protocol see SI) in combination with pump-probe-based optical detection (pump: 1064 nm, probe: 810 nm) of ufPL particles (4 h incubation of 5 $\mu g/cm^2$ ufPL at 37 °C prior to imaging). (A) and (B) overview images while (C) and (D) and zoomed images of MRC-5 cells which engulfed ufPL CB particles. Yellow arrow heads indicate particles horizontally smeared due to optical trapping.

Our label-free detection technique links the CB location directly to its biological context and allows dynamic imaging of cells as laser powers are moderate. Additionally, it should be noted that a substantial portion (indicated by yellow arrow heads) of the CB particles in Figure 3-2A are horizontally smeared by

optical trapping suggesting that not all particles were engulfed by the cells [237, 238]. We note that the trapping effects seem less pronounced compared to our previously published study employing white light generation. See also Figure 3-1C and D as a reference.

To illustrate the applicability of this novel technique in biological fluids, we detected black carbon (BC) in urine. The urine samples were collected from children in the framework of the COGNAC (COGNition and Air pollution in Children) study, which enrolled children (aged 9 – 12 years) from three different primary schools in Flanders, Belgium (more details can be found in SI). 2 μL of undiluted urine was squeezed between two coverslips and imaged with similar parameters as in Figure 3-1C-D. Autofluorescence, which is a common observation in urine, is distinctly visible as green emission (filter: 520-570 nm, Figure 3-3A), upon two-photon excitation with our pump-probe picosecond laser excitation [239, 240]. In pump-probe absorption experiments however, this auto-fluorescence is not showing up at all (Figure 3-3A). Absorbing (carbon) particles are clearly visible, here coloured in red and marked by the yellow arrow head. Background-free detection of carbon particulates by pump-probe microscopy is therefore advantageous for difficult samples suffering from fluorescence. At the same time, this is further evidence that particulates are being translocated inside the human body.

Next, pump-probe microscopy was combined with a microfluidic device to detect and count carbon particles. In this case, an event is a particle passing through the focus. These results do not deliver absolute numbers of carbon particles in solution but quantification can be obtained from the data after calibration. The counted absolute numbers of events follow the concentration nicely inversely proportionally despite the large number of events in the 100x diluted suspension (Figure 3-3B). We also simulated the number of events that could potentially be measured by such a setup (see SI). Overall, the simulation results correlate very well with our experimentally acquired data provided that sample rate and thresholds are set according to the experimental conditions.

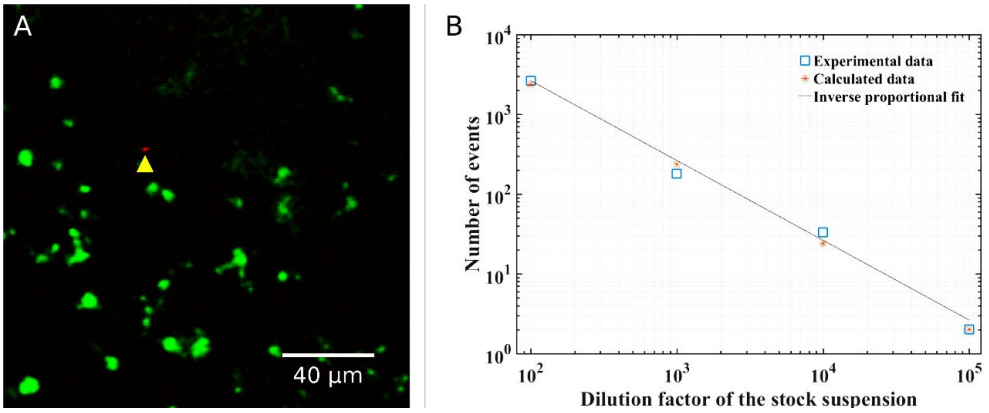

Figure 3–3: Detection of BC in urine samples by pump-probe imaging.

(A) Optical imaging of urine samples. Pump-probe imaging of CB particles urine (red, marked by yellow arrowhead), at room temperature upon illumination with 5 mW average laser power in both beams at the sample at 1064 nm (pump) and a probe wavelength of 952 nm. Two-photon excited autofluorescence of urine and simultaneously excited by the pump-probe ps-laser coloured green (filter: 520-570 nm). (B) Counted CCB particles (blue markers) in diluted suspensions by combining a microfluidic device and pump-probe detection. Shown is also an inverse proportional fit (coefficient of determination, R^2 = 0.99). The power was adjusted to 10 mW in both beams and the probe beam adjusted to 951 nm. We also estimated the amount of particles to be measured by such a setup, these data are shown in red.

To conclude, pump-probe microscopy of CB particulates is a straightforward flexible approach without the need of sample pre-treatment that can be implemented on multiphoton setups suited for coherent Raman imaging. Although we have not tried different lasers within the framework of this paper, there are reports employing cheap continuous wave-lasers for pump-probe imaging [215, 241]. The nature of the detected signal makes it almost background-free and hence very versatile in terms of choice of additional fluorophores for cell labelling and context generation. Owing to the nonlinear nature of the signal, our technique comes with inherent 3D sectioning capabilities and high imaging depths when using longer wavelengths of excitation. These capabilities allow to monitor and gain a better understanding of body regulatory action for example, the actual uptake and clearance of CB particles by the human body. Considering that pump-probe imaging can be used to locate and count particles in body fluids, this technique is also interesting

regarding (occupational) personal exposure monitoring. We are thus convinced that this method can play an important role in medical and environmental research where the acute and chronic impact and role of particulates is to be assessed at micro and macro scale levels. We therefore anticipate that our approach has broad applications in the field of nanomedicine, nanotechnology and environmental sciences. It will allow for further insight in epidemiological and toxicological behaviour since it allows to screen human tissues and body fluids for the presence of CB.

3.5 Supplementary information

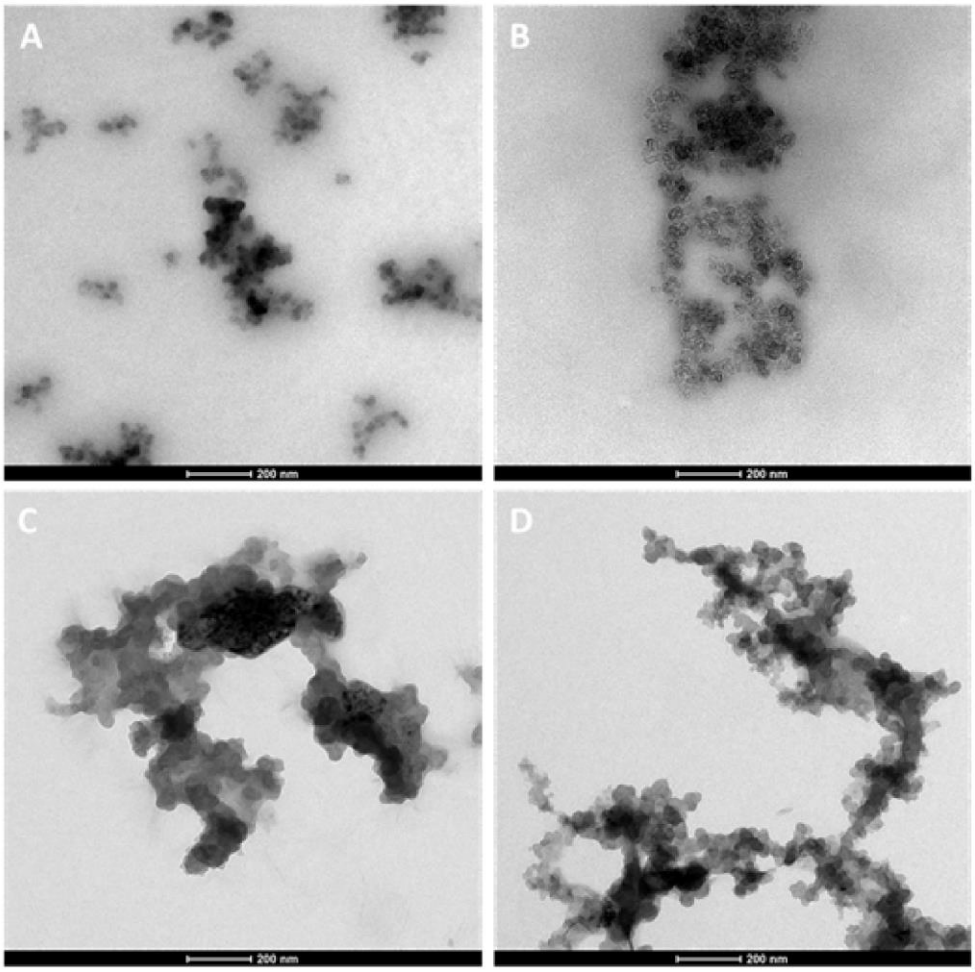

Figure S3–1: TEM images of the different carbon black particles.
(A) ufPL, (B) ufP90, (C) CCB, (D) fCB.

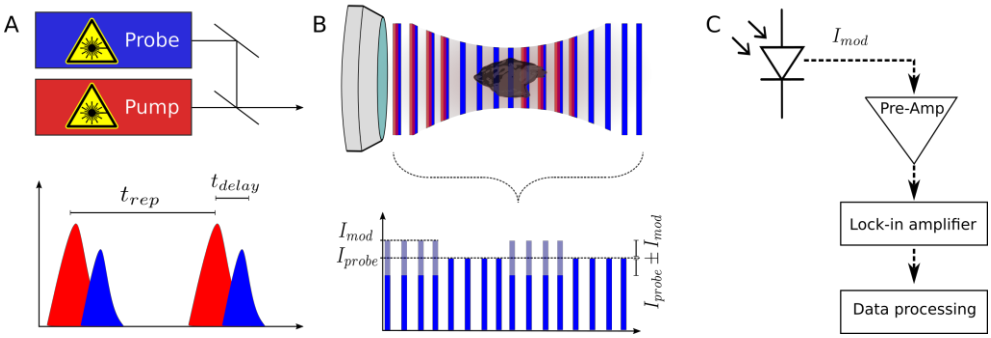

Figure S3–2: Schematic representation of the pump-probe microscopy approach for CB particles.

(A) The pump pulses are shown in red, probe pulses in blue and are overlaid in space and time. t_{delay} denotes the temporal distance between pump and probe pulse, t_{rep} the pulse cycle time directly linked to the repetition rate of the laser. (B) In an actual experiment, the modulated pump and unmodulated Stokes beams focussed on particles where they interact with particulates. I_{probe} is the average intensity of the probe beam when no pump beam is interacting which varies by a modulation intensity I_{mod} upon interaction. (C) The varying modulation intensity is read-out by a photodiode, amplified and read out by a lock-in amplifier and then further processed for imaging.

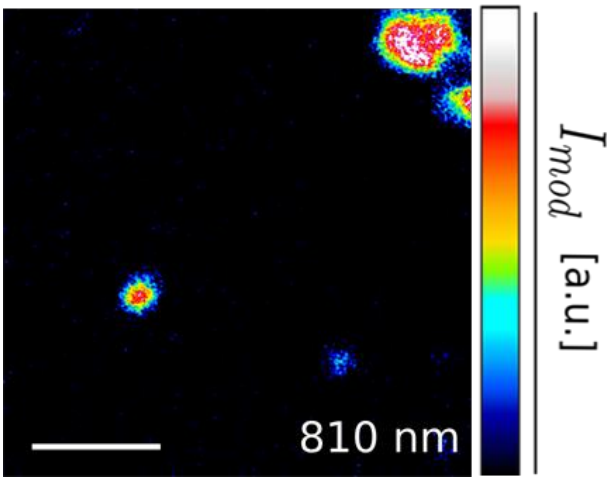

Figure S3–3: Pump-probe imaging of dry ufPL particles.

The typical dwell time is 6 μs per pixel at a resolution of 512x512 pixels. Powers: 4 mW (Pump, 1064 nm), 10 mW (Probe, 810 nm). Scale bar: 3 μm.

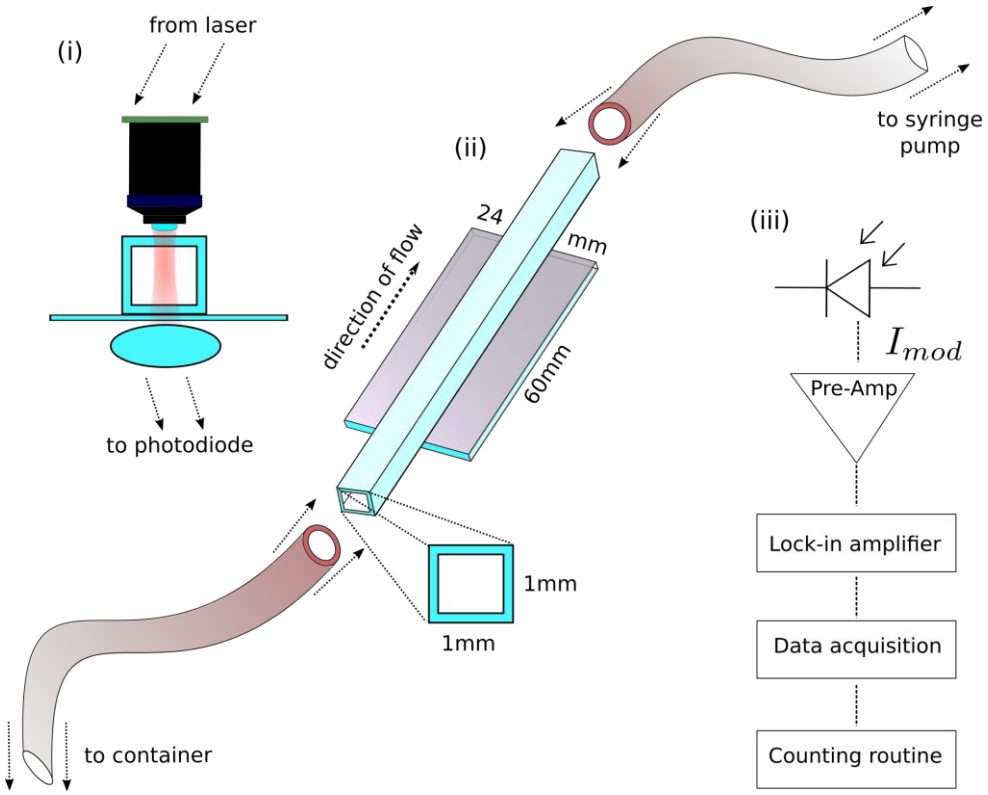

Figure S3–4: Sketch of the microfluidics setup which was used for particle counting.

The principle is demonstrated in (i) and (ii) where a water immersion objective (NA = 1.05, XPlan, Olympus, Japan) focuses light into a square capillary glued onto a cover slip. A condenser lens (cyan) collects the light in forward direction. The flow through the capillary is sustained by two Teflon hoses glued to the glass walls. One hose is connected to a syringe pump, the other is in contact with a small vessel containing the suspension. After the condenser, the modulation transfer is detected by a photodiode, amplified and read out by a lock-in amplifier. A data-acquisition device monitors the lock-in signal. Finally, a down sampling and counting routine counts spikes inside the signal trace.

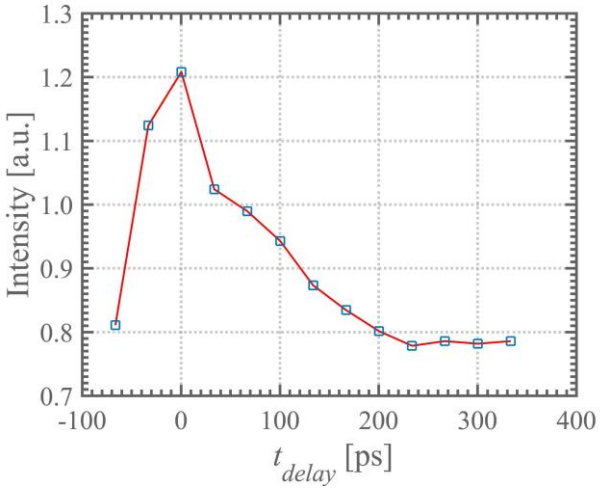

Figure S3–5: Pump probe delay scan of CCB particles.

Pump-probe images of in ultrapure water suspended CCB were taken while stepwise scanning a delay stage. The laser illumination was adjusted to less than 5 mW average power at the sample at 1064 nm (pump) and a probe wavelength of 910 nm (9 W peak power and a power density of about 1 GW/cm^2). A negative delay means that the pump pulse arrives after the probe pulse.

Chapter 4
Fibril-based quantification of large cell-induced deformations

---

This chapter is based on:
3D full-field quantification of cell-induced large deformation in fibrillary biomaterials by combining non-rigid image registration with label-free second harmonic generation.
Jorge-Peñas A.*, **Bové H.***, Sanen K., Vaeyens M-M., Steuwe C., Roeffaers M., Ameloot M., Van Oosterwyck H.
Biomaterials. 2017 Aug;136:86-97. IF(2015)=8.557.

* Authors contributed equally.

Declaration of own contribution: Hannelore Bové jointly designed the experiments. She performed all experiments. She also participated in writing of the manuscript.

4.1 Abstract

To advance our current understanding of cell-matrix mechanics and its importance for biomaterials development, advanced three-dimensional (3D) measurement techniques are necessary. Cell-induced deformations of the surrounding matrix are commonly derived from the displacement of embedded fiducial markers, as part of traction force microscopy (TFM) procedures. However, these fluorescent markers may alter the mechanical properties of the matrix or can be taken up by the embedded cells, and therefore influence cellular behavior and fate. In addition, the currently developed methods for calculating cell-induced deformations are generally limited to relatively small deformations, with displacement magnitudes and strains typically of the order of a few microns and less than 10% respectively. Yet, large, complex deformation fields can be expected from cells exerting tractions in fibrillar biomaterials, like collagen. To circumvent these hurdles, we present a technique for the 3D full-field quantification of large cell-generated deformations in collagen, without the need of fiducial markers. We applied non-rigid, Free Form Deformation (FFD)-based image registration to compute full-field displacements induced by MRC-5 human lung fibroblasts in a collagen type I hydrogel by solely relying on second harmonic generation (SHG) from the collagen fibrils. By executing comparative experiments, we show that comparable displacement fields can be derived from both fibrils and fluorescent beads. SHG-based fibril imaging can circumvent all described disadvantages of using fiducial markers. This approach allows measuring 3D full-field deformations under large displacement (of the order of 10 μm) and strain regimes (up to 40%). As such, it holds great promise for the study of large cell-induced deformations as an inherent component of cell-biomaterial interactions and cell-mediated biomaterial remodeling.

4.2 Introduction

During the last decade studies have shown significant differences in morphology and behavior of cells when embedded in 3D environments compared to seeding them onto two-dimensional (2D) substrates [242-244]. A critical component is the extracellular matrix (ECM), which provides biophysical and biochemical cues to resident cells via cell-matrix interactions. It is generally accepted that along with the chemical signals, mechanical properties and cues play a crucial role during many physiological and pathological processes including development, growth, regeneration and disease states like cancer metastasis [245-247]. Hence, the quantification of cell-matrix mechanical interactions within 3D environments is extremely important for enhancing our current understanding of these processes, as well as for developing biomaterials that exploit the role of these mechanical interactions in controlling cell fate [248-251].

Cell-matrix mechanical interactions are most commonly investigated using traction force microscopy. In TFM, tractions are computed from measured cell-induced matrix displacements (see Note 1 in SI for a brief explanation of the basis steps of TFM) [252]. TFM involves solving an inverse problem, which requires a mathematical (computational) approach that, apart from displacement data, requires information on ECM mechanical (elastic) properties. This method was initially developed for cells on 2D planar substrates [253-255] that have a number of practical advantages compared to 3D, such as the use of non-degradable substrates with linear elastic properties that are stable over time, compatibility with high resolution imaging and the availability of well-established methods to recover high resolution displacement and traction fields. More recently, TFM has been extended to the recovery of 3D force fields exerted by cells encapsulated in linear elastic, non-fibrillar [256] and non-linear elastic, fibrillar ECMs [257]. Especially for 3D setups traction recovery is not trivial, neither experimentally nor computationally, among others because of the continuous remodeling of the ECM by cells, which could alter the local constitutive behavior of the matrix and therefore compromise the validity of recovered tractions [258]. On the other hand, cell-induced matrix displacements already provide quantitative information on the magnitude, orientation and distribution of cell-matrix mechanical interactions [258], avoiding the tedious

task of characterizing ECM mechanical properties and the computational complexity of solving for the unknown forces.

To calculate cell-induced matrix displacements, fluorescent beads are typically embedded into the extracellular matrix to act as fiducial markers. This approach allows computing the displacements by well-established particle tracking algorithms [256, 259] and other algorithms based on local grey scale distribution such as digital image/volume correlation, also known as particle image velocimetry (PIV; see Note 1 in SI for a brief explanation of PIV) [260]. Still, the use of external markers brings about several drawbacks: fluorescent beads could alter the matrix mechanical properties and cells could detach and engulf the beads from the ECM, which could affect cell behavior and introduce errors caused by bead motion. Moreover, the accuracy and spatial resolution of the computed displacements strongly depends on the bead density used in the experiments. It must be high enough to capture cell-induced complex matrix deformations in order to avoid the loss of local, high-frequency spatial information [261, 262]. Recently, PIV has been used to quantify cell-induced displacements in 3D fibrillar ECMs by directly imaging (by means of confocal reflectance microscopy) the fibrils without the need of fiducial markers [257, 263]. However, the quality of the displacements computed from fibril image data has not been compared yet to displacements computed from fluorescent bead image data, which can be considered the reference method. Moreover, while PIV has been proved suitable for quantifying displacements under relatively small strain (less than 10%) regimes [263], alternative algorithms based on iterative image warping schemes such as fast iterative digital volume correlation [264] or non-rigid FFD-based image registration [265] should be considered to deal with large strains. These algorithms allow capturing large material deformations while providing a significant increase in the spatial resolution of the computed displacements by combining a coarse-to-fine approach with an iterative image warping process.

In this study, we demonstrate that FFD-based image registration (see Note 1 in SI for a brief explanation of the FFD algorithm), combined with label-free, SHG imaging, enables to accurately calculate cell-induced, full field displacements in fibrillar collagen under large deformations (defined here as strain magnitudes larger than 10%). The SHG-signal of collagen type I fibrils has the advantage of

yielding high contrast and submicron resolution images in a non-invasive, label-free manner [266, 267], making the use of fluorescent beads for displacement field calculations superfluous. In order to assess the quality of the displacements computed from SHG imaging, they will be compared to the displacements obtained from a high density of fluorescent beads attached to the collagen fibrils, which act as control.

4.3 Materials and methods

4.3.1 Materials and products

All chemicals were purchased from Sigma-Aldrich (Belgium) unless stated otherwise.

4.3.2 Cell culture

Human fetal lung fibroblasts (MRC-5 cell line, ATCC CCL-171, LGC Standards, France) were cultured in 75-cm² flasks in Minimum Essential Medium (MEM, Life Technologies, Belgium) supplemented with 10% fetal bovine serum (FBS, Biochrom AG, Germany), 100 U/mL penicillin, and 100 μg/mL streptomycin at 37°C, 5% CO2 and 95% humidity. At 80-90% confluency cells were routinely sub-cultured using trypsin-EDTA to detach cells. Cells for traction force experiments were seeded on Ibidi μ-slide 8 well plates (Ibidi GmbH, Germany) at a density of 15,000 cells/well and incubated overnight to allow for cell adherence. After washing three times with phosphate buffered saline (PBS), cells were treated for 45 minutes with 12.5 μM CellTracker^{TM} Green CMFDA (Life technologies, Belgium) in serum free cell culture medium. After exposure, cells were washed three times with PBS, detached and mixed with collagen solution before polymerization at a concentration of 15,000 cells/mL.

4.3.3 Synthesis of Collagen Type I Gels with high density of attached beads

Cell-seeded collagen type I hydrogels containing a high density of fluorescent beads were prepared according to a method described previously [257] with some modifications. Briefly, hydrogels were prepared on ice by mixing 8 volumes of collagen consisting of rat tail collagen (collagen type I, 10.31 mg/mL, Corning, The Netherlands) and bovine skin collagen (collagen type I, 5.9 mg/mL, Nutragen, Advanced Biomatrix, Germany) in complete MEM at a ratio of 1:2 and final concentrations of 2.4 or 4.0 mg/mL diluted with an appropriate volume of 10x MEM. Next, 10% (vol/vol) sodium bicarbonate (23 mg/mL) containing 1.0 mg/mL or 1.5 mg/mL fluorescent polystyrene beads (0.2 μm or 1 μm diameter respectively, carboxylated, ex/em 580/605, Invitrogen, Belgium) was added. The pH of the mixture was neutralized using

1 M sodium hydroxide, after which 1 volume of cells were embedded as described in the previous section. The resulting mixture was cast in Ibidi μ-slide 8 well plates (Ibidi GmbH, Germany) at 300 μL/well. The gels were polymerized for 15 min at 37°C and subsequently immersed with complete MEM after which they were allowed to set for 18 h before the start of the displacement experiments.

The spatial resolution of the matrix displacement field directly depends on the density of the sampling points used to capture matrix deformations. In fibrillar biopolymers, the achievable spatial resolution would be mainly limited by the density of the fibrillar network, where fibrils naturally act as the sampling locations of local deformations, while embedded beads must be attached to the fibrils to correctly reflect matrix displacements. Hence, to perform a fair comparison between bead-based and fibril-based matrix displacements, the density of the attached beads must be high enough to comply with the Nyquist sampling theorem and to act as fiducial markers of the fibrils deformations. To match the displacement sampling between both bead-based and fibril-based images, the bead density was increased. At the same time the bead diameter was lowered from 1 to 0.2 μm in order to keep the total mass of beads in the collagen hydrogel reasonable. Distances between the attached fluorescent beads of the different hydrogel-bead formulations (0.2 μm vs. 1 μm fluorescent beads) were determined using the Nearest Neighbor Distances Calculation plugin of the image processing package Fiji (ImageJ v1.47, Open source software, http://fiji.sc/Fiji). These nearest neighbor distances were plotted against their appearance frequency in histograms using MATLAB (The MathWorks Inc, Natick, MA USA). A Gaussian was fitted to the data. The increase in bead density resulted in a decreased mean bead-bead distance from 8.4 to 4.8 μm (Supplementary Figure S4-3), correlating to a two-fold enhancement of the sampling frequency.

4.3.4 Image acquisition

Three-dimensional image stacks were acquired using a Zeiss LSM510 META NLO scan head mounted on an inverted laser scanning microscope (Zeiss Axiovert 200M, Zeiss, Germany) and a LD C-Apochromat 40x/1.1 W Korr UV-Vis-IR water immersion objective (Zeiss). The microscope is equipped with a motorized,

programmable stage placed on a vibration isolation table in an air-conditioned room kept at a constant temperature of 22°C. Cells were kept at 37°C and 5% CO_2 during the displacement experiments by means of a stage incubator (Tempcontrol 37-2 digital, PeCon, Erbach, Germany).

Label-free SHG imaging of the hydrogels was performed using a femtosecond pulsed laser (MaiTai DeepSee, Spectra-Physics, USA) tuned to a central wavelength of 810 nm as excitation source. The beam was reflected by a short-pass 650 nm dichroic beam splitter and focused onto the sample with an average excitation power of approximately 5 mW on the stage. The SHG signals from the collagen fibrils were epi-collected, discriminated from the autofluorescence of the embedded cells with a 442 nm dichroic beam splitter and transmitted through a 5 nm wide band pass filter with a central wavelength of 405 nm. An analogue photomultiplier tube (Zeiss) was employed for detection in non-descanned mode.

For imaging the CellTracker™-labeled cells inside the hydrogels, a 30 mW air-cooled Argon ion laser (LASOS Lasertechnik GmbH, Germany) emitting at 488 nm (~ 3 μW maximum radiant power at the sample) was employed. A band-pass filter 500 – 530 nm was used for filtering the emission signal. For imaging the fluorescent beads attached to the collagen fibrils, excitation at 543 nm (~ 3 μW maximum radiant power at the sample) was performed by using a 5 mW Helium Neon laser (LASOS Lasertechnik GmbH). A band-pass filter 565 – 615 nm was used for filtering the emission signal. A fixed pinhole size of 160 μm was used.

4.3.5 Sham experiments

Three different sham experiments were conducted to rule out or compensate for displacements not related to cellular activity.

First, bead attachment to the fibrils was verified to avoid erroneous displacements caused by the motion of advected and/or diffusing beads. Image series of 50 frames of control acellular hydrogels were acquired. The resulting 1024x1024 images with a pixel size of 0.22 x 0.22 μm^2 were recorded using a pixel dwell times of 1.6 μs. Temporal and spatio-temporal image correlation spectroscopy (TICS and STICS) analyses were performed using custom written MATLAB routines, which have been published previously by the Wiseman

Research Group of McGill University [268, 269]. Brief explanation of the image correlation spectroscopy analyses can be found in Supplementary Information (Note 2).

Secondly, time-lapses of control acellular hydrogels were recorded and analyzed to detect the existence of spurious displacements. Over time, z-stacks of fibrils and beads were acquired at the top, middle and bottom part of different hydrogels (total hydrogel height of ~1.5 mm, 15 minutes z-stack acquisition time). Then, for each time point the displacements with respect to the last time point (0 s time interval between z-stacks, 2 h total acquisition time) were computed following the same image processing steps as for the real experiments with cells (see section 4.3.7 – 4.3.11). To assess any dependency on experimental setup, protocol or personal handling, the existence of spurious displacements was analyzed for two sets of three control hydrogels prepared independently by two different persons and imaged on two different setups, with one setup being the acquisition system used for all other experiments (see section 4.3.4), and the other one being an upright microscope (BX61WI Olympus, Tokyo, Japan) with motorized focusing and a 25x/1.05 water immersion objective.

Thirdly, to rule out any errors induced by the method used to compute the displacements (see section 4.3.7 – 4.3.11), 3D synthetic image data of hydrogel volumes containing embedded fluorescent beads as acquired by an optical microscope were generated and analyzed by means of a previously developed TFM simulator [270]. Briefly, this simulator generates ground truth displacements (for known tractions that serve as input) and corresponding microscope images of fluorescent beads in non-deformed and deformed hydrogel configurations, taking into account 'non-ideal' microscope aspects, such as the microscope's point spread function, camera resolution and various sources of noise. By comparing the displacements computed from the synthetic microscope data to the ground truth displacements, errors related to image registration can be assessed. In order to simulate our sham experiments, images were generated for zero tractions, meaning that recovered displacements should also be zero (or corresponding to simulated noise levels), and the parameters of the simulated hydrogel and imaging system were selected to mimic our experimental setup. More specifically, the images of the

hydrogel were generated using a model for the point spread function of a laser scanning confocal microscope with a 1.1 NA water immersion objective lens, providing a final voxel size of 0.44 x 0.44 x 0.3 μm^3. The hydrogel contained 0.2 μm fluorescent beads (emission wavelength 605 nm) and its refractive index was set to 1.43. For each simulated time point, the generated z-stacks were corrupted with new realizations of Gaussian and Poissonian noise.

4.3.6 Assay for cell-induced deformations

A 173 x 173 x 45 μm^3 volume was imaged on average around each cell, including ~7 μm of fibrils/fluorescent beads above and below the cell body. The z-stacks were acquired sufficiently distant from top and bottom of the hydrogel and comprised an average of 41 images with a voxel size of 0.34 x 0.34 x 1 μm^3 recorded using a pixel dwell time of 6.4 μs. After imaging the volume under cellular tractions, the embedded cells were treated with 25 μM cytochalasin B and then reimaged every ~8 minutes for 1 h during cellular relaxation, until the force-free relaxed state of the gel was obtained. The acquired z-stacks were processed as described in section 4.3.7 – 4.3.11.

4.3.7 Pre-processing of acquired images

Prior to the calculation of the displacements, raw image data were enhanced by a two-step process consisting of a noise filtering step followed by a contrast stretching operation to highlight the structures of interest - beads, fibrils or cells - from the image background. More specifically, fibril and cell images were processed by penalized least squares-based denoising [271] and bead images were edge filtered by a difference of Gaussians operator to simultaneously boost blob-like structures and to reduce noise.

4.3.8 Image registration for displacement field calculation

The calculation of the displacement fields was split into two different registration processes: a rigid registration where the acquired images were globally aligned to correct for the translational shifts of the microscope stage, followed by a non-rigid registration where the local displacements induced by cellular forces were estimated.

In particular, to correct for stage drift while assuring temporal consistency for time lapse acquisitions, we have performed rigid registration of the images on consecutive time points and then expressed the position of the registered images in a global frame of reference. As for the non-rigid registration, we have made use of a B-spline-based Free Form Deformation approach [265]. Briefly, in FFD-based image registration, the transformation model that warps the image of the stressed state (*i.e.,* hydrogel loaded by cellular tractions) is given by a multivariate B-spline function. The algorithm overlays the image of the relaxed state (*i.e.,* after adding cytochalasin B) with a regular mesh, and then defines the mesh nodes as the control points of the B-spline curves. Subsequently, the position of these control points is tuned iteratively during the optimization process warping the image of the stressed matrix until it matches the one of the relaxed condition, providing as output a full displacement field, *i.e.* at each voxel of the registered images. Although the method warps the image of the stressed state to fit the one of the relaxed state, note that both the underlying transformation model and the resulting displacement field are defined from relaxed to stressed state.

Regarding the similarity metric and the optimization strategy required for both the rigid and non-rigid registrations, we used the normalized correlation coefficient as the similarity metric and a stochastic gradient descent method with adaptive estimation of the step size as the optimizer [272].

Finally, we performed the image registration following a coarse-to-fine multiscale strategy, which allowed us to cope with different levels of matrix deformations while providing smooth displacement fields. Specifically, we used a three-level multiscale approach with 72 x 72 x 44 voxels, 36 x 36 x 22 voxels, and 18 x 18 x 11 voxels mesh size for the coarsest, intermediate and finest scales, respectively.

4.3.9 Removal of errors caused by engulfed beads in bead-based displacement fields

To ignore the beads engulfed by the cell and minimize errors in the calculation of the displacements, we supplied a binary mask of the segmented cell to the FFD-based image registration algorithm. To obtain the mask, the cell body was thresholded by Otsu's binarization algorithm.

While the cell mask ensures that engulfed beads are not corrupting the displacements adjacent to the cell surface, it does not prevent that non-zero displacements are recovered inside the cell body. This is caused by the connected mesh used for FFD-based registration, which will propagate the mesh deformations located close to the cell surface to its surroundings, including the cell interior. Therefore, the final displacement field provided by the algorithm was reset to zero inside the cell mask.

4.3.10 Comparison of cell-induced displacement fields

The displacement fields obtained from bead and fibril images were compared by calculating the difference in terms of displacement magnitude and direction at every spatial coordinate for every analyzed cell. Additionally, the mean and standard deviation of these differences were computed for a subset of displacements, namely those reaching at least 30% of the peak displacement magnitude for each particular cell.

4.3.11 Implementation

The computational workflow was implemented in MATLAB, except for FFD-based displacement field estimation, which was computed using Elastix [273], an open source multiplatform software for image registration. The integration of the elastix based FFD image registration on the main computational workflow was done as in [265]. The software program Paraview 4.3.1 (Kitware Inc., NY USA) was used for the 3D rendering of segmented cells and the visualization of 3D vector fields.

4.4 Results

A schematic overview of the performed analyses is depicted in Figure 4-1, which summarizes the methodology followed for both sham experiments and cell-populated gels.

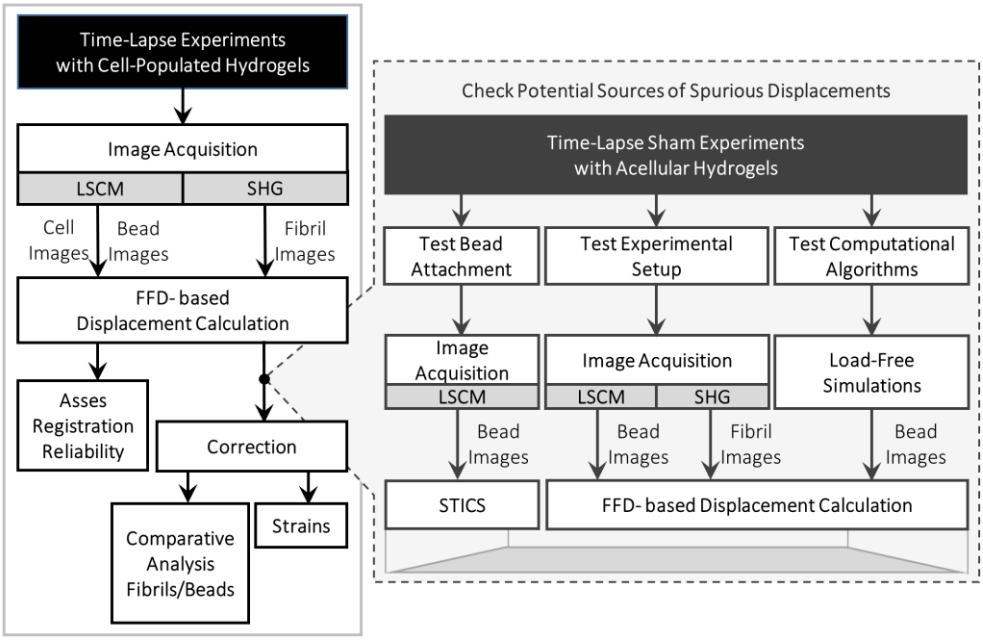

Figure 4–1: Schematic overview of the performed analyses and validations.
LSCM: Laser Scanning Confocal Microscope; SHG: Second Harmonic Generation; FFD: Free Form Deformation; STICS: Spatio-Temporal Image Correlation Spectroscopy.

4.4.1 Sham experiments show spurious displacement patterns

For the correct interpretation of calculated displacements, it is important to verify to what extent the experimental setup and protocols as well as image registration procedures can give rise to spurious displacements that are not related to any cellular activity. In this regard, three different sham experiments were conducted.

First, the bead attachment to the fibrils was checked using image correlation spectroscopy to prevent errors induced by the motion of non-attached beads. Supplementary Figure S4-4 shows the spatial and temporal cross-correlation information for acquired time-series of beads embedded in the hydrogel. If beads would have moved during the time-lapse, the correlation peak would change over different time-lags (τ). Our results did not present the lateral shift (indicative of advected beads) or broadening of the correlation peak (indicative of diffusing beads) over different time-lags and thus confirm the attachment of beads.

Secondly, to rule out any dependency on experimental setup, protocol or personal handling, displacements were calculated from data acquired on two different setups from control hydrogels (without cells) prepared by various persons. Figure 4-2 (fibril-based images) and Supplementary Figure S4-5 (bead-based images of the same specimen) show the resulting displacement maps for each vector component from data acquired on the main microscopy setup (as described in section 4.3.4). A spurious displacement pattern in the results provided by both fibrils and beads can be seen. Displacement magnitude varies smoothly with depth, but is rather constant within the imaging plane. When looking at the time lapses, we noticed that this pattern was present most of the time, however it was less evident at certain time points. Similar displacement patterns were observed for sham experiments conducted on the additional acquisition setup (Olympus BX61WI upright microscope; data not shown).

Thirdly, we checked by using synthetic data if the observed spurious pattern of displacements was caused by an error in the algorithms used to compute the displacements. However, the displacements computed from the synthetic data were negligible (Supplementary Figure S4-6).

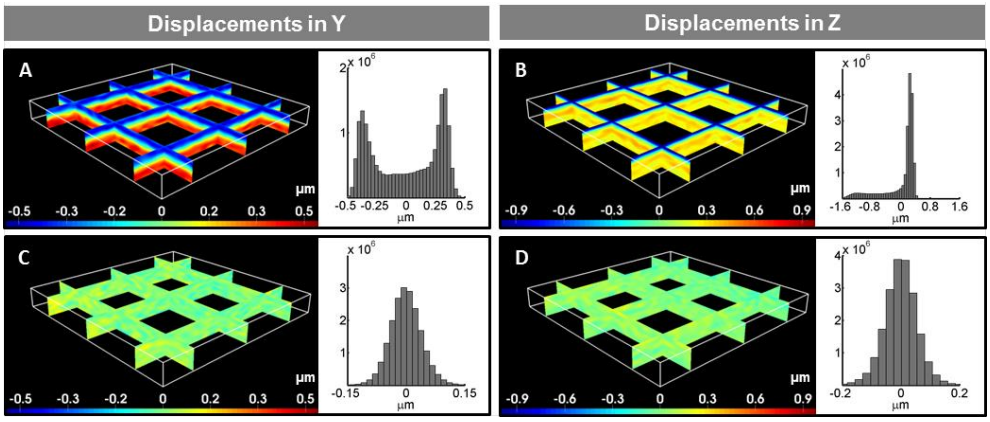

Figure 4–2: Spurious displacements present in cell-free sham experiments.
Spurious displacements obtained from fibril-based images in cell-free sham experiments, (A, B) before and (C, D) after correction. Axial cross-sections at multiple locations of the acquired volume and histograms (right insets) for the (A) Y- and (B) Z-components of the computed displacement field, and their corrected versions (C) and (D), respectively. Bounding box: 220 x 220 x 23 μm^3.

4.4.2 Spurious displacement patterns can be corrected

We accounted for the spurious displacement pattern by calculating the average displacement vector for each XY-plane and subtracting it from the local displacement vector of each point in the corresponding plane. Histograms of the recovered displacements from the sham experiments, before and after the proposed correction, are shown on the right side of Figure 4-2 and Supplementary Figure S4-5. Whereas the spurious displacements presented a multimodal histogram, it became symmetric and unimodal after applying the correction, resembling a Gaussian-like random distribution of errors with zero mean. After applying the described correction only negligible errors with standard deviation ~ 0.05 μm are found (Supplementary Figure S4-7), which is negligible compared to the displacements calculated in cell populated hydrogels and which were of the order of 1-10 μm after the correction (see also section 4.4.4). Additionally, the effectiveness of the correction method was evaluated on the displacements computed under cellular tractions. After correction, it can be observed (Figure 4-3) that the spurious displacement pattern is leveled out.

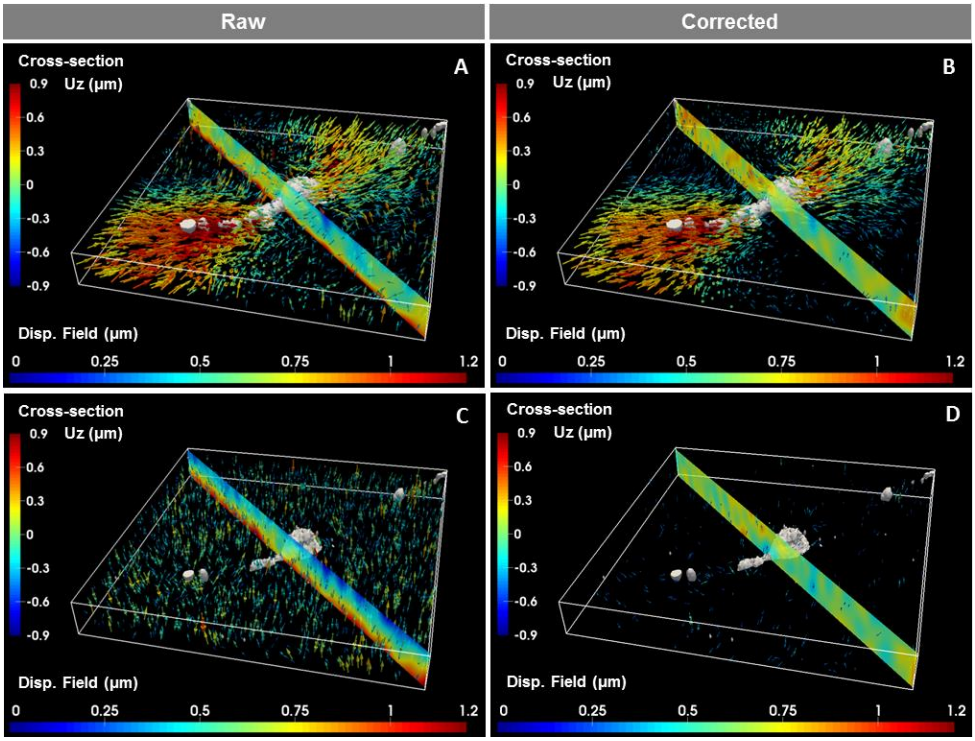

Figure 4–3: 3D displacements in cell-populated hydrogels.

3D displacements in cell-populated hydrogels (A,C) before and (B,D) after correction for spurious displacements computed from fibril-based images. Displacements are induced by a MRC-5 fibroblast (white) (A,B) before and (C,D) 40 minutes after adding cytochalasin B. Displacement vector fields (arrows) and the Z-component (cross-section) of the displacements are shown simultaneously. Note the different color scales for the Z-component in the cross-section ('Cross-section') and the displacement vector magnitude in the imaged region ('Disp. Field'). Bounding box: 170 x 170 x 21 μm^3.

4.4.3 Multiscale FFD allows the recovery of large deformations induced by MRC-5 fibroblasts

To measure the deformations induced by MRC-5 fibroblasts embedded in the collagen hydrogel, we imaged the collagen matrix around the cells with SHG microscopy before and after force relaxation with cytochalasin and evaluated the local displacement and strain fields via FFD-based image registration. As can be seen in Figure 4-4, these cells spread inside the hydrogel to an elongated and polarized configuration, while contracting the collagen hydrogel around their

force poles located at the extremes of their principal axis resulting in a local alignment of the fibrils. This behavior was observed for cells embedded in both 2.4 and 4.0 mg/mL hydrogels.

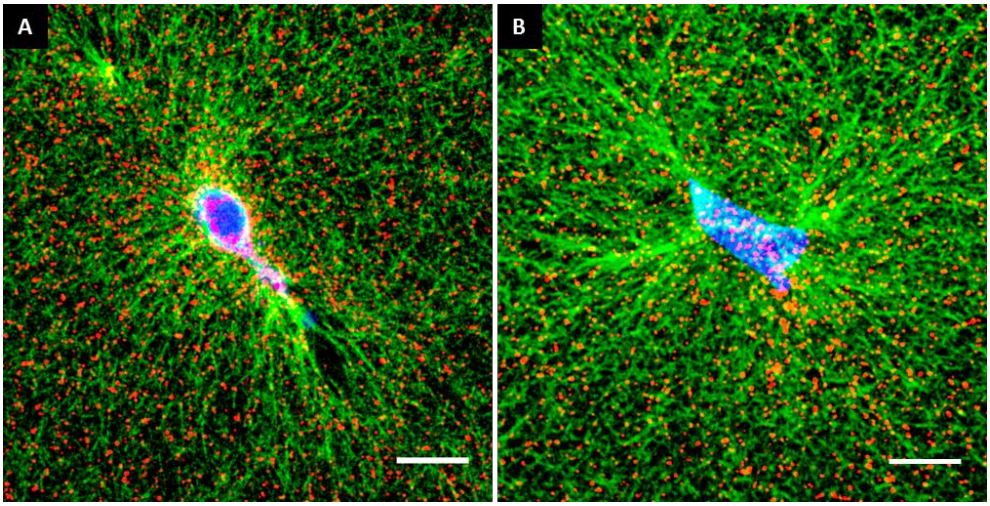

Figure 4–4: Cell-induced alignment of collagen fibrils.
Cross-sections of (A) 2.4 mg/mL and (B) 4.0 mg/mL collagen hydrogels showing MRC-5 fibroblast (blue) induced alignment of collagen fibrils (green) with a high density of fluorescent beads (red) attached. Beads engulfed or adsorbed by the cell are shown in magenta. Scale bar: 25 μm.

The feasibility of FFD to register both fibril- and bead-based images was demonstrated for a number of representative cells (N=9 per collagen concentration). Figure 4-5 and Supplementary Figure S4-8 show fibril- (A) and bead-based (B) images in the unstressed (red) and stressed (green) hydrogels for collagen concentrations of 2.4 and 4.0 mg/mL, respectively. After image registration they both (C and D) appear predominantly as yellow when the images in the unstressed and stressed state coincide. The latter registered images generated by the estimated deformations qualitatively show the success of the registration procedure and therefore the coherence and reliability of the computed displacements.

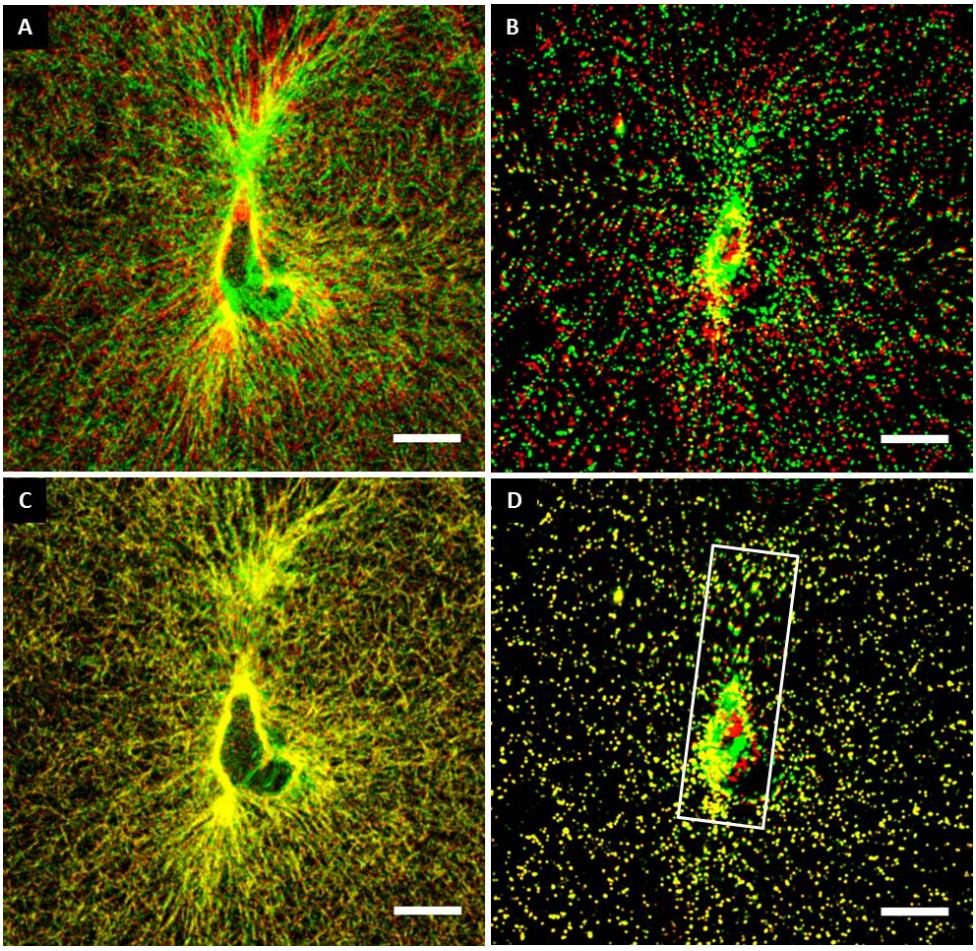

Figure 4–5: FFD-based image registration of the cell-induced stressed vs. unstressed hydrogel.

FFD-based image registration of the unstressed (84 minutes after addition of cytochalasin B) and stressed (before addition of cytochalasin B) gel with 2.4 mg/mL collagen concentration. Pseudo-colored cross-sections of the collagen hydrogel showing the (A) fibril- and (B) bead-based images before the registration, and their registered results (C) and (D), respectively, that lead to the recovered displacement field. The fibrils/beads in the unstressed and stressed hydrogel are pseudo-colored in red and green, respectively. Fibrils/beads appear as yellow where both the unstressed and stressed conditions match. (D) The beads engulfed by the cell are ignored during the registration process (delineated area) to avoid artifacts in the recovered displacements. Scale bars: 25 μm.

Once displacement fields are obtained (see section 4.4.4), any additional strain measure can be calculated. Here, we report results in terms of the Green-

Lagrange strain tensor **E** (Eq. 4-1), which is commonly used in nonlinear solid mechanics, and which is defined as:

$$\mathbf{E} = \tfrac{1}{2}\,(\mathbf{F}^{\mathrm{T}}\mathbf{F} - \mathbf{I}) \qquad \text{(Eq.4-1)}$$

with **F** the deformation gradient tensor and **I** the identity tensor. Looking at example cells in Figure 4-6 and Supplementary Figure S4-9, strain components up to 40% are calculated near the cell's force poles, demonstrating the existence of large strains for both 2.4 and 4.0 mg/mL collagen concentrations. Taken together Figures 4-5 and 4-6, and Supplementary Figures S4-8 and S4-9, FFD proves to be successful in registering fibril-based and bead-based images, even for large deformation conditions and dense fibrillary networks.

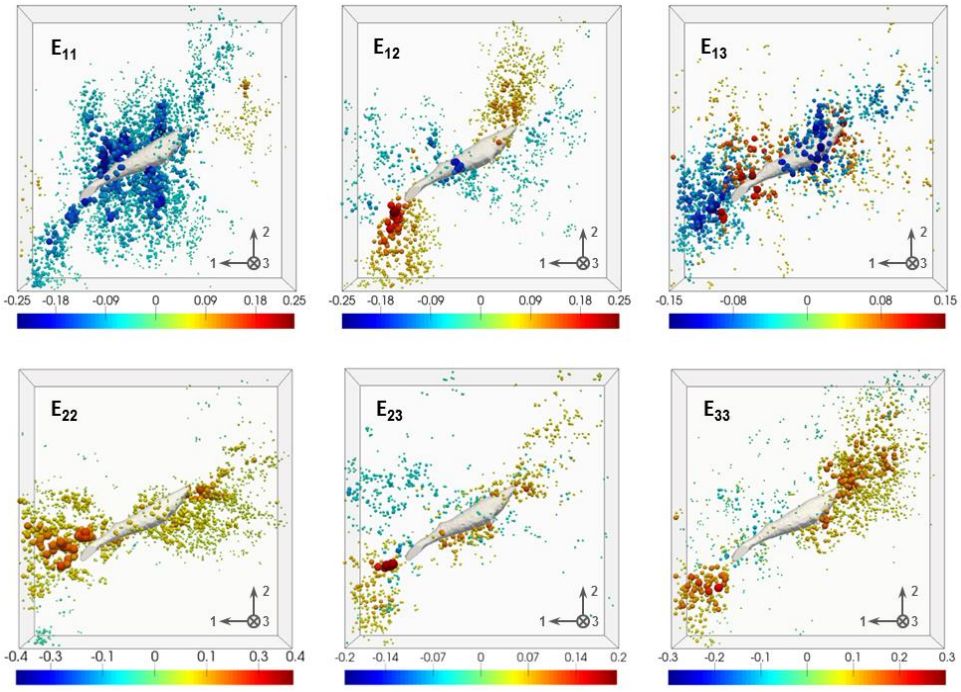

Figure 4–6: Symmetric Green-Lagrange strain tensor for a sample cell in 2.4 mg/mL collagen depicted in Figure S10A.

The maps have been uniformly sampled at random locations to allow the 3D visualization of each component of the tensor. According to the Green-Lagrange strain tensor, six strain components can be expressed: E_{11}, E_{22} and E_{33} representing the normal strains in the x_1, x_2 and x_3 directions respectively, and E_{12}, E_{23} and E_{13} representing the shear strains in the x_1 - x_2, x_2 – x_3 and x_1 – x_3 planes respectively. The reference frame for the x_1, x_2 and x_3 directions is indicated in the lower right corner of each panel.

4.4.4 Both fibrils and beads provide comparable displacement fields

Using external markers, such as fluorescent beads, to track displacements implies several drawbacks, as mentioned in the introduction. In this regard, we comparatively examined whether identical displacement fields can be derived from bead- and fibril-based images acquired by Second Harmonic Generation (SHG).

The results are shown in Figure 4-7 and Supplementary Figures S4-10 and S4-11. A qualitative comparison of the results does not reveal substantial differences between both fields in terms of distribution, orientation or magnitude of the displacements for cells embedded in both 2.4 and 4.0 mg/mL collagen hydrogels. Maximum displacements were typically ~6 μm, ranged between 1.2 and 14 μm and were located near the cell's poles. Of the two poles, the one that displayed the most 'pointed' (slender) shape was associated to the overall maximum displacement. Displacement vectors were pointing towards the cells' center, suggesting contractile forces. Displacement fields were found to be anisotropic, with largest displacements along the direction of cell elongation, *i.e.* aligned with the cell's polarity.

To quantitatively compare the retrieved displacement fields from both bead- and fibril-based images, we computed the relative difference (in %) between their displacement magnitudes and the absolute difference (degrees) between their direction at every spatial coordinate (Figures 4-8 and 4-9 A,B and Supplementary Figures S4-12 and S4-13). These results show relatively low differences in general, with mean and standard deviation values for the magnitude in the range of -6 to 3 and 4 to 15 %, respectively; and with mean and standard deviation values for the direction in the range of 3 to 11 and 2 to 8 degrees, respectively. As expected, relative differences tend to increase for small displacement magnitudes, because of the small denominator. Since in general, one is more interested in regions of large displacements (which are found near the cell-hydrogel interface), further quantitative analysis was restricted to points that exhibited a displacement magnitude larger than the 30% of the peak value for that cell (as estimated from the bead data, which was used as the reference). Figures 4-8 C,D and 4-9 C,D summarize the numerical results for each cell embedded in 2.4 and 4.0 mg/mL collagen hydrogels, respectively, displaying relatively low quantitative differences between the

displacements computed from fibril- and bead-based images, both in terms of magnitude and orientation.

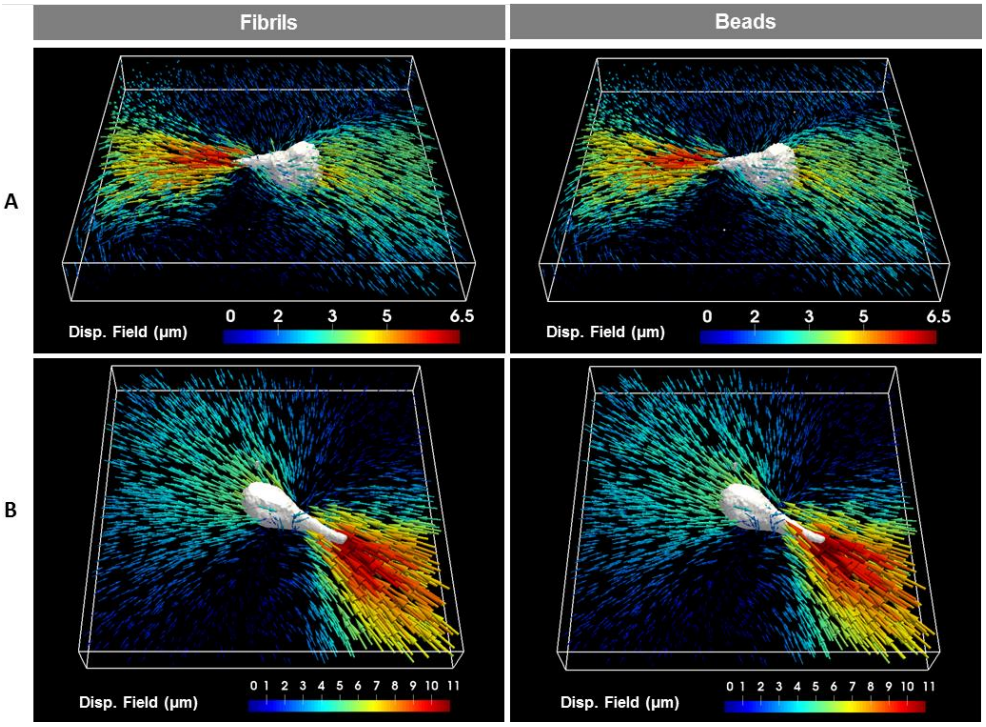

Figure 4–7: Representative 3D displacements induced by two different MRC-5 fibroblasts embedded collagen hydrogels.

The different MRC-5 fibroblasts were embedded in (A) 2.4 mg/ml and (B) 4.0 mg/ml collagen hydrogels, respectively. Displacement fields were obtained from the registration of fibril-based images (left column) and bead-based images (right column). Bounding box: (A) 170 x 170 x 24 μm^3 and (B) 170 x 170 x 23 μm^3.

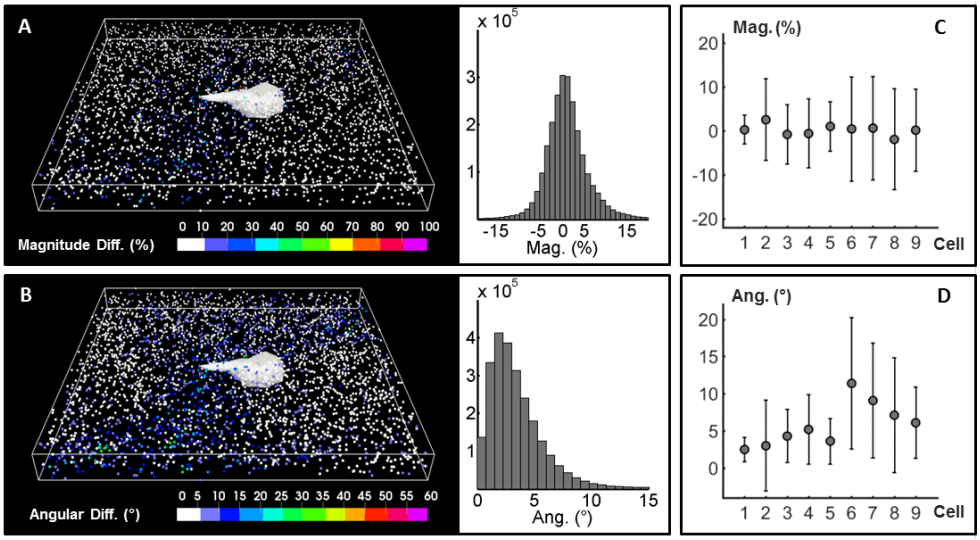

Figure 4–8: Quantitative comparison between the displacements computed from fibril- and bead-based images for cells in 2.4 mg/mL collagen hydrogels.

(A) Map of the relative difference (%) between displacement magnitudes and (B) the angle (degrees) between displacement vector directions for the displacement fields in Figure 4-7A. The map is uniformly sampled at random locations to allow the 3D visualization of the differences for the whole volume. Histograms of the differences (right insets) are computed from those regions exhibiting a displacement magnitude larger than 30% of its peak value. Mean differences (± standard deviation) between the fibril- and bead-based displacements for nine different cells (C and D).

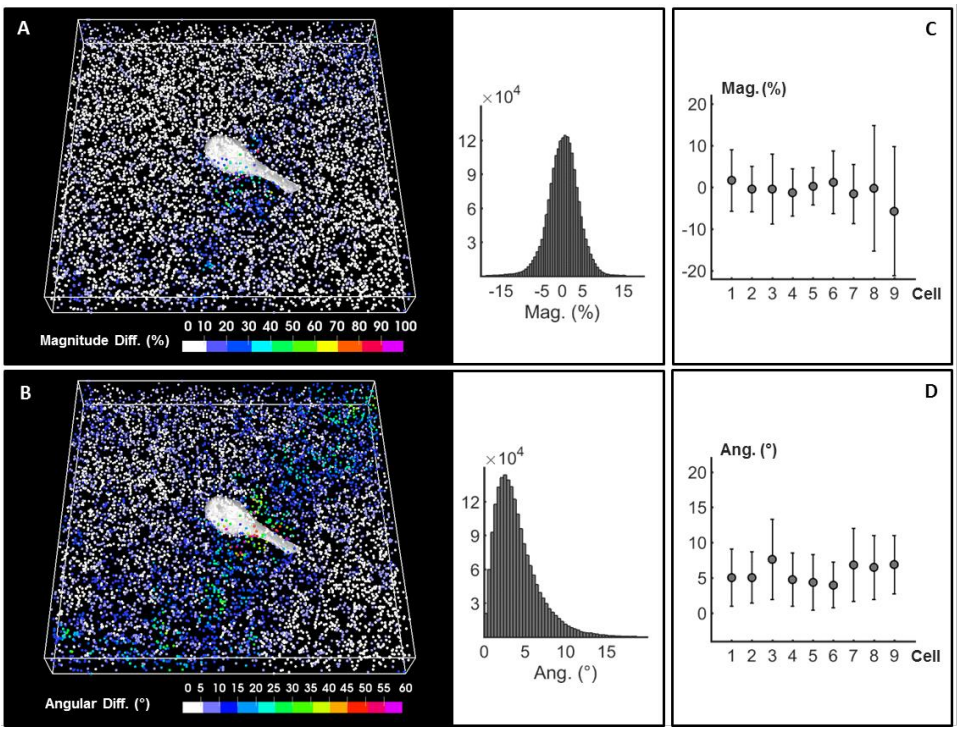

Figure 4–9: Quantitative comparison between the displacements computed from fibril- and bead-based images for cells in 4.0 mg/mL collagen gels.

Map of the relative difference (%) between (A) displacement magnitudes and the angle (degrees) and between (B) displacement vector directions for the displacement fields in Figure 4-7B. The map is uniformly sampled at random locations to allow the 3D visualization of the differences for the whole volume. Histograms of the differences (right insets) are computed from those regions exhibiting a displacement magnitude larger than 30% of its peak value. Mean differences (± standard deviation) between the fibril- and bead-based displacements for nine different cells (C,D).

4.5 Discussion

Here, we have compared two approaches to quantify large deformations in fibrillar type I collagen hydrogels of different concentrations, induced by MRC-5 human lung fibroblasts. Sham experiments revealed a spurious pattern of displacements not originating from cellular activity. As the same pattern was observed in the displacements computed from both beads and fibrils, its origin cannot be attributed to any of them. Also, the used image registration algorithms, the specifics of our experimental protocols and equipment as source of the spurious displacements were excluded by using synthetic data and repeating the experiments under different conditions. Note that the pattern was observed for each displacement component independently. Recently, a depth-dependent lateral shift in the apparent position of a fluorescent point source, termed wobble effect, has been reported [274]. This wobble is caused by both the coverslip tilt and the aberrations introduced by the microscope system, producing a distortion effect that resembles the pattern we noticed in the X- and Y-components of the displacement fields computed from our sham experiments. Analogously to our results, the wobble effect has been reported for microscopes and objectives from different manufacturers with varying magnitude and direction, resulting in a microscope-dependent distortion. However, contrary to our results, the wobble effect is supposed to remain stable in time under similar imaging conditions and thus, other effects may have contributed to our spurious displacement pattern as well. The pattern of the Z-component of the displacements may have been caused by slight imprecisions in the vertical positioning of the image acquisition system. This source of misalignment has already been suggested by Steinwachs *et al*. [257]. Different from our correction method, they pre-corrected acquired z-stacks before the calculation of the cell-induced displacements, which produced slightly low-pass filtered images that would attenuate the artefactual displacement distribution we detected in our sham experiments.

As the spurious displacements observed in the control experiments are likely to be present in the real experiments with cell-populated hydrogels as well, it is necessary to correct for them. The correction can easily be done by calculating the average displacement vector for each XY-plane and subtracting it from the

local displacement vector of each point in the corresponding plane. After correction, the spurious displacement pattern is leveled out, in both control experiments and experiments with cells.

FFD-based non-rigid image registration was used to calculate the displacement fields generated by the MRC-5 fibroblasts. As we previously showed [265], this technique provides a powerful alternative to capture a wide range of locally non-uniform displacements overcoming most of the limitations inherent to other methods. Indeed, it does not rely on tracking fluorescent beads and it can be intuitively viewed as an enhanced version of the block-matching PIV method. Furthermore, whereas previous efforts to estimate the deformations of fibrillar networks directly from fibril-based images were mainly limited to relatively small displacements (order of 1-2 μm, [257] and [263]) and strains (less than 10%, [263]), we have shown here that multiscale FFD can be used to consistently recover large displacements (of the order of 10 μm), large strains (shown here up to 40%) and any complexity associated to this. Therefore, FFD provides a versatile solution to reliably quantify displacements in TFM experiments that deal with large deformation regimes.

The displacement fields that were induced by human lung fibroblasts looked qualitatively similar to those reported for elongated, polarized breast carcinoma cells in fibrillar collagen gels [257, 263] in the sense that they were all aligned with the cell's polarity and the result of mostly contractile forces. As mentioned in the previous paragraph magnitudes of displacements and strains were much higher in our experiments. Given the fact that collagen concentration was of the same order of magnitude (2-4 mg/ml) for all these studies, it seems likely that differences can be at least partially attributed to the difference in cell type.

Finally, our comparative study of cell-induced deformations exposed negligible differences between the displacements computed from beads and fibrils. These differences were assessed both qualitatively from the visual inspection of recovered displacements (Figures 4-7, S4-10 and S4-11) and quantitatively (Figures 4-8, 4-9, and S4-12, S4-13), showing average differences in magnitude and angle that were typically of less than 10% and less than 10 degrees, respectively. It is important to remark that the equivalence between the displacements computed from beads and fibrils would remain valid only under the following conditions. First, the algorithm used for the recovery of the matrix

displacements should be capable of cancelling out the potential effects derived from the motion of beads engulfed by the cells. Secondly, the bead density should be high enough to comply with the Nyquist sampling theorem and thus, a large number of beads need to be bound to collagen fibrils. Indeed, compared to previously reported bead densities [275], our setup presented a 5-fold reduction in bead-bead distance, with average values of ~4.8 μm. Note that for cells inducing highly varying (non-uniform) displacement patterns in space, lower bead densities will lead to a loss of the high frequency content of the cell induced displacements, affecting the estimated magnitudes and spreading them over larger volumes, *i.e.* reducing their spatial resolution. Apart from these conditions, selecting between fibrils and beads to compute the displacement field in TFM experiments will also depend on specific experimental requirements. For instance, while fibrillar networks can be fluorescently labeled, they can also be imaged by label-free techniques such as confocal reflection microscopy [257, 263], and SHG as done here, providing an extra available channel that can be used to simultaneously acquire other fluorescently labelled cellular structures related to cell force generation, such as the cell's actin cytoskeleton. Moreover, fibril images provide structural information and how the cells may remodel the fibrillar structure of a biomaterial, which can be an important determinant of cell fate [266]. Finally, the use of beads may have an impact on the mechanical properties of the biomaterial or on cell behavior, *e.g.* due to bead engulfment.

In conclusion, this novel approach combines non-rigid image registration with label-free SHG imaging and enables the recovery of complex and large deformations induced by cells in fibrillar environments. It is a straightforward technique, without the need of conventionally used fluorescent beads, with all their drawbacks. Comparison with bead-based imaging revealed a good qualitative and quantitative correspondence between fibril-based and bead-based displacement fields. The ability to recover complex and large deformations broadens the applicability in the fast growing field of traction force microscopy. Additionally, it may also advance biomaterial and tissue engineering studies where large cell-induced matrix displacements are part of cell-biomaterial interactions and cell-mediated biomaterial remodelling in soft fibrillar materials.

4.6 Supplementary information

Note 1: brief explanation of traction force microscopy

Basic steps of traction force microscopy

In general, TFM experiments consist of the following four basic steps:

1. *Fabrication of a (biomimetic) matrix including fiducial markers and cells*

In this research, collagen type I hydrogels are employed. Human lung fibroblasts are cultured in the 3D matrix, and both fiducial markers and collagen fibrils are imaged to track the cell-induced displacements.

2. *Microscopic imaging of the stressed and relaxed state of the matrix*

Once the cells have exerted their tractions forces for the desired amount of time, two image stacks must be acquired; the first one while the cells are adhered to the hydrogel and exert forces (stressed state), and the second one after releasing the cellular forces by cell detachment or drug treatment (relaxed state). Note that two image stacks are the absolute minimum to calculate the displacements. However, one can also follow the relaxation process after treatment by continuously capturing image stacks over time.

3. *Calculation of the bead displacements*

By applying image processing based algorithms, the two image stacks are compared to obtain the displacement field of the matrix. For tracking bead displacements, cross-correlation based Particle Tracking Velocimetry (PTV) [256] and Particle Image Velocimetry (PIV) [260] are the preferred methods [265]. However, to overcome their limitations (*vide infra*, image registration for traction force microscopy) several methods have been proposed allowing non-rigid image registration.

4. *Recovery of the exerted forces from the displacement fields*

Finally, cell forces can be recovered by combining the calculated displacement field with a model of the matrix/hydrogel's mechanical properties. Recovering forces from non-linear elastic, fibrillar materials such as collagen type I is not straightforward. Nevertheless, cell-induced matrix displacements often provide enough quantitative information related to the biological questions.

Image registration for traction force microscopy

Particle Tracking Velocimetry

The PIV method tracks the individual displacements of all beads between the images in the stressed and relaxed state. While this approach is conceptually straightforward, tracking a large number of particles might be computationally intensive, and challenging for high particle densities during the particle matching step [265].

Particle Image Velocimetry

PIV is also known as block-matching or digital image (2D)/volume (3D) correlation. The basic principle of the standard block-matching algorithm for 2D images is schematically illustrated in Figure S4-1A. First, both image stacks of the stressed and relaxed state are divided into image blocks, *i.e.* small rectangular windows. Then, the bulk shift of each block is computed by comparing every block with its corresponding one in the other state. One of the limitations of PIV is the assumption that the local deformation within each block is a simple rigid translation, which is generally not the case. Also, there is a loss in spatial resolution as it averages the displacements of the volume of each block. To overcome the described limitations, several methods have been proposed allowing non-rigid deformation of the image blocks (Figure S4-1B). This approach involves fitting of each block deformation to a polynomial model of which parameters are iteratively computed. In this way the averaging effect is avoided since the displacement field at any point within each block can be easily interpolated [265].

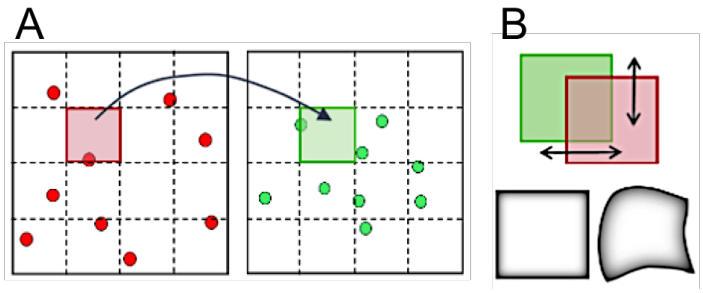

Figure S4–1: Schematic representation of the PIV algorithm in TFM.
(A) In the PIV algorithm, the images of both the relaxed (red) and stressed (green) state of the matrix are divided into multiple blocks to execute a piecewise comparison. (B) In general, the deformation model for each block is assumed to be a rigid translation (top). However, also non-rigid deformation models have been considered to overcome limitations related to rigid image registration (bottom). Adapted from Jorge-Peñas *et al.* [265]; originally published under CC-BY 4.0 license, copyright © 2015. Available from: https://doi.org/10.1371/journal.pone.0144184.

Free-Form Deformation (FFD)

As for non-rigid registration, in this research a B-spline-based FFD approach was used (Figure S4-2) [265]. First, the FFD algorithm overlays the image of the relaxed state with a uniform deformable mesh and defines subsequently the mesh nodes as control points of the B-spline curves. Next, the position of these control points is tuned iteratively, including three major steps: (i) similarity metric, which involves comparison of the reference (relaxed state) and target (stressed state) images, (ii) optimization strategy, which checks how the reference image should be warped, (iii) transformation model which includes an update of the positions of the control points of the mesh and results in a warped reference image given by a multivariate B-spline function (for more information on B-splines in image registration the following references are recommended: [276, 277]). These steps are iterated until the image of the stressed matrix matches the one of the relaxed condition. The output is a full displacement field meaning that displacements are determined at each voxel of the registered images.

Finally, we performed image registration following a coarse-to-fine multiscale strategy. In the coarsest scale, a large value for the mesh size is used. Next iteration, the mesh size is decreased and the algorithm is applied again but taking into account the information on the displacements provided by the previous scale. In this way, the displacement field can be refined without introducing excessive errors. This allowed us to cope with different levels of matrix deformations while providing smooth displacement fields.

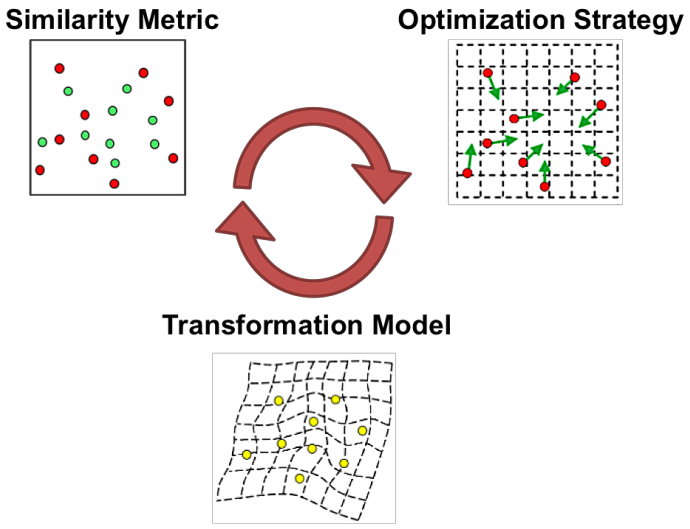

Figure S4–2: Schematic representation of the FFD algorithm in TFM.
The control points of the B-spline curves are tuned iteratively. Similarity metric: comparison of the bead locations in images of the relaxed (red) and deformed (green) matrix. Optimization strategy: determination of how the uniform deformable mesh should be warped to align the beads of the relaxed matrix with their counterparts in the stressed matrix. Transformation model: the position of the control points is update. This three-step process is iterated and at the end the beads have been registered (yellow). The deformed mesh provides the displacement field. Adapted from Jorge-Peñas et al. [265]; originally published under CC-BY 4.0 license, copyright © 2015. Available from: https://doi.org/10.1371/journal.pone.0144184.

Note 2: brief explanation image correlation spectroscopy

All image correlation spectroscopy variants are based on the analysis of fluorescence fluctuations measured within an observation area. The fluctuations of fluorescence intensity, δ_i, recorded in the image series are defined as:

$$\delta_i(x,y,t) = i(x,y,t) - \langle i(x,y,t) \rangle_{XY} \quad \text{(Eq. S4-1)}$$

where $<\ldots>_{XY}$ denotes spatial averaging of the stack of images; *x* and *y* represent spatial coordinates of the considered pixel, *t* is the time of the considered image in the time series, and *i(x,y,t)* indicates the intensity at *(x,y)* and time *t*.

The fluctuations can be defined as temporal intensity fluctuations between images taken at different times in a time lapse (*i.e.* temporal image correlation spectroscopy*;* TICS) and spatial intensity fluctuations across a given image (*i.e.* spatio-temporal image correlation spectroscopy; STICS). The spatial fluctuations include changes in the number of static or slowly moving fluorophores in space, while temporal fluctuations reflect dynamic variations in the amount of fluorophores at a given spot over time since the fluorescent molecules undergo transport.

TICS can be employed for measuring the magnitude of the diffusion coefficient and/or flow speed of slowly moving particles from an image time lapse [269, 278, 279]. To obtain a single temporal autocorrelation function *G (0,0,τ)*, all autocorrelation functions yielding from each pixel location are averaged:

$$G(0,0,\tau) = \left\langle \frac{\langle \delta_i(x,y,t)\, \delta_i(x,y,t+\tau) \rangle_{XY}}{\langle i(x,y,t) \rangle_{XY} \langle i(x,y,t+\tau) \rangle_{XY}} \right\rangle_T \quad \text{(Eq. S4-2)}$$

where <…> indicates the averaging of all images in space ($_{XY}$) or time ($_T$); and τ denotes the time-lag.

In STICS, the spatial information derived from the two-dimensional spatial correlations is combined with the time-dependent transport measured using the temporal correlation. The average correlation function for all time-lag τ separated pairs of images is represented by $G(\xi,\eta,\tau)$ [268, 279]:

$$G(\xi,\eta,\tau) = \left\langle \frac{\langle \delta_{i(x,y,t)}\, \delta_i(x+\xi,y+\eta,t+\tau)\rangle_{XY}}{\langle i(x,y,t)\rangle_{XY}\, \langle i(x+\xi,y+\eta,t+\tau\rangle_{XY}} \right\rangle_T \qquad \text{(Eq. S4-3)}$$

where ξ and η denote the spatial lag variables in x and y, respectively.

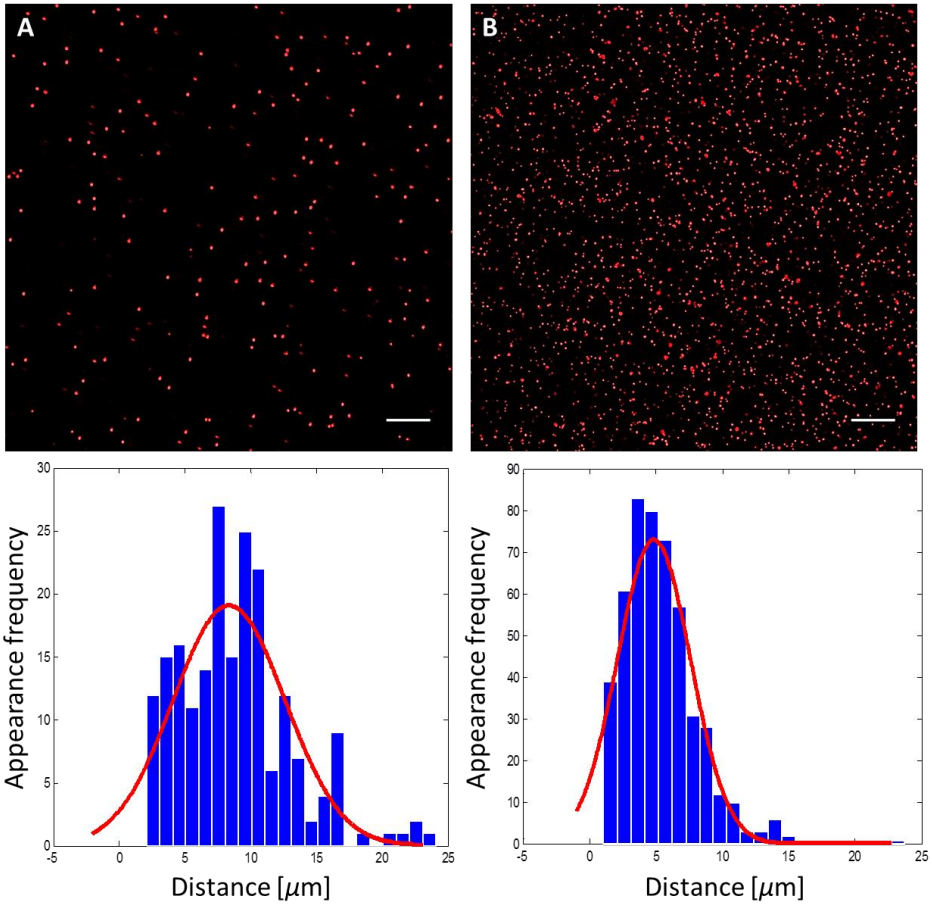

Figure S4–3: Neighbor bead-bead distance distribution histograms of fiducial markers in collagen hydrogels.

Confocal section and nearest neighbour bead-bead distance distribution histogram of (A) 1 μm and (B) 200 nm fluorescent beads inside the collagen type I hydrogel. Scale bars: 20 μm.

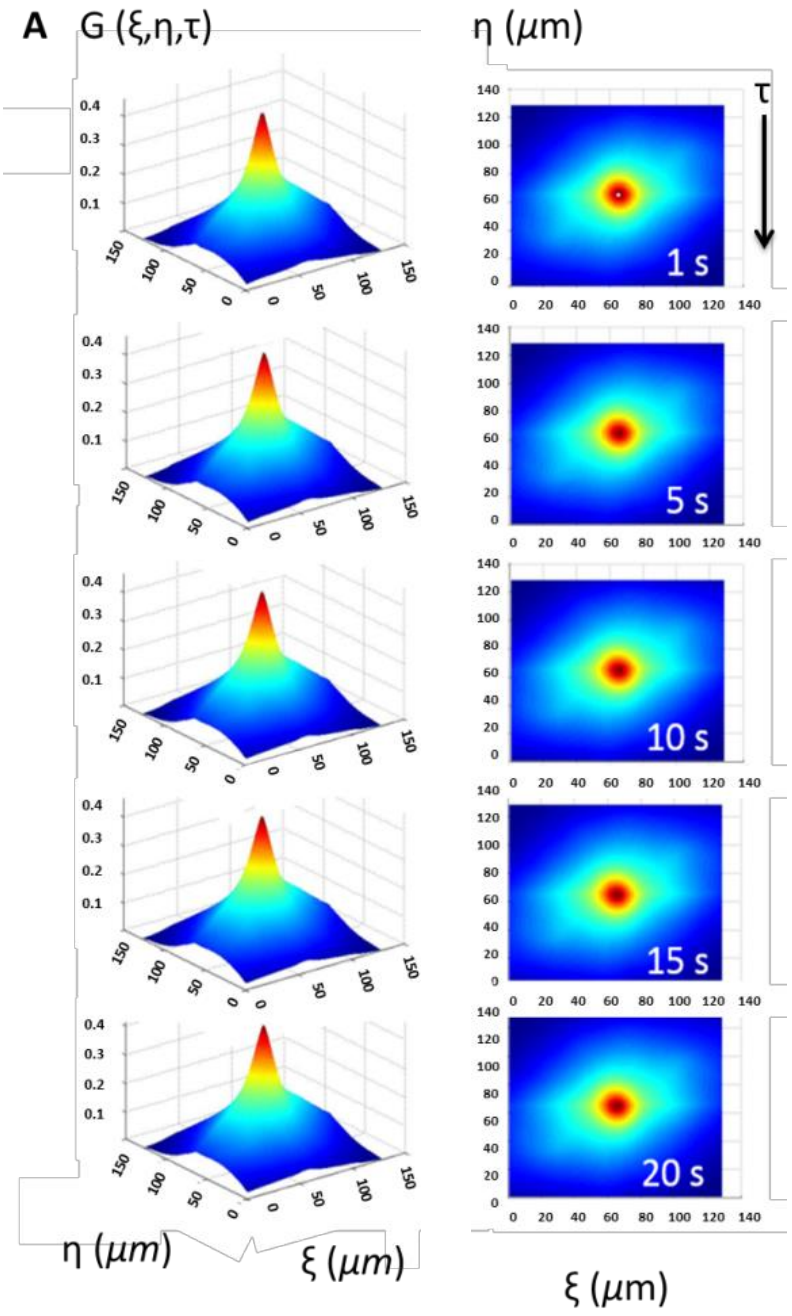
A
G (ξ,η,τ)
η (μm)
τ
1 s
5 s
10 s
15 s
20 s
η (μm)
ξ (μm)
ξ (μm)

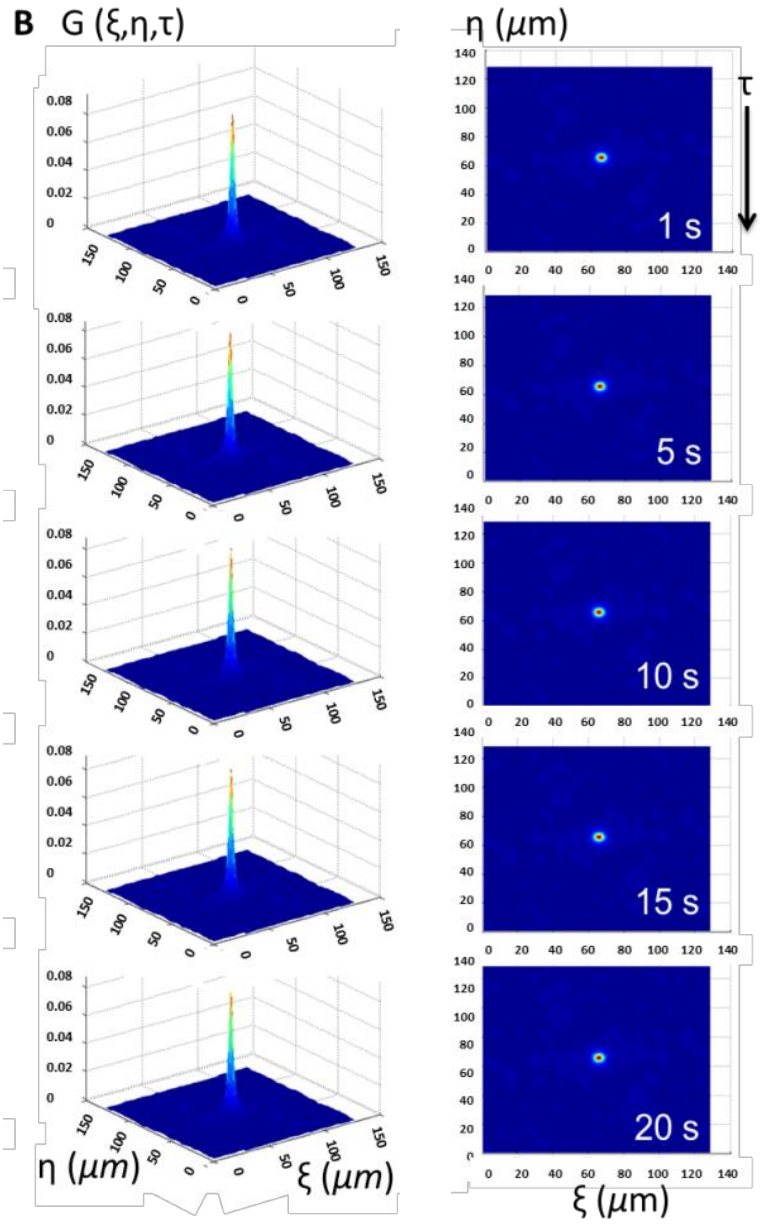

Figure S4–4: Evaluation of the attachment of fiducial markers to collagen fibrils. Evaluation of the attachment of (A) 1 μm and (B) 0.2 μm fluorescent beads to the collagen type I fibrils by spatiotemporal image correlation spectroscopy. No broadening or lateral shift of the autocorrelation peaks is observed, indicating that there is no diffusion or flow of the beads.

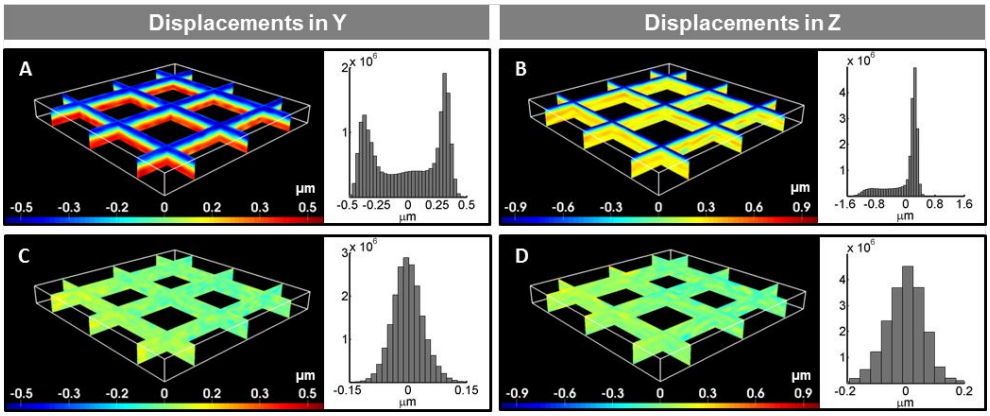

Figure S4–5: Spurious displacements obtained from bead-based images in cell-free sham experiments.

(A, B) Before and (C, D) after correction. Axial cross-sections at multiple locations of the acquired volume and histograms (right insets) for the (A) Y- and (B) Z-components of the computed displacement field, and their corrected versions (C) and (D), respectively. Bounding box: 220 x 220 x 23 μm^3.

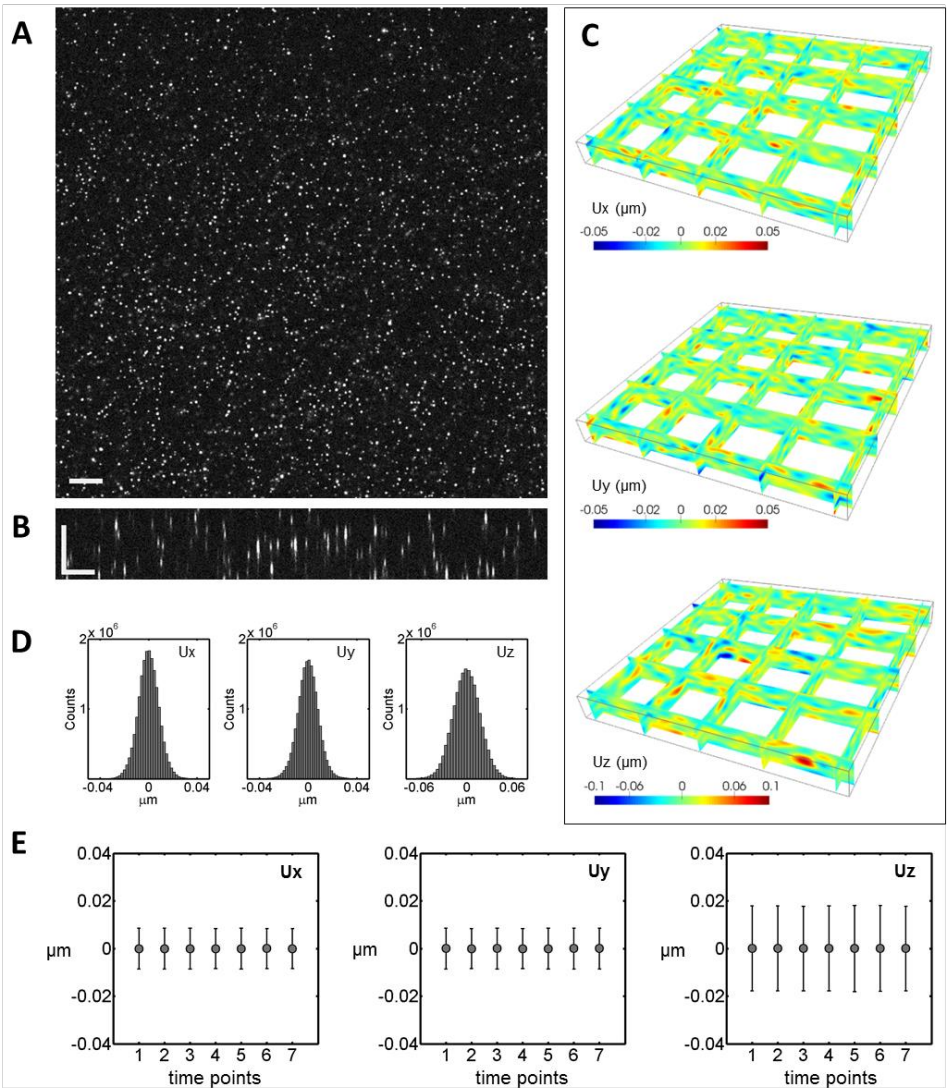

Figure S4–6: Evaluation of detection limit of the FFD-based displacement calculation method with synthetic data.

Sample (A) cross-section and (B) axial-section of simulated hydrogel volume containing fluorescent beads. The scale bar: 15 μm. (C) Axial sections at multiple locations of the simulated volume (bounding box: 220 x 220 x 23 μm^3) showing displacements without the spurious distribution observed in real sham experiments and (D) their corresponding histograms. Mean errors (± standard deviation) in the raw (non-corrected) displacements for different time points (E). The obtained small variance in (D) and (E) is caused by the time-varying noise introduced in the simulated images.

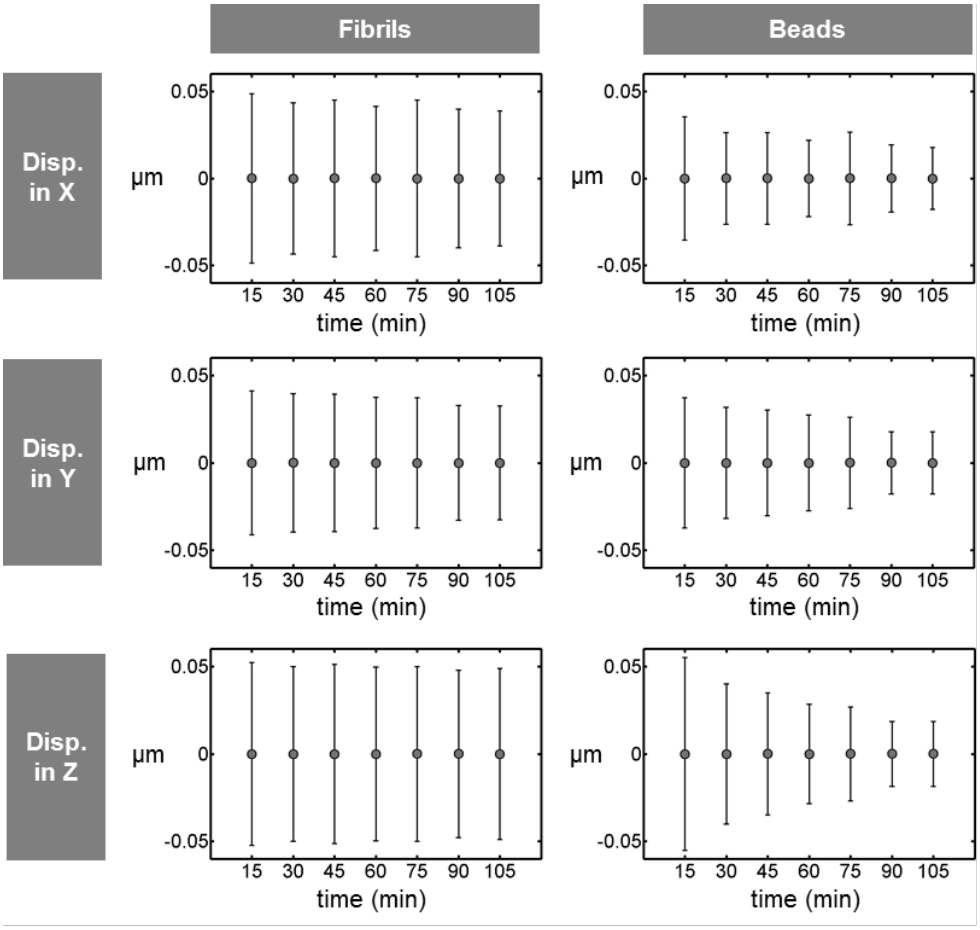

Figure S4–7: Detection limit of the FFD-based displacement calculation method from sham experiments.

Mean errors (± standard deviation) in the X- (top row), Y- (middle row) and Z- (bottom row) components of the displacements computed from fibril- (left column) and bead-based (right column) images after the proposed correction (see main text).

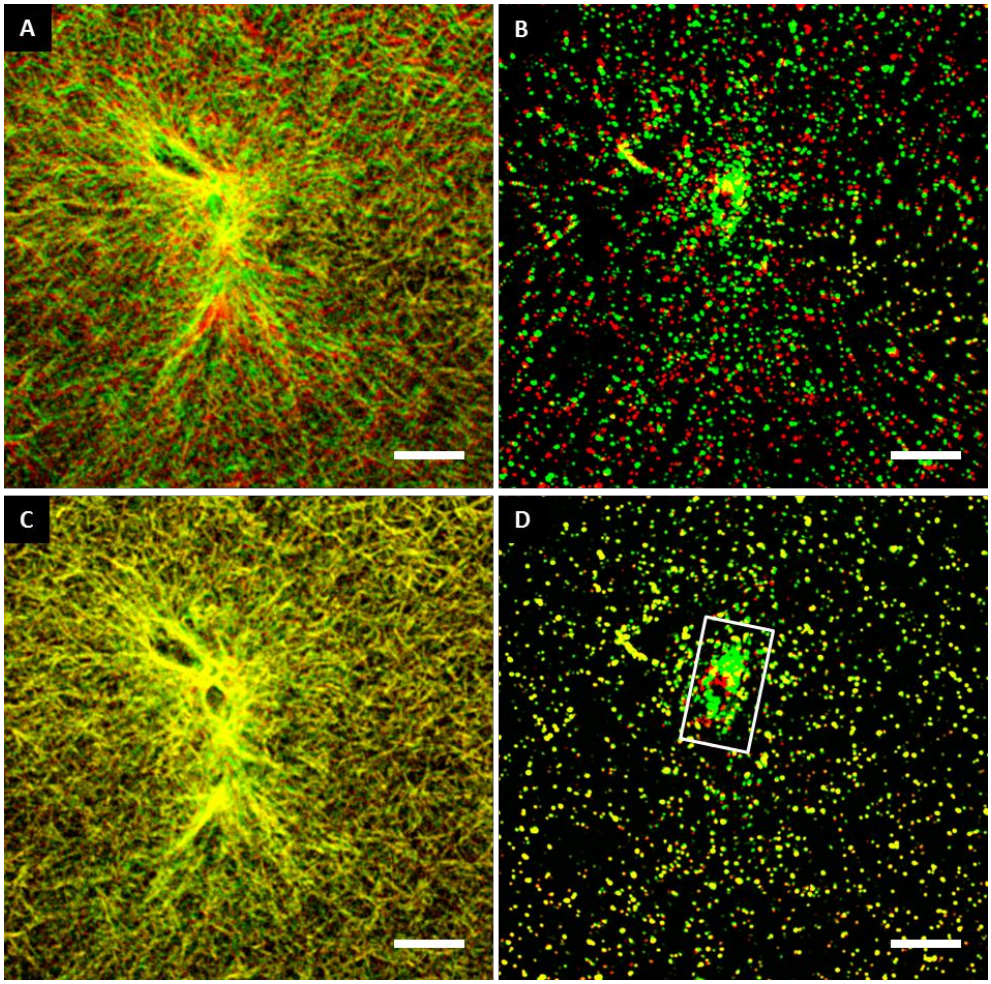

Figure S4–8: FFD-based image registration of the cell-induced stressed vs. unstressed 4.0 mg/mL hydrogel.

FFD-based image registration of the unstressed and stressed (before addition of cytochalasin B) gel of 4.0 mg/ml collagen concentration. Pseudo-colored cross-sections of the collagen hydrogel showing the (A) fibril- and (B) bead-based images before the registration, and their registered results (C) and (D), respectively, that lead to the recovered displacement field. The fibrils/beads in the unstressed and stressed hydrogel are pseudo-colored in red and green, respectively. Fibrils/beads appear as yellow where both the unstressed and stressed conditions match. The beads engulfed by the cell are ignored during the registration process (D, delineated area) to avoid artifacts in the recovered displacements. Scale bars: 25 μm.

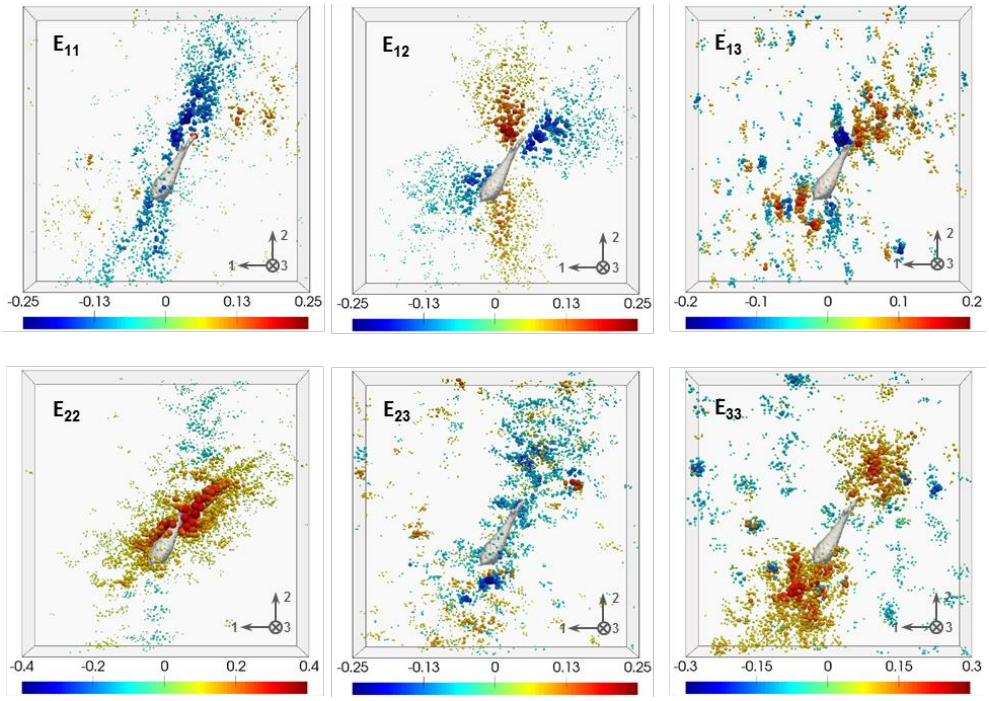

Figure S4–9: Symmetric Green-Lagrange strain tensor.

Exemplar symmetric Green-Lagrange strain tensor for a sample cell in 4.0 mg/mL collagen depicted in Figure S4-11B. The maps have been uniformly sampled at random locations to allow the 3D visualization of each component of the tensor. According to the Green-Lagrange strain tensor, six strain components can be expressed: E_{11}, E_{22} and E_{33} representing the normal strains in the x_1, x_2 and x_3 directions respectively, and E_{12}, E_{23} and E_{13} representing the shear strains in the x_1 - x_2, x_2 – x_3 and x_1 – x_3 planes respectively. The reference frame for the x_1, x_2 and x_3 directions is indicated in the lower right corner of each panel.

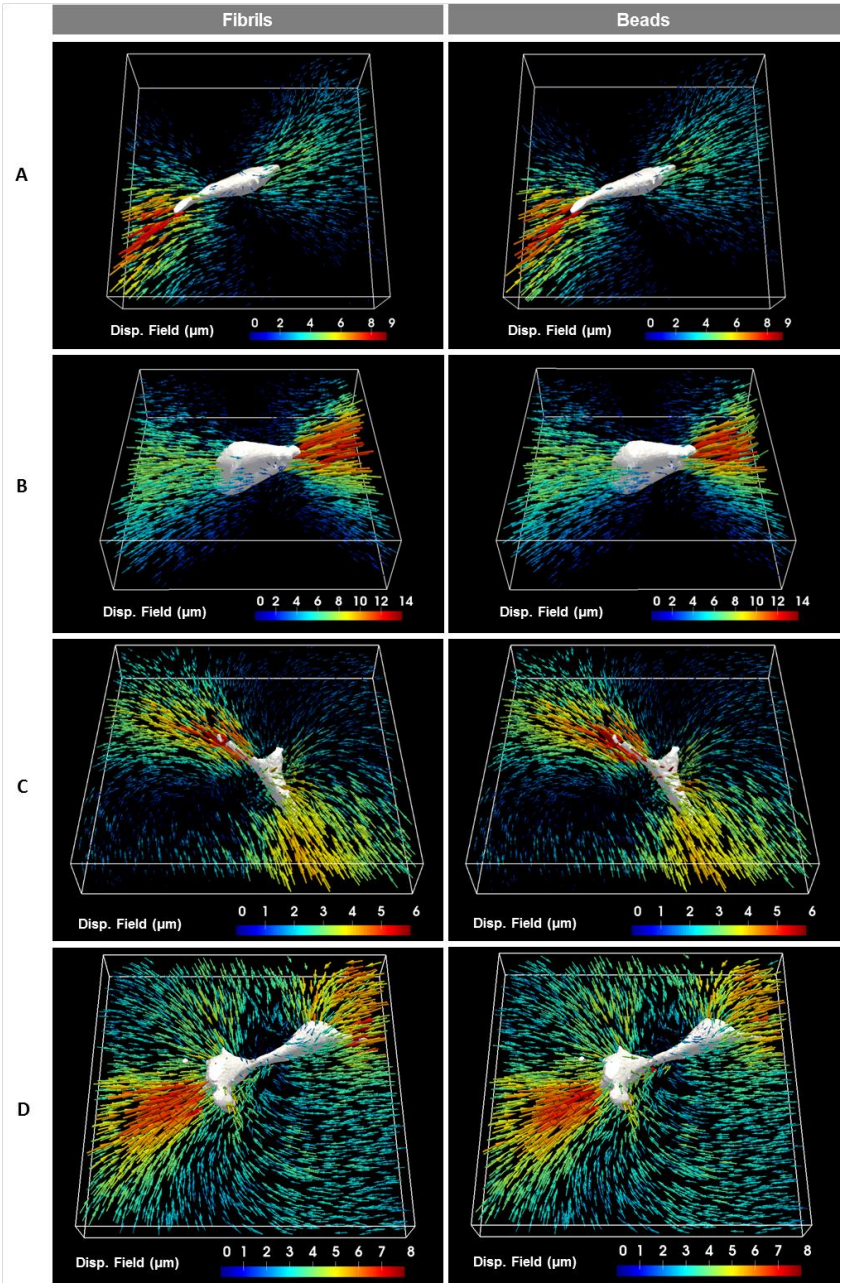

Figure S4–10: Representative 3D displacements induced by 4 different MRC-5 fibroblasts embedded in 2.4 mg/mL hydrogels.

(A, B,C,D) obtained from the registration of fibril-based images (left column) and bead-based images (right column). Bounding box: (A) 170 x 170 x 46 μm^3, (B) 165 x 170 x 48 μm^3, (C) 173 x 172 x 30 μm^3 and (D) 166 x 168 x 22 μm^3.

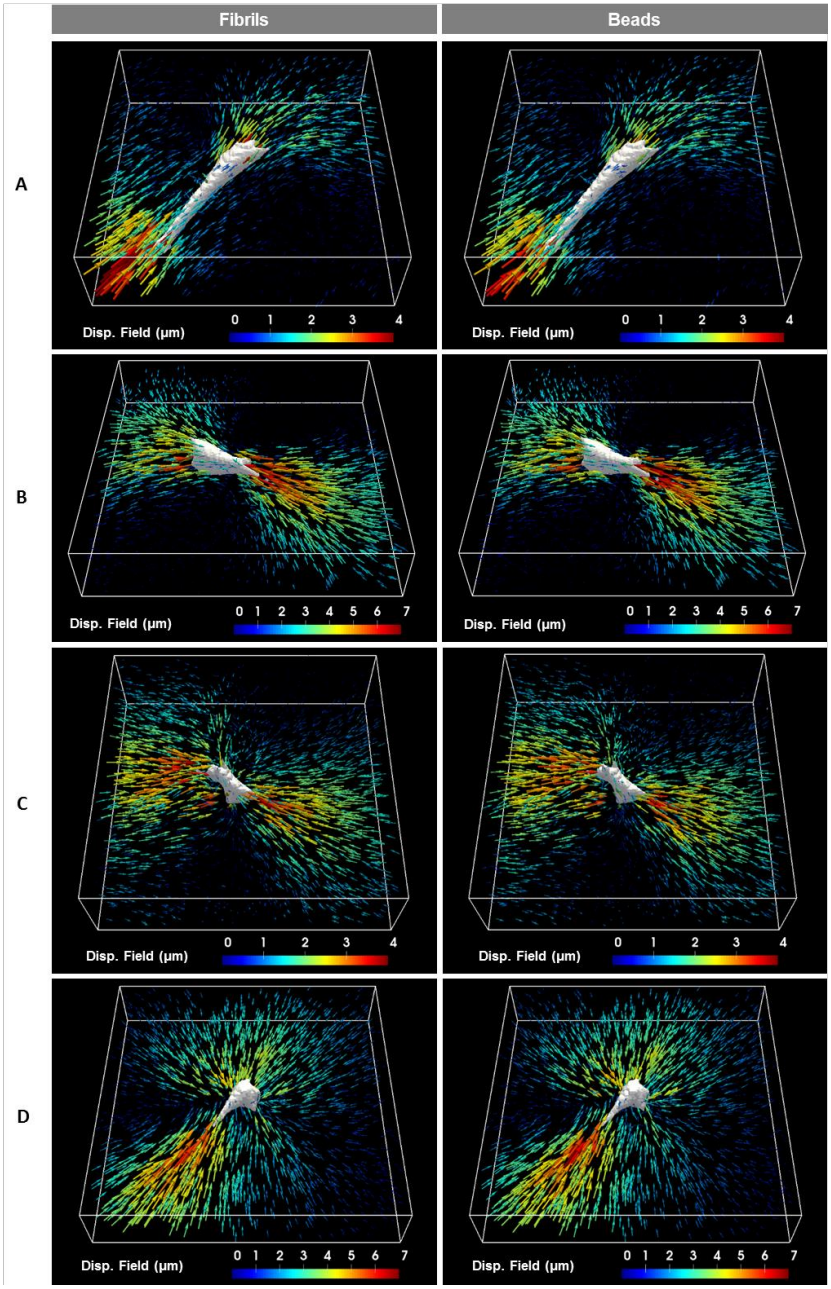

Figure S4–11: Representative 3D displacements induced by 4 different MRC-5 fibroblasts embedded in 4.0 mg/mL hydrogels.

(A, B,C,D) obtained from the registration of fibril-based images (left column) and bead-based images (right column). Bounding box: (A) 172 x 172 x 49 μm^3, (B) 173 x 173 x 37 μm^3, (C) 172 x 172 x 51 μm^3 and (D) 172 x 172 x 34 μm^3.

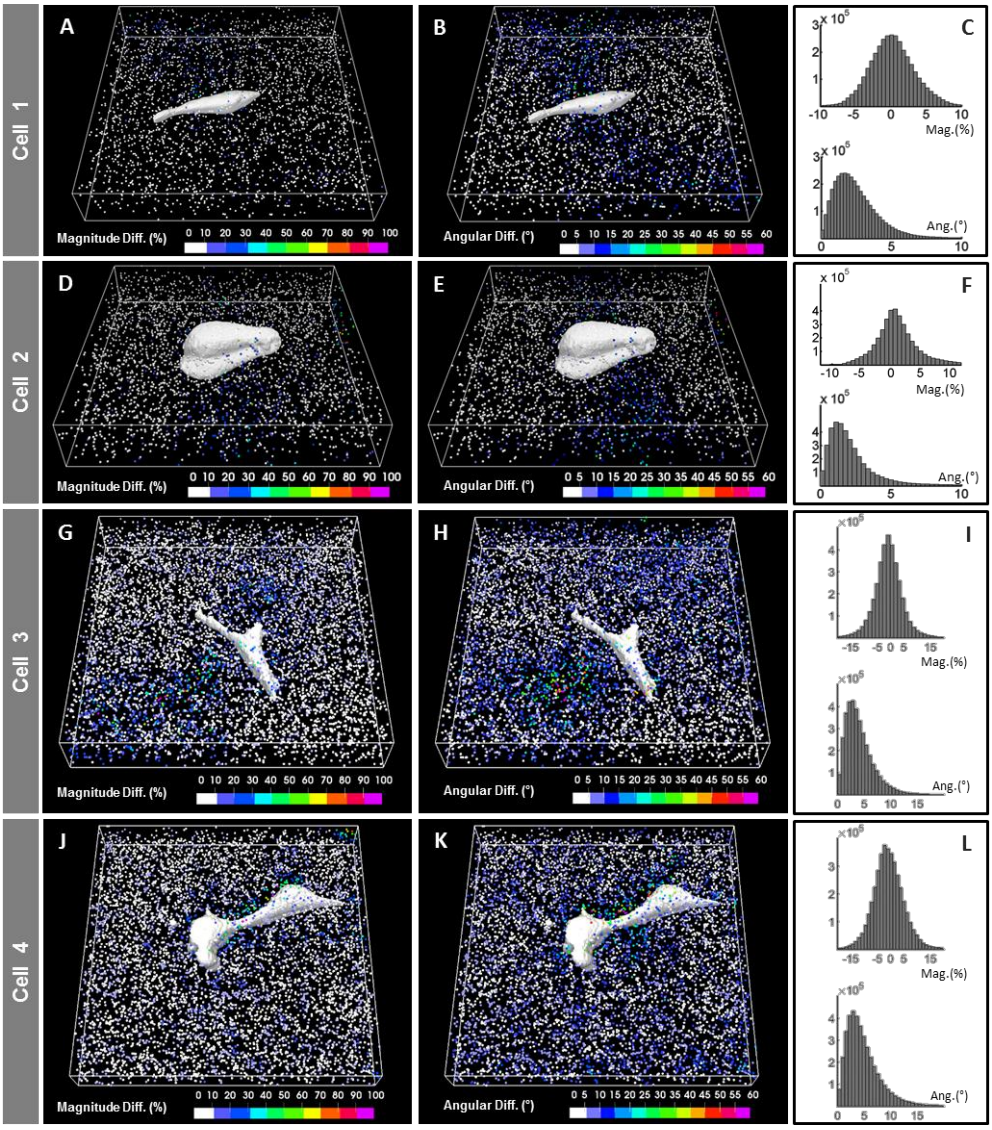

Figure S4–12: Quantitative comparison between the displacements computed from fibril- and bead-based images for cells in 2.4 mg/mL collagen hydrogels.

For the displacement fields shown in Figure S4-10 A (cell 1), S4-10 B (cell 2), S4-10 C (cell3) and S4-10 D (cell4). Map of the relative difference (%) between (A, D, G and J) displacement magnitudes and (B, E, H and K) the angle (degrees) between displacement vector directions. (C, F, I and L) Histograms of the differences are computed from those regions exhibiting a displacement magnitude larger than 30% of its peak value.

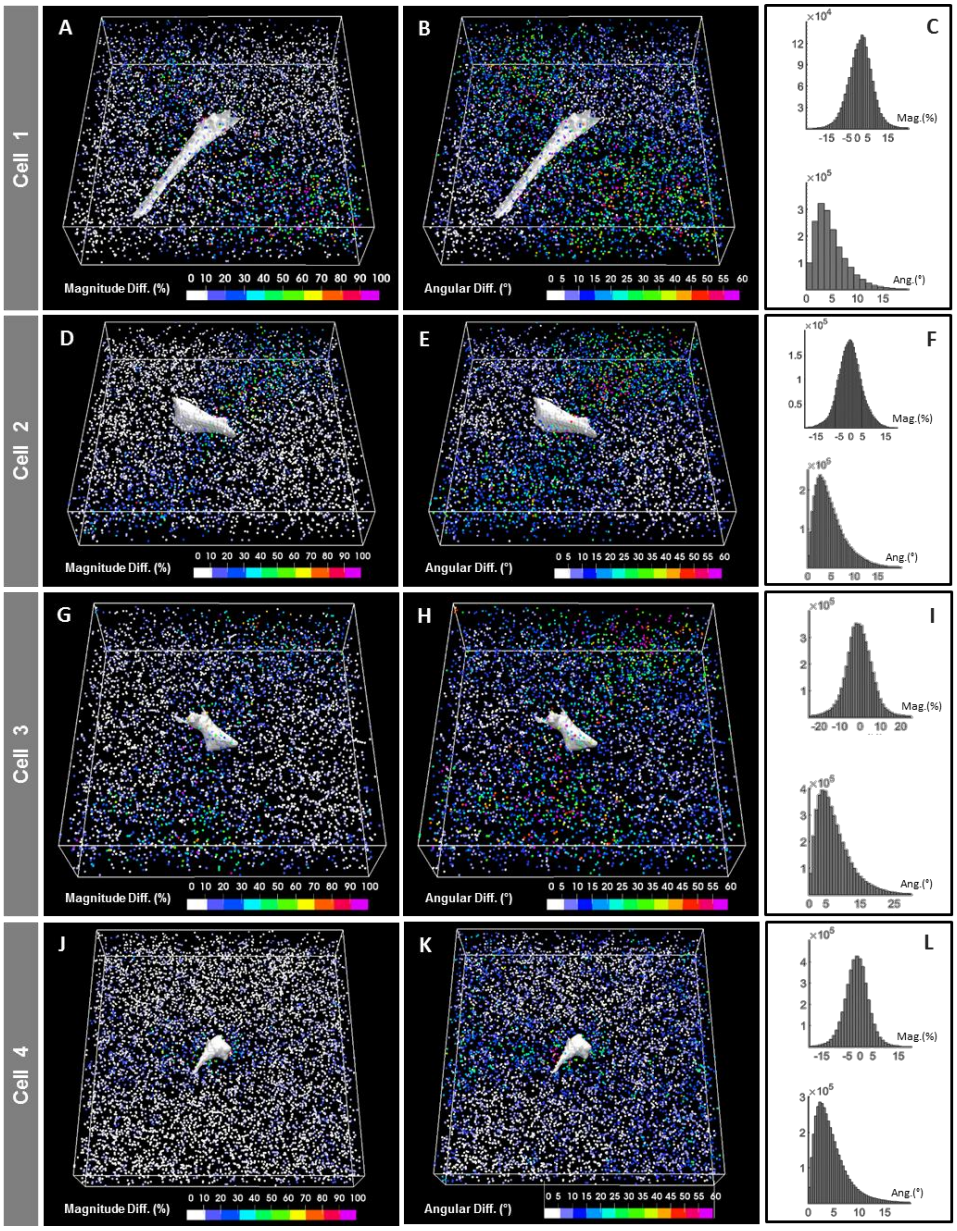

Figure S4–13: Quantitative comparison between the displacements computed from fibril- and bead-based images for cells in 4.0 mg/mL collagen hydrogels.

For the displacement fields shown in Figure S4-11 A (cell 1), S4-11 B (cell 2), S4-11 C (cell3) and S4-11 D (cell4). Map of the relative difference (%) between (A, D, G and J) displacement magnitudes and (B, E, H and K) the angle (degrees) between displacement vector directions. (C, F, I and L) Histograms of the differences are computed from those regions exhibiting a displacement magnitude larger than 30% of its peak value.

Chapter 5
Application of WL detection technique in real biological samples

This chapter is based on:

Children's urinary environmental carbon load: a novel marker reflecting residential ambient air pollution exposure?

Saenen N.*, **Bové H.***, Steuwe C., Roeffaers M., Provost E., Lefebvre W., Vanpoucke C., Ameloot M., Nawrot T.

American Journal of Respiratory and Critical Care Medicine 2017. IF(2015)=13.118.

* Authors contributed equally.

Declaration of own contribution: Hannelore Bové executed all calibration, optimization and validation experiments. She jointly performed the urinary carbon measurements and all related analyses. She also contributed in writing the manuscript.

5.1 Abstract

Ambient air pollution, including black carbon, entails a serious public health risk because of its carcinogenic potential and as climate pollutant. To date, an internal exposure marker to black carbon particles having cleared from the circulation into the urine does not exist. We developed and validated a novel method to measure black carbon particles in a label-free way in urine.

We detected urinary carbon load in 289 children (aged 9-12 years) using white-light generation under femtosecond pulsed laser illumination[1]. Children's residential black carbon concentrations were estimated based on a high-resolution spatial temporal interpolation method.

We were able to detect urinary black carbon in all children, with an overall average (SD) of 98.2 x 10^5 (29.8 x 10^5) particles/mL. The urinary black carbon load was positively associated with medium-term up to chronic (one month or more) residential black carbon exposure, *i.e.* +5.33 x 10^5 particles/mL higher carbon load (95% CI: 1.56 x 10^5 to 9.10 x 10^5 particles/mL) for an interquartile range (IQR) increment in annual residential black carbon exposure. Consistently, children who lived closer to a major road (≤ 160 m) had higher urinary black carbon load (6.93 x 10^5 particles/mL; 95% CI: 0.77 x 10^5 to 13.1 x 10^5).

Urinary black carbon mirrors the accumulation of medium-term up to chronic exposure to combustion-related air pollution. This specific biomarker reflects internal systemic black carbon particles, cleared from the circulation into the urine, providing its utility to unravel the complexity of particulate-related health effects.

[1] In this chapter, BC detection in urine was performed by white-light generation under femtosecond pulsed illumination instead of pump-probe imaging since the latter was still under active development at the time of these measurement. However, both techniques can be employed for detecting urinary carbon load.

5.2 Introduction

Current ambient outdoor air pollution is responsible for 4.2 million premature deaths worldwide [2], ranked within the top ten of important risk factors for public health. Children are especially vulnerable to the detrimental effects of air pollution and have for the same ambient concentrations a higher internal dose compared to adults due to their higher respiratory rate. Combustion-related particulate matter (PM) air pollution, including black carbon, is associated in early life with lower birth weight [280], decreased cognitive function in children [23, 24], impaired cognitive aging [25], increased cardiovascular morbidity and mortality [19, 281] as well as respiratory diseases [282] and lung cancer in adult life [283]. Three hypotheses are formulated to rationalize these findings. First, particles produce pulmonary oxidative stress and inflammation with a systemic release of cytokines [19]. Second, the smallest particles translocate from the lungs into the circulation with effects in different organ systems. Third, particles interact with pulmonary receptors or nerves with effects *via* the autonomic nervous system [284]. Experimental studies on animals have shown that a substantial fraction of intratracheally introduced ultrafine particles could translocate into the systemic circulation [285], and even may translocate via the olfactory nerve to the brain when deposited in the nose [123]. However, in humans the subject of particle translocation is still under debate as to date studies failed to find a considerable fraction of inhaled particles translocated into the circulation. Furthermore, the clinical significance how these ultrafine particles contribute to health remains unclear.

Although some air pollution associations are established as causal [19], risks might be considerably underestimated due to exposure misclassification. In most epidemiological studies, the exposure to PM air pollution, including black carbon, is not measured at the individual or time-activity pattern level. Instead, spatial temporal models are used, which basically use land cover data that is based on multiple primary sources (*i.e.,* road networks, line and point locations of potential sources, building density, etc.) to estimate the daily residential exposure values [78, 286] which results in incomplete information about residential mobility. In these studies, the bulk of exposure measurement error, which is typically "Berkson-like", lead to unbiased but more variable health

effect estimates [287]. Despite increased understanding of the health consequences of combustion-related air pollution; a critical barrier to progress in the field is our limited ability to monitor adequately personalized exposure over the life course. To overcome these shortcomings, we postulated the translocating nature of black carbon particles from the circulation into the urine so that these particles in urine form a biomarker reflecting exposure. Within this framework, we detected and quantified black carbon particles in urine of 289 children living in the northern part of Belgium with relatively low annual ambient black carbon concentrations in the study area ranging from 1.07 to 1.96 $\mu g/m^3$.

5.3 Materials and methods

5.3.1 Calibration experiments for black carbon detection in urine

In this research, we employed a label-free and biocompatible imaging technique based on the non-incandescence related white-light generation potential of carbonaceous particles under femtosecond illumination [206]. Summarized, the heterogeneous and absorptive (dark color) nature of carbonaceous particles gives rise to the white-light phenomenon. For the signal to occur, these two conditions should explicitly be fulfilled. Therefore, (i) the possible contribution of any non-carbonaceous material (except for noble metals, they are able to generate plasmons) is excluded, since they do not comply with the aforementioned conditions; (ii) carbon-containing materials such as endogenous structures with carbon backbones will not generate the white-light since they do not contain multiple absorbing sites; and (iii) the material generating this signal should be in particle form for exhibiting the heterogeneity and absorptive character.

Here, several experiments were conducted to assess the potential for cross-reactivity or to assess specificity more generally. First, we validated and calibrated the application method for urine imaging using artificial urine. The employed artificial urine contained urea and inorganic salts. It was prepared by dissolving 2.43 g urea (Janssen Chimica, Belgium), 0.30 g sodium citrate dehydrate (Janssen Chimica), 0.63 g sodium chloride, 0.45 g potassium chloride, 0.16 g ammonium chloride (Merck Chemicals, Belgium), 0.09 g calcium chloride dehydrate, 0.10 g magnesium sulfate heptahydrate (Acros Organics, Belgium), 0.03 g sodium hydrogen carbonate (Sigma-Aldrich, Belgium), 0.26 g sodium sulfate (UCB, Belgium), 0.10 g sodium phosphate monobasic monohydrate (Sigma-Aldrich, Belgium), and 0.01 g sodium hydrogen phosphate in 200 mL ultrapure water (composition adapted from Chutipongtanate *et al.* [288]). This artificial urine solution was imaged under identical imaging conditions as used for analyzing the 'real' urine samples; to check for any signal coming from, for example, urinary salt crystals. Secondly, background signals from naturally present carbonaceous particles in the air and detection chambers were checked by measuring empty Ibidi wells. Thirdly, cross-reactivity from the most structurally and chemically resembling particles available, named silica

particles [289], was checked under identical imaging conditions. The employed silica and carbon nanotubes were retrieved from Sigma Aldrich (S5130, fumed, 7 nm), and Joint Research Centrum (multi-walled carbon nanotubes, reference material NM400) and National Institute of Health (single-walled carbon nanotubes, reference material 2483), respectively. Fourth, cross-reactivity from other carbonaceous materials was checked by measuring carbon nanotubes. Fifth, Raman spectroscopy measurements were executed on dried urine samples. A drop of urine was dried on a cleaned microscopy slide and sealed using a cover slip. Raman spectra were collected with a CCD camera (Newton, Andor, UK) equipped with a blazed grating monochromator (IHR320, Horiba, Japan). A 633 nm Helium Neon Laser (Research and Electro-Optics INC, USA) with an average power at the samples of 1 mW was used. The Raman signal passed a long pass filter of 645 nm. The integration time was 10 s and averages of 6 scans are shown. Data were collected in air at room temperature.

5.3.2 Optimized experimental protocol for black carbon detection in urine.

The carbonaceous particles in the urine samples were analyzed and images collected using a Zeiss LSM510 META NLO (Carl Zeiss, Jena, Germany) mounted on an Axiovert 200 M equipped with a two-photon femtosecond pulsed laser (MaiTai DeepSee, Spectra-Physics, USA). A 40x/1.1 water immersion objective (LD C-Apochromat 40x/1.1 W Korr UV-Vis-IR, Carl Zeiss) was used and the laser was tuned to a central wavelength of 810 nm with a ~ 9.7 mW radiant power at the sample position. Black carbon particle emission was detected *via* analogue photomultiplier detection in epi-configuration in non-descanned mode after the signal passed through a 400 – 410 nm band pass filter. The resulting images had a field view of 225 x 225 μm^2 with 512x512 pixel resolution (0.44 x 0.44 μm^2 pixel size) and a 3.2 μs pixel dwell time. The point spread function radius ($1/e^2$ level) in X- and Y-direction is about 350 nm. All data were recorded at room temperature (22°C).

From optimization measurements we found that 120 images obtained from 10-frame time lapses at three different positions in four different aliquots of one urine sample are necessary to gain highly reproducible results (<5 % coefficient of variation of three repeated measurements for 20 individuals, data not

shown). Urine samples were aliquoted at 200 μL/well in Ibidi μ-slide 8 well plates (Ibidi GmbH, Germany). All images were taken 300 μm above the bottom glass.

To count the number of black carbon particles in the time frames of each urine sample, a peak-find algorithm in Matlab (Matlab 2010, MathWorks, The Netherlands) was used, which counts connected pixels above a threshold value. A threshold value of 15% lower than the highest intensity value was chosen, which gave highly reproducible values. The average amount of black carbon particles obtained in this way was normalized using the focal volume estimated from the point spread function of the optical system to obtain results expressing the total amount of detected black carbon in the imaged volume. Finally, the results are expressed as the number of detected black carbon particles per milliliter urine.

5.3.3 Validation experiments of optimized urinary carbon load technique

The optimized technique for measuring carbon load in urine was validated by spiking urine with known concentrations of carbon black nanopowder (US Research Nanomaterials, USA). However, it should be noted that carbon black powder in solution tends to form larger aggregates. Therefore the following precautions were taken: (i) diluting in urine helps to gain better dispersity, since the proteins are beneficial, (ii) the stock solution was ultrasonicated in a water bath for a sufficient amount of time, (iii) the dilution series was additionally sonicated, (iv) all solutions and dilutions were freshly prepared, just before measuring them, (v) all solutions and dilutions were checked visually and by dynamic light scattering for aggregates, (vi) all solutions and dilutions appeared to be stable for up to two hours after preparation, which is a sufficient amount of time to measure the calibration curve. From the spiked urine samples seven 10-frame time lapses were acquired using the optimized experimental protocol as described below. The number along the vertical axis was determined by counting the number of detected particles in each collected time series and by subsequently normalizing this number to the amount of particles per millilitre urine using the focal volume estimated from the point spread function. The amount of detected particles is expressed as a mean with standard deviation

and plotted against the known concentration of added carbon black. The curve was linearly fitted.

Repeatability of urinary carbon load was assessed by calculating the coefficient of variation of urine samples taken at 3 different time points (± one month from each other) (n=19) and analyzed using the optimized experimental protocol.

5.3.4 Study population and sample collection

We conducted this study in the framework of the COGNAC (COGNition and Air pollution in Children) study, which enrolled children (aged 9 – 12 years) from three different primary schools (Tienen, Zonhoven, Hasselt) in Flanders, Belgium [24]. In total, we invited 770 children of which 334 children participated (43%) to the study between January 2012 and February 2014. Parents were asked to fill out a questionnaire in order to get additional lifestyle information of the mother's education (up to high school diploma – college or university degree), exposure to passive tobacco smoke and child's ethnicity, residence, transportation from and to the school, general health, state of mind and physical activity. Written informed consent was obtained from the parents and oral consent from the children. The study protocol was approved by the ethical committees of Hasselt University and East-Limburg Hospital, Belgium. Spot urine samples (available for 289 children) were collected on the first examination day using designated metal and black carbon-free sample jars (Yvsolab, Belgium) and placed at 4°C until chronic storage at -80°C. To avoid external contamination from carbon particles we aliquoted urine samples in a clean room with filtered air (Genano®310, Genano OY, Espoo, Finland). Osmolality of urine was measured by the advanced Cryptomatic Osmometer.

5.3.5 Residential exposure estimates

We constructed estimates of ambient exposure [black carbon, nitrogen dioxide (NO_2) and particulate matter ≤ 2.5 μm ($PM_{2.5}$),], based on their residential address(es), using a spatial temporal interpolation method [290]. The interpolation method uses land cover data obtained from satellite images (CORINE land cover data set) and pollution data of fixed monitoring stations. Coupled with a dispersion model [286] that uses emissions from point sources and line sources, this model chain provides daily exposure values in a high-

resolution receptor grid. Overall model performance was evaluated by leave-one-out cross-validation including 14 monitoring points for black carbon, 44 for NO_2, and 34 for $PM_{2.5}$. Validation statistics of the interpolation tool gave a spatiotemporal explained variance of more than 0.74 for black carbon [291], 0.78 for NO_2 [292], and 0.80 for $PM_{2.5}$ [292]. We calculated different exposure windows by averaging daily concentrations over a period preceding the examination day, *i.e.* recent exposure (one day and one week before urine sampling), medium-term exposure (one month before sampling) and chronic exposure (one year and two years before sampling). When a child had more than one residential address at the moment of the study, we calculated a weighted average using the proportion of time spent at each location as weights. In addition, we also calculated the residential proximity to major roads, defined as highways and other national roads (a road with more than 10,000 motor vehicles/day), using geographic information system functions (ArcGIS 9.3).

5.3.6 Statistical analyses

Statistics were carried out using SAS software (version 9.3, SAS Institute Inc., Cary, NC, USA). Partial Pearson correlation coefficients were calculated to evaluate the correlations between urinary carbon load and recent, medium-term or chronic exposure to black carbon, NO_2 and $PM_{2.5}$ as well as residential proximity to major roads (living twice as close to major roads). To improve normality of the distributions we log-transformed residential proximity to major roads. Multiple linear regressions were performed to assess the independent associations between urinary carbon load and recent, medium-term, chronic exposure, or residential proximity to major roads, while accounting for person-related factors, including age, sex, and body mass index (BMI) of the child, mother's education, and urinary osmolality as well as a time-related factor, including month of examination. Results were presented as a change in urinary carbon load (particles per mL urine) for an interquartile range (IQR) increment in recent, medium-term or chronic exposure, living twice as close to the nearest major road.

In a sensitivity analysis, we evaluated whether osmolality, creatinine, education of father (up to high school diploma – college or university degree), occupation of either parents (unemployed or not qualified worker – qualified worker, white-

collar assistant, or teaching staff – self-employed, specialist, or member of management), exposure to passive smoke (none – ≤ 10 cigarettes/day – > 10 cigarettes/day), physical activity (hours/week), or vegetable/fruit intake from own garden (percentage) affects the association between urinary carbon load and residential black carbon exposure. Additionally, we also checked the independence of recent and chronic residential black carbon exposure on urinary carbon load.

Finally, we calculated the ability to predict child's residential black carbon exposure based on the urinary carbon load. For this purpose, we estimated sensitivity and specificity of the prediction using receiver-operating characteristic (ROC) plots. Children were stratified according to their chronic residential black carbon exposure with the 75^{th} percentile as cutoff point (1.64 $\mu g/m^3$).

5.4 Results

5.4.1 Calibration, optimization and validation of the label-free optical detection of carbon particles in urine

From the calibration and optimization experiments, we arrived at the following conclusions: (i) The employed detection technique is very specific for the detection of carbon particles in urine and does not detect other types of carbonaceous or non-carbonaceous particles by cross-reactivity, as shown by silica nanoparticles and carbon nanotubes (SI, Note 1). Furthermore, no background signal could be observed from the artificial urine solution. (ii) Raman fingerprints of aggregates found in dried urine samples are identical to the fingerprints of carbon-based reference particles (SI, Figure S5-1). (iii) Protocol parameters such as the optimal detection plane and measurement repetition rate were optimized to minimize the intra-sample variation. A flowchart of the optimized protocol is depicted in Figure 5-1.

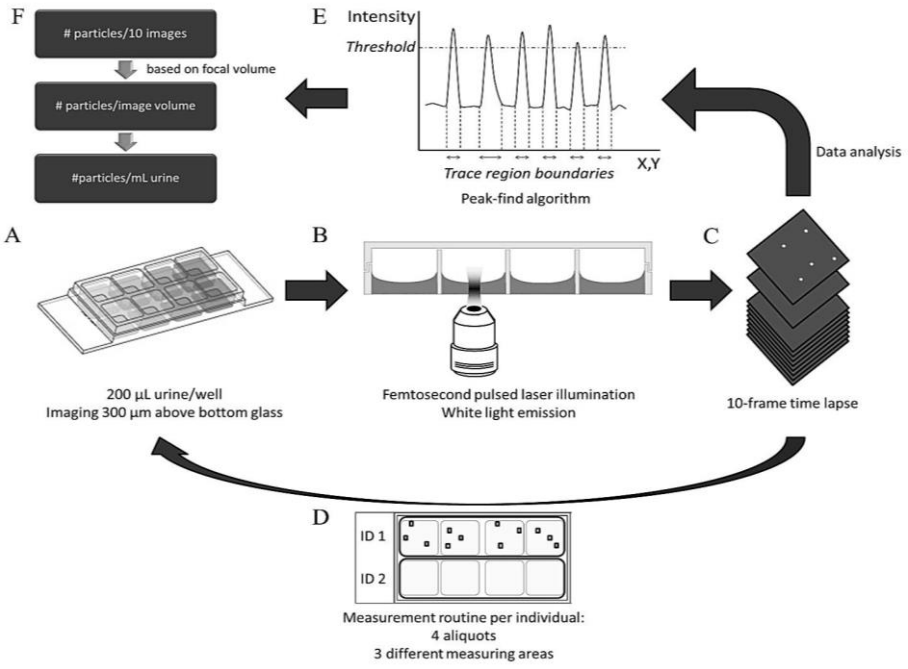

Figure 5–1: Flowchart of the optimized experimental protocol for black carbon detection in urine.

Caption on next page.

(A) Each urine sample is aliquoted at 200 μL/well in an Ibidi μ-slide 8 well and images are taken 300 μm above the bottom glass of the well plate. (B) The samples are illuminated using a two-photon femtosecond pulsed laser tuned to a central wavelength of 810 nm (~ 9.7 mW radiant power at the sample position) and the white light generated by the black carbon particles naturally present in the urine is detected via analogue photomultiplier detection in epi-configuration in non-descanned mode using a 40x/1.1 water immersion objective at room temperature. (C) 10 consecutive images are taken at one identical location in the same well. The resulting images have a field of view of 225 x 225 μm² with a 512x512 pixel resolution (0.44 x 0.44 μm² pixel size) and a pixel dwell time of 3.2 μs. (D) In total, 120 images are obtained by recording 10-frame time lapses at three different locations in four different aliquots of one individual (ID) resulting in highly reproducible results (<5% coefficient of variation). (E) To determine the number of black carbon particles in the images, a peak-find algorithm counting connected pixels above a threshold value (15% lower than the highest intensity value) was used. (F) The average amount of particles detected in the different time lapses is normalized to the image volume using the focal volume estimated from the point spread function of the optical system. Finally, the result is expressed as the total relative number, *i.e.* the number of detected black carbon particles per milliliter urine. All images of each individual are analyzed in this way to retrieve a number of detected black carbon particles per milliliter urine sample.

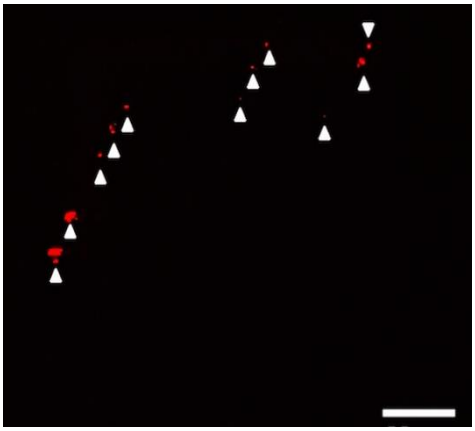

Figure 5–2: Black carbon particles in urine.

Black carbon particles and aggregates (indicated by arrowheads) visualized by femtosecond pulsed laser excitation at 810 nm and observation at 400 – 410 nm. Scale bar: 20 μm.

The optimized experimental protocol was validated by measuring and analyzing artificial urine spiked with increasing concentrations (0 to 120 μg/mL) of carbon black nanopowder. A linear relation was observed (R^2=0.98) between the amount of added and detected carbonaceous particles (SI, Figure S5-2). Black carbon particle detection in urine by femtosecond pulsed laser microscopy is visualized in Figure 5-2. Repeatability of spot urine samples taken at three different time points (± one month from each other) (n=19) showed an average coefficient of variation of 20%.

5.4.2 Urinary carbon load and residential black carbon exposure

Demographic and lifestyle characteristics are presented in Table 5-1. Children (50.5% boys) were on average (SD) 10.3 (1.2) years old. The distribution over mother's low, and high educational class was 116 (40.1%), and 173 (59.9%), respectively. The children's BMI was 17.4 (2.9). Median (interquartile range, IQR) modeled exposures of black carbon, particulate matter with an aerodynamic diameter ≤ 2.5 μm ($PM_{2.5}$) and nitrogen dioxide (NO_2) over various time windows of exposure ranging from recent exposure (one day and one week before urine sampling), medium-term exposure (one month before urine sampling), and chronic exposure (one and two years before urine sampling) as well as median distance (IQR) from residence to major roads are given in Table 5-2 and Table S5-1. The Pearson correlation coefficient between chronic (one year) and recent (one day and one week) residential black carbon exposure was 0.15 (95% CI: 0.04 to 0.26) and 0.09 (95% CI: -0.03 to 0.20), respectively. The corresponding correlation between chronic and medium-term (one month) residential black carbon exposure was 0.36 (95% CI: 0.26 to 0.46).

Urinary black carbon load averaged (IQR) 98.2 x 10^5 (29.8 x 10^5) particles per mL urine (Table 5-1) and did not differ between boys and girls (*P*=0.55). There was no association between urinary carbon load and child's age (*P*=0.74), weight (*P*=0.81), height (*P*=0.99), BMI (*P*=0.90), education of the mother (low versus high: +2.25 x 10^6, 95% confidence intervals (CI): -3.38 x 10^5 to 7.89 x 10^5, *P*=0.14), education of the father (low versus high: +1.61 x 10^5, 95% CI: -3.87 x 10^5 to 7.10 x 10^5, *P*=0.10), highest occupation of either parents (low versus high: +8.83 x 10^5, 95% CI: -1.28 x 10^5 to 1.89 x 10^5, *P*=0.14), physical

activity (P=0.48), exposure to passive smoking (P>0.43), vegetable or fruit from own garden, (P=0.77). Osmolality was significantly associated with urinary carbon load, *i.e.*, +3.1 x 10^5 particles/mL (95% CI: 0.22 x 10^4 to 6.1 x 10^5) for an interquartile range (IQR) increment in osmolality (229 mOsm/kg), while urinary creatinine concentration was not a predictor of the urinary carbon load (P=0.82).

Table 5–1: Characteristics of the participants.

Anthropometric characteristics	
Boys	143 (50.5%)
Age, years	10.3 (1.2)
Body Mass Index	17.4 (2.9)
Weight, kg	37.0 (9.6)
Length, cm	145 (1.0)
Lifestyle characteristics	
Mother's education	
Up to high school diploma	116 (40.1%)
College or university diploma	173 (59.9%)
Father's education[a]	
Up to high school diploma	132 (47.3%)
College or university diploma	147 (52.7%)
Most prestigious category of occupation of either parents	
Unemployed or not qualified worker	23 (7.9%)
Qualified worker, white-collar assistant or teaching staff	118 (40.8%)
Self-employed, specialist or management member	148 (51.2%)
Exposure to passive tobacco smoke	
None	263 (78.3%)
≤ 10 Cigarettes/day	44 (13.1%)
> 10 Cigarettes/day	29 (8.6%)
Physical activity, hours/week	3.3 (2.4)
Urinary characteristics	
Osmolality, mOsm/kg	927.9 (212.3)
Creatinine, mg/dL[b]	127.0 (48.9)
Carbon load, particles/mL	98.2 x 10^5 (29.8 x 10^5)

N=289. Arithmetic mean (SD) is given for the continuous variables. Number (%) is given for the categorical variables. Data available for [a] 279 participants, [b] 276 participants.

Table 5–2: Residential exposure characteristics.

Residential exposure	Median	25th percentile	75th percentile
Recent black carbon, μg/m³			
1-day	1.45	1.19	2.23
1-week	1.68	1.27	2.27
Medium-term black carbon, μg/m³			
1-month	1.63	1.38	1.83
Chronic black carbon, μg/m³			
1-year	1.54	1.43	1.64
2-years	1.53	1.43	1.65
Distance to major roads, m	330.60	126.70	820.40

N=289.

Both before (Figure 5-3A-B) and after adjustment (Figure 5-3B) for *a priori* chosen covariates including sex, age, BMI, mother's education, month of examination, and urinary osmolality, carbonaceous particles in urine were positively correlated to medium-term black carbon exposure (*partial r*=0.12, 95% CI: -0.002 to 0.23), chronic annual residential black carbon (*partial r*=0.17, 95% CI: 0.05 to 0.28) as well as residential proximity to the nearest major road (*partial r*=0.15, 95% CI: 0.03 to 0.26). The corresponding results for an IQR increment of medium-term black carbon and chronic annual residential black carbon exposure were $+5.90 \times 10^5$ particles/mL (95% CI: -0.81×10^4 to 11.9×10^5) and $+5.33 \times 10^5$ particles/mL (95% CI: 1.56×10^5 to 9.10×10^5) more urinary carbonaceous particles, respectively. Furthermore, children living close to a major road (first tertile: ≤160 m or median: ≤330.6 m) had 7.29×10^5 particles/mL (95% CI: 1.12×10^5 to 13.5×10^5; *P*=0.02) or 8.78×10^5 particles/mL (95% CI: 3.14×10^5 to 14.4×10^5, *P*=0.0024) higher urinary carbon load respectively compared with those living further away (> 160 m or >330.6 m). Correspondingly, living twice as close to the nearest major road was associated with $+2.02 \times 10^5$ particles/mL (95% CI: 4.09×10^4 to 3.64×10^5) higher urinary carbon load. In addition, similar patterns were found for medium-term to chronic annual residential NO_2 as well as chronic annual $PM_{2.5}$ exposure (Figure S5-3). All recent exposure time windows (one day and one week) of black carbon, NO_2 and $PM_{2.5}$ were not correlated with the carbonaceous particles in urine.

Sensitivity analysis showed a robust association between urinary carbon load and residential, annual BC exposure with and without adjustment for osmolality, with replacing osmolality by creatinine or by adjusting for both osmolality and creatinine as measures of urine concentration. (Table S5-2). Furthermore, no changes were observed when the main model with *a priori* chosen covariates was additionally adjusted for education of the father, highest occupation of either parents, exposure to passive smoking, physical activity, creatinine, or vegetable/fruit intake from own garden (Table S5-2). Furthermore, we also showed independence of the recent and chronic residential exposure on the internal urinary carbon load (Table S5-2).

Finally, Figure 5-4 shows the ROC curve analysis with sensitivity and 1 minus specificity (false positive ratio) of chronic residential black carbon exposure (75^{th} percentile as cut off point – 1.64 $\mu g/m^3$) in association with children's urinary carbon load. The model adjusted for aforementioned *a priori* chosen covariates had an area under the curve (AUC) value of 0.74 (95% CI: 0.67 to 0.81).

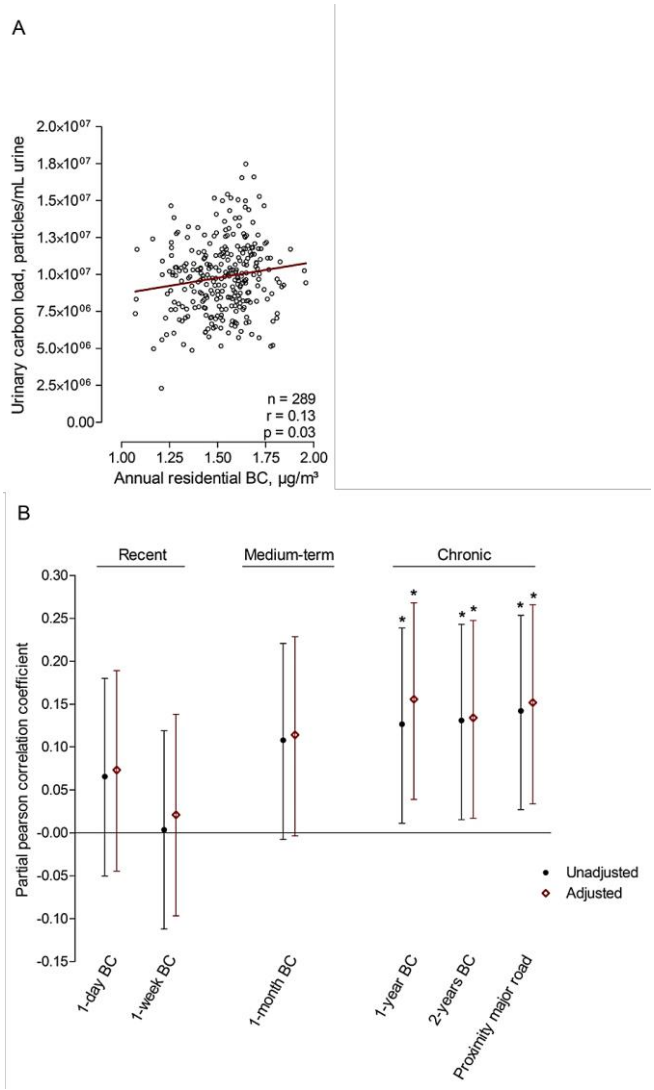

Figure 5–3: Correlation between urinary black carbon load and residential exposure to recent up to chronic black carbon or proximity to major roads.

(A) Dose-response relation between urinary black carbon load and annual residential black carbon exposure, adjusted for urinary osmolality. (B) Unadjusted and partial Pearson correlation coefficient and 95% confidence intervals between urinary black carbon load and residential recent (1-day and 1-week before urine sampling), medium-term (1-month before urine sampling) or chronic black carbon exposure (1-year and 2-years before urine sampling) or residential proximity to major roads (log_{10}). Partial correlation coefficients were adjusted for a priori chosen covariates including gender, age, BMI, mother's education, month of examination, and urinary osmolality. * $P < 0.05$.

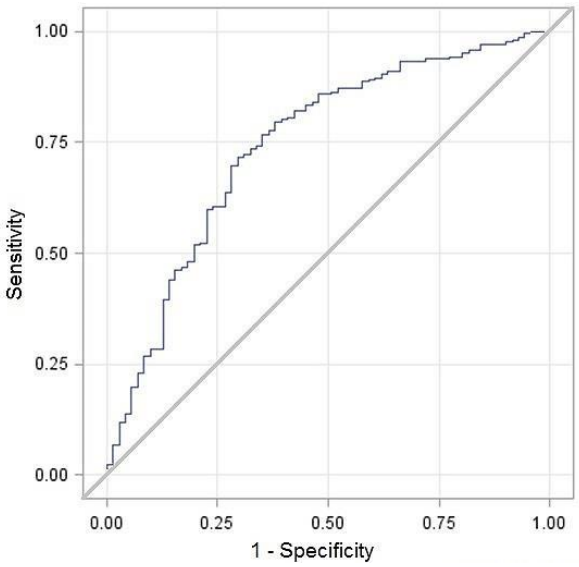

Figure 5–4: Receiver operating characteristics (ROC) curve for urinary carbon load distinguishing between high and low residential black carbon exposure.

Performance of urinary carbon load to differentiate between high (> 75th percentile: 1.64 $\mu g/m^3$) and low (≤ 1.64 $\mu g/m^3$) exposure to chronic residential black carbon exposure. The model was adjusted for gender, age, BMI, mother's education, month of examination, and urinary osmolality.

5.5 Discussion

In the prospect that ultrafine particles may translocate in the circulation and cleared into the urine, we developed a method to measure urinary black carbon load as an exposure matrix of carbonaceous particles in a population at fairly low exposure levels, more specifically in children as a susceptible subgroup for the detrimental effects of air pollution. Overall, our results demonstrate the use of white-light generation of black carbon particles in urine under femtosecond pulsed laser illumination as a measure for exposure to combustion-related black carbon air pollution. The novel information from our work comprises the following: (i) urinary black carbon load mirrors medium-term to chronic ambient exposure, even at low environmental concentrations; (ii) our method requires no additional labeling or preparation procedure and the raw data can be analyzed using a simple peak-find algorithm; (iii) detection of black carbon particles in urine reflects the passage of black carbon particles from the circulation into the urine.

Different experimental rat studies have demonstrated that ultrafine particles can translocate from the lung into the circulation [293, 294]. These particles can accumulate at sites of vascular inflammation [295] and have direct access to intracellular compartments such as proteins, organelles and DNA [294]. Furthermore, Oberdörster *et al.* [123] demonstrated that intranasally instilled solid ultrafine particles translocate along axons of the olfactory nerve into the central nervous system. In this regard, Maher *et al.* [88] recently identified the presence of magnetite nanoparticles, formed by combustion and/or friction derived heating in the human brain. Suggested pathways for particle translocation into the circulation are either across the alveolar epithelium or across the intestinal epithelium from particles that have been cleared *via* mucous ingested into the gastrointestinal tract [123]. Nevertheless, the issue of particle translocation in humans is still controversial. Nemmar *et al.* [10] showed that inhaled technetium-99m labeled ultrafine carbon particles could rapidly pass into the system circulation. Other studies, however, using short-term inhalation (up to two days) of technetium-99m labeled ultrafine carbon particles found that most of the inhaled particles were retained in the lung periphery and in the conducting airways without substantial translocation to the systemic circulation

[100, 102, 296]. Mills *et al*. [102] reported that the radioactive moiety of the label, rather than the particle itself, was detected in the blood. Wiebert and colleagues found no significant translocation of inhaled 35 nm carbon particles to the circulation in humans [100]. Another study [103] on pulmonary deposition and retention of indium-111 labeled ultrafine carbon particles in healthy individuals only found marginal translocation of particles from lungs to blood (0.3%). Moreover, there was no observable elimination of particles from the body via urine one week post-administration. These studies, which are based on labeling techniques and short-term exposure conditions, contrast with our current findings using label-free white light detection of urinary black carbon in children continuously exposed to low levels of air pollution as in real life. Because of the stability of inhaled ultrafine carbon particles, long-term retention in the human lung is expected and may accumulate to a chronic particle load [296]. In this regard, Churg and Brauer [297] and Brauer *et al.* [298] observed that large quantities of fine and ultrafine aggregates retain in the human lung parenchyma whereby ultrafine particles make up only a small fraction of the retained total. Furthermore, a recent study showed that circulation levels of 5 nm gold particles were greater compared to inhaled 30 nm particles [295]. The smallest particles are in steady state as they are retained longer with potential translocation mechanisms from the lungs to the system [123, 296]. This is in line with our observations that residential medium-term to chronic ambient black carbon concentrations are significantly associated with urinary black carbon load. In contrast to our method, labelling studies are not able to detect the background load of particles in urine.

In the past, efforts have been made to identify a reliable and effective biomarker for combustion-related exposure. Oxidative stress is considered as one of the mechanisms through which traffic-related air pollution exerts its effects on human health. The urinary excretion of 8-oxo-7,8-dihydro-2-deoxyguanosine is used as a biomarker of response to evaluate the pro-oxidant effects of vehicle exhaust emissions on DNA [299]. Another example is the metabolite of benzene, urinary trans, trans muconic acid, which has been considered as a proxy-biomarker for traffic [300, 301]. However, the aforementioned biomarkers are not specifically related to combustion-associated air pollution. Furthermore, these biomarkers do not reflect chronic exposure. More recently, carbon load in

alveolar macrophages has been used as a biomarker of exposure to traffic exhaust pollution and biomass smoke exposure [81, 302]. However, this technique requires semi-invasive sampling procedures (sputum induction) with success rates of approximately 60% [302, 303], and identified black carbon particles using light microscopy, thereby underestimating the total amount of carbon load [81]. Our current technique to detect carbon load in urine does not require invasive sampling procedures and uses label-free white-light generation detection to determine the amount of black carbon particles in urine, a technique specifically suited to detect carbonaceous particles. Aside from continuous analysis, we established ROC curves to separate residential chronic low (75^{th} percentile) exposed from higher exposed children for black carbon and showed an area under de curve of 0.74. Therefore, our novel exposure biomarker has the ability to distinguish between true- and false positives.

We acknowledge some limitations of our study. First, ambient black carbon particles in the air could have contaminated the urine samples. By using a clean room with filtered air to handle the urine samples and using sterile metal-free collection tubes, we avoid potential external contamination of carbon particles. Furthermore, no background signals from naturally present carbonaceous particles in the air were observed in the detection chambers or in the sterile metal-free collection tubes. Second, we cannot exclude that black carbon particles detected in urine might mirror particles entered through food or drinks, or even uptake through skin instead of translocation from the lungs to the system. However, in our sensitivity analysis, consuming vegetables or fruit from own garden did not predict the carbon load in urine. Third, urban air consists of particles with a size between 0.02 and 100 μm, with primary particle size ranging from 6 to 100 nm [304]. Diesel particles usually consists of aggregates with a diameter of 10 to 40 nm [43]. Particles with a diameter up to 75 nm may diffuse and accumulate in the mesangium of the glomerulus [305]. The glomerular filtration instigates renal clearance of particles with a size of 10 nm and smaller [305]. While it is possible to detect the smallest particles present in the urine it is not possible to determine their size and distribution due to the diffraction limit in optical microscopy. Fourth, our external exposure estimates of black carbon relates on modelled residential exposure, and not on personal monitoring. Measurement *via* personal exposure samplers is not practical to

assess long-term exposure of large population samples. Validation statistics of the exposure model showed an explained spatiotemporal variance of >0.74 for black carbon. Fifth, the current analysis to determine the particle concentration in urine is based on the focal volume estimated from the system's point spread function. A great solution to this limitation would be the algorithm developed by the research group of Prof. K. Braeckmans (UGhent), which determines the actual apparent image volume from single particle tracking data taking into account image processing settings [306-308]. Unfortunately, the algorithm is not applicable to our data, since carbonaceous particles in aqueous solutions are prone to optical trapping (*vide supra*, chapter 2 and 3).

In conclusion, we showed for the first time that urinary black carbon load in children is associated with medium-term to chronic exposure to ambient combustion related pollution. This specific biomarker reflects internal systemic black carbon particles providing its utility to unravel the complexity of particulate-related health effects, and can be used in different study populations over the entire life course.

5.6 Supplementary information

Note 1: specificity and cross-reactivity of detection technique

It is important to realize that the described signal, namely the white-light generation under femtosecond pulsed laser illumination, is a very distinct and specific signal for carbonaceous particles. A detailed description of the discussed signal can be found in the following paper: Bové *et al.* "Biocompatible Label-Free Detection of Carbon Black Particles by Femtosecond Pulsed Laser Microscopy." *Nano letters* 16.5 (2016): 3173-3178. Summarized, the heterogeneous and absorptive (dark color) nature of carbonaceous particles gives rise to the white-light phenomenon. This means that for the signal to occur, these two conditions should be met. Therefore, (i) excluding the possible contribution of any other non-carbonaceous material (except for noble metals, they are able to generate plasmons); (ii) carbon-containing materials such as endogenous structures with carbon backbones; (iii) the material generating this signal should be in particle form for exhibiting the heterogeneity and absorptive character.
Different experiments were conducted to assess the potential cross-reactivity or general specificity:

1) **Control experiment using artificial urine:** to check for background signals from, for example, salt crystals or urea in the urine, an artificial urine solution was imaged using identical imaging conditions. No background signals were detected.
2) **Cross-reactivity with similar non-carbonaceous particles:** no signals are expected from non-carbonaceous or other types of particles, since they do not comply with the minimal requirements for generating the white-light signal. To further proof the independence from other particles, silica particles – which are the most resembling (structurally and chemically) particles available – were imaged under identical imaging conditions. As expected, no white-light signal can be observed from this type of particles.
3) **Cross-reactivity with other carbonaceous materials:** no other carbonaceous materials are expected to be found in urine, except for possibly carbon nanotubes. Therefore, we performed additional measurements on carbon nanotubes and some signal is generated by this

type of carbonaceous materials. However, the signal was further analyzed and it was found that: (i) this signal is much weaker than the signal from carbon black or black carbon particles, meaning that at the laser powers described in the manuscript the contribution of the carbon nanotubes is essentially zero; (ii) there is a lifetime of the signal observable meaning that mainly fluorescence is probed instead of white-light generation which is instantaneous (autofluorescence was excluded from the signal detection by choosing appropriate optical filters); (iii) the majority of the carbon nanotube signal is present at other wavelengths than probed in this manuscript so that this signal essentially does not contribute to the signal in the white light channel.

4) Additionally, **Raman spectroscopy measurements** on dried urine samples were executed (Figure E1). It is clear from these results that black aggregates found in dried urine generate a fingerprint identical to the fingerprint from carbon particles. This is clear evidence that the white light signal is: (i) generated by carbon in particle form, (ii) the signal is very specific, (iii) the technique also works in extremely challenging conditions, since the autofluorescence from dried urine is extremely bright and omnipresent. We like to emphasize that the large aggregates/agglomerates of carbon are formed by drying the urine, when we inspect the urine in fluid state no such aggregates/agglomerates are detectable. We also have to mention that, as the Raman and white light measurements were performed on different set-ups and even in different institutes, it was not possible to retrieve the exact location of particular carbon aggregates (not all set-ups are equipped with a motorized stage to determine coordinates from samples). As a result, we performed white-light and Raman spectroscopy on two different aggregates/ agglomerates but in the same dried urine samples to provide all necessary convincing evidence.

To conclude, the white-light generation by carbonaceous particles is a very distinct and specific signal. The necessary tests were conducted to prove this statement. We believe that this method is very specific and even more specific than the absorption-based air measurements, which are currently performed.

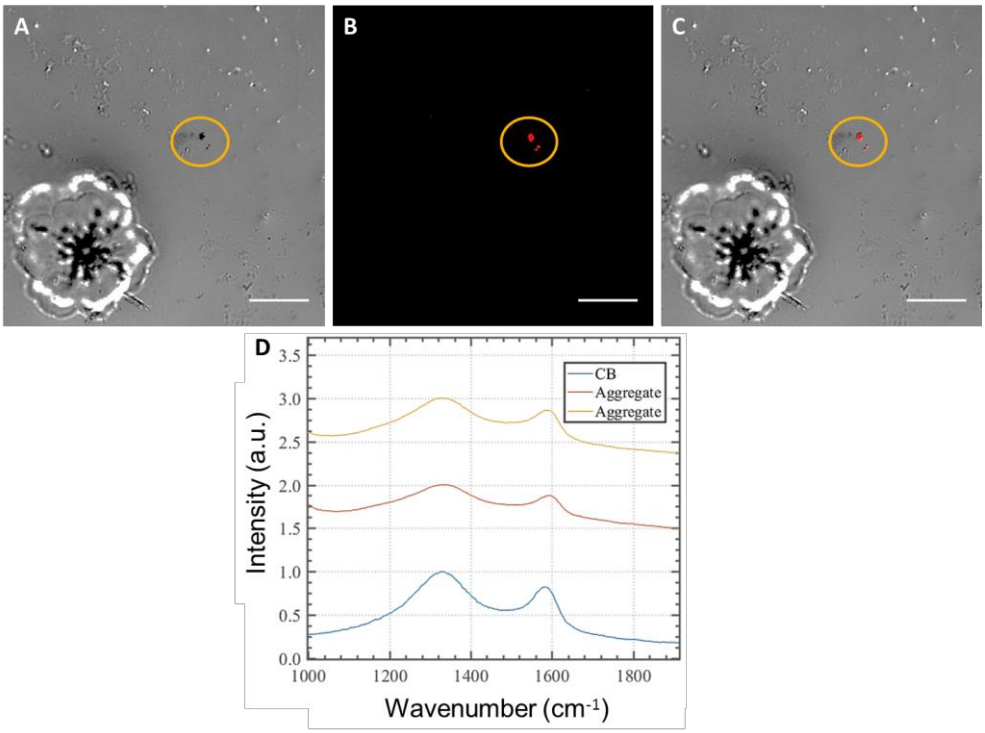

Figure S5–1: Evidence of carbon aggregates in dried urine samples.
(A) Light microscopy image of some carbon aggregates (orange circle) in a dried urine sample. (B) White-light detection of the corresponding aggregates. (C) Overlay image of images A and B. (D) Raman fingerprints of the aggregates compared to the fingerprint of carbon black particles (reference material). Raman spectra of all data collected display very broad D-peaks (left peak) and G-peaks (right peak) typical of amorphous carbon. Scale bars: 15 μm.

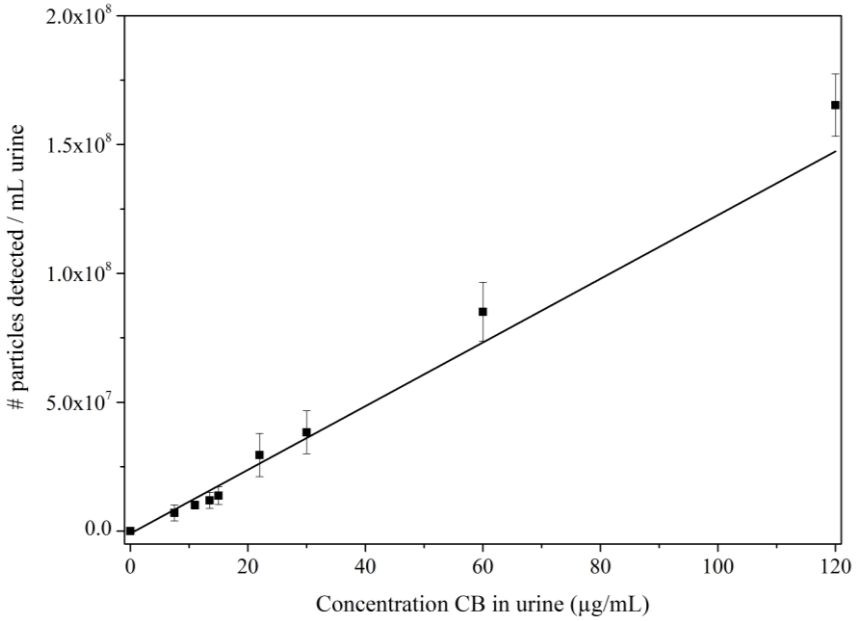

Figure S5–2: Relation between the added concentration CB in artificial urine and the amount of particles detected per mL urine.

The data are average ± standard deviation (n=7) and fitted linearly (R^2=0.98).

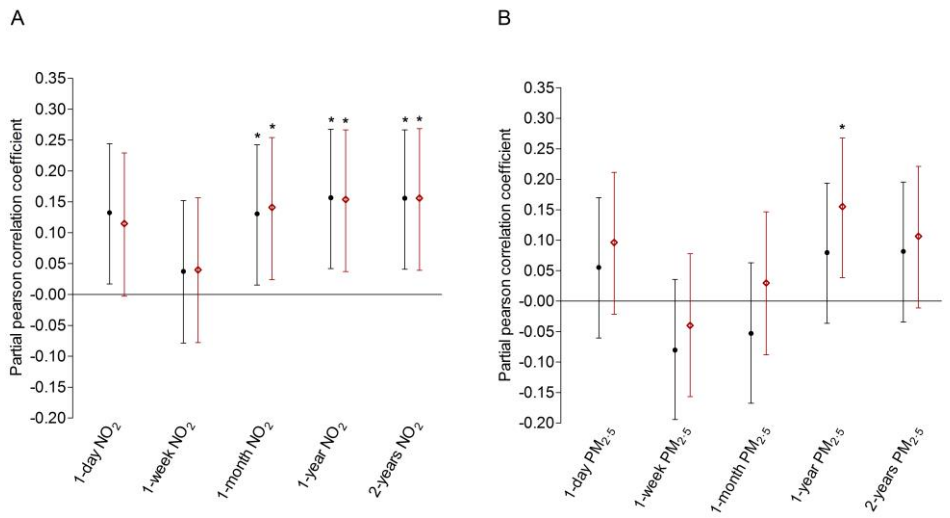

Figure S5–3: Unadjusted and adjusted Pearson correlation coefficient.

Unadjusted and adjusted (partial) Pearson correlation coefficient (95% Confidence Intervals) between urinary black carbon load and residential recent (1-day and 1-week before urine sampling), medium-term (1-month before urine sampling), or chronic (1-year and 2-years before urine sampling) NO_2 (A) and $PM_{2.5}$ (B) exposure (n=289). Partial correlation coefficients were adjusted for *a priori* chosen covariates including sex, age, BMI, mother's education, month of examination, and urinary osmolality. * $P < 0.05$.

Table S5–1: Recent, medium-term and chronic NO_2 and $PM_{2.5}$ exposure characteristics.

	Median	25th percentile	75th percentile
Recent			
NO_2, $\mu g/m^3$			
1-day	26.0	19.5	31.7
1-week	24.2	20.4	28.7
$PM_{2.5}$, $\mu g/m^3$			
1-day	11.4	8.7	21.8
1-week	13.1	9.4	17.3
Medium-term			
NO_2, $\mu g/m^3$			
1-month	22.4	20.2	24.1
$PM_{2.5}$, $\mu g/m^3$			
1-month	11.9	10.7	14.0
Chronic			
NO_2, $\mu g/m^3$			
1-year	21.4	19.9	22.7
2-years	22.2	20.4	23.5
$PM_{2.5}$, $\mu g/m^3$			
1-year	14.3	13.8	15.2
2-years	15.2	14.3	15.5

N=289.

Table S5–2: Sensitivity analysis on the association between urinary carbon load and annual residential black carbon exposure.

	Urinary carbon load, x 10^5 particles/mL	95% CI, x 10^5 particles/mL			*P*-value
Unadjusted model	4.26	0.71	to	7.80	0.019
+ osmolality	3.96	0.41	to	7.50	0.029
+ creatinine	3.63	0.02	to	7.23	0.049
+ osmolality and creatinine	3.58	-0.02	to	7.18	0.051
Main model	5.34	1.56	to	9.11	0.006
+ creatinine	5.03	1.21	to	8.84	0.010
+ physical activity	5.15	1.37	to	8.94	0.008
+ education father	4.87	1.08	to	8.66	0.012
+ highest occupation either parent	4.80	0.93	to	8.66	0.015
+ passive smoking exposure	5.24	1.61	to	9.18	0.005
+ vegetables or fruit from garden	5.44	1.66	to	9.22	0.005
+ recent black carbon exposure	5.49	1.62	to	9.63	0.006

The unadjusted model describes the association between urinary carbon load and 1-year residential black carbon exposure. The main model describes the same association, adjusted for gender, age, BMI, mother's education, month of examination, and urinary osmolality. Sensitivity analysis shows the estimates presented as a change in urinary carbon load (particles/mL) for an IQR increment (0.21 $\mu g/m^3$) in annual residential black carbon exposure, with additional adjustment for osmolality and/or creatinine in the unadjusted model, and creatinine, physical activity, education of the father, passive smoking exposure, vegetable or fruit intake from own garden, or short-term (1-week) residential black carbon exposure in the main model.

Chapter 6
Multiparametric analysis of the detrimental effects of carbon black particles on human lung fibroblasts

---

This chapter is based on:

Polluting combustion-derived particles inhibit human lung fibroblast-mediated matrix remodeling via an oxidant- and size-dependent mechanism at relevant doses.

Bové H., Devoght J., Rasking L., Peters M., Jorge-Peñas A., Van Oosterwyck H., Roeffaers M., Ameloot M.

Manuscript under review.

6.1 Abstract

The continuously growing human exposure to combustion-derived particles (CDPs), a major component of ambient particulates, drive in depth investigation of the involved complex toxicological mechanisms of these particles. The current study evaluated the hypothesis that CDPs could affect cellular remodeling of the extracellular matrix due to their underlying toxicological mechanisms. The effects of CDPs on the human lung fibroblast cell line (MRC-5) were investigated at concentrations comparable to human *in vivo* exposure, both in 2D cell culture and in 3D collagen type I hydrogels to mimic more closely the natural cell environment.

A multi-parametric analysis was employed, including label-free detection of CDPs and three-dimensional (3D) cell-induced displacement microscopy (CDM) to evaluate cell-mediated matrix remodeling. The analysis revealed that carbonaceous particles induce numerous detrimental effects in human lung fibroblasts, including oxidative stress, mitochondrial damage and energy storage depletion. Additionally, 3D CDM showed that matrix displacement fields induced by human lung fibroblasts are disturbed when exposed to carbonaceous particles, resulting in inhibition of matrix remodeling. Moreover, ultrafine particles revealed stronger toxicological and inhibitory effects compared to their larger counterparts.

An oxidant- and size-dependent toxicological mechanism in human lung fibroblasts after CDPs exposure is responsible for impaired cell-mediated collagen matrix remodeling. This unraveled *in vitro* pathway, by which ultrafine particles alter the fibroblasts' vital role of matrix remodeling, extends our knowledge about the attribution of these biologically active particles in impaired lung tissue repair mechanisms, and development and exacerbation of chronic lung diseases. The new insights may even pave the way to precautionary actions.

6.2 Introduction

Human exposure to combustion-derived carbonaceous particles (CDPs) has increased substantially in recent years. Traffic exhaust, for example, constitutes a major environmental contaminant of diesel soot or black carbon (BC) derived from the incomplete combustion of fuels [34]. Additionally, multiple carbon black (CB) particle types are intentionally engineered *via* controlled combustion processes for their use in consumer products like printer toner cartridges, car tires and rubber [38]. Consequently, hazardous exposure to this of type of particles is not limited to occupational settings but also includes daily receptivity of environmental pollutant particulates [27].

The respiratory system is a major route of unintentional exposure to aerosolized carbonaceous particles. Once inhaled, CDPs can reach the deepest regions of the respiratory tract depending on their sizes. Especially, fine (diameter < 2.5 μm) and ultrafine particles (diameter < 0.1 μm) tend to deposit in the deeper bronchial-alveolar regions of the lungs where they are not rapidly degraded but accumulate and eventually translocate to the blood and other target organs [27, 88, 309].

There is increasing evidence that exposure to CDPs can lead to numerous adverse health effects [27, 113]. Moreover, these particles are thought to be more harmful to human health than particulate matter that is not generated by combustion (*e.g.*, friction or evaporation) [27, 29, 31, 32, 310]. Grahame and Schlesinger, for instance, have concluded that BC particles are the dominant environmental cause of cardiovascular morbidity and mortality [33]. Furthermore, epidemiological and experimental studies have shown that CDPs may attribute to the modulation and aggravation of pulmonary disorders such as asthma and lung fibrosis and can even lead to lung cancer [27, 113, 119, 311]. The constant human exposure to CDPs warrant in depth investigation of the involved toxicological mechanisms of these particles behind the observed illnesses. Both *in vitro* and *in vivo* studies have already elucidated that carbonaceous particle exposure can induce cytotoxic injury, impaired redox regulation, inflammation and tissue remodeling [27, 113, 312]. In chronic lung diseases (*e.g.,* asthma or chronic obstructive pulmonary disease), to which inhalation of CDPs appears to contribute, tissue remodeling has shown to

contribute to structural and functional alterations in the lungs. Yet, the exact toxicological mechanisms involved and their interconnections are still not fully unraveled. In a previous study of our research groups, we have shown that the tubulin cytoskeleton of lung fibroblasts is heavily disturbed after an incubation period exceeding four hours with carbonaceous particles and that the overall cellular morphology is changing due to the particulate toxicological effects [206]. Consequently, we hypothesize that CDPs may impair cell-induced remodeling of the extracellular matrix (ECM) due to their underlying toxicological mechanism.

Hence, this study was designed to decipher the distinct toxicological mechanism underlying the detrimental effects of CDPs and to evaluate whether this affects the cell-induced remodeling of the surrounding matrix. The study was performed using lung fibroblasts. Despite the fact that lung epithelial cells and macrophages constitute the first barrier in the lungs, fibroblasts are as critical to evaluate since they are the main connective tissue cell type and maintain the stroma for numerous other cells including alveolar epithelial cells [313]. In damaged lung tissue, fibroblasts are responsible for the main repair mechanisms including building new ECM and contracting the novel matrix to match it with undamaged tissue [314, 315]. Consequently, it is of critical importance to evaluate their remodeling capacity under CDP exposure.

In vitro studies are still the preferred method to study particle toxicology [316, 317]. Yet, a major challenge is the use of relevant particle concentrations, since *in vivo* exposure cannot be converted directly to *in vitro* concentrations [316, 318, 319]. To date, the majority of studies use unrealistically high particle concentrations despite the fact that a few studies have attempted to relate real-life particulate exposure to *in vitro* concentrations [318, 320]. These studies have shown that biologically relevant culture concentrations range between 0.2 – 20 $\mu g/cm^2$. An *in vitro* dose of 20 $\mu g/cm^2$ represents exposure of high-risk individuals (*e.g.,* asthmatic) to ambient levels of atmospheric particles (79 $\mu g/m^3$) over a 24 h period [318, 320]. Additionally, *in vitro* studies generally focus on traditional two-dimensional (2D) assays. These 2D assays have limited complexity and poor physiological relevance as cells naturally reside in a 3D extracellular matrix that is usually softer than cell culture plastics and provides the necessary mechanical cues. Moreover, traditional assays do not study whether normal cell behavior or functioning is preserved upon survival. Hence,

to improve our toxicological understanding, three-dimensional (3D) cell-induced displacement microscopy (CDM) is employed to examine the detrimental effects of biologically relevant CDPs doses on human lung fibroblasts in a 3D collagen type I hydrogel at the microscopic level.

6.3 Materials and methods

6.3.1 Materials and products

All materials were purchased from Sigma-Aldrich (Belgium) unless stated otherwise.

6.3.2 Carbon black particles

Three types of carbon black particles (CBs) were tested: ultrafine carbon black nanopowder (ufPL; PlasmaChem GmbH, Germany), ultrafine Printex 90 (ufP90; Orion Engineered Carbons, Germany) and conductive carbon black nanopowder (CCB; US Research Nanomaterials, USA). Stock suspensions of CBs (2 mg/mL) were prepared in Iscove's Modified Dulbecco's Medium (IMDM; Life Technologies, Belgium) supplemented with 10% fetal bovine serum (FBS; Biochrom AG, Germany) and 1 % penicillin streptomycin by sonicating 30 min using an ultrasonic bath and stored at 4°C in the dark until further use. Prior to utilization, stock suspensions were sonicated in a water bath (Branson 5800, 40 kHz, Emerson, USA) for 20 min. Working suspensions were prepared in complete IMDM immediately before experiments.

6.3.3 Characterization of carbon black particles

Identical particles were used in another study and further details on the physicochemical characterization can be found there [206].

Endotoxin concentrations of CBs as dispersed in complete IMDM were quantified with the Pierce Limulus Amebocyte Lysate (LAL) chromogenic endotoxin quantitation kit (0.1 – 1.0 endotoxin units (EU)/mL; Fisher Scientific, Belgium). The assay was performed according to the manufacturer's instructions. Briefly, particles in IMDM were sonicated as described above. The particle suspensions were centrifuged for 30 min at 22,000 g and the supernatants were collected and centrifuged. This procedure of supernatant centrifugation was repeated three times and the endotoxin levels in the resulting supernatants were determined. Four endotoxin standards (0.1 to 1 EU/mL) were used to generate a standard curve to calculate endotoxin levels. The light absorbance was monitored at 410 nm using the microplate reader Fluostar Optima (BMG Labtech, Belgium).

6.3.4 Cell culture and CB treatment

Human lung fibroblasts (MRC-5 cell line, ATCC CCL-171, LGC Standards, France) were cultured (37 °C, 5 % CO_2) in Minimum Essential Medium (MEM) supplemented with 10 % fetal bovine serum (FBS; Biochrom AG, Germany), 100 U/mL penicillin, and 100 μg/mL streptomycin. At 70-80 % confluency cells were routinely subcultured using trypsin-EDTA to detach cells.
Just before the experiments, CB stock solutions were sonicated and diluted to required concentrations using complete IMDM. Cells were exposed to CB concentrations of 5, 10, 15, 20, and 25 μg/cm² for generally 24 h. To expose cells to identical CB concentration, the doses were adapted considering the corresponding cultured surface and volumes.

6.3.5 Detection of abiotic ROS generation

Intrinsic ability of CB particles to generate reactive oxygen species (ROS) in abiotic conditions was measured by a dithiothreitol assay (DTT; Fisher Scientific) as described by Koike *et al.* [321]. In short, the oxidation of 50 μL of 1 mM DTT in Tris-HCl buffer (1 mM, pH 8.0) by ROS generated by carbon black particles samples (5 – 25 μg/cm², prepared as described in section 6.3.1) was determined by 5-minute incubation with 50 μL of 5'5-dithiobis(2-nitrobenzoic acid) (0.1 mM in 0.1 M Tris-HCl buffer pH 8.0; Fisher Scientific). The formation of 5-mercapto-2-nitrobenzoic acid was measured by a Fluostar Optima spectrophotometer at 412 nm. Blanks and samples were run in triplicate.

6.3.6 Detection of biotic ROS generation

Biotic ROS generation was monitored by employing a 2',7'-dichlorodihydrofluorescein diacetate (DCF-DA, Sigma Aldrich) staining. Dose-dependent measurements were performed by incubating cells with CB particles (5 – 25 μg/cm², 24 h), followed by staining with 20 μM DCF-DA for 15 min at 37 °C. Cells were washed three times with PBS and analyzed using a BD Fortessa flow cytometer (BD Biosciences; Belgium) at excitation and emission wavelengths of 488 and 530 nm, respectively. For each sample, analysis of 10,000 cells was performed.

6.3.7 Mitochondrial morphology imaging

Mitochondrial morphology of control and CB-treated (20 μg/cm² of ufPL, ufP90 and CCB; 24 h) cells was evaluated by staining the mitochondria overnight (16 h) with 2 μL (= 200,000 particles) CellLight® Mitochondria-GFP, BacMam 2.0 in 350 μL culture medium per well.

Images of the stained mitochondria were acquired using a Zeiss LSM510 META NLO scan head mounted on an inverted laser-scanning microscope (Zeiss Axiovert 200M; Zeiss, Germany) and a 40x/1.1 water immersion objective. A 30 mW air-cooled Argon ion laser (LASOS Lasertechnik GmbH, Germany) emitting at 488 nm (~ 3 μW maximum radiant power at the sample) was used as excitation source and a band-pass filter 500 – 530 nm was used for filtering the emission light. Carbon black particles were visualized by femtosecond pulsed laser excitation (~ 4 mW average laser power at the sample, 810 nm, 150 fs, 80 MHz, MaiTai DeepSee, Spectra Physics, USA) and filtering of the emission signal by a 400 – 410 nm band-pass filter in the non-descanned mode. The resulting 1024x1024 images with a pixel size of 0.09 μm were recorded at a pixel dwell time of 12.8 μs. Images were captured using the AIM 4.2 software (Carl Zeiss) and processed with the image-processing program Fiji (ImageJ v1.47, open source software, http://fiji.sc/Fiji).

6.3.8 Mitochondrial function assay

Mitochondrial membrane potential dynamics were studied using the mitochondrial selective probe MitoTracker® Red (CMXROS; Life Technologies) according to manufacturer's recommendations. Cells were prepared as described above and exposed to 20 μg/cm² of CB suspensions for various time periods. Following three washing steps, cells were incubated with 500 nM CMXROS for 15 min. After eliminating debris, analysis of 10,000 cells was performed on a BD Fortessa flow cytometer using 488 nm excitation and 615 nm emission wavelengths.

6.3.9 Metabolic activity assay

Metabolic activity of CB-treated cells was measured using Cell-Titer Glo luminescent cell viability assay (Promega, The Netherlands) according to supplier's instructions. Cells were cultured as described above, but in white

opaque walled 96-well plates (Greiner Bio-One, Belgium). Controls were included to correct for autoluminescence.

6.3.10 Actin cytoskeleton imaging

Cells exposed to vehicle or CB solutions were fixed with 4 % paraformaldehyde containing 4 % sucrose in PBS for 20 min. Permeabilization was performed using 0.3 % Triton X-100 for 30 min followed by a 1 h block with 2 % BSA in PBS. The actin staining solution of phalloidin Alexa Fluor 647 (Life Technologies, Belgium) diluted 1:40 in PBS containing 2 % BSA and 0.1 % Triton X-100 was incubated for 1 h. Between different experimental steps, the cells were washed three times with PBS. Before confocal imaging, all wells were aspired and 200 μL Immu-Mount (Thermo Scientific Shandon^{TM} Immu-Mount^{TM}, Thermo Fisher Scientific) was added.

Images of the stained cells were acquired using the confocal system described above. For imaging the actin cytoskeleton, excitation at 633 nm was performed using a 5 mW Helium Neon laser (LASOS Lasertechnik GmbH, Germany, 3 μW maximum radiant power at the sample). Band-pass filter 650 – 710 nm was used for filtering the emission signal. The resulting 1024x1024 images with a pixel size of 0.17 μm were recorded at a pixel dwell time of 9.6 μs. Images were captured using the AIM 4.2 software and processed with the image-processing program Fiji.

6.3.11 Quantification of cell-induced displacements

The effect of CB particles on the displacements generated by cells was evaluated using cell-induced displacement microscopy according to a method described by us previously [322]. Briefly, cells incubated with vehicle or three different types of CB particles at 20 μg/cm^2 for 24 h were washed three times with PBS and stained for 45 min with 12.5 μM CellTracker^{TM} Green CMFDA (Life Technologies) in serum-free IMDM. The latter to discriminate the vital from the dead cells during the CDM measurements. Next, cells were washed three times with PBS, detached and embedded in a 3D collagen type I hydrogel at a final concentration of 15,000 cells/mL collagen.

Hydrogels were prepared on ice by mixing 8 volumes of collagen consisting of 1:2 ratio of rat tail collagen (collagen type I, 10.31 mg/mL, Corning, The

Netherlands) and bovine skin collagen (collagen type I, 5.9 mg/mL, Nutragen, Advanced Biomatrix, Germany) in complete MEM at a final concentration of 2.4 mg/mL diluted with an appropriate amount of 10x MEM. Next, 10% (vol/vol) sodium bicarbonate (23 mg/mL) containing 1.5 mg/mL fluorescent polystyrene beads (0.2 µm diameter, carboxylated, ex/em 580/605, Invitrogen, Belgium) was added. The pH of the mixture was neutralized using 1 M sodium hydroxide, after which 1 volume of cells were embedded.

The hydrogels including the exposed cells were allowed to set for 18 h before the start of the displacement experiments. An image stack of a collagen volume (173 x 173 x 45 μm^3 on average) around the cell of interest was acquired using an inverted laser-scanning microscope as described above but at 37°C and 5% CO_2 by means of a stage incubator (Tempcontrol 37-2 digital, PeCon, Erbach, Germany). After imaging the hydrogel under cellular tractions, the embedded cells were treated with 25 μM cytochalasin B and re-imaged until a force-free relaxed state of the hydrogel was achieved. Calculation of the displacement fields was performed from both bead- and fibril-based images using non-rigid image registration.

6.3.12 Collagen type I matrix remodeling imaging

Label-free second harmonic imaging of the collagen type I hydrogels was performed using the confocal system described above. A femtosecond pulsed laser (MaiTai DeepSee, Spectra-Physics, USA) at 810 nm was used as excitation source at an average laser power of 5 mW measured on the stage. The second harmonic signal from the collagen fibrils were epi-collected after passing a 442 nm dichroic beam splitter and a 5 nm wide band pass filter with a central wavelength of 405 nm. An analogue photomultiplier tube (Zeiss) was employed for detection.

For imaging the CellTracker™-labeled cells inside the hydrogels, a 30 mW air-cooled Argon ion laser (LASOS Lasertechnik GmbH, Germany) emitting at 488 nm (~ 3 µW maximum radiant power at the sample) was employed. A band-pass filter 500 – 530 nm was used for filtering the emission signal.

Images were captured using the AIM 4.2 software and processed with the image-processing program Fiji.

6.3.13 Statistical analysis

In general, every experiment was repeated three times with triplicates of each condition. Data are represented as means ± standard deviation and were analyzed using the commercially available software GRAPHPAD (Graphpad Prism 6, Graphpad Software Inc., USA) and JMP (JMP Pro 12, SAS Institute Inc., USA). Analysis of variance (ANOVA) or linear mixed model followed by the post-test Dunnett, for multiple comparisons, was performed.

6.4 Results and discussion

6.4.1 Characterization of CBs

The three different CBs under investigation in this study were thoroughly characterized, as described in our previous work (*vide supra,* chapter 2) [206]. One fine (CCB; diameter < 2.5 μm) and two ultrafine (ufPL and ufP90; diameters < 0.1 μm) particle types were tested of which all key physicochemical characteristics are summarized in Table 6-1.

Table 6–1: Physico-chemical characteristics of the three different types of carbon black particles.

N.A.: not applicable. BET: Brunauer, Emmett and Teller; specific surface area of a sample. N.D: not detectable.

	Provider	Provider data				Characterization study				
		Aerodynamic diameter (nm)	Shape	Purity (%)	BET surface area (m^2/g)	Hydrodynamic diameter (nm)		Zeta potential (mV) (mean±SD)		Endotoxin (U/mL)
						Ultrapure water	Complete IMDM	KCl solution	Complete IMDM	
ufPL	PlasmaChem GmbH	13	spherical	> 99	550	112	171	-12 ± 1	-17 ± 2	N.D.
ufP90	Orion Engineered Carbons	14	spherical	100	350	156	218	+29 ± 6	-22.45 ± 0.01	N.D.
CCB	US Research Nanomaterials	150	spherical	> 95	N.A. (95)[1]	165	226	-48 ± 2	-24 ± 3	0.12

[1]The value was estimated according to reference [323].

Before cellular exposure, the aggregation state of the CB particles in aqueous environments was evaluated. All particle types tend to aggregate when suspended in ultrapure water or cell culture medium, which is clear from TEM images [206] and measured hydrodynamic diameters (Table 6-1). This observation is in line with the literature showing similar particle aggregation in cell culture medium [125, 324]. Nevertheless, it has also been reported that aciniform aggregates can maintain the large surface area and other characteristics related to individual (ultra)fine particles [325, 326].

Since carbon-based materials are among the most sorptive materials, CBs have the ability to bind many different proteins to their surface, which constitute the so-called protein corona [327, 328]. As a result, when suspended in complete culture medium, the hydrodynamic diameter of the CB particles/aggregates is

even larger and their zeta potential is approximately -20 mV regardless their native surface potential.

Endotoxins, bacterial contaminants, may have adverse effects that can mask the true biological effects of particles if their presence is overlooked.[329] While carbonaceous particles are naturally present in the atmosphere containing all sorts of contaminants, it is still important to have an idea about the possible contribution of endotoxins to observed toxicological effects. Therefore, a quantitative Limulus Amebocyte Lysate (LAL) assay for the detection of gram-negative bacterial endotoxins was performed. For CCB, a minimal endotoxin level of 0.12 EU/mL was measured, which is at the lower detection limit of the assay. No measurable endotoxin contamination was detected in CB samples ufPL and ufP90. Note that this small quantity is comparable and even lower than generally found in, for example, cell culture media and additives such as fetal bovine serum.[330] Additionally, the endotoxin level is lower than the current US Food and Drug Administration limit (0.5 EU/mL) [331] and will not affect the cell culture studies [330, 332].

6.4.2 Various CBs have similar inherent oxidative capacity

Earlier literature reports have emphasized the pivotal role of oxidative stress in carbon-based particle toxicology [27, 113, 129]. Moreover, it has been postulated that particle surface area and reactivity determine the degree of reactive oxygen species (ROS) production [125, 128]. To check oxidative stress as a decisive toxicological factor, as a first step, the inherent oxidative ability of the different CBs in abiotic (cell-free) conditions was measured using a dithiothreitol (DTT) assay.

All CBs oxidized DTT in a dose-dependent manner (Figure 6-1). Interestingly, all particles have nearly similar oxidative potential. This is in contrast to the literature, where size-dependent – and corresponding surface area-dependent – effects are described [125, 321]. However, it should be noticed that only marginal differences of several nanomols in DTT consumption are reported when comparing different particle sizes and concentrations even at particle concentrations of up to 100 $\mu g/cm^2$, which is 4-fold higher than those employed in this study [321]. Additionally, it is not always clear how long the particles are left to react with DTT. Here, we used the same procedure as for CB suspension

preparation and cell experiments (for experimental details see materials and methods), since this will give the most representative results.

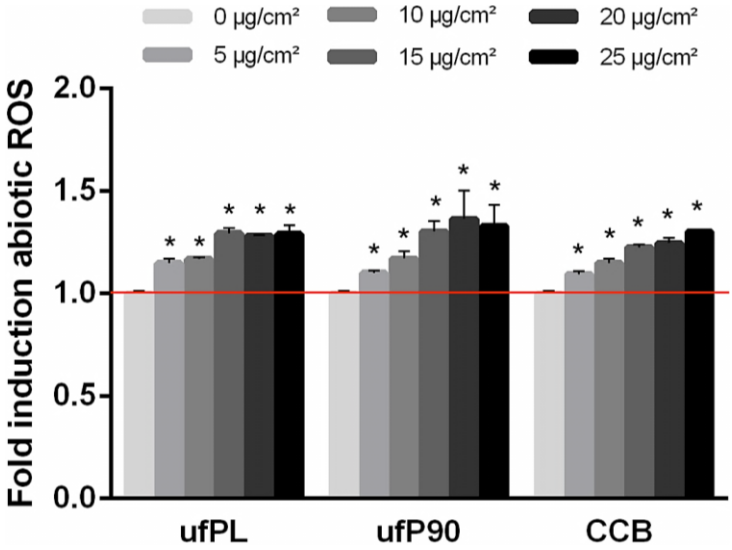

Figure 6–1: ROS production of CBs under abiotic conditions.

Inherent oxidative potential of the three different carbon black particle types at the different concentrations tested in this study. Particle solutions prepared according to procedure for cell experiments (30 min ultrasonication) and left to react with DDT for 5 min. Red line: background oxidation level in blank cell culture solution (IMDM) was set as reference. Data are represented as means ± standard deviation (SD) (n = 3). Statistically different from control marked by * $p < 0.05$.

6.4.3 CBs enhance oxidative stress in human lung fibroblasts

The ability of particles to cause oxidative stress in cells is a key factor in determining their toxicity [333]. To further explore the role of oxidative stress under biotic conditions, a 2',7'-dichlorodihydrofluorescein diacetate (DCF-DA) staining was performed. Even though DCF-DA is often called a 'hydrogen peroxide-detecting probe', the range of ROS detected is much broader including hydroxyl radicals, carbonate radicals and nitrogen dioxides [334]. In the presence of a wide variety of representative ROS, the non-fluorescent cell-permeant dye is converted to highly fluorescent cell-retained species. The percentage of fluorescent-positive cells was used for assessing the extent of ROS production in human lung fibroblasts (MRC-5 cell line).

The analysis showed significant increase in ROS production in cells after 24 h incubation at even the lowest CB concentration (Figure 6-2). The vast majority of ROS is produced under biotic conditions, since at least 8-fold ROS generation compared to the control is detected. In agreement with earlier reports, no clear dose-dependent response curves are observed, in which the ROS production stagnates or even declines [335-337]. We hypothesize that the activation of a cellular antioxidant network, which counterbalances ROS at higher concentrations of CB, is responsible for this observation [338, 339].

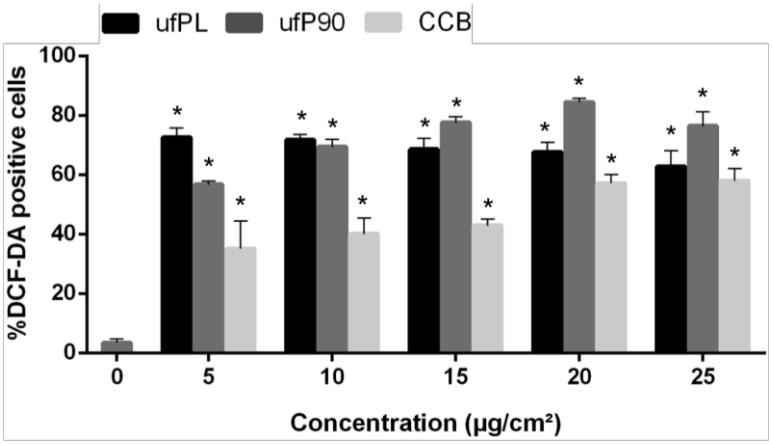

Figure 6–2: ROS production of CBs under biotic conditions.

Human lung fibroblasts (MRC-5 cell line) were exposed to different concentrations (5 – 25 μg/cm²) of three different types of CBs for 24 hours at 37°C. At the end of the exposure a DCF-DA assay was conducted to determine ROS production under biotic conditions. All data are represented as means ± SD (n = 3). * Statistically different from control $p < 0.0001$.

Interestingly, while the particles did not exhibit differential inherent oxidative potential in the absence of cells, their intracellular ROS production significantly varies ($p < 0.05$). This difference in abiotic and biotic ROS production might be explained by the dissimilar amounts of internalized CBs (as observed by optical and confocal microscopy, see Figure 6-3A-D) or diverse interactions of the particulates with their biological target [125], which clearly indicates the need of multi-parametric analysis. Moreover, the ROS analysis elucidated similar results for both types of ultrafine particles (ufPL and ufP90), while the larger, fine

particles (CCB) showed less ROS production. This observed differential results between the smallest and largest particles are in line with the expectations.

6.4.4 Interconnections of ROS production, mitochondrial damage and ATP depletion

Diverse nanoparticles varying in size and chemical composition have shown to induce structural damage and contribute to oxidative stress in mitochondria [324, 338]. Hence, the observed ROS production warrants further investigation of mitochondrial involvement in the toxicological outcome of CB particles.

As a first indication, the location of the produced ROS was determined employing CellROX™ reagents specifically targeting different cellular components. The results (data not shown) showed significant ($p < 0.05$) localization of ROS in the mitochondria and/or nuclei of the cells produced by the smallest particles (ufPL and ufP90). The results for the largest particles (CCB) were not significant. These results point to the mitochondria as sites targeted by adverse particle actions.

Mitochondrial injury may include structural damage and/or dysfunction. The morphology and integrity of the cellular mitochondria was evaluated using CellLight® Mitochondria-GFP expressing fluorescent fusion proteins specifically targeting these organelles. Mitochondria are morphologically dynamic organelles, which continuously undergo fission and fusion processes to form interconnecting tubular networks into small isolated organelles and *vice versa* [340]. This enables the cell to meet its metabolic needs and cope with internal or external stresses [341]. The control cells (Figure 6-3A) depicted this typical tubular-like morphology indicating healthy mitochondria. In contrast, when the human lung fibroblasts were exposed to CBs (Figure 6-3B to 6-3D) a substantial loss of the normal morphology of the mitochondrial organization occurred; they became more intermediate (tubular with swelling regions) and even fragmented (globular fragments) [342]. This loss of the typical tubular morphology and resulting fragmentation is a strong demonstration of compromised mitochondrial dynamics. In fact, defects in the fusion process will result in mitochondria that appear swollen and spherical, instead of tubular-like [343]. Overall, this outcome indicates that exposure to CBs results in interruption of the fusion-fission equilibrium and mitochondrial dynamics.

Deposition of CBs in mitochondria may be the reason for mitochondrial damage. Li *et al.* have already confirmed by employing electron microscopy imaging that ultrafine particulates preferentially localize in mitochondria, induce major structural damage and can contribute to oxidative stress [344]. This is in agreement with our findings. The inset of Figure 3B clearly shows co-localization (indicated by arrowheads and yellow color) of the ultrafine ufPL particles, visualized by probing their white-light generation as published previously [206], with the mitochondria (10.6 % Manders' coefficient). Also, the ufP90 particles show some co-localization with the mitochondrial organization but to a smaller extent (7.5 % Manders' coefficient). In contrast, the larger, fine CCB particles do not show any co-localization with the cellular mitochondria. This also explains the smaller extent of ROS production induced by the latter.

The ROS production and subsequent oxidative stress may result in mitochondrial dysfunction. Mitochondria are the major sites of ROS production in mammalian cells [345]. During oxidative phosphorylation, oxygen is reduced to water through controlled addition of electrons *via* the respiratory chain [345]. However, occasionally some of these electrons escape from the respiratory chain. Electron acceptance by molecular oxygen results in the formation of a range of ROS species such as superoxide anion radicals, hydrogen peroxides and hydroxyl radicals [346]. CBs localized inside the mitochondria can alter their normal functioning and disrupt the electron transport chain due to either blocking electron transport or accepting an electron and transferring it to molecular oxygen [347]. The maintenance of the mitochondrial membrane potential (MMP) in mitochondria is vital for proper oxidative phosphorylation functioning and is considered a critical marker to evaluate mitochondrial perturbation [348, 349].

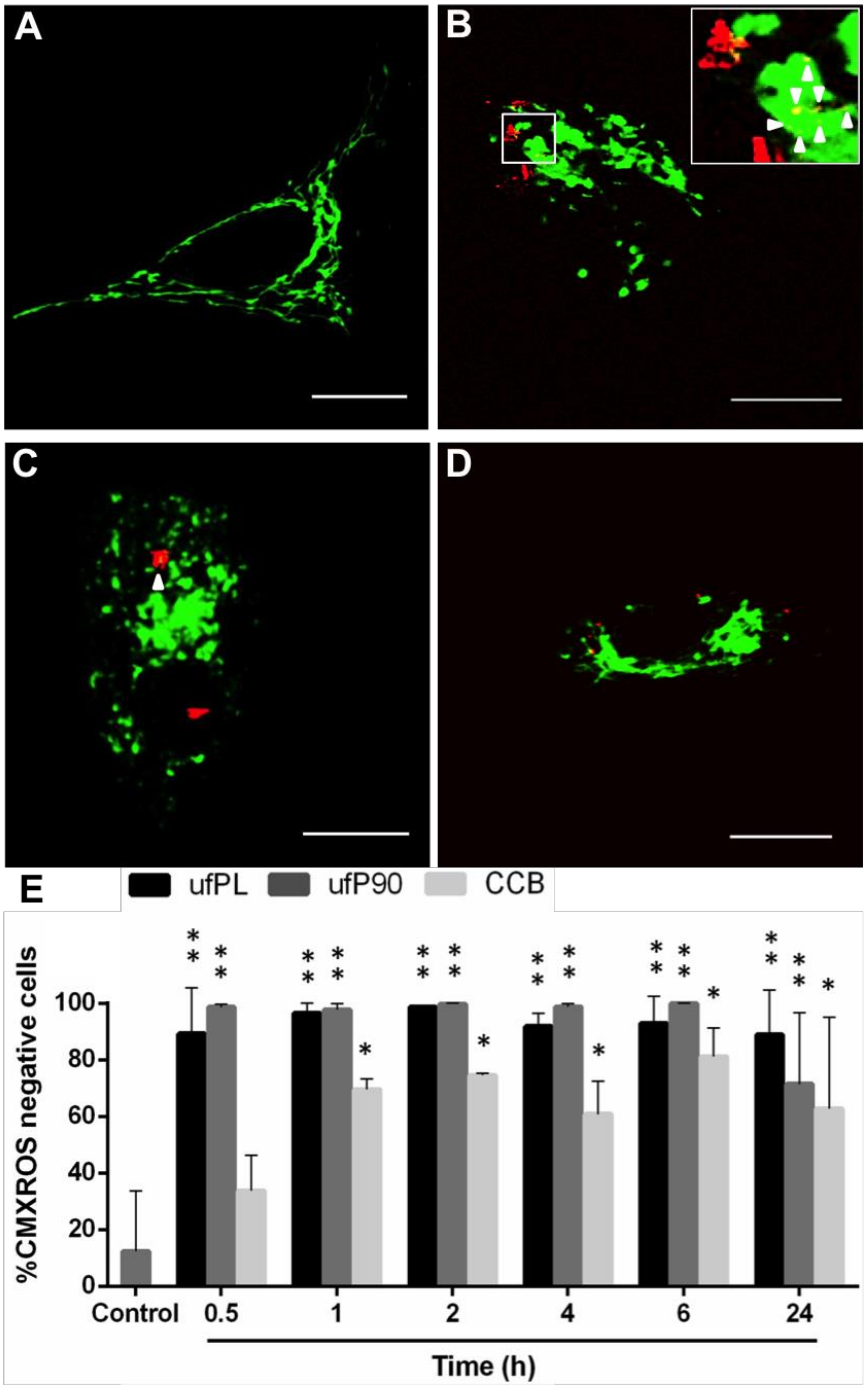

Figure 6–3: Mitochondrial damage by CBs in human lung fibroblasts.

Caption on next page.

Human lung fibroblasts (MRC-5 cell line) were exposed for 24 hours to 20 μg/cm² of three different types of CBs at 37°C. Their mitochondrial organization was examined using CellLight® Mitochondria-GFP (green, Ex/Em 488/510 nm, ~3 μW radiant power at the samples) and CB particles were imaged under femtosecond pulsed illumination (red, 4 mW average laser power at the samples, emission detection: 400 – 410 nm in non-descanned mode). Co-localization between CBs and mitochondria is yellow due to the overlapping colors and additionally indicated by arrowheads. Representative images are shown from: (A) control condition (0 μg/cm²), scale bar: 15 μm; (B) incubation with ufPL particles, scale bar: 5 μm; (C) incubation with ufP90 particles, scale bar: 5 μm; (D) incubation with CCB particles, scale bar: 10 μm. (E) Time course study (0.5 – 24 h) of the loss of mitochondrial membrane potential after exposure to 20 μg/cm² of three different types of CBs at 37°C. After incubation, the cells were labeled with CMXROS fluorochromes and the percentage of CMXROS negative cells was determined. Data are represented as means ± SD (n = 3). Statistically different from control marked by * $p < 0.05$ and ** $p < 0.0005$.

We examined the MMP in lung fibroblasts in a time course study using MitoTracker® Red CMXROS (Figure 6-3E). CMXROS is a fluorochrome that passively diffuses through the membrane of viable cells and is selectively sequestered in mitochondria with an active membrane potential. The study revealed a time-dependent decline of MMP when cells are exposed to CB compared to the control, which is significant within 30 or 60 minutes for the smallest and largest particles, respectively. In general, the maximum loss of MMP was reached after about 2 hours of exposure, which is in agreement with other studies [126]. At this point, almost all cells incubated with ufPL and ufP90 lost their MMP, while 20 % of the cells exposed to CCB remained unaffected. As loss in MMP alters normal functioning of the electron transport chain, this will ultimately result in enhanced ROS production in mitochondria leading to further mitochondrial membrane damage [348].

Adenosine triphosphate (ATP) is generated by oxidative phosphorylation in mitochondria [350]. As shown by the loss of MMP, damage is caused to the mitochondrial respiratory chain. To evaluate the effect of CB particles on the cellular ATP level in fibroblasts, a Cell-Titer glow luminescent cell viability assay was employed. It is clear from the corresponding results (Figure 6-4) that the metabolic activity – expressed by the depletion of ATP content – is affected significantly. Additionally, it is observed that the drop in the ATP level of cells treated with ultrafine ufPL, ufP90 particles is more pronounced than fibroblasts

incubated with the larger, fine CCB particulates. This is in agreement with the abovementioned results of mitochondrial damage.

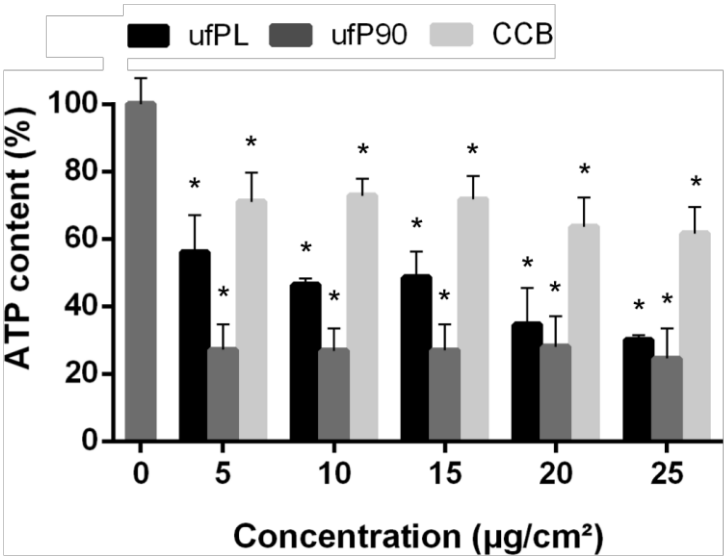

Figure 6–4: Intracellular ATP content depletion by CBs in human lung fibroblasts. Human lung fibroblasts (MRC-5 cell line) were exposed to different concentrations (5 – 25 μg/cm²) of three different types of CBs for 24 hours at 37°C. Intracellular ATP content was determined by Cell-Titer glow luminescent cell viability assay. Data are represented as means ± SD (n = 3). Statistically different from control marked by * $p < 0.0001$.

In summary, ROS production, and structural and functional damage of mitochondria was confirmed by various assays. The mitochondrial damage results in metabolic arrest in the cells by a decrease in ATP yield. Generally, the observed toxicological effects are quite common phenomena upon cellular exposure to most nanoparticle types [344, 351]. However, to get a better idea about the severity of the observed effects in the employed cell type, it would have been interesting to include a reference particle for comparison. In this regard, one can think of polystyrene nanoparticles which are defined as negative control in the FP7 Quality-Nano project (European Union-funded infrastructure for quality in nanomaterials safety testing) or other nanoparticles whose cytotoxicity have been widely studied like gold nanoparticles [352]. However, due to time constrains within the project, we solely focused on the effects of carbonaceous particles.

6.4.5 CBs inhibit cell-mediated matrix remodeling

In a previous study, we have shown that carbon black particles are capable of disturbing the fibrillar tubulin cytoskeletal structure in human lung fibroblasts [206]. This observation warrants further in depth investigation. Hence, we studied the arrangement of the actin cytoskeleton of the cells (Figure S6-1). It can be seen that, similar to the findings on the tubulin cytoskeleton, the actin filaments are disturbed after an incubation period exceeding 4 hours. Moreover, no clear stress fibers are observable compared to the control cell. In agreement with previous experiments the larger, fine CCB particles have a less pronounced cellular effect than the smaller ultrafine ufPL and ufP90 particles (data not shown), disturbing the cytoskeleton to a lesser extent.

Since the cells - in addition to a disrupted cytoskeleton - appear smaller and more irregular shaped, their overall health is questionable. Hence, the extent and mode of cell death was investigated, which showed that ultrafine but not fine carbonaceous particles are able to induce apoptotic cell death in human lung fibroblasts (Figure S6-2). However, the extent of apoptotic cell death (< 50 % at a concentration of 20 μg/cm²) is not in agreement with the degree of observed disturbed processes.

Hence, we hypothesized that the cells, which remain vital after particulate incubation, become mechanically dysfunctional due to the cytoskeletal disturbances. To test this hypothesis in a more physiological relevant environment, human lung fibroblasts were embedded in a 3D collagen type I hydrogel. Under normal conditions, fibroblasts are able to remodel their surrounding matrix by attaching to collagen fibrils and contract them by exerting mechanical tension [353]. In general, collagen contraction assays are performed to evaluate matrix remodeling [354]. However, results from this type of assay lack crucial information such as changes in the interplay at the extracellular matrix – cellular level and, moreover, the general result is biased by the proliferation rate of the embedded cells. Hence, we studied cell-mediated matrix remodeling at the cellular level under normal and exposed conditions using 3D cell-induced displacement microscopy [322]. As far as we know, CDM is employed here to study toxicological effects by particulates for the first time.

Representative 3D collagen matrix displacements induced by fibroblasts exposed to plain culture medium (negative control) or three different CB particle types are shown in Figure 6-5A to D. These images show that the matrix displacements induced by control cells are significantly different from displacements of cells exposed to ultrafine (ufP90 and ufPL) and fine (CCB) particles. This visual observation is confirmed by quantitative analysis of cells under each condition (Figure 6-5E). The median±SD of 3D cell-induced matrix displacements drops from 3.7±1.0 μm (negative control) to 0.4±0.3, 0.9±0.4 and 1.9±0.5 μm for the ultrafine (ufPL, ufP90) and fine (CCB) particles, respectively. Also, it is clear that the ultrafine particles are causing more detrimental effects to the cells ability of restructuring the extracellular matrix than the larger particles. Furthermore, these findings correspond well with the changes observed in the organization of the extracellular matrix after fibroblast remodeling as can be seen from the imaging of the collagen type I matrix using second harmonic generation (Figure 6-6). Whereas the control cells nicely contract and align the collagen fibrils at their force poles, the fibril distribution is more randomly oriented around cells exposed to CBs.

The observed size-dependent effects are of significant relevance since it are especially the ultrafine particles that can penetrate deep into the lung tissue where fibroblasts are residing. Moreover, it is certainly worrying that those smallest particulates have the ability to inhibit fibroblast-mediated matrix remodeling. It is in fact this cell type that has the responsibility to dynamically remodel the extracellular matrix during reparative processes in injured or diseased lungs.

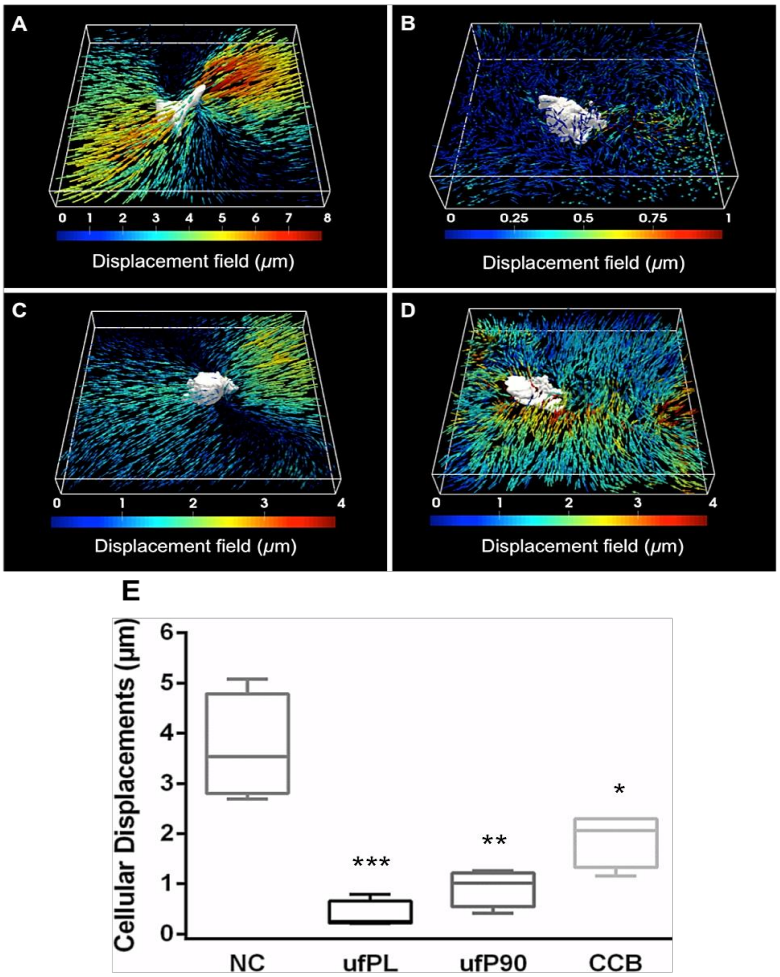

Figure 6–5: Impaired human lung fibroblast displacements in 3D collagen type I hydrogels induced by CBs.

Human lung fibroblasts (MRC-5 cell line) were exposed for 24 hours to 20 μg/cm² of three different types of CBs at 37°C and embedded in 3D collagen type I hydrogels to study their ability to generate matrix displacements. Representative 3D displacements induced by fibroblasts (cell body in white) incubated with (A) culture medium (NC, negative control), bounding box 172x172x21 μm^3; (B) ufPL, bounding box 173x172x46 μm^3; (C) ufP90, bounding box 167x170x11 μm^3; and (D) CCB, bounding box 172x172x26 μm^3; obtained from the registration of fibril-based images. Note, on the right some displacements of a lower localized cell are visible. (E) Data analysis of the 3D distribution of matrix displacements under the different conditions. Data are represented as box-plots (medians and quartiles; n = 4). Statistically different from control *p < 0.005; **p < 0.0005; ***p < 0.0001.

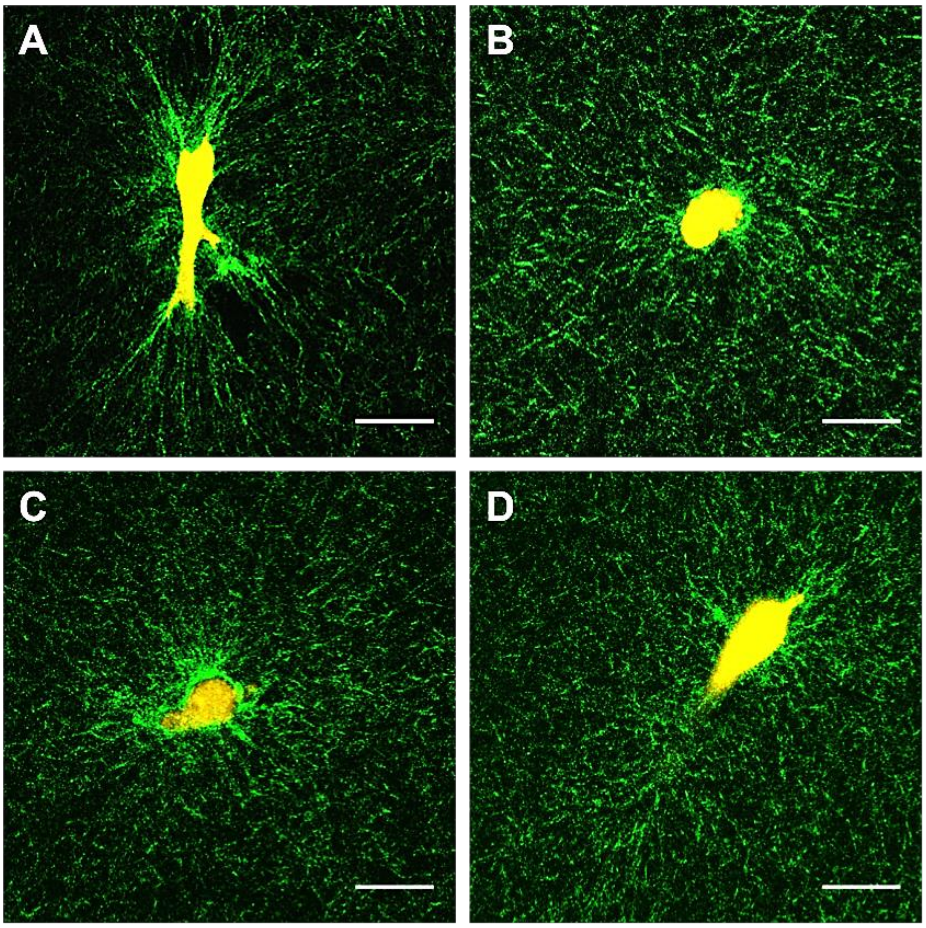

Figure 6–6: Inhibited collagen type I matrix remodeling by human lung fibroblasts exposed to CBs.

Human lung fibroblasts (MRC-5 cell line) were exposed for 24 hours to 20 μg/cm² to three different types of CBs at 37°C and embedded in 3D collagen type I hydrogels to study cell-mediated matrix remodeling. Representative images of collagen type I (second harmonic imaging, green) remodeling induced by fibroblasts (cell body in yellow) are shown incubated with (A) vehicle, (B) ufPL, (C) ufP90, and (D) CCB. Scale bars: 30 μm.

6.4.6 ATP depletion as plausible inhibitory mechanism of cell-mediated matrix remodeling?

Nevertheless, the key question that remains is how all the CB-induced toxicological effects relate to the impaired matrix displacements. We postulate that the carbon-induced metabolic arrest in the cells, expressed by ATP depletion, is a valid explanation for the disturbed cytoskeleton network and consequently the inhibited matrix remodeling. It is already known that cellular ATP depletion in mammalian cells results in dramatic perturbation of the cytoskeleton [355-357]. In 1980, Bershadsky *et al.* already observed that inhibitors of the energy metabolism cause gradual disorganization of actin microfilament bundles in fibroblasts [357]. Additionally, an almost identical mechanism of ATP-dependent cytoskeletal disruption after mitochondrial dysfunction in endothelial cells during simulated ischemia has been described [358]. Summarized, ATP is crucial for the polymerization of the actin component of the cytoskeleton and is therefore warranted to maintain its structural integrity [359]. The actin network regulates cell shape and the distribution of stresses on the substrate, thereby mediating the mechanical interactions of the cell with the ECM [360-362]. Consequently, if the network is disturbed this may lead to impaired force generation. Furthermore, there is a strong correlation (Pearson correlation coefficient = 0.87; Goodness of fit R^2 = 0.76) between the observations made for mitochondrial dysfunction and the impaired matrix displacements strengthening our postulated hypothesis.

Overall, cytoskeletal disruption induced by an oxidant-dependent mechanism is a valid explanation for the observed inhibition of fibroblast-mediated collagen matrix remodeling after carbonaceous particle exposure. In addition, our results show that the toxicological and inhibitory effects are size-dependent; more specifically ultrafine particles are more harmful to human lung fibroblasts than their fine counterparts. These findings provide valuable knowledge about the *in vitro* mechanism by which ultrafine particles alter the normal behavior of human lung fibroblasts. Due to the pivotal role of the latter in the repair of damaged tissues, mechanically dysfunctional fibroblasts may eventually lead to loss of lung tissue structure and functionality. This can explain why exposure to air pollution is found to attribute to the development or exacerbation of chronic lung

diseases such as asthma [311]. To evaluate whether such effects are indeed linked to respiratory diseases further studies are clearly necessary for example using an air-liquid interface cell exposure system as recently reported by Chortarea *et al.* [363].

In conclusion, due to the inevitable exposure of humans to polluting combustion-derived particles it is imperative to investigate their potential detrimental effects on human lung cells at relevant doses. In the present study we have proven that carbonaceous particles induce various deleterious effects *via* an oxidant-dependent mechanism, including: (i) generation of ROS under both abiotic and biotic conditions, (ii) mitochondrial damage and dysfunction, and (iii) ATP depletion. Furthermore, it was shown that matrix displacements were disturbed when human lung fibroblasts were exposed to CB particles, resulting in the inhibition of matrix remodeling by these cells. Since ATP is a key component for cell-induced matrix contraction, the described oxidant-dependent toxicological mechanism can be a valid explanation for the observed impaired cell-induced remodeling. Moreover, it can be concluded that ultrafine particles are generally causing more adverse effects in human lung fibroblasts compared to their larger counterparts. These novel insights are of critical importance, since they show that ultrafine carbonaceous particles have the ability to inhibit the physiological relevant function of fibroblasts, namely mechanical functionality to remodel the extracellular matrix. This provides essential information on those nanoparticles destructively involved in *e.g.* impaired tissue remodeling or repair processes in lung damage and diseases associated to inhalation of particulate matter. It also suggests new potential strategies to attenuate the toxicity induced by carbonaceous particle exposure, like for example ROS scavenging antioxidant treatment.

6.5 Supplementary information

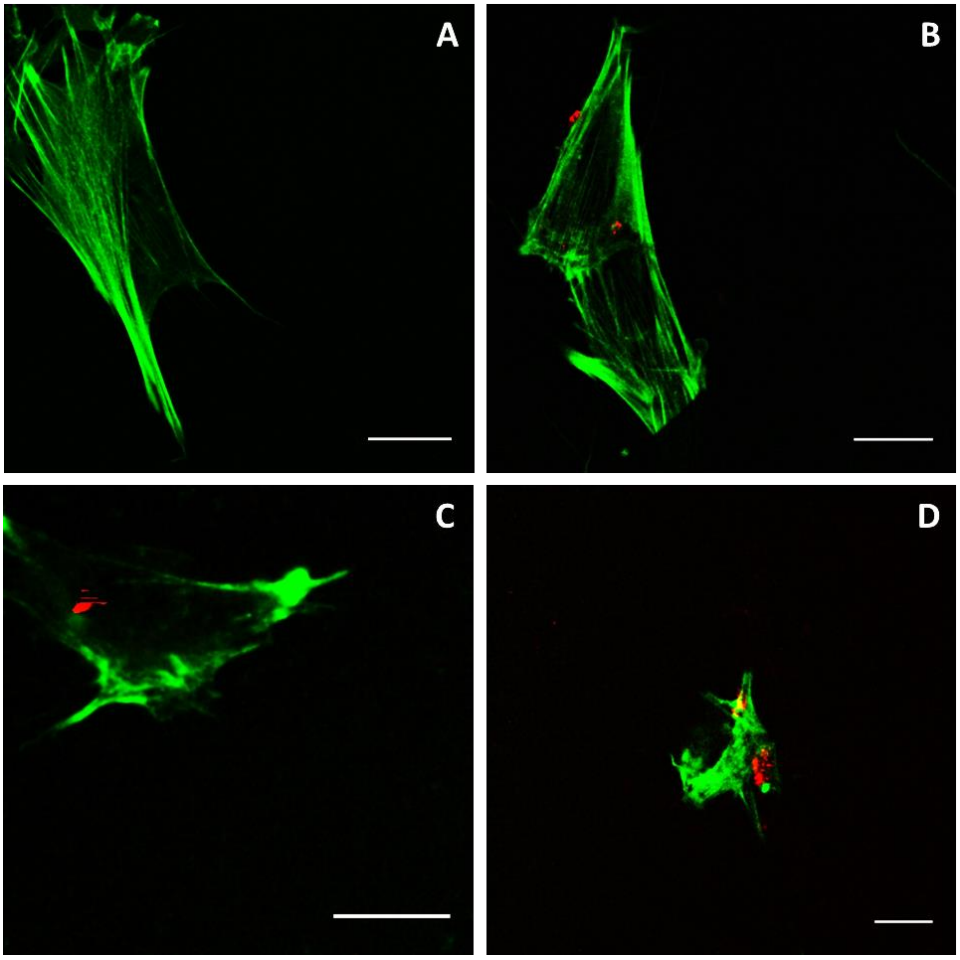

Figure S6–1: Co-localization study of the actin cytoskeleton of MRC-5 lung fibroblasts and engulfed carbon particles.

Actin cytoskeleton (green, Ex/Em 650/668 nm, ~ 3 μW radiant power at the sample) of normal human lung fibroblasts incubated with 5 μg/cm^2 ufPL particles (red, 4 mW average laser power at the sample, emission detection: 400 – 410 nm in non-descanned mode) at 37 °C. (A) Control cells. (B) 4 h incubation. (C) 8 h incubation. (D) 24 h incubation. Scale bars: 20 μm.

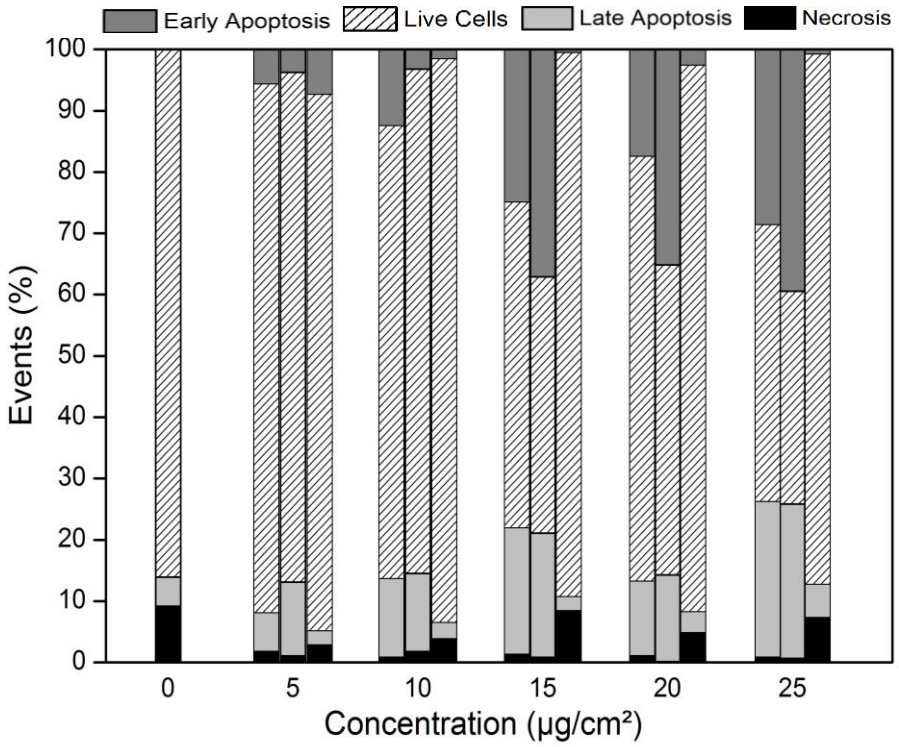

Figure S6–2: Extent and mode of cell death of human lung fibroblasts after CB exposure.

Human lung fibroblasts (MRC-5 cell line) were exposed to different concentrations (5 – 25 μg/cm²) of three different types of CBs for 24 hours at 37°C. At the end of the exposure an Annexin V – propidium iodide assay was conducted to determine the extent and mode (live, early or late apoptosis and necrosis) of cell death. From left to right: ufPL, ufP90 and CCB.

Chapter 7

General discussion and outlook

7.1 Need smoke to be black to constitute an offence?

In order to put the work described in this dissertation into perspective, the ancient research question, raised in *The Lancet* on October 10th 1903, is an excellent starting point [316]:*"Need smoke be "black" to constitute an offence?"*. The authors discuss it being regrettable that the Public Health Act of London specifies offensive smoke to be black, while there is abundance of smoke having less pronounced tints causing intolerable nuisance [316]. This debate clearly illustrates that determining the injurious effects of (black) smoke – referring to particulate air pollution – has been a question for at least a century. In fact, it is a crucial question that remains largely unresolved hitherto.

In 2003, a WHO working group recommended reevaluation of black smoke as part of the reconsideration of the WHO air quality guidelines [364]. Despite the increased evidence provided by expanded research in this field following this recommendation, the WHO concluded in 2012 that there are not yet enough toxicological or clinical studies to (i) evaluate health effect differences between exposure to black carbon and PM, or (ii) identify any distinctive mechanism of black carbon effects [32]. When carefully looking through the literature, it becomes clear that a critical barrier to progress in the field is constituted by the lack of adequate analytical methods to measure black particles and especially those in complex biological samples, since only the latter will allow direct associations of actual levels of exposure to toxicological effects.

Thus, in order to give a conclusive answer to the question *"Need smoke be "black" to constitute an offence?"*, new methods should be developed that allow for quantitative and qualitative determination of CDPs in different systems under various conditions. The first research aim of this dissertation was formulated accordingly.

7.2 Novel optical-based analytical techniques for the detection of CDPs

The formulated research aim is interdisciplinary in nature and does not follow the traditional disciplinary boundaries. It calls for solutions that cut across normal academic divisions, which does not mean it is a matter of breaking down the question into many pieces but reassemble all the pieces from different

perspectives. As described in chapter 2 and 3, we developed two novel optical-based analytical techniques for probing CDPs. The development of both techniques was only possible through the excellent cooperation between the different collaborating research groups and disciplines, namely (bio)physics, engineering and environmental sciences. This is an excellent example showing that interdisciplinary research pays off.

Since the detection of carbonaceous particles holds great promise for future applications (*vide infra*, section 7.3), the intellectual property of the white-light generation by carbon-based materials under femtosecond pulsed illumination was secured in a patent application, which is currently (May 15, 2017) in the PCT phase. This experience of proof-of-concept application adds a whole new dimension to academic research as such. Suddenly, aspects like laser cost, labor intensity of the method and equipment miniaturization become essential. To date, the white-light approach to detect CDPs in biomedical settings requires a high number of personnel-hours and puts a high load on the research equipment. Therefore, in the next phase, a dedicated, stand-alone system will be developed for automatic as well as user-independent determination of CDPs.

7.3 Application of the novel detection techniques in real biological samples

The critical barrier to progress in the field of particulate toxicology and epidemiology was imposed by the limited ability to adequately probe carbonaceous particles in complex biological samples. As shown through the application of both optical-based analytical techniques in various biological matrices, the methods have finally pushed the boundaries of the different research fields to the next level and opened doors to many new opportunities in both fundamental and applied research. First of all, as shown in chapters 2, 3 and 6, the presented methodological approaches can be used in *in vitro* studies to further explore the toxicological events after CDP exposure. Secondly, since the applicability and usefulness of the WL technique is proven in real biological samples (chapter 5), various epidemiological studies can be set up to specifically identify the impact of carbonaceous particle exposure on human health effects.

In the past, *in vitro* toxicology research was restricted to the available techniques, like light and electron microscopy (*vide supra*, chapter 1). As a result of their limitations, crucial and accurate data is missing about carbonaceous particles interacting with cells or tissues. More specifically, essential information on the amount of internalization and related uptake pathways of those particles as well as their co-localization with cellular compartments is lacking. In this regard, the described analytical techniques can contribute significantly and result in new insights, as they allow label-free and biocompatible detection of carbon-based particles in complex biological samples. For example, we showed in chapter 2 that CB particles heavily disturb the fibrillar cytoskeletal structure of lung fibroblasts. This provided novel insights into the toxicological behavior of carbonaceous particles and stimulated us to elucidate the underlying mechanism in chapter 6. Here, it was shown that an oxidant-dependent pathway is underlying the observed toxicological effects and mitochondrial damage plays a major role. In light of their detrimental consequences, the localization of carbonaceous particles inside mitochondria has already been studied repeatedly by electron microscopy (*e.g.,* [84, 324, 344]). However, not all studies report the same internalization and compartment accumulation despite the fact that similar toxicological effects are reported. Moreover, an in contradiction, they often indicate that intracellular particle accumulation is dissociated from the observed cytotoxicity [365]. Since TEM is a cumbersome method with a small field of view, it is arguable whether this method leads to reliable outcomes. We anticipate that our novel analytical methods might finally result in a better substantiated insight into the related research question: whether the particles locate inside the mitochondria and cause therefore damage to these organelles or whether it is due to an indirect effect. Additionally, as our techniques are label-free and biocompatible, they can also be perfectly used to dynamically study the carbonaceous particle uptake and accumulation inside cells and their organelles. In other words, we are convinced that our optical methods will provide valuable information about the bio-kinetics and bioaccumulation as well as toxicological impact of chronic exposure. Moreover, we foresee the applicability of our methods to the detection of other carbon-based materials such as diesel exhaust particles or soot in general, carbon nanotubes and graphene quantum dots.

Previously, two major limitations in environmental exposure assessment were expressed, namely missing and controversial information about particle translocation in humans, and exposure misclassification. Through the developed techniques, the necessary evidence was provided to finally resolve both limitations. Hence, we believe that the development of the new internal exposure marker of carbonaceous particles (chapter 5) will definitely lead to improved epidemiological studies, risk assessment, and estimates of the burden of disease related to ambient air pollution. For example, bio-kinetics and bioaccumulation inside the human body and specific organs can be studied. Subsequently, epidemiological studies can be accompanied by actual and individual exposure levels to more accurately determine the association between exposure and health effects. Moreover, with the described techniques being available, other markers should be re-evaluated to check whether different or more accurate information can be acquired. For instance, to date, carbon loading in macrophages is evaluated by optical transmission microscopy to assess chronic exposure to air pollution. However, several issues are reported with regard to the techniques, like low contrast of the particles compared to the background and exclusion of particles taken up by the nuclei, which might even be the most critical ones [81]. Our techniques, however, provide better contrast images, enable determination of the distribution in three dimensions and even allow for the detection of the smallest particles. Another interesting application would be to quantify carbon-based particles on plant tissue such as ivy leaves, since it has already been proven that plants are excellent environmental probes [9, 366, 367].

7.4 Air quality regulations

Exposure to air pollutants is beyond the control of individuals and requires regulation by public authorities at regional, national and international levels. The most recent EU key directive on ambient air quality (directive 2008/50/EC) recognizes the need for reducing air pollution levels to minimize the harmful effects on human health. However, the limit values adopted for particulate matter are still higher than the WHO recommendations. Moreover, the EU directive recognizes that there is no identifiable threshold for $PM_{2.5}$ below which it would not pose a risk and states that policies should aim at a general

reduction of the exposure levels. Already several studies postulated to add BC to the ambient air quality regulations as a valuable additional indicator [29, 33, 368]. In this dissertation, it has been demonstrated that carbon loading in urine can serve as an individual assessment marker of one of the most toxic components within the $PM_{2.5}$ fraction. This marker will allow detailed risk assessments over an entire life span. Hence, it has the potential to finally provide the right evidence to promulgate a BC $PM_{2.5}$ standard.

To come back to the question "Need smoke to be black to constitute an offence?", the most correct answer would be no. Air pollution consists of many different components, which can cause harmful effects to the human body. Nonetheless, current evidence is pointing into the direction of combustion-related particles and more specifically BC, so a more applicable question to raise here is: "Does black smoke constitute an offence?". Throughout this dissertation, we provide evidence about detrimental effects caused by carbon-based particles (chapter 2 and 6). However, this is just the start of a new era. Having now the new detection techniques as presented here, more focused and comprehensive research can be conducted.

Summary

In 2015, it is estimated that worldwide 4.2 million people died prematurely because of the consequences of air pollution [369]. Moreover, ambient pollution has been identified as the leading cause of the global disease burden. The core of atmospheric pollutant particles is represented by CDPs, such as CB and BC, which are produced during incomplete combustion processes of, for example, diesel fuel. Various studies indisputably demonstrated that exposure to CDPs is associated with a wide range of adverse health effects including, among others, cardiovascular and pulmonary diseases as well as lung cancer. Recent investigations have even promulgated this type of particles to be more harmful to the human health than other subcomponents of particulate air pollution.

Although great progress has been made in comprehending the interactions of CDPs with biological systems, improved methods to probe these particles in complex environments and to gain detailed information about their corresponding adverse impact, are still needed. Hence, this dissertation focused on the persisting demand of analytical techniques for the qualitative and quantitative determination of carbonaceous particles in biologically relevant samples. Consequently, two novel optical-based analytical methods were developed using white-light generation under femtosecond pulsed laser illumination and pump-probe imaging. Both techniques were evaluated in various complex biological environments, such as human lung fibroblasts and urine samples. These results clearly showed that both techniques have numerous advantages over existing technology as these are label-free, biocompatible and straightforward approaches that discriminate background signals from biological components and can be easily combined with various fluorochromes. Furthermore, it was shown that both techniques can be employed to measure black carbon particles in urine and that urinary loading can serve as an exposure matrix to CDP-based air pollution, reflecting the passage of black carbon particles from circulation into urine.

Additionally, advances were made in the field of displacement microscopy by making the quantification of large cell-induced deformations possible and by studying these displacements in a label-free manner using SHG from collagen fibrils instead of the traditionally used fiducial markers. In this dissertation, this advanced method has been employed to elucidate the toxicological effects of

carbonaceous particles, which proved that those particles can inhibit lung fibroblast-mediated matrix remodeling via an oxidant-dependent mechanism.

During the past four years, great advances have been made but we are not there yet. First of all, in light of our patent application, an automatized, prototype set-up needs to be built to make high-throughput screening of biological samples possible. Secondly, additional toxicological studies should be performed to answer crucial questions about particle internalization and co-localization inside cellular organelles and to confirm the proposed oxidant-dependent pathway. Thirdly, epidemiological studies should be set-up to closely study the effect of carbon-based materials on human health and golden standards based on optical microscopy should be re-evaluated.

In summary, the two optical-based analytical techniques and advanced displacement microscopy method described in this dissertation pushed the boundaries of toxicological and epidemiological studies to the next level and opened doors to many new opportunities in both fundamental and applied research. We believe that eventually these contributions will result in an improved understanding of the specific toxicology effects of CDPs and direct associations of those particles with adverse health effects. It might even lead to novel or additional indicators for more precise air quality strategies and regulatory proposals.

Nederlandse samenvatting

In 2015 stierven er naar schatting wereldwijd 4,2 miljoen personen vroegtijdig aan de gevolgen van luchtvervuiling [369]. Bovendien werd luchtverontreiniging geïdentificeerd als de voornaamste oorzaak van ziektes wereldwijd. De meest voorkomende luchtverontreinigende deeltjes zijn gerelateerd aan verbrandingsprocessen, de zogenaamde roetdeeltjes. Deze partikels worden geproduceerd tijdens de onvolledige verbranding van brandstoffen, zoals diesel. Verschillende studies hebben reeds onweerlegbaar aangetoond dat blootstelling aan deze deeltjes gepaard gaat met uiteenlopende ziektebeelden, zoals onder andere hart- en longziekten alsook longkanker. Recente onderzoeken hebben zelfs bewezen dat deeltjes afkomstig van verbrandingsprocessen schadelijker zijn voor de menselijke gezondheid dan andere deelcomponenten van fijn stof.

Ondanks het vele onderzoek naar de interactie van koolstofpartikels met biologische systemen zijn er geen (geavanceerde) methodes beschikbaar voor het accuraat detecteren van deze deeltjes in complexe omgevingen. Dit is echter wel nodig om betere inzichten te bekomen omtrent de oorzaken van de nadelige effecten van roetdeeltjes. Bijgevolg lag de focus van dit doctoraatsproefschrift op de dwingende nood aan analysetechnieken voor het kwalitatief en kwantitatief bepalen van koolstofdeeltjes in biologisch relevante omgevingen. Als resultaat werden er twee nieuwe optisch-gebaseerde analysemethoden ontwikkeld welke gebruik maken van enerzijds wit-licht uitzending na het beschijnen met een femtoseconde gepulste laser en anderzijds *pump-probe* detectie. Beide technieken werden geëvalueerd in verschillende complexe, biologische stalen, zoals humane longfibroblasten en urinestalen. Deze resultaten toonden aan dat beide technieken enorm veel voordelen hebben. Het zijn namelijk labelvrije en biocompatibele benaderingen welke ook toelaten om de achtergrondsignalen van biologische componenten uit te sluiten en welke gecombineerd kunnen worden met verschillende fluorochromen. Daarenboven werd er aangetoond dat beide technieken gebruikt kunnen worden voor het meten van roetdeeltjes in urine. De verkregen informatie over de urinaire roetlading kan gebruikt worden als een blootstellingsmarker aan roetdeeltjes afkomstig van fijn stof, wat de passage van deze deeltjes vanuit het systeem naar de urine reflecteert.

Ook werd er vooruitgang geboekt in het onderzoeksveld van de verplaatsingsmicroscopie. Allereerst door het kwantificeren van grote cel-

geïnduceerde verplaatsingen mogelijk te maken. Ten tweede door de verplaatsingen te bestuderen op een labelvrije manier aan de hand van SHG van de collageenfibrillen in plaats van gebruik te maken van de traditionele referentiepartikels. In dit proefschrift werd deze geavanceerde methode gebruikt om de toxische effecten van koolstofdeeltjes te bestuderen, wat aantoonde dat deze deeltjes de longfibroblast-gemedieerde matrixvervormingen kunnen belemmeren via een oxidant-afhankelijk mechanisme.

Tijdens de laatste vier jaren is er een grote technologische vooruitgang geboekt. De eindmeet is echter nog niet in zicht. In de eerste plaats, gelet op onze octrooiaanvraag, zal er een geautomatiseerd prototype opstelling gebouwd worden om een hoge verwerkingscapaciteit van biologische stalen mogelijk te maken. Ten tweede zullen er extra toxicologische studies uitgevoerd moeten worden om cruciale vragen te kunnen beantwoorden over de opname van de koolstofdeeltjes en hun lokalisatie in cellulaire organellen, en om de voorgestelde oxidant-afhankelijke route te bevestigen. Ten derde, bijkomende epidemiologische studies dienen opgezet te worden om het effect van roetdeeltjes op de menselijke gezondheid nader te bestuderen en om gouden standaarden gebaseerd op optische transmissiemicroscopie opnieuw te evalueren.

Samengevat, de twee optisch-gebaseerde analysetechnieken en geavanceerde verplaatsingsmicroscopie methode beschreven in dit proefschrift verschoven de grenzen van toxicologische en epidemiologische studies naar een hoger niveau en opende deuren naar veel nieuwe mogelijkheden in zowel fundamenteel als toegepast onderzoek. Wij zijn van mening dat uiteindelijke deze bijdragen zullen resulteren in een beter begrip van de specifieke toxicologische effecten van koolstofdeeltjes en het associëren van de deeltjes met alle nadelige gevolgen voor de gezondheid. We zijn er ook van overtuigd dat het zelfs kan leiden tot nieuwe of aanvullende indicatoren voor nauwkeurigere luchtkwaliteitstrategieën en -beheersmaatregelen.

References

1. Guerreiro, C.*, et al.*, Air quality in Europe - 2016 report. In: *European Environment Agency reports*, **2016**. NO 28/2016.
2. Forouzanfar, M.H.*, et al.*, Global, regional, and national comparative risk assessment of 79 behavioural, environmental and occupational, and metabolic risks or clusters of risks, 1990-2015. *Lancet*, **2016**.
3. Brauer, M.*, et al.*, Ambient air pollution exposure estimation for the global burden of disease 2013. *Environ. Sci. Technol.*, **2016**. 50(1): p. 79-88.
4. WHO, World Health Organization. Health Effects of Particulate Matter: policy implications for countries in eastern Europe, Caucasus and central Asia. In: *WHO reports*, **2013**.
5. Srimuruganandam, B. and S.S. Nagendra, Source characterization of PM 10 and PM 2.5 mass using a chemical mass balance model at urban roadside. *Sci. Total Environ.*, **2012**. 433: p. 8-19.
6. Esworthy, R., Air quality: EPA's 2013 changes to the particulate matter standard. *Congressional Research Service*, **2013**: p. 7-5700.
7. Sillanpää, M.*, et al.*, Chemical composition and mass closure of particulate matter at six urban sites in Europe. *Atmos. Environ.*, **2006**. 40: p. 212-223.
8. Masri, S., C.-M. Kang, and P. Koutrakis, Composition and sources of fine and coarse particles collected during 2002–2010 in Boston, MA. *J. Air Waste Manag. Assoc.*, **2015**. 65(3): p. 287-297.
9. Castanheiro, A., R. Samson, and K. De Wael, Magnetic-and particle-based techniques to investigate metal deposition on urban green. *Sci. Total Environ.*, **2016**. 571: p. 594-602.
10. Nemmar, A.*, et al.*, Passage of inhaled particles into the blood circulation in humans. *Circulation*, **2002**. 105(4): p. 411-414.
11. Guarieiro, L.L.N. and A.L.N. Guarieiro, Vehicle Emissions: What Will Change with Use of Biofuel?, in: *Biofuels - Economy, Environment and Sustainability*, Z. Fang, Editor. **2013**, INTECH Open Access Publisher.
12. Kim, K.-H., E. Kabir, and S. Kabir, A review on the human health impact of airborne particulate matter. *Environ. Int.*, **2015**. 74: p. 136-143.
13. WHO. World Health Organization. Ambient (outdoor) air quality and health. Fact sheet **2016**.
14. Ling, S.H. and S.F. van Eeden, Particulate matter air pollution exposure: role in the development and exacerbation of chronic obstructive pulmonary disease. *Int. J. Chron. Obstruct. Pulmon. Dis.*, **2009**. 4(1): p. 233-243.
15. Guarnieri, M. and J.R. Balmes, Outdoor air pollution and asthma. *Lancet*, **2014**. 383(9928): p. 1581-1592.
16. Gauderman, W.J.*, et al.*, The effect of air pollution on lung development from 10 to 18 years of age. *N. Engl. J. Med.*, **2004**. 351(11): p. 1057-1067.

17. Anderson, J.O., J.G. Thundiyil, and A. Stolbach, Clearing the air: a review of the effects of particulate matter air pollution on human health. *J. Med. Toxicol.*, **2012**. 8(2): p. 166-175.
18. Martinelli, N., O. Olivieri, and D. Girelli, Air particulate matter and cardiovascular disease: a narrative review. *Eur. J. Intern. Med.*, **2013**. 24(4): p. 295-302.
19. Brook, R.D*., et al.*, Particulate matter air pollution and cardiovascular disease: An update to the scientific statement from the American Heart Association. *Circulation*, **2010**. 121(21): p. 2331-2378.
20. Loomis, D*., et al.*, The carcinogenicity of outdoor air pollution. *Lancet Oncol.*, **2013**. 14(13): p. 1262.
21. IARC, Working Group on the Evaluation of Carcinogenic Risks to Humans. Outdoor air pollution. In: *IARC monographs on the evaluation of carcinogenic risks to humans*, **2016**. 109.
22. Chen, H*., et al.*, Living near major roads and the incidence of dementia, Parkinson's disease, and multiple sclerosis: a population-based cohort study. *Lancet*, **2017**.
23. Sunyer, J., The neurological effects of air pollution in children. *Eur. Respiratory Soc.*, **2008**. 32(3): p. 535-537.
24. Saenen, N.D*., et al.*, Recent versus chronic exposure to particulate matter air pollution in association with neurobehavioral performance in a panel study of primary schoolchildren. *Environ. Int.*, **2016**. 95: p. 112-119.
25. Colicino, E*., et al.*, Telomere length, long-term black carbon exposure, and cognitive function in a cohort of older men: the VA normative aging study. *Environ. Health Perspect.*, **2017**. 125: p. 76-81.
26. WHO, World Health Organization. Health relevance of particulate matter from various sources. In: *Report on a WHO workshop, Bonn, Germany 26-27 March 2007*, **2007**.
27. Donaldson, K*., et al.*, Combustion-derived nanoparticles: a review of their toxicology following inhalation exposure. *Part. Fibre Toxicol.*, **2005**. 2(1): p. 10.
28. Hester, R. and R. Harrison, *Airborne Particulate Matter: Sources, Atmospheric Processes and Health*. Issues in Environmental Science and Technology. Vol. 42. **2016**: Royal Society of Chemistry.
29. Janssen, N.A*., et al.*, Black Carbon as an Additional Indicator of the Adverse Health Effects of Airborne Particles Compared with PM 10 and PM 2.5. *Environ. Health Perspect.*, **2011**. 119(12): p. 1691.
30. Stanek, L.W*., et al.*, Attributing health effects to apportioned components and sources of particulate matter: an evaluation of collective results. *Atmos. Environ.*, **2011**. 45(32): p. 5655-5663.

31. Krzyzanowski, M., B. Kuna-Dibbert, and J. Schneider, Health effects of transport-related air pollution. In: *WHO reports*, **2005**.
32. Janssen, N.A*., et al.*, Health effects of black carbon. In: *WHO reports*, **2012**.
33. Grahame, T.J. and R.B. Schlesinger, Cardiovascular health and particulate vehicular emissions: a critical evaluation of the evidence. *Air Qual. Atmos. Health*, **2010**. 3(1): p. 3-27.
34. Long, C.M., M.A. Nascarella, and P.A. Valberg, Carbon black vs. black carbon and other airborne materials containing elemental carbon: physical and chemical distinctions. *Environ. Pollut.*, **2013**. 181: p. 271-286.
35. Watson, A.Y. and P.A. Valberg, Carbon black and soot: two different substances. *Am. Ind. Hyg. Assoc.*, **2001**. 62(2): p. 218-228.
36. SCCS, Scientific Committee on Consumer Safety. Opinion on carbon black (nano-form). In: *SCCS report*, **2015**. SCCS/1515/13.
37. Wang, M.J*., et al.*, *Carbon black*. Kirk-Othmer encyclopedia of chemical technology. **2003**.
38. McCunney, R*., et al.*, *Carbon Black*. Patty's Toxicology. **2001**: John Wiley & Sons.
39. IARC, Working Group on the Evaluation of Carcinogenic Risks to Humans. Carbon black, titanium dioxide, and talc. In: *IARC monographs on the evaluation of carcinogenic risks to humans*, **2010**. 93: p. 1.
40. Gray, C.A. and H. Muranko, Studies of robustness of industrial aciniform aggregates and agglomerates—Carbon black and amorphous silicas: A review amplified by new data. *J. Occup. Env. Med.*, **2006**. 48(12): p. 1279-1290.
41. US Environmental Protection Agency. Report to Congress on Black Carbon. In: *US EPA reports*, **2012**. EPA-450/R-12-001.
42. Burtscher, H., Physical characterization of particulate emissions from diesel engines: a review. *J. Aerosol Sci.*, **2005**. 36(7): p. 896-932.
43. Shi, J.P., D. Mark, and R.M. Harrison, Characterization of particles from a current technology heavy-duty diesel engine. *Environ. Sci. Technol.*, **2000**. 34(5): p. 748-755.
44. Levy, L*., et al.*, Does carbon black disaggregate in lung fluid? A critical assessment. *Chem. Res. Toxicol.*, **2012**. 25(10): p. 2001-2006.
45. ICBA, International Carbon Black Association. Carbon black user's guide, safety, health, and environmental information. In: *User's guide*, **2004**.
46. IARC, Working Group on the Evaluation of Carcinogenic Risks to Humans. Printing processes and printing inks, carbon black and some nitro compounds/views and expert opinions of an IARC Working Group on the Evaluation of Carcinogenic Risks to Humans, Lyon, 10-17 October 1995. In:

IARC monographs on the evaluation of carcinogenic risks to humans, **1996**.
47. Kuhlbusch, T.*, et al.*, Measurement of elemental and organic carbon in Europe. *JRC Scientific and Technical Reports*, **2009**.
48. OECD, Organization for Economic Co-operation and Development. SIDS initial assessment report for SIAM 21 on carbon black. In: *Assessment report*, **2005**. CAS No. 1333-86-4.
49. US Environmental Protection Agency. Action Memorandum Re: Inert Reassessment - Carbon Black. In: *US EPA reports*, **2005**. CAS Reg. No. 1333-86-4.
50. Vallette, J., Avoiding contaminants in tire-derived flooring: a healthy building report. In: *Healty Building Network*, **2013**.
51. Gminski, R.*, et al.*, Genotoxic effects of three selected black toner powders and their dimethyl sulfoxide extracts in cultured human epithelial A549 lung cells in vitro. *Environ. Mol. Mutagen.*, **2011**. 52(4): p. 296-309.
52. Grigoratos, T. and G. Martini, Brake wear particle emissions: a review. *Environ. Sci. Pollut. Res.*, **2015**. 22(4): p. 2491-2504.
53. Grigoratos, T. and G. Martini, Non-exhaust traffic related emissions. Brake and tyre wear PM. In: *JRC Scientific and Policy Reports*, **2014**.
54. Shrestha, G., S.J. Traina, and C.W. Swanston, Black carbon's properties and role in the environment: A comprehensive review. *Sustainability*, **2010**. 2(1): p. 294-320.
55. Bond, T.C.*, et al.*, Bounding the role of black carbon in the climate system: A scientific assessment. *J. Geophys. Res.*, **2013**. 118(11): p. 5380-5552.
56. Petzold, A.*, et al.*, Recommendations for reporting" black carbon" measurements. *Atmos. Chem. Phys.*, **2013**. 13(16): p. 8365-8379.
57. Dai, X.*, et al.*, Black carbon in a temperate mixed-grass savanna. *Soil Biol. Biochem.*, **2005**. 37(10): p. 1879-1881.
58. Zhang, R.*, et al.*, Variability in morphology, hygroscopicity, and optical properties of soot aerosols during atmospheric processing. *Proc. Natl. Acad. Sci.*, **2008**. 105(30): p. 10291-10296.
59. Schmidt, M.W.*, et al.*, Comparative analysis of black carbon in soils. *Global Biogeochem. Cycles*, **2001**. 15(1).
60. Golber, E., *Black carbon in the environment: properties and distribution*. Environmental Science and Technology Series. **1985**: New York, John Wiley.
61. Hoet, P.H., I. Brüske-Hohlfeld, and O.V. Salata, Nanoparticles–known and unknown health risks. *J. Nanobiotechnology*, **2004**. 2(1): p. 12.
62. Status of black carbon monitoring in ambient air in Europe. In: *European Environment Agency, Technical report*, **2013**. No 18/2013.

63. *Aardbeien meten fijn stof: buitenlandse interesse voor origineel universiteitsonderzoek AIRbezen*, in *Gazet van Antwerpen*. 2014: Antwerpen.
64. Andreae, M. and A. Gelencsér, Black carbon or brown carbon? The nature of light-absorbing carbonaceous aerosols. *Atmos. Chem. Phys.*, **2006**. 6(10): p. 3131-3148.
65. Chen, C. and H. Wang, *Biomedical applications and toxicology of carbon nanomaterials*. **2016**: John Wiley & Sons.
66. Xing, B., N. Senesi, and C.D. Vecitis, *Engineered Nanoparticles and the Environment: Biophysicochemical Processes and Toxicity*. Vol. 4. **2016**: John Wiley & Sons.
67. Richards-Kortum, R.*, et al.*, Survey of endogenous biological fluorophores. *Handbook of Biomedical Fluorescence*, **2003**: p. 237-264.
68. Masiello, C.A., New directions in black carbon organic geochemistry. *Mar. Chem.*, **2004**. 92(1): p. 201-213.
69. WHO, World Health Organization. Air quality guidelines: global update 2005: particulate matter, ozone, nitrogen dioxide, and sulfur dioxide. In: *WHO reports*, **2006**.
70. Lack, D.A.*, et al.*, Characterizing elemental, equivalent black, and refractory black carbon aerosol particles: a review of techniques, their limitations and uncertainties. *Anal. Bioanal. Chem.*, **2014**. 406(1): p. 99-122.
71. Moosmüller, H., R. Chakrabarty, and W. Arnott, Aerosol light absorption and its measurement: A review. *J. Quant. Spectrosc. Radiat. Transfer*, **2009**. 110(11): p. 844-878.
72. Schulz, C.*, et al.*, Laser-induced incandescence: recent trends and current questions. *Appl. Phys. B*, **2006**. 83(3): p. 333-354.
73. Schwarz, J.*, et al.*, Single-particle measurements of midlatitude black carbon and light-scattering aerosols from the boundary layer to the lower stratosphere. *J. Geophys. Res.*, **2006**. 111(D16).
74. Chan, T.*, et al.*, Time-resolved measurements of black carbon light absorption enhancement in urban and near-urban locations of southern Ontario, Canada. *Atmos. Chem. Phys.*, **2011**. 11(20): p. 10407-10432.
75. Weingartner, E.*, et al.*, Absorption of light by soot particles: determination of the absorption coefficient by means of aethalometers. *J. Aerosol Sci.*, **2003**. 34(10): p. 1445-1463.
76. Baumgardner, D.*, et al.*, Soot reference materials for instrument calibration and intercomparisons: a workshop summary with recommendations. *Atmos. Meas. Tech.*, **2012**. 5: p. 1869-1887.

77. Lefebvre, W*., et al.*, Presentation and evaluation of an integrated model chain to respond to traffic- and health-related policy questions. *Environmental Modelling & Software*, **2013**. 40: p. 160-170.
78. Beelen, R*., et al.*, Effects of long-term exposure to air pollution on natural-cause mortality: an analysis of 22 European cohorts within the multicentre ESCAPE project. *Lancet*, **2014**. 383(9919): p. 785-795.
79. Shafran-Nathan, R., I. Levy, and D.M. Broday, Exposure estimation errors to nitrogen oxides on a population scale due to daytime activity away from home. *Sci. Total Environ.*, **2017**. 580: p. 1401-1409.
80. Sajani, S.Z*., et al.*, Is particulate air pollution at the front door a good proxy of residential exposure? *Environ. Pollut.*, **2016**. 213: p. 347-358.
81. Bai, Y*., et al.*, Carbon loading in airway macrophages as a biomarker for individual exposure to particulate matter air pollution—A critical review. *Environ. Int.*, **2015**. 74: p. 32-41.
82. You, R*., et al.*, Nanoparticulate carbon black in cigarette smoke induces DNA cleavage and Th17-mediated emphysema. *Elife*, **2015**. 4: p. e09623.
83. Somani, P.R. and M. Umeno, *Importance of transmission electron microscopy for carbon nanomaterials research*. In: Modern Research and Educational Topics in Microscopy. Vol. 3. **2007**. 634-642.
84. Belade, E*., et al.*, A comparative transmission electron microscopy study of titanium dioxide and carbon black nanoparticles uptake in human lung epithelial and fibroblast cell lines. *Toxicol. In Vitro*, **2012**. 26(1): p. 57-66.
85. Oberdörster, G*., et al.*, Principles for characterizing the potential human health effects from exposure to nanomaterials: elements of a screening strategy. *Part. Fibre Toxicol.*, **2005**. 2(1): p. 8.
86. Zhang, R*., et al.*, Reduced pulmonary function and increased pro-inflammatory cytokines in nanoscale carbon black-exposed workers. *Part. Fibre Toxicol.*, **2014**. 11(1): p. 73.
87. Parent, P*., et al.*, Nanoscale characterization of aircraft soot: a high-resolution transmission electron microscopy, Raman spectroscopy, X-ray photoelectron and near-edge X-ray absorption spectroscopy study. *Carbon*, **2016**. 101: p. 86-100.
88. Maher, B.A*., et al.*, Magnetite pollution nanoparticles in the human brain. *Proc. Natl. Acad. Sci.*, **2016**. 113(39): p. 10797-10801.
89. La Rocca, A*., et al.*, Characterisation of soot in oil from a gasoline direct injection engine using Transmission Electron Microscopy. *Tribol. Int.*, **2015**. 86: p. 77-84.
90. Patel, M*., et al.*, Morphology, structure and chemistry of extracted diesel soot—Part I: Transmission electron microscopy, Raman spectroscopy, X-ray photoelectron spectroscopy and synchrotron X-ray diffraction study. *Tribol. Int.*, **2012**. 52: p. 29-39.

91. Sadezky, A.*, et al.*, Raman microspectroscopy of soot and related carbonaceous materials: spectral analysis and structural information. *Carbon*, **2005**. 43(8): p. 1731-1742.
92. Potgieter-Vermaak, S.*, et al.*, Degradation potential of airborne particulate matter at the Alhambra monument: a Raman spectroscopic and electron probe X-ray microanalysis study. *J. Raman Spectrosc.*, **2012**. 43(11): p. 1570-1577.
93. Tomašević, M. and M. Aničić, Trace element content in urban tree leaves and SEM-EDAX characterization of deposited particles. *FU Phys. Chem. Tech.*, **2010**. 8(1): p. 1-13.
94. Zhang, C.*, et al.*, Discriminating sources of anthropogenic heavy metals in urban street dusts using magnetic and chemical methods. *J. Geochem. Explor.*, **2012**. 119: p. 60-75.
95. Qian, P.*, et al.*, Magnetic properties of airborne particulate matter in Shanghai during dust storm events and the implications for heavy metal contaminant sources. *Environ. Earth Sci.*, **2014**. 72(10): p. 4167-4178.
96. Vercauteren, J.*, et al.*, Chemkar PM10: An extensive look at the local differences in chemical composition of PM10 in Flanders, Belgium. *Atmos. Environ.*, **2011**. 45(1): p. 108-116.
97. Plascencia-Villa, G.*, et al.*, High-resolution analytical imaging and electron holography of magnetite particles in amyloid cores of Alzheimer's disease. *Sci. Rep.*, **2016**. 6.
98. Kong, H.*, et al.*, Size-dependent cytotoxicity of nanocarbon blacks. *Int. J. Mol. Sci.*, **2013**. 14(11): p. 22529-22543.
99. Oberdörster, G.*, et al.*, Extrapulmonary translocation of ultrafine carbon particles following whole-body inhalation exposure of rats. *J. Toxicol. Environ. Health A*, **2002**. 65(20): p. 1531-1543.
100. Wiebert, P.*, et al.*, No significant translocation of inhaled 35-nm carbon particles to the circulation in humans. *Inhal. Toxicol.*, **2006**. 18(10): p. 741-747.
101. Brown, J.S.*, et al.*, Generation of radiolabeled "soot-like" ultrafine aerosols suitable for use in human inhalation studies. *Aerosol Science & Technology*, **2000**. 32(4): p. 325-337.
102. Mills, N.L.*, et al.*, Do inhaled carbon nanoparticles translocate directly into the circulation in humans? *Am. J. Respir. Crit. Care Med.*, **2006**. 173(4): p. 426-431.
103. Klepczyńska-Nyström, A.*, et al.*, The pulmonary deposition and retention of indium-111 labeled ultrafine carbon particles in healthy individuals. *Inhal. Toxicol.*, **2012**. 24(10): p. 645-651.

104. Sanchez-Crespo, A.*, et al.*, 111Indium-labeled ultrafine carbon particles; a novel aerosol for pulmonary deposition and retention studies. *Inhal. Toxicol.*, **2011**. 23(3): p. 121-128.
105. Rai, P.K., Environmental magnetic studies of particulates with special reference to biomagnetic monitoring using roadside plant leaves. *Atmos. Environ.*, **2013**. 72: p. 113-129.
106. Norouzi, S.*, et al.*, Biomagnetic monitoring of heavy metals contamination in deposited atmospheric dust, a case study from Isfahan, Iran. *J. Environ. Manage.*, **2016**. 173: p. 55-64.
107. Lu, S., S. Bai, and Q. Xue, Magnetic properties as indicators of heavy metals pollution in urban topsoils: a case study from the city of Luoyang, China. *Geophys. J. Int.*, **2007**. 171(2): p. 568-580.
108. Oberdorster, G.*, et al.*, Extrapulmonary translocation of ultrafine carbon particles following whole-body inhalation exposure of rats. *J. Toxicol. Environ. Health A*, **2002**. 65.
109. Schipper, M.L.*, et al.*, A pilot toxicology study of single-walled carbon nanotubes in a small sample of mice. *Nat. Nanotechnol.*, **2008**. 3(4): p. 216-221.
110. Schrand, A.M.*, et al.*, Preparation of cells for assessing ultrastructural localization of nanoparticles with transmission electron microscopy. *Nat. Protoc.*, **2010**. 5(4): p. 744-757.
111. Donnet, J.-B., *Carbon black: science and technology*. Materials Chemistry. **1993**: CRC Press.
112. Bond, T.C. and R.W. Bergstrom, Light absorption by carbonaceous particles: An investigative review. *Aerosol Sci. Technol.*, **2006**. 40(1): p. 27-67.
113. Donaldson, K.*, et al.*, Mechanism of action of combustion-derived nanoparticles, in: *Toxicology, Survival and Health Hazards of Combustion Products*, D. Purser, R. Maynard, and J. Wakefield, Editors. **2015**, Royal Society of Chemistry. p. 361-381.
114. Arnal, C.*, et al.*, Experimental and kinetic study of the interaction of a commercial soot with NO at high temperature. *Combust. Sci. Technol.*, **2012**. 184(7-8): p. 1191-1206.
115. Tankersley, C.G., A. Bierman, and R. Rabold, Variation in heart rate regulation and the effects of particle exposure in inbred mice. *Inhal. Toxicol.*, **2007**. 19(8): p. 621-629.
116. Geiser, M. and W.G. Kreyling, Deposition and biokinetics of inhaled nanoparticles. *Part. Fibre Toxicol.*, **2010**. 7(1): p. 2.
117. Smith, L.E.*, et al.*, Targeting of lung cancer mutational hotspots by polycyclic aromatic hydrocarbons. *J. Natl. Cancer Inst.*, **2000**. 92(10): p. 803-811.

118. Schins, R.P., Mechanisms of genotoxicity of particles and fibers. *Inhal. Toxicol.*, **2002**. 14(1): p. 57-78.
119. van Tongeren, M.*, et al.*, Longitudinal analyses of chest radiographs from the European carbon black respiratory morbidity study. *Eur. Respir. J.*, **2002**. 20(2): p. 417-425.
120. Baan, R.*, et al.*, Carcinogenicity of carbon black, titanium dioxide, and talc. *Lancet Oncol.*, **2006**. 7(4): p. 295.
121. Mills, N.L.*, et al.*, Adverse cardiovascular effects of air pollution. *Nat. Clin. Pract. Cardiovasc. Med.*, **2009**. 6(1): p. 36-44.
122. Brook, R.D.*, et al.*, Insights into the mechanisms and mediators of the effects of air pollution exposure on blood pressure and vascular function in healthy humans. *Hypertension*, **2009**. 54(3): p. 659-667.
123. Oberdorster, G.*, et al.*, Translocation of inhaled ultrafine particles to the brain. *Inhal. Toxicol.*, **2004**. 16.
124. Dick, C.A.*, et al.*, The role of free radicals in the toxic and inflammatory effects of four different ultrafine particle types. *Inhal. Toxicol.*, **2003**. 15(1): p. 39-52.
125. Hussain, S.*, et al.*, Oxidative stress and proinflammatory effects of carbon black and titanium dioxide nanoparticles: role of particle surface area and internalized amount. *Toxicology*, **2009**. 260(1): p. 142-149.
126. Hussain, S.*, et al.*, Carbon black and titanium dioxide nanoparticles elicit distinct apoptotic pathways in bronchial epithelial cells. *Part. Fibre Toxicol.*, **2010**. 7(1): p. 10.
127. Brown, D.M.*, et al.*, Increased inflammation and intracellular calcium caused by ultrafine carbon black is independent of transition metals or other soluble components. *Occup. Environ. Med.*, **2000**. 57.
128. Oberdorster, G., E. Oberdorster, and J. Oberdorster, Nanotoxicology: an emerging discipline evolving from studies of ultrafine particles. *Environ. Health Perspect.*, **2005**. 113.
129. Boland, S., S. Hussain, and A. Baeza-Squiban, Carbon black and titanium dioxide nanoparticles induce distinct molecular mechanisms of toxicity. *Wiley Interdiscip. Rev. Nanomed. Nanobiotechnol.*, **2014**. 6(6): p. 641-652.
130. Driscoll, K.E., Role of inflammation in the development of rat lung tumors in response to chronic particle exposure. *Inhal. Toxicol.*, **1996**. 8: p. 139-153.
131. Dellinger, B.*, et al.*, Role of free radicals in the toxicity of airborne fine particulate matter. *Chem. Res. Toxicol.*, **2001**. 14(10): p. 1371-1377.
132. Rouse, R.L.*, et al.*, Soot nanoparticles promote biotransformation, oxidative stress, and inflammation in murine lungs. *Am. J. Respir. Cell Mol. Biol.*, **2008**. 39(2): p. 198-207.

133. Donaldson, K., P.H. Beswick, and P.S. Gilmour, Free radical activity associated with the surface of particles: a unifying factor in determining biological activity? *Toxicol. Lett.*, **1996**. 88(1-3): p. 293-298.
134. Hirano, S*., et al.*, Oxidative-stress potency of organic extracts of diesel exhaust and urban fine particles in rat heart microvessel endothelial cells. *Toxicology*, **2003**. 187(2): p. 161-170.
135. Bonvallot, V*., et al.*, Organic compounds from diesel exhaust particles elicit a proinflammatory response in human airway epithelial cells and induce cytochrome p450 1A1 expression. *Am. J. Respir. Cell Mol. Biol.*, **2001**. 25(4): p. 515-521.
136. Gurgueira, S.A*., et al.*, Rapid increases in the steady-state concentration of reactive oxygen species in the lungs and heart after particulate air pollution inhalation. *Environ. Health Perspect.*, **2002**. 110(8): p. 749.
137. Donaldson, K*., et al.*, Free radical activity of PM10: iron-mediated generation of hydroxyl radicals. *Environ. Health Perspect.*, **1997**. 105: p. 1285.
138. Squadrito, G.L*., et al.*, Quinoid redox cycling as a mechanism for sustained free radical generation by inhaled airborne particulate matter. *Free Radic. Biol. Med.*, **2001**. 31(9): p. 1132-1138.
139. Dybdahl, M*., et al.*, Inflammatory and genotoxic effects of diesel particles in vitro and in vivo. *Mutat. Res. Genet. Toxicol. Environ. Mutagen.*, **2004**. 562(1): p. 119-131.
140. Li, X*., et al.*, Free radical activity and pro-inflammatory effects of particulate air pollution (PM10) in vivo and in vitro. *Thorax*, **1996**. 51(12): p. 1216-1222.
141. Dasenbrock, C*., et al.*, The carcinogenic potency of carbon particles with and without PAH after repeated intratracheal administration in the rat. *Toxicol. Lett.*, **1996**. 88(1): p. 15-21.
142. Nikula, K*., et al.*, Comparative pulmonary toxicities and carcinogenicities of chronically inhaled diesel exhaust and carban black in F344 rats. *Toxicol. Sci.*, **1995**. 25(1): p. 80-94.
143. Godschalk, R.W*., et al.*, Exposure-route-dependent DNA adduct formation by polycyclic aromatic hydrocarbons. *Carcinogenesis*, **2000**. 21(1): p. 87-92.
144. Deng, X*., et al.*, Airborne fine particulate matter induces multiple cell death pathways in human lung epithelial cells. *Apoptosis*, **2014**. 19(7): p. 1099-1112.
145. Reisetter, A.C*., et al.*, Induction of inflammasome-dependent pyroptosis by carbon black nanoparticles. *J. Biol. Chem.*, **2011**. 286(24): p. 21844-21852.

146. HEI, Health Effects Institute. Diesel exhaust: A critical analysis of emissions, exposure, and health effects. In: *Special Reports*, **1995**.
147. ASTM, *American Society for Testing Materials D3053-13a, Standard on Terminology Relating to Carbon Black*. **2013**, West Conshohocken, PA: ASTM International.
148. Castro, L.*, et al.*, Carbonaceous aerosol in urban and rural European atmospheres: estimation of secondary organic carbon concentrations. *Atmos. Environ.*, **1999**. 33(17): p. 2771-2781.
149. Tankersley, C.G., A. Bierman, and R. Rabold, Variation in heart rate regulation and the effects of particle exposure in inbred mice. *Inhal. Toxicol.*, **2007**. 19(8): p. 621-629.
150. Bond, T.C.*, et al.*, Historical emissions of black and organic carbon aerosol from energy-related combustion, 1850–2000. *Global Biogeochem. Cycles*, **2007**. 21(2).
151. Lamarque, J.-F.*, et al.*, Historical (1850–2000) gridded anthropogenic and biomass burning emissions of reactive gases and aerosols: methodology and application. *Atmos. Chem. Phys.*, **2010**. 10(15): p. 7017-7039.
152. Wang, R., *Global Emission Inventory and Atmospheric Transport of Black Carbon: Evaluation of the Associated Exposure*. **2015**, Beijing, China: Springer Theses.
153. Chow, J.C.*, et al.*, Aerosol light absorption, black carbon, and elemental carbon at the Fresno Supersite, California. *Atmos. Res.*, **2009**. 93(4): p. 874-887.
154. OECD, Organization for Economic Co-operation Development. Methods of measuring air pollution: report of the working party on methods of measuring air pollution and survey techniques. *OECD Reports*, **1964**.
155. Wang, H.-F.*, et al.*, Adsorption at a carbon black microparticle surface in aqueous colloids probed by optical second-harmonic generation. *J. Phys. Chem. C.*, **2007**. 111(25): p. 8708-8715.
156. Ferrari, A.*, et al.*, Raman spectrum of graphene and graphene layers. *Phys. Rev. Lett.*, **2006**. 97(18): p. 187401-187404.
157. Belousova, I.*, et al.*, The investigation of nonlinear optical limiting by aqueous suspensions of carbon nanoparticles. *Opt. Commun.*, **2004**. 235(4): p. 445-452.
158. Zelensky, S., Laser-induced non-linear light scattering in a suspension of black-body particles. *Semicond. Phys. Quantum Electron. Optoelectron.*, **2004**. 7(2): p. 190-194.
159. Rulik, J.J.*, et al.*, Laser-induced incandescence in aqueous carbon black suspensions: the role of particle vaporization. *Semicond. Phys. Quantum Electron. Optoelectron.*, **2007**. 10(2): p. 6-10.

160. Strek, W.*, et al.*, Laser-induced white-light emission from graphene ceramics–opening a band gap in graphene. *Light Sci. Appl.*, **2015**. 4(1): p. e237.
161. Hamilton, B.*, et al.*, White light emission from C60 molecules confined in molecular cage materials. *Adv. Mater.*, **1993**. 5(7-8): p. 583-585.
162. Imholt, T.*, et al.*, Nanotubes in microwave fields: light emission, intense heat, outgassing, and reconstruction. *Chem. Mater.*, **2003**. 15(21): p. 3969-3970.
163. Fougeanet, F. and J.-C. Fabre. Nonlinear mechanisms in carbon-black suspension in a limiting geometry. In: *MRS Proceedings*. **1997**. Cambridge University Press.
164. Li, H.*, et al.*, Carbon nanodots: synthesis, properties and applications. *J. Mater. Chem.*, **2012**. 22(46): p. 24230-24253.
165. Ghosh, S.*, et al.*, Photoluminescence of carbon nanodots: dipole emission centers and electron–phonon coupling. *Nano Lett.*, **2014**. 14(10): p. 5656-5661.
166. Robertson, J., Diamond-like amorphous carbon. *Mater. Sci. Eng. R-Rep.*, **2002**. 37(4): p. 129-281.
167. Ferrari, A. and J. Robertson, Resonant Raman spectroscopy of disordered, amorphous, and diamond-like carbon. *Phys. Rev. B*, **2001**. 64(7): p. 075414.
168. Casiraghi, C., A. Ferrari, and J. Robertson, Raman spectroscopy of hydrogenated amorphous carbons. *Phys. Rev. B*, **2005**. 72(8): p. 085401.
169. Ferrari, A.C. and J. Robertson, Raman spectroscopy of amorphous, nanostructured, diamond–like carbon, and nanodiamond. *Phil. Trans. Roy. Soc. London Series*, **2004**. 362(1824): p. 2477-2512.
170. Ferrari, A.C., Raman spectroscopy of graphene and graphite: disorder, electron–phonon coupling, doping and nonadiabatic effects. *Solid State Commun.*, **2007**. 143(1): p. 47-57.
171. Ferrari, A.C. and D.M. Basko, Raman spectroscopy as a versatile tool for studying the properties of graphene. *Nat. Nanotechnol.*, **2013**. 8(4): p. 235-246.
172. O'Haver, T., *A pragmatic introduction to signal processing with applications in scientific measurement*. **1997**, Maryland: Department of Chemistry and Biochemistry University of Maryland at College Park.
173. Cadusch, P.*, et al.*, Improved methods for fluorescence background subtraction from Raman spectra. *J. Raman Spectrosc.*, **2013**. 44(11): p. 1587-1595.
174. Malola, S., H. Häkkinen, and P. Koskinen, Raman spectra of single-walled carbon nanotubes with vacancies. *Phys. Rev. B*, **2008**. 77(15): p. 155412.

175. Wang, B.*, et al.*, Effect of bending on single-walled carbon nanotubes: A Raman scattering study. *Phys. Rev. B*, **2010**. 81(11): p. 115422.
176. Ferroir, T.*, et al.*, Carbon polymorphism in shocked meteorites: Evidence for new natural ultrahard phases. *Earth Planet. Sci. Lett.*, **2010**. 290(1): p. 150-154.
177. Yoo, C. and W. Nellis, Phase transformations in carbon fullerenes at high shock pressures. *Science*, **1991**. 254(5037): p. 1489-1491.
178. Usman, A., W.-Y. Chiang, and H. Masuhara, Optical trapping of nanoparticles by ultrashort laser pulses. *Sci. Prog.*, **2013**. 96(1): p. 1-18.
179. Usman, A., W.-Y. Chiang, and H. Masuhara. Femtosecond trapping efficiency enhanced for nano-sized silica spheres. In: *SPIE NanoScience + Engineering*. **2012**. International Society for Optics and Photonics.
180. Li, Q.*, et al.*, Photoluminescent carbon dots as biocompatible nanoprobes for targeting cancer cells in vitro. *J. Phys. Chem. C*, **2010**. 114(28): p. 12062-12068.
181. Kwon, W.*, et al.*, Control of photoluminescence of carbon nanodots via surface functionalization using para-substituted anilines. *Sci. Rep.*, **2015**. 5.
182. Carpene, E.*, et al.*, Ultrafast carrier dynamics in tetrahedral amorphous carbon: carrier trapping versus electron–hole recombination. *New J. Phys.*, **2007**. 9(11): p. 404.
183. Michelsen, H.A., Understanding and predicting the temporal response of laser-induced incandescence from carbonaceous particles. *J. Chem. Phys.*, **2003**. 118(15): p. 7012-7045.
184. Link, S. and M.A. El-Sayed, Spectral properties and relaxation dynamics of surface plasmon electronic oscillations in gold and silver nanodots and nanorods. *J. Phys. Chem. B*, **1999**. 103: p. 8410-8426.
185. Ahmadi, T.S., S.L. Logunov, and M.A. El-Sayed, Picosecond dynamics of colloidal gold nanoparticles. *J. Phys. Chem.*, **1996**. 100(20): p. 8053-8056.
186. Hodak, J., I. Martini, and G.V. Hartland, Ultrafast study of electron–phonon coupling in colloidal gold particles. *Chem. Phys. Lett.*, **1998**. 284(1): p. 135-141.
187. Kotaidis, V.*, et al.*, Excitation of nanoscale vapor bubbles at the surface of gold nanoparticles in water. *J. Chem. Phys.*, **2006**. 124(18): p. 184702.
188. Lapotko, D., Optical excitation and detection of vapor bubbles around plasmonic nanoparticles. *Opt. Express*, **2009**. 17(4): p. 2538-2556.
189. Lapotko, D., Pulsed photothermal heating of the media during bubble generation around gold nanoparticles. *Int. J. Heat Mass Transfer*, **2009**. 52(5): p. 1540-1543.

190. Kim, H.*, et al.* Coherent anti-Stokes generation from single nanostructures. In: *SPIE BiOS: Biomedical Optics*. **2009**. International Society for Optics and Photonics.
191. Beversluis, M.R., A. Bouhelier, and L. Novotny, Continuum generation from single gold nanostructures through near-field mediated intraband transitions. *Phys. Rev. B*, **2003**. 68(11): p. 115433.
192. Danckwerts, M. and L. Novotny, Optical frequency mixing at coupled gold nanoparticles. *Phys. Rev. Lett.*, **2007**. 98(2): p. 026104.
193. Palomba, S., M. Danckwerts, and L. Novotny, Nonlinear plasmonics with gold nanoparticle antennas. *J. Opt. A-Pure Appl. Op.*, **2009**. 11(11): p. 114030.
194. Haug, T.*, et al.*, Hot-electron intraband luminescence from single hot spots in noble-metal nanoparticle films. *Phys. Rev. Lett.*, **2015**. 115(6): p. 067403.
195. Kramberger, C.*, et al.*, Linear plasmon dispersion in single-wall carbon nanotubes and the collective excitation spectrum of graphene. *Phys. Rev. Lett.*, **2008**. 100(19): p. 196803.
196. Ajayan, P., S. Iijima, and T. Ichihashi, Electron-energy-loss spectroscopy of carbon nanometer-size tubes. *Phys. Rev. B*, **1993**. 47(11): p. 6859.
197. Pichler, T.*, et al.*, Localized and delocalized electronic states in single-wall carbon nanotubes. *Phys. Rev. Lett.*, **1998**. 80(21): p. 4729.
198. Stöckli, T.*, et al.*, Plasmon excitations in graphitic carbon spheres. *Phys. Rev. B*, **1998**. 57(24): p. 15599.
199. Ding, D.*, et al.*, Multiphoton ionization of fullerene (C60). *J. Phys. Chem.*, **1993**. 97(11): p. 2500-2504.
200. Pratt, S.T., J.L. Dehmer, and P.M. Dehmer, Photoelectron angular distributions from resonant multiphoton ionization of atomic carbon. *J. Chem. Phys.*, **1985**. 82(2): p. 676-680.
201. Streibel, T. and R. Zimmermann, Resonance-Enhanced Multiphoton Ionization Mass Spectrometry (REMPI-MS): Applications for Process Analysis. *Annu. Rev. Anal. Chem.*, **2014**. 7: p. 361-381.
202. Sydlik, U.*, et al.*, Ultrafine carbon particles induce apoptosis and proliferation in rat lung epithelial cells via specific signaling pathways both using EGF-R. *Am. J. Physiol. Lung Cell. Mol. Physiol.*, **2006**. 291(4): p. L725-L733.
203. Bortner, C. and J. Cidlowski, Apoptotic volume decrease and the incredible shrinking cell. *Cell Death Differ.*, **2002**. 9(12): p. 1307-1310.
204. Guerreiro, C.*, et al.*, Air quality in Europe — 2015 report. In: *European Environment Agency Rep*, **2015**.
205. Atkinson, R.W.*, et al.*, Fine particle components and health—a systematic review and meta-analysis of epidemiological time series studies of daily

mortality and hospital admissions. *J. Expo. Sci. Environ. Epidemiol.*, **2015**. 25(2): p. 208-214.
206. Bové, H*., et al.*, Biocompatible label-free detection of carbon black particles by femtosecond pulsed laser microscopy. *Nano Lett.*, **2016**. 16(5): p. 3173-3178.
207. Min, W*., et al.*, Coherent nonlinear optical imaging: beyond fluorescence microscopy. *Annu. Rev. Phys. Chem.*, **2011**. 62: p. 507-530.
208. Villafana, T.E*., et al.*, Femtosecond pump-probe microscopy generates virtual cross-sections in historic artwork. *Proc. Natl. Acad. Sci.*, **2014**. 111(5): p. 1708-1713.
209. Zewail, A.H., Femtochemistry. Past, present, and future. *Pure Appl. Chem.*, **2000**. 72(12): p. 2219-2231.
210. Knee, J.L. and A.H. Zewail, Ultrafast laser spectroscopy of chemical reactions. *Spectroscopy*, **1988**. 3(5): p. 44-53.
211. Zewail, A.H., *Femtochemistry: ultrafast dynamics of the chemical bond*. Vol. 3. **1994**: World Scientific.
212. Graf, J*., et al.*, Nodal quasiparticle meltdown in ultrahigh-resolution pump-probe angle-resolved photoemission. *Nature Phys.*, **2011**. 7(10): p. 805-809.
213. Terada, Y*., et al.*, Real-space imaging of transient carrier dynamics by nanoscale pump-probe microscopy. *Nat. Photon.*, **2010**. 4(12): p. 869-874.
214. Tzallas, P*., et al.*, Extreme-ultraviolet pump-probe studies of one-femtosecond-scale electron dynamics. *Nature Phys.*, **2011**. 7(10): p. 781-784.
215. Min, W*., et al.*, Imaging chromophores with undetectable fluorescence by stimulated emission microscopy. *Nature*, **2009**. 461(7267): p. 1105-1109.
216. Tong, L*., et al.*, Label-free imaging of semiconducting and metallic carbon nanotubes in cells and mice using transient absorption microscopy. *Nat Nano*, **2012**. 7(1): p. 56-61.
217. Hartland, G.V., Ultrafast studies of single semiconductor and metal nanostructures through transient absorption microscopy. *Chem. Sci.*, **2010**. 1(3): p. 303-309.
218. Chong, S., W. Min, and X.S. Xie, Ground-state depletion microscopy: detection sensitivity of single-molecule optical absorption at room temperature. *J. Phys. Chem. Lett.*, **2010**. 1(23): p. 3316-3322.
219. Mehl, B.P*., et al.*, The end is different than the middle: spatially dependent dynamics in ZnO rods observed by femtosecond pump–probe microscopy. *J. Phys. Chem. Lett.*, **2011**. 2(14): p. 1777-1781.
220. Lo, S.S*., et al.*, Imaging the extent of plasmon excitation in Au nanowires using pump-probe microscopy. *Opt. Lett.*, **2013**. 38(8): p. 1265-1267.

221. Simpson, M.J*., et al.*, Separation of distinct photoexcitation species in femtosecond transient absorption microscopy. *ACS Photonics*, **2016**. 3(3): p. 434-442.
222. Chen, T*., et al.*, Optical imaging of non-fluorescent nanodiamonds in live cells using transient absorption microscopy. *Nanoscale*, **2013**. 5(11): p. 4701-4705.
223. Li, J*., et al.*, Highly sensitive transient absorption imaging of graphene and graphene oxide in living cells and circulating blood. *Sci. Rep.*, **2015**. 5: p. 12394.
224. Fu, D*., et al.*, Probing skin pigmentation changes with transient absorption imaging of eumelanin and pheomelanin. *J. Biomed. Opt.*, **2008**. 13(5): p. 054036-054037.
225. Miyazaki, J*., et al.*, Sub-diffraction resolution pump-probe microscopy with shot-noise limited sensitivity using laser diodes. *Opt. Express*, **2014**. 22(8): p. 9024-9032.
226. Edwards, I.A., R. Menendez, and H. Marsh, *Introduction to carbon science*. **2013**: Butterworth-Heinemann.
227. Margraf, J.T*., et al.*, The electronic structure of amorphous carbon nanodots. *J. Phys. Chem. B*, **2015**. 119(24): p. 7258-7265.
228. Reckmeier, C*., et al.*, Luminescent colloidal carbon dots: optical properties and effects of doping. *Opt. Express*, **2016**. 24(2): p. 312-340.
229. Sui, L*., et al.*, Ultrafast carrier dynamics of carbon nanodots in different pH environments. *Phys. Chem. Chem. Phys.*, **2016**. 18(5): p. 3838-3845.
230. Fischer, M.C*., et al.*, Invited review article: pump-probe microscopy. *Rev. Sci. Instrum.*, **2016**. 87(3): p. 031101.
231. Kastrup, L. and S.W. Hell, Absolute optical cross section of individual fluorescent molecules. *Angew. Chem. Int. Ed.*, **2004**. 43(48): p. 6646-6649.
232. Jain, P.K*., et al.*, Calculated absorption and scattering properties of gold nanoparticles of different size, shape, and composition: applications in biological imaging and biomedicine. *J. Phys. Chem. B*, **2006**. 110(14): p. 7238-7248.
233. Forget, S. and S. Chénais, Fundamentals of Organic Lasers, in: *Organic Solid-State Lasers*. **2013**, Springer. p. 13-73.
234. Shirdel, J*., et al.*, Absorption and fluorescence spectroscopic characterisation of the circadian blue-light photoreceptor cryptochrome from Drosophila melanogaster (dCry). *Chem. Phys.*, **2008**. 352(1): p. 35-47.
235. Chen, H*., et al.*, Modification in light absorption cross section of laboratory-generated black carbon-brown carbon particles upon surface reaction and hydration. *Atmos. Environ.*, **2015**. 116: p. 253-261.

236. Lunov, O.*, et al.*, Modeling receptor-mediated endocytosis of polymer-functionalized iron oxide nanoparticles by human macrophages. *Biomaterials*, **2011**. 32(2): p. 547-555.
237. Piazza, R., Thermophoresis: moving particles with thermal gradients. *Soft Matter*, **2008**. 4(9): p. 1740-1744.
238. Malacarne, L.*, et al.*, Soret effect and photochemical reaction in liquids with laser-induced local heating. *Opt. Express*, **2011**. 19(5): p. 4047-4058.
239. Anwer, A.G.*, et al.*, Distinctive autofluorescence of urine samples from individuals with bacteriuria compared with normals. *Clin. Chim. Acta*, **2009**. 401(1): p. 73-75.
240. Bukowski, E.J. and F.V. Bright, Minimizing urine autofluorescence under multi-photon excitation conditions. *Appl. Spectrosc.*, **2004**. 58(9): p. 1101-1105.
241. Wei, L. and W. Min, Pump-probe optical microscopy for imaging nonfluorescent chromophores. *Anal. Bioanal. Chem.*, **2012**. 403(8): p. 2197-2202.
242. Cukierman, E.*, et al.*, Taking cell-matrix adhesions to the third dimension. *Science*, **2001**. 294(5547): p. 1708-1712.
243. Pampaloni, F., E.G. Reynaud, and E.H. Stelzer, The third dimension bridges the gap between cell culture and live tissue. *Nat. Rev. Mol. Cell Biol.*, **2007**. 8(10): p. 839-845.
244. Loessner, D.*, et al.*, Bioengineered 3D platform to explore cell–ECM interactions and drug resistance of epithelial ovarian cancer cells. *Biomaterials*, **2010**. 31(32): p. 8494-8506.
245. Mammoto, T. and D.E. Ingber, Mechanical control of tissue and organ development. *Development*, **2010**. 137(9): p. 1407-1420.
246. Gilbert, P.M.*, et al.*, Substrate elasticity regulates skeletal muscle stem cell self-renewal in culture. *Science*, **2010**. 329(5995): p. 1078-1081.
247. Carey, S.P.*, et al.*, Biophysical control of invasive tumor cell behavior by extracellular matrix microarchitecture. *Biomaterials*, **2012**. 33(16): p. 4157-4165.
248. Huebsch, N.*, et al.*, Harnessing traction-mediated manipulation of the cell/matrix interface to control stem-cell fate. *Nat. Mater.*, **2010**. 9(6): p. 518-526.
249. Lutolf, M.P., P.M. Gilbert, and H.M. Blau, Designing materials to direct stem-cell fate. *Nature*, **2009**. 462(7272): p. 433-441.
250. Ghosh, K.*, et al.*, Cell adaptation to a physiologically relevant ECM mimic with different viscoelastic properties. *Biomaterials*, **2007**. 28(4): p. 671-679.
251. Bott, K.*, et al.*, The effect of matrix characteristics on fibroblast proliferation in 3D gels. *Biomaterials*, **2010**. 31(32): p. 8454-8464.

252. Wang, J. and B. Li, The principles and biological applications of cell traction force microscopy. *Microscopy: Science, Technology, Applications and Education*, **2010**: p. 449-458.
253. Oliver, T., K. Jacobson, and M. Dembo, Traction forces in locomoting cells. *Cell Motil. Cytoskeleton*, **1995**. 31(3): p. 225-240.
254. Dembo, M.*, et al.*, Imaging the traction stresses exerted by locomoting cells with the elastic substratum method. *Biophys. J.*, **1996**. 70(4): p. 2008-2022.
255. Lee, J.*, et al.*, Traction forces generated by locomoting keratocytes. *J. Cell Biol.*, **1994**. 127(6): p. 1957-1964.
256. Legant, W.R.*, et al.*, Measurement of mechanical tractions exerted by cells in three-dimensional matrices. *Nat. Methods*, **2010**. 7(12): p. 969-971.
257. Steinwachs, J.*, et al.*, Three-dimensional force microscopy of cells in biopolymer networks. *Nat. Methods*, **2015**.
258. Stout, D.A.*, et al.*, Mean deformation metrics for quantifying 3D cell–matrix interactions without requiring information about matrix material properties. *Proc. Natl. Acad. Sci.*, **2016**. 113(11): p. 2898-2903.
259. Han, S.J.*, et al.*, Traction microscopy to identify force modulation in subresolution adhesions. *Nat. Methods*, **2015**. 12(7): p. 653-656.
260. Tolić-Nørrelykke, I.M.*, et al.*, Spatial and temporal traction response in human airway smooth muscle cells. *Am. J. Physiol., Cell Physiol.*, **2002**. 283(4): p. C1254-C1266.
261. Sabass, B.*, et al.*, High resolution traction force microscopy based on experimental and computational advances. *Biophys. J.*, **2008**. 94(1): p. 207-220.
262. Colin-York, H.*, et al.*, Super-resolved traction force microscopy (STFM). *Nano Lett.*, **2016**. 16(4): p. 2633-2638.
263. Kim, J.*, et al.*, Three-Dimensional Reflectance Traction Microscopy. *PloS one*, **2016**. 11(6): p. e0156797.
264. Bar-Kochba, E.*, et al.*, A fast iterative digital volume correlation algorithm for large deformations. *Exp. Mech.*, **2015**. 55(1): p. 261-274.
265. Jorge-Peñas, A.*, et al.*, Free Form Deformation–Based Image Registration Improves Accuracy of Traction Force Microscopy. *PloS one*, **2015**. 10(12): p. e0144184.
266. Sanen, K.*, et al.*, Label-free mapping of microstructural organisation in self-aligning cellular collagen hydrogels using image correlation spectroscopy. *Acta Biomater.*, **2016**. 30: p. 258-264.
267. Pavone, F.S. and P.J. Campagnola, *Second harmonic generation imaging*. **2013**: CRC Press.
268. Hebert, B., S. Costantino, and P.W. Wiseman, Spatiotemporal image correlation spectroscopy (STICS) theory, verification, and application to

protein velocity mapping in living CHO cells. *Biophys. J.*, **2005**. 88(5): p. 3601-3614.
269. Wiseman, P.W., Image correlation spectroscopy: mapping correlations in space, time, and reciprocal space. *Methods Enzymol.*, **2013**. 518: p. 245-267.
270. Jorge-Peñas, A*., et al.*, Validation tool for traction force microscopy. *Comput. Methods Biomech. Biomed. Engin.*, **2015**. 18(13): p. 1377-1385.
271. Garcia, D., Robust smoothing of gridded data in one and higher dimensions with missing values. *Comput. Stat. Data Anal.*, **2010**. 54(4): p. 1167-1178.
272. Klein, S*., et al.*, Adaptive stochastic gradient descent optimisation for image registration. *Int. J. Comput. Vision*, **2009**. 81(3): p. 227-239.
273. Klein, S*., et al.*, Elastix: a toolbox for intensity-based medical image registration. *IEEE Trans. Med. Imaging*, **2010**. 29(1): p. 196-205.
274. Carlini, L*., et al.*, Correction of a depth-dependent lateral distortion in 3D super-resolution imaging. *PloS one*, **2015**. 10(11): p. e0142949.
275. Koch, T.M*., et al.*, 3D traction forces in cancer cell invasion. *PloS one*, **2012**. 7(3): p. e33476.
276. Schwarz, L.A., Non-rigid registration using free-form deformations. *Ph.D. dissertation, Dept. Comput. Sci., Tech. Univ. Munchen*, **2007**.
277. Jorge-Peñas, A., Development and validation of computational tools for semi-3D traction force microscopy. *Ph.D. dissertation, University of Navarra*, **2013**.
278. Kolin, D.L. and P.W. Wiseman, Advances in image correlation spectroscopy: measuring number densities, aggregation states, and dynamics of fluorescently labeled macromolecules in cells. *Cell Biochem. Biophys.*, **2007**. 49(3): p. 141-164.
279. Kolin, D.L., S. Costantino, and P.W. Wiseman, Sampling effects, noise, and photobleaching in temporal image correlation spectroscopy. *Biophys. J.*, **2006**. 90(2): p. 628-639.
280. Pedersen, M*., et al.*, Ambient air pollution and low birthweight: a European cohort study (ESCAPE). *Lancet Respir. Med.*, **2013**. 1(9): p. 695-704.
281. Nawrot, T.S*., et al.*, Public health importance of triggers of myocardial infarction: a comparative risk assessment. *Lancet*, **2011**. 377(9767): p. 732-740.
282. Guerra, S*., et al.*, Relation between circulating CC16 concentrations, lung function, and development of chronic obstructive pulmonary disease across the lifespan: a prospective study. *Lancet Respir. Med.*, **2015**. 3(8): p. 613-620.

283. Raaschou-Nielsen, O*., et al.*, Air pollution and lung cancer incidence in 17 European cohorts: prospective analyses from the European Study of Cohorts for Air Pollution Effects (ESCAPE). *Lancet Oncol.*, **2013**. 14(9): p. 813-822.
284. Pieters, N*., et al.*, An epidemiological appraisal of the association between heart rate variability and particulate air pollution: a meta-analysis. *Heart*, **2012**. 98(15): p. 1127-1135.
285. Shimada, A*., et al.*, Translocation pathway of the intratracheally instilled ultrafine particles from the lung into the blood circulation in the mouse. *Toxicol. Pathol.*, **2006**. 34(7): p. 949-957.
286. Lefebvre, W*., et al.*, Presentation and evaluation of an integrated model chain to respond to traffic-and health-related policy questions. *Environ. Modell. Softw.*, **2013**. 40: p. 160-170.
287. Sheppard, L*., et al.*, Confounding and exposure measurement error in air pollution epidemiology. *Air Qual. Atmos. Health*, **2012**. 5(2): p. 203-216.
288. Chutipongtanate, S. and V. Thongboonkerd, Systematic comparisons of artificial urine formulas for in vitro cellular study. *Anal. Biochem.*, **2010**. 402(1): p. 110-112.
289. Kelly, J.T. and B. Asgharian, Nasal molds as predictors of fine and coarse particle deposition in rat nasal airways. *Inhal. Toxicol.*, **2003**. 15.
290. Janssen, S*., et al.*, Spatial interpolation of air pollution measurements using CORINE land cover data. *Atmos. Environ.*, **2008**. 42(20): p. 4884-4903.
291. Lefebvre, W*., et al.*, Validation of the MIMOSA-AURORA-IFDM model chain for policy support: modeling concentrations of elemental carbon in Flanders. *Atmos. Environ.*, **2011**. 45(37): p. 6705-6713.
292. Maiheu, B*., et al.*, Identifying the Best Available Large-Scale Concentration Maps for Air Quality in Belgium. Study Commissioned by the Flemish Environment, MIRA. *Flemish Institute for Technological Research: Mol, Belgium.*, **2013**.
293. Meiring, J.J*., et al.*, The influence of hydrogen peroxide and histamine on lung permeability and translocation of iridium nanoparticles in the isolated perfused rat lung. *Part. Fibre Toxicol.*, **2005**. 2.
294. Geiser, M*., et al.*, Ultrafine particles cross cellular membranes by nonphagocytic mechanisms in lungs and in cultured cells. *Environ. Health Perspect.*, **2005**: p. 1555-1560.
295. Miller, M.R*., et al.*, Inhaled Nanoparticles Accumulate at Sites of Vascular Disease. *ACS nano*, **2017**.
296. Moller, W*., et al.*, Deposition, retention, and translocation of ultrafine particles from the central airways and lung periphery. *Am. J. Respir. Crit. Care Med.*, **2008**. 177(4): p. 426-432.

297. Churg, A. and M. Brauer, Human lung parenchyma retains PM2.5. *Am. J. Respir. Crit. Care Med.*, **1997**. 155(6): p. 2109-2111.
298. Brauer, M.*, et al.*, Air pollution and retained particles in the lung. *Environ. Health Perspect.*, **2001**. 109(10): p. 1039.
299. Lettieri Barbato, D.*, et al.*, Traffic air pollution and oxidatively generated DNA damage: can urinary 8-oxo-7,8-dihydro-2-deoxiguanosine be considered a good biomarker? A meta-analysis. *Biomarkers : biochemical indicators of exposure, response, and susceptibility to chemicals*, **2010**. 15(6): p. 538-545.
300. Staessen, J.A.*, et al.*, Renal function, cytogenetic measurements, and sexual development in adolescents in relation to environmental pollutants: a feasibility study of biomarkers. *Lancet*, **2001**. 357(9269): p. 1660-1669.
301. Kicinski, M.*, et al.*, Neurobehavioral performance in adolescents is inversely associated with traffic exposure. *Environ. Int.*, **2015**. 75: p. 136-143.
302. Kulkarni, N.*, et al.*, Carbon in airway macrophages and lung function in children. *N. Engl. J. Med.*, **2006**. 355(1): p. 21-30.
303. Jacobs, L.*, et al.*, Air pollution-related prothrombotic changes in persons with diabetes. *Environ. Health Perspect.*, **2010**. 118(2): p. 191.
304. Xiong, C. and S. Friedlander, Morphological properties of atmospheric aerosol aggregates. *Proc. Natl. Acad. Sci.*, **2001**. 98(21): p. 11851-11856.
305. Choi, C.H.J.*, et al.*, Targeting kidney mesangium by nanoparticles of defined size. *Proc. Natl. Acad. Sci.*, **2011**. 108(16): p. 6656-6661.
306. Röding, M.*, et al.*, Measuring absolute nanoparticle number concentrations from particle count time series. *J. Microsc.*, **2013**. 251(1): p. 19-26.
307. Röding, M.*, et al.*, Measuring absolute number concentrations of nanoparticles using single-particle tracking. *Phys. Rev. E*, **2011**. 84(3): p. 031920.
308. Röding, M.*, et al.*, Self-calibrated concentration measurements of polydisperse nanoparticles. *J. Microsc.*, **2013**. 252(1): p. 79-88.
309. Miller, M.R.*, et al.*, Inhaled Nanoparticles Accumulate at Sites of Vascular Disease. *ACS nano*, **2017**. 11(5): p. 4542-4552.
310. Mills, N.L.*, et al.*, Combustion-derived nanoparticulate induces the adverse vascular effects of diesel exhaust inhalation. *European heart journal*, **2011**. 32(21): p. 2660-2671.
311. Dobrovolskaia, M.A.*, et al.*, Ins and Outs in Environmental and Occupational Safety Studies of Asthma and Engineered Nanomaterials. *ACS nano*, **2017**.

312. Stone, V., H. Johnston, and M.J. Clift, Air pollution, ultrafine and nanoparticle toxicology: cellular and molecular interactions. *IEEE Trans. Nanobioscience*, **2007**. 6(4): p. 331-340.
313. Adamson, I., C. Hedgecock, and D. Bowden, Epithelial cell-fibroblast interactions in lung injury and repair. *Am. J. Pathol.*, **1990**. 137(2): p. 385.
314. Desmouliere, A*., et al.*, Apoptosis mediates the decrease in cellularity during the transition between granulation tissue and scar. *Am. J. Pathol.*, **1995**. 146(1): p. 56.
315. Glaros, T., M. Larsen, and L. Li, Macrophages and fibroblasts during inflammation, tissue damage and organ injury. *Front. Biosci.*, **2009**. 14: p. 3988-3993.
316. Han, X*., et al.*, Assessing the relevance of in vitro studies in nanotoxicology by examining correlations between in vitro and in vivo data. *Toxicology*, **2012**. 297(1): p. 1-9.
317. Hayes, A.W. and C.L. Kruger, *Hayes' principles and methods of toxicology*. **2014**: CRC Press.
318. Li, N*., et al.*, Particulate air pollutants and asthma: a paradigm for the role of oxidative stress in PM-induced adverse health effects. *Clin. Immunol.*, **2003**. 109(3): p. 250-265.
319. Kroll, A*., et al.*, Cytotoxicity screening of 23 engineered nanomaterials using a test matrix of ten cell lines and three different assays. *Part. Fibre Toxicol.*, **2011**. 8(1): p. 9.
320. Phalen, R.F., M.J. Oldham, and A.E. Nel, Tracheobronchial particle dose considerations for in vitro toxicology studies. *Toxicol. Sci.*, **2006**. 92(1): p. 126-132.
321. Koike, E. and T. Kobayashi, Chemical and biological oxidative effects of carbon black nanoparticles. *Chemosphere*, **2006**. 65(6): p. 946-951.
322. Jorge-Penas, A*., et al.*, 3D full-field quantification of cell-induced large deformation in fibrillary biomaterials by combining non-rigid image registration with label-free second harmonic generation. *Biomaterials*, **2017**. 136: p. 86-97.
323. Thiele, G., M. Poston, and R. Brown. A case study in sizing nanoparticles. Micromeritics Analytical Services and MVA Scientific Consultants **2010**.
324. Xia, T*., et al.*, Comparison of the abilities of ambient and manufactured nanoparticles to induce cellular toxicity according to an oxidative stress paradigm. *Nano Lett.*, **2006**. 6(8): p. 1794-1807.
325. Long, T.C*., et al.*, Nanosize titanium dioxide stimulates reactive oxygen species in brain microglia and damages neurons in vitro. *Environ. Health Perspect.*, **2007**: p. 1631-1637.
326. Phenrat, T*., et al.*, Aggregation and sedimentation of aqueous nanoscale zerovalent iron dispersions. *Environ. Sci. Technol.*, **2007**. 41(1): p. 284-290.

327. Ruh, H.*, et al.*, Identification of serum proteins bound to industrial nanomaterials. *Toxicol. Lett.*, **2012**. 208(1): p. 41-50.
328. Xia, X.R.*, et al.*, Mapping the surface adsorption forces of nanomaterials in biological systems. *ACS nano*, **2011**. 5(11): p. 9074-9081.
329. Li, Y. and D. Boraschi, Endotoxin contamination: a key element in the interpretation of nanosafety studies. *Nanomedicine*, **2016**. 11(3): p. 269-287.
330. Ryan, J., Endotoxins and cell culture. *Corning Life Sciences Technical Bulletin*, **2004**: p. 1-8.
331. Gorbet, M.B. and M.V. Sefton, Endotoxin: the uninvited guest. *Biomaterials*, **2005**. 26(34): p. 6811-6817.
332. Gould, M., Endotoxin in vertebrate cell culture: its measurement and significance. *In Vitro Monogr.*, **1984**. 5(Tissue Culture Association): p. 125-136.
333. Donaldson, K.*, et al.*, The biologically effective dose in inhalation nanotoxicology. *Acc. Chem. Res.*, **2012**. 46(3): p. 723-732.
334. Wojtala, A.*, et al.*, Methods to monitor ROS production by fluorescence microscopy and fluorometry. *Methods Enzymol*, **2014**. 542: p. 243-262.
335. Cao, Y.*, et al.*, Carbon black nanoparticles promote endothelial activation and lipid accumulation in macrophages independently of intracellular ROS production. *PloS one*, **2014**. 9(9): p. e106711.
336. Frikke-Schmidt, H.*, et al.*, Effect of vitamin C and iron chelation on diesel exhaust particle and carbon black induced oxidative damage and cell adhesion molecule expression in human endothelial cells. *Toxicol. Lett.*, **2011**. 203(3): p. 181-189.
337. Vesterdal, L.K.*, et al.*, Carbon black nanoparticles and vascular dysfunction in cultured endothelial cells and artery segments. *Toxicol. Lett.*, **2012**. 214(1): p. 19-26.
338. Manke, A., L. Wang, and Y. Rojanasakul, Mechanisms of nanoparticle-induced oxidative stress and toxicity. *Biomed. Res. Int.*, **2013**. 2013.
339. Sies, H., *Oxidative stress*. **2013**: Elsevier.
340. Sheridan, C. and S.J. Martin, Mitochondrial fission/fusion dynamics and apoptosis. *Mitochondrion*, **2010**. 10(6): p. 640-648.
341. Youle, R.J. and A.M. Van Der Bliek, Mitochondrial fission, fusion, and stress. *Science*, **2012**. 337(6098): p. 1062-1065.
342. Alaimo, A.*, et al.*, Deregulation of mitochondria-shaping proteins Opa-1 and Drp-1 in manganese-induced apoptosis. *PloS one*, **2014**. 9(3): p. e91848.
343. Chen, H., A. Chomyn, and D.C. Chan, Disruption of fusion results in mitochondrial heterogeneity and dysfunction. *J. Biol. Chem.*, **2005**. 280(28): p. 26185-26192.

344. Li, N.*, et al.*, Ultrafine particulate pollutants induce oxidative stress and mitochondrial damage. *Environ. Health Perspect.*, **2003**. 111.
345. Murphy, M.P., How mitochondria produce reactive oxygen species. *Biochem. J.*, **2009**. 417(1): p. 1-13.
346. Boonstra, J. and J.A. Post, Molecular events associated with reactive oxygen species and cell cycle progression in mammalian cells. *Gene*, **2004**. 337: p. 1-13.
347. Turrens, J.F., Mitochondrial formation of reactive oxygen species. *J. Physiol.*, **2003**. 552(2): p. 335-344.
348. Nel, A.*, et al.*, Toxic potential of materials at the nanolevel. *Science*, **2006**. 311(5761): p. 622-627.
349. Santos, S.M.*, et al.*, Interaction of fullerene nanoparticles with biomembranes: from the partition in lipid membranes to effects on mitochondrial bioenergetics. *Toxicol. Sci.*, **2013**: p. kft327.
350. Berg, J.M., J.L. Tymoczko, and L. Stryer, *Biochemistry, Fifth Edition*. **2002**: W.H. Freeman.
351. Soenen, S.J.*, et al.*, Cellular toxicity of inorganic nanoparticles: common aspects and guidelines for improved nanotoxicity evaluation. *Nano Today*, **2011**. 6(5): p. 446-465.
352. Soenen, S.J.*, et al.*, Cytotoxic effects of gold nanoparticles: a multiparametric study. *ACS nano*, **2012**. 6(7): p. 5767-5783.
353. Asaga, H., S. Kikuchi, and K. Yoshizato, Collagen gel contraction by fibroblasts requires cellular fibronectin but not plasma fibronectin. *Exp. Cell Res.*, **1991**. 193(1): p. 167-174.
354. Warheit, D.B.*, et al.*, Development of a short-term inhalation bioassay to assess pulmonary toxicity of inhaled particles: comparisons of pulmonary responses to carbonyl iron and silica. *Toxicol. Appl. Pharmacol.*, **1991**. 107.
355. Kabakov, A.E. and V.L. Gabai, *Heat shock proteins and cytoprotection: ATP-deprived mammalian cells*. **1997**: Springer.
356. Hinshaw, D.*, et al.*, ATP and microfilaments in cellular oxidant injury. *Am. J. Pathol.*, **1988**. 132(3): p. 479.
357. Svitkina, T.M., A. Neyfakh, and A.D. Bershadsky, Actin cytoskeleton of spread fibroblasts appears to assemble at the cell edges. *J. Cell Sci.*, **1986**. 82(1): p. 235-248.
358. Nishimura, Y., L.H. Romer, and J.J. Lemasters, Mitochondrial dysfunction and cytoskeletal disruption during chemical hypoxia to cultured rat hepatic sinusoidal endothelial cells: the pH paradox and cytoprotection by glucose, acidotic pH, and glycine. *Hepatology*, **1998**. 27(4): p. 1039-1049.
359. Pollard, T.D. and G.G. Borisy, Cellular motility driven by assembly and disassembly of actin filaments. *Cell*, **2003**. 112(4): p. 453-465.

360. Geiger, B., J.P. Spatz, and A.D. Bershadsky, Environmental sensing through focal adhesions. *Nat. Rev. Mol. Cell Biol.*, **2009**. 10(1): p. 21-33.
361. Schwarz, U.S. and M.L. Gardel, United we stand–integrating the actin cytoskeleton and cell–matrix adhesions in cellular mechanotransduction. *J. Cell Sci.*, **2012**. 125(13): p. 3051-3060.
362. Oakes, P.W. and M.L. Gardel, Stressing the limits of focal adhesion mechanosensitivity. *Curr. Opin. Cell Biol.*, **2014**. 30: p. 68-73.
363. Chortarea, S.*, et al.*, Human Asthmatic Bronchial Cells are more Susceptible to Sub-Chronic Repeated Exposures of Aerosolized Carbon Nanotubes at Occupationally-Relevant Doses than Healthy Cells. *ACS nano*, **2017**.
364. WHO, World Health Organization. Health aspects of air pollution with particulate matter, ozone and nitrogen dioxide: report on a WHO working group, Bonn, Germany 13-15 January 2003. **2003**.
365. Sutariya, V.B. and Y. Pathak, *Biointeractions of nanomaterials*. **2014**: CRC Press.
366. Brackx, M.*, et al.*, Hyperspectral leaf reflectance of Carpinus betulus L. saplings for urban air quality estimation. *Environ. Pollut.*, **2017**. 220: p. 159-167.
367. Baldacchini, C.*, et al.*, How does the amount and composition of PM deposited on Platanus acerifolia leaves change across different cities in Europe? *Environ. Sci. Technol.*, **2017**.
368. Bloemen, H.T.*, et al.*, Monitoring Black Smoke? Its Value for Monitoring the Impact of Abatament Measures. In: *RIVM Letter Report*, **2007**. 863001004.
369. Forouzanfar, M.H.*, et al.*, Global, regional, and national comparative risk assessment of 79 behavioural, environmental and occupational, and metabolic risks or clusters of risks in 188 countries, 1990–2013: a systematic analysis for the Global Burden of Disease Study 2013. *The Lancet*, **2015**. 386(10010): p. 2287-2323.

Curriculum vitae

Hannelore Bové was born on September 4th 1990 in Neerpelt. In 2008 she obtained her degree Technical Secondary Education (Technisch Secundair Onderwijs) in the study option Technical Sciences (Techniek-wetenschappen) at WICO campus Sint-Maria in Neerpelt. In the same year she began her higher education studies at Hasselt University where she graduated summa cum laude in 2013 as Master in Biomedical Sciences with specialization Bio-electronics and Nanotechnology. Her thesis entitled 'Micro- and nanostructured molecularly imprinted polymers for advanced recognition of endocrine disruptors' was conducted at the Institute for Materials Research under supervision of Prof. dr. A. Ethirajan. In September 2013, she started her PhD at the Biomedical Research Institute of Hasselt University and the Centre for Surface Chemistry and Catalysis of KU Leuven. During this period, she participated in various assignments and courses framed within the Doctoral School for Medicine and Life Sciences and the Leuven Arenberg Doctoral School, like project management, biosafety and academic English. She was active as member of different teaching teams of various courses in the study programs Biomedical Sciences, Biology and Medicine. Furthermore, she co-organized the third μFIBR symposium and received in 2014 a FWO aspirant mandate. The results obtained during her PhD work were partially published in international journals, presented at various (inter)national congresses and translated in a patent application. At the 9th Biomedica Summit in 2015 she received the price for best poster presentation.

Bibliography

Publications

Publications from this work

- **Bové H***, Steuwe C*, Fron E, Slenders E, D'Haen J, Fujita Y, Uji-i H, vandeVen M, Roeffaers M, Ameloot M. *Biocompatible label-free detection of carbon black particles by femtosecond pulsed laser microscopy.* Nano Letters (2016); 16 (5): 3173–3178. IF(2015) = 13.779. *Equally contributing first authors.
- Jorge-Peñas A*, **Bové H***, Sanen K, Vaeyens M-M, Steuwe C, Roeffaers M, Ameloot M, Van Oosterwyck H. *3D full-field quantification of cell-induced large deformation in fibrillary biomaterials by combining non-rigid image registration with label-free second harmonic generation.* Biomaterials (2017); 136: 86-97. IF(2015) = 8.557. *Equally contributing first authors.
- Saenen N*, **Bové H***, Steuwe C, Roeffaers M, Provost E, Lefebvre W, Vanpoucke C, Ameloot M, Nawrot T. Children's urinary environmental carbon load: a novel marker reflecting residential ambient air pollution exposure? American Journal of Respiratory and Critical Care Medicine (2017). IF(2015)=13.118. * Equally contributing first authors.

Publications from collaborative projects

- Kellens E, **Bové H**, Conradi M, D'Olieslaeger L, Wagner P, Landfester K, Junkers T, Ethirajan A. *Improved molecular imprinting based on colloidal particles made from miniemulsion: A case study on testosterone and its structural analogues.* Macromolecules (2016); 49 (7): 2559–2567. IF(2015) = 5.554.
- Peters M, Zaquen N, D'Olieslaeger L, **Bové H**, Vanderzande D, Hellings N, Junkers T, Ethirajan A. *PPV-based conjugated polymer nanoparticles as a versatile bioimaging probe: A closer look at the inherent optical properties and nanoparticle–cell interactions.* Biomacromolecules (2016); 17 (8): 2562–2571. IF(2015) = 5.583.

Patent

Ameloot M, **Bové H**, Nawrot T, Roeffaers M, Steuwe C, vandeVen M. *PCT application: carbonaceous particles*. Filed on 2017-01-12, assigned to Hasselt University and KU Leuven.

Oral presentations

Bové H, Steuwe C, vandeVen M, Roeffaers M, Ameloot M

Label-free detection of carbonaceous particles using femtosecond pulsed illumination to assess their in vitro toxicology.

- Royal Belgian Society for Microscopy. *Brussels, Belgium*. September 8th-9th, 2016.
- Interuniversity Attraction Poles. *Liège, Belgium.* September 12th, 2016.
- *In vitro* toxicology for Safety Assessment (ESTIV). *Juan-les-Pins, France*. October 17th – 20th, 2016.

Bové H, Van Oosterwyck H, Roeffaers M, Ameloot M

Pollutant carbonaceous particles inhibit human lung fibroblast-mediated extracellular matrix remodeling.

- F-TALES, Nanomaterials in biomedical sciences. *Ghent, Belgium*. September 19th – 20th, 2017.

Selected poster presentations

- **Bové H**, Devoght J, Jorge-Peñas A, D'Haen J, Van Oosterwyck H, Roeffaers M, Ameloot M. *Carbon black nanoparticles induce apoptotic cell death in human lung fibroblasts.* 9th Biomedica Summit. *Genk, Belgium.* June 2nd – 3th, 2015.
- **Bové H**, Steuwe C, Roeffaers M, Ameloot M. *Label-free imaging of carbon black particles using femtosecond pulsed illumination to assess their in vitro toxicology.* Advances in Cell Engineering, Imaging and Screening (ACEIS). *Leuven, Belgium.* November 17th – 18th, 2016.

- **Bové H**, Steuwe C, Saenen N, vandeVen M, Nawrot T, Roeffaers M, Ameloot M. *White particles of dust: Closing the gap in the diagnostic market.* Innovation for Health (IFH). *Rotterdam, the Netherlands.* February 16th, 2017.
- **Bové H**, Steuwe C, Saenen N, Nawrot T, Roeffaers M, Ameloot M. *White-light detection of carbonaceous particles to assess their in vitro and in vivo toxicology.* Methods and applications in fluorescence (MAF). *Bruges, Belgium.* September 10th – 13th, 2017.

Best poster presentation award

Bové H, Devoght J, Jorge-Peñas A, D'Haen J, Van Oosterwyck H, Roeffaers M, Ameloot M. *Carbon black nanoparticles induce apoptotic cell death in human lung fibroblasts.* 9th Biomedica Summit. *Genk, Belgium.* June 2nd – 3th, 2015.

Bursaries

- FWO PhD Fellowship entitled "Advanced optical imaging of changes in the mechanobiology of lung cells induced by carbonaceous nanoparticles employing a 3D in vitro lung model" for 2 x 2 years starting at October 1st, 2014.
- French Society of Cellular Pharmaco-Toxicology travel grant to attend the ESTIV 2016 congress in Juan-les-Pins, France.

Dankwoord

Last but not least…

In mijn ogen is dit het belangrijkste onderdeel van mijn doctoraatsproefschrift, want zonder de hulp en steun van velen zouden de andere hoofdstukken niet bestaan. Tijdens mijn doctoraat hebben namelijk zeer veel personen een belangrijke bijdrage geleverd en ik wil iedereen hiervoor dan ook heel graag bedanken in deze allerlaatste bladzijden van mijn thesis.

Een viertal jaar geleden, na een toch wel zenuwslopende sollicatieprocedure, kreeg ik de kans om een doctoraat met bidiplomering te starten aan de Universiteit Hasselt en Katholieke Universiteit Leuven. Een opportuniteit die zijn oorsprong vond in de samenwerking tussen mijn promotoren Prof. dr. Marcel Ameloot en Prof. dr. Maarten Roeffaers, en copromotor Prof. dr. Hans Van Oosterwyck. Al snel gaven ze mij de vrijheid om zelf een FWO-project uit te werken waarin ik mijn biomedische achtergrond kon combineren met de expertises van de onderzoeksgroepen, bedankt hiervoor.

Allereerst een woord van dank aan mijn promotor van de hoofdinstelling UHasselt, Prof. dr. Marcel Ameloot. Marcel, het heeft even geduurd voordat ik u bij uw voornaam durfde aan te spreken door de diepe, maar weliswaar positieve, indruk die u nagelaten heeft tijdens mijn studententijd. Doorheen de jaren kon ik steeds bij u terecht voor antwoorden op mijn vragen en nieuwe ideeën voor wetenschappelijke problemen. Bovendien wist u altijd mijn bezorgdheden te relativeren. U vond ook altijd een manier om mij te blijven motiveren, bijvoorbeeld met pralines of taart voor het opruimen of kuisen van de Biofysica-ruimtes. Bedankt voor alle kansen en om me het belang van interdisciplinair onderzoek bij te brengen aan de hand van veel boeiende *kruisbestuivingen*.

Daarnaast wil ik mijn KU Leuven promotor Prof. dr. Maarten Roeffaers bedanken voor zijn onvoorwaardelijk enthousiasme over het koolstofverhaal. Maarten, ik heb ontzettend veel geleerd van u, zoals het kritisch analyseren van onderzoeksresultaten en manuscriptteksten om zo te streven naar perfectie en niet te *settelen* voor minder. Bedankt om steeds - vrijwel onmiddellijk - tijd te maken voor een gesprek, ook al blijft het tot op de dag van vandaag moeilijk om me te oriënteren en uw kantoor terug te vinden. Bovendien waardeer ik enorm

uw bijdrage aan de vooruitgang van het project en de manier waarop u mij wist te stimuleren en inspireren op zowel wetenschappelijk als persoonlijk vlak.

Verder wil ik Prof. dr. Ivo Lambrichts, Prof. dr. Hans Van Oosterwyck, Prof. dr. Luc Michiels en Prof. dr. Johan Hofkens bedanken voor hun rol in mijn doctoraatscommissie waarbij ze waardevolle input gegeven hebben ter vormgeving van de wetenschappelijke inhoud van het onderzoeksproject. Daarnaast ben ik hen ook dankbaar voor hun functie in mijn doctoraatsjury, net als Prof. dr. Sven Hendrix, Prof. dr. Tim Nawrot, Prof. dr. Kevin Braeckmans en Prof. dr. Roeland Samson. In het bijzonder voor het kritisch lezen en beoordelen van mijn doctoraatsproefschrift, jullie opbouwende suggesties en adviezen hebben de kwaliteit van mijn thesis versterkt.

Onderzoek vereist uiteraard ook enige vorm van financiering, ik wil dan ook het FWO bedanken voor de financiële ondersteuning tijdens mijn doctoraat.

Ook de goede administratieve omkadering mag ik zeker niet vergeten, want ondanks het feit dat de bidiplomering een verrijkende factor was tijdens mijn doctoraat bracht het ook heel wat extra papierwerk en afspraken met zich mee. Ik wil hiervoor dan ook zeker een aantal mensen van de Geneeskunde & Levenswetenschappen en Arenberg doctoral schools alsook andere administratieve instanties hartelijk bedanken, met name: Stefanie Kerkhofs, Kim Pannemans, Sophie Indestege, Indra Hautekiet, Leen Cuypers en Annemie Schellens. Over administratieve ondersteuning gesproken, Véronique jij verdient een dikke pluim of nog beter een standbeeld! Iedere dag - ongeacht of het een werk-, zon- of feestdag is - sta jij klaar voor alle doctoraatstudenten van BIOMED om ze doorheen de laatste fase van hun doctoraat te loodsen. Niets is je te veel en we kunnen altijd bij je binnenvallen met grote of kleine bezorgdheden, waarvoor heel veel dank! Rani, dankjewel voor de administratieve ondersteuning, om verdwenen pakjes op te sporen of te helpen dweilen wanneer ons kantoor volledig onder water stond na een hevige stortbui. Daarnaast heb ik ook een fantastische ondersteuning mogen ervaren van de financiële dienst bij het plaatsen van ‘dringende’ bestellingen, het boeken van vluchten en hotels voor congressen, … waarvoor dank aan Jean, Laura, Hilde en Jessica.

Een extra verrijking tijdens mijn doctoraat was ongetwijfeld het beschermen van onze intellectuele eigendom in de vorm van een octrooi. An Voets, bedankt om vanaf het eerste moment te geloven in de patenteerbaarheid van het koolstofverhaal. Zonder jou zouden we nooit stilgestaan hebben bij deze mogelijkheid. Dankjewel voor alle ondersteuning, zoals het nalezen van aanvragen, het herhaaldelijk uitleggen van het verschil tussen nieuwe en inventieve bevindingen en zoveel meer. In dit opzicht dien ik ook alle medewerkers van de diensten TTO (UHasselt) en LRD (KU Leuven) alsook Nele Weyens te complimenteren voor alle hulp en adviezen.

Door de interdisciplinaire aard van mijn onderzoek heb ik de eer gehad om samen te werken met verschillende onderzoeksgroepen. Het was niet altijd even evident om mijn tijd en focus gelijk te verdelen, maar gelukkig kon ik steeds rekenen op ontzettend veel personen. Ik wil alvast iedereen bedanken voor het geduld en de hulp.

Toen ik me vier jaar geleden bij het Biofysica team vervoegde, kwam ik direct in een dynamische en toffe groep terecht. Eén voor één unieke personen met uitgesproken complementaire talenten: Ben met zijn fotografische bedrevenheid, Kristof met zijn gesofisticeerde woordenschat, Rik en Nick met hun indrukwekkende MATLAB skills, Sarah met haar nauwgezette en gestructureerde werkwijze, Kathleen met haar "the-art-of-making-collagen-hydrogels" vaardigheden en Rozhin who was always very optimistic and ready to help others. Later werd de groep uitgebreid met Daniel, Martin, Eli, Srujan en Bart. Bowlingen, boerengolfen, karten, lasergamen, spelletjesavonden, … dit heeft allemaal bijgedragen aan een fijne groepssfeer, waarvoor dank! Ik wens ieder van jullie een fantastische toekomst toe.

Er zijn ook enkele Biofysica-collega's die in het bijzonder een extra dankwoordje verdienen voor de intense samenwerking tijdens de afgelopen jaren.

Kathleen, dankjewel om jouw *lab skills* te delen met mij en te zorgen voor de nodige afleiding en ontspanning, zoals onze wekelijkse Zumba sessies of de WhatsApp-groep waarin ik mijn dagelijkse verhalen kwijt kon toen je van job veranderde. Jij bent de meest creatieve, zorgzame en onbaatzuchtige persoon

die ik ken en ik ben er heel zeker van dat je een fantastische toekomst tegemoet gaat! Eli, mijn MATLAB-redder in nood! Bedankt voor de talloze programma's die je voor me geschreven en herschreven hebt, zelfs alle lasagnes ter wereld kunnen jouw werk niet belonen. Dankjewel om altijd naar me te luisteren, het is een eer om samen met jou de Biofysica groep af te ronden. Martin, bedankt om me theoretisch te ondersteunen en me up-to-date te houden met de laatste wetenschappelijke literatuur alsook *tips and tricks* te geven bij het verzorgen van mijn bloemen en planten. De geadopteerde orchidee staat nog steeds mooi in bloei op uw bureel, iets waar ik helaas nooit in slaagde.

Graag wil ik ook alle stagestudenten bedanken die onder mijn begeleiding in het labo gestaan hebben. Jullie hebben allemaal op jullie eigen manier meegeholpen om vorm te geven aan dit onderzoek. Hierbij een speciaal woord van dank aan Jens en Leentje, jullie waren de meest gedreven studenten ooit!

Ook de collega's van de onderzoeksgroepen Fysiologie en Morfologie wil ik bedanken voor alle hulp in het labo en de fijne babbels aan het koffieapparaat, in de celkweek of de Fysiologie-gang.

Allereerst een woordje van dank voor de altijd opgewekte Petra! Jij deed er mij altijd aan denken om te (blijven) glimlachen. Je wist altijd een manier te vinden om een lach op mijn gezicht te toveren en we weten allemaal dat dit geen gemakkelijke klus is ☺. Duizend maal dank voor de talloze keren dat je aan de slag ging met mijn cellen en er op vrijdag zelfs op anticipeerde dat ze nog gesplitst moesten worden. Ook bedankt om te luisteren, de rotzooi van iedereen op te ruimen en gewoon om jezelf te zijn! Sophie, Silke, Sofie, Lize, Dorien en Jens bedankt voor de fijne en ontspannende babbels! Sophie en Silke, ik ben er zeker van dat jullie een fantastisch doctoraat zullen afleveren! Jelle en Veerle, ook al zijn jullie er nog niet zo lang, toch hebben we reeds mogen samenwerken aan de gloednieuwe microscopen, bedankt voor het vlot verloop hiervan.

De lijst is eindeloos: Jessica, dankjewel om me doorheen de laatste fase te gidsen - ik heb jou als fantastisch voorbeeld gehad om te volgen - en bedankt voor de vloeibare aanmoediging ☺. Elien, bedankt voor alle steun en babbels in de gang. Ik ben er zeker van dat je een fantastisch doctoraat zal afleggen over twee jaar! Een dikke merci aan Rosette, Jo, Christel, Igna, Leen, Katrien en Kim voor de introducties van toestellen en de bijhorende *troubleshooting*. Regine bedankt voor het onderhouden van de celkweek en het steriliseren van glaswerk en tipjesdozen.

Ook in Leuven stond er steeds een fantastisch team van personen klaar om complementair mee samen te werken en me te helpen. Christian, ik heb de eer gehad om nauw te mogen samenwerken met jou. Jouw enorme kennis over allerlei onderwerpen blijft mij iedere keer weer verbazen. Ik heb enorm veel van je geleerd, waarvoor dank! Veel succes met de rest van jouw carrière! Alvaro, thank you for running your MATLAB code over and over again on the fibroblasts and to make nice images in Paraview. I very much enjoyed collaborating with you. I wish you all the best in your future career. Pinaki, thank you for the compression and shear experiments on collagen hydrogels, it was an interesting experience. Marie-Mo, bedankt om de controle experimenten uit te voeren en veel succes met het afronden van jouw doctoraat.

Daarnaast wil ik ook alle medewerkers van nationale en internationale samenwerkingen bedanken daarbij in het bijzonder Prof. dr. Tim Nawrot en Nelly Saenen. Het was zeer aangenaam en leerrijk om de 'urine'-studie met jullie op te zetten, waarvoor dank. Nelly, succes met het afronden van jouw doctoraat. Also, I would also like to thank dr. James Phillips and Celia Murray-Dunning for their hospitality when visiting the University College London for experiments on collagen hydrogels.

De allerlaatste pagina van mijn thesis wijd ik met alle plezier aan de allerbelangrijkste personen in mijn leven.

Laurenz, kleine (grote) broer, ik ben enorm trots op jouw verwezenlijkingen aan de Universiteit van Oxford! You made me a very proud sister. Ondanks dat je jonger bent dan mij, ben je mijn grote voorbeeld! Bedankt voor alle steun en ontspannende momenten door jouw hilarische moppen en aanstekelijke schaterlach. Tanya, I am very happy you joined the family and I wish you and my brother all the best in BXL.

Mama en papa, bedankt voor alle kansen die jullie mij gegeven hebben. Dankjewel om steeds klaar te staan en te blijven geloven in mij. Jullie hebben een enorm bijdrage geleverd op zeer veel verschillende vlakken, gaande van het klaarmaken van eten voor ons na een afmattend lange werkdag tot therapeutische telefoongesprekken. Bedankt voor alles en bovenal voor de warme en inspirerende thuisomgeving die jullie mij altijd geboden hebben.

Ook mijn schoonfamilie – Elly & Peter, Line & Kai en Boni – wil ik graag bedanken om mij op te nemen in hun familie en voor de motiverende woorden.

Martijn, liefste schat, jij verdient geen A5, maar een extra hoofdstuk als dank! In goede en in slechte tijden… En laat het nu net dat laatste zijn wat ik uitgetest heb tijdens de voorbije periode. Toch bleef je me altijd steunen in al mijn beslissingen, mijn bezorgdheden relativeren - "*het leven is geen ponykamp"* en "*zwemmen, zwemmen, blijven zwemmen*" - en begrip opbrengen tijdens het vele avond- en weekendwerk. Als pro in (wetenschaps)communicatie heb je altijd de juiste woorden klaar om me gerust te stellen en moed in te spreken. Jij haalt het beste in mij naar boven! DANKJEWEL voor alles, maar vooral om me onvoorwaardelijk lief te hebben. Ik hou van jou!